Experimental and Numerical Study of the Behavior of Three-Way Catalytic Converters under Different Engine Operation Conditions

By

Yuetao Zhang

Bachelor of Science in Automotive Engineering, 1998
Bachelor of Science in Computer Technology and Application, 1998
Tsinghua University, China

Master of Science in Power Machinery and Engineering, 2001
Tsinghua University, China

Submitted to the Department of Mechanical Engineering in Partial Fulfillment of the Requirements for the Degree of

Doctor of Philosophy in Mechanical Engineering

at the

Massachusetts Institute of Technology

September 2005

Author _____
Department of Mechanical Engineering
August, 2005

Certified by _____
Wai K. Cheng
Professor of Mechanical Engineering
Thesis Advisor

Accepted by _____
Lallit Anand
Professor of Mechanical Engineering
Chairman, Department Graduate Committee

Experimental and Numerical Study of the Behavior of Three-Way Catalytic Converters under Different Engine Operation Conditions

By

Yuetao Zhang

Submitted to the Department of Mechanical Engineering
August 2005 in partial fulfillment of the requirements for the degree of
Doctor of Philosophy

Abstract

The thesis reports the studies on how the three-way catalytic converters behave under different operation conditions. The main focus of the work is in the oxygen storage capacity of the three-way catalyst. Rich-to-lean air/fuel ratio step-change experiments were carried out to quantify the oxygen storage capacity. Results show that the amount of oxygen stored is dependent on how much oxygen is present in the exhaust. Thus the oxygen storage capacity is not a fixed value, rather it is determined by the equilibrium between the storage sites and the feed stream. A numerical model was developed to characterize the oxygen storage capacity. The model matches well with the experiments.

The effects of catalyst age and fuel sulfur content on oxygen storage were measured. The results show that the aging effects and fuel sulfur effects are decoupled. The storage capacity decreases by 10% for every 150ppm increase in fuel sulfur, and it scales with $(age^{-0.84})$.

Different modes of air/fuel ratio modulations were tested on the catalysts, since such modulation is the practice to keep conversion efficiency high and to increase robustness of the catalyst during transients. The results show that within a certain range, the tail-pipe NO emission is not sensitive to the variations in frequency and amplitude. When the modulation is biased towards lean, NO will eventually breakthrough when the oxygen storage capacity saturates. The observed saturation point matches well with the oxygen storage capacity observed in the air/fuel lean step experiments.

A flow reactor is set up for controlled studies on catalytic actions. Results show that at typical steady state catalyst temperatures the pollutants removal rate is limited by the mass transfer speed of the slowest diffusing species in the exhaust. The experiments quantify the aging effects on conversion efficiency degradation. Results show that the front part of a catalyst loses its effectiveness exponentially with aging. The loss of effectiveness is not uniform along the catalyst; the degradation is less severe towards the back of the catalyst.

A comprehensive practical model was developed based on previous works and the experiments of this project. The model takes into account oxygen storage capacity and aging effects. The comparison of the model with experiments shows good agreement.

Thesis Advisor: Wai K. Cheng
Title: Professor of Mechanical Engineering

Acknowledgements

First and foremost I wanted to thank my thesis advisor, Prof. Wai Cheng, who has guided me through and been very closely involved in this project. Without your help, I would never have made it this far. In the past four years, Prof. Cheng has been my role model of critical thinking, problem solving, being confident in face of problems and most important of all being hands-on. I'm sure I will benefit from the experience for a lifetime.

My thesis committee deserves many thanks. I have greatly benefited from the suggestions and guidance from Prof. Wai Cheng, Prof. John Heywood, and Prof. Bora Mikic. You have made sure the project is going in the right direction.

I can never thank Prof. John Heywood, director of the Sloan Automotive Lab, enough for admitting me to the Sloan Lab and fulfilling my childhood dream. And thanks for providing us with the world-class research facilities and cultivating an atmosphere in which we can always learn from one another, and are constantly reminded of the energy and environmental issues that we cannot shy away from.

The project would not have been possible without the financial support from the sponsors, the Industrial Engine & Fuels Consortium, whose member companies include Delphi, Daimler-Chrysler, Ford, GM, and Saudi Aramco. The consortium has not only provided financial supports, but the feedback and suggestions have been most invaluable.

I am in debt to the lab administrative, Ms Leslie Regan - the graduate administrative of Mechanical Engineering, Thane Dewitt - the lab supervisor, and Raymond Phan - our lab technician. Without your help, life would not have been this easy.

I have also received tremendous amount of help from friends inside and outside of the lab. Morgan Andreae, Kevin Lang, Jeff Mathews, Halim Santoso have been my group for afternoon soda breaks every other day. I enjoyed sharing ideas on energy, technologies, politics and flying machines. The brainteasers helped my brain from rusting up doing research everyday. Yong Li, Gang Tan, Yujie Wei, and Ronggui Yang are my other team I can take breaks with on all other days. The nerdy talks have made our breaks very productive and less a waste of time. And Yianni Kitsopanidis, Liang Liu, Nuria Margarit, Fiona McClure, Jenny Topinka are the best friends one can ask for. I wanted to thank all my friends for constantly showing your helping hands, sharing your ideas and, most important of all, the friendship.

Last but not least, I wanted to express my gratefulness to my family. My wife, Ying, has been most patient and supportive throughout. My parents have been constantly encouraging me to pursue this degree. Thank you all for your support, patience, and love. I wouldn't have been able to fulfill my dream without any of these.

Yuetao Zhang
Cambridge, August 2005

Table of Contents

List of Figures

List of Tables

Nomenclature

Acronyms

BC	Boundary Condition
CLD	Chemi-Luminescence Detector
CO	Carbon Monoxide
CPI	Cells Per square Inch
CPSI	Cells Per Square Inch
EGR	Exhaust Gas Recirculation
EPA	Environmental Protection Agency
FFID	Fast Flame Ionization Detector
FID	Flame Ionization Detector
GPM	Grams Per Mile
HC	Hydrocarbon
HEGO	Heated Exhaust Gas Oxygen sensor
IC	Initial Condition
LN2	Liquid Nitrogen
MAP	Manifold Air Pressure
MON	Motor Octane Number
MPG	Miles Per Gallon
MY	Model Year
NDIR	Non-Dispersive InfraRed
NLEV	National Low Emission Vehicles
NOx	Nitrogen Oxides
ODE	Ordinary Differential Equation
OEM	Original Equipment Manufacturer
OSC	Oxygen Storage Capacity
PDE	Partial Differential Equation
PGM	Platinum Group Metal (platinum, palladium and rhodium)
ppm	part per million
RON	Research Octane Number

SCFM	Standard Cubic Feet per Minute
SEM	scanning electron microscopic
SI	Spark Ignition
SULEV	Super Ultra Low Emissions Vehicle
SUV	Sports Utility Vehicle
TWC	Three-Way Catalytic Converters
UEGO	Universal Exhaust Gas Oxygen sensor
ULEV	Ultra Low Emissions Vehicle
VOC	Volatile Organic Compounds
WOT	Wide Open Throttle

Symbols

a	length of side
A	cross-section area
C_i	concentration of I
D	Diameter
D_{ab}	diffusivity of binary mixture
D_h	hydraulic diameter
E	activation energy
F	Faraday constant
I	light intensity
I_0	incoming light intensity
$[i]$	concentration of i in k-mole/m^3
k_b	backward reaction rate constant
k_e	thermal equilibrium constant
k_f	forward reaction rate constant
L	length
$\dot{m}_e$	exhaust gas flow rate
M_i	molecular weight of i
P	perimeter
r	reaction rate

Sh	Sherwood number
$Sh \cdot \xi$	Effective Sherwood number
t	time
T	absolute temperature in K
v	speed
V	voltage
W_i	molecular weight of I
X_i	mole fraction of i
Y_i	mass fraction of i
Z	oxygen storage sites
Z_{O2}	oxidized oxygen storage sites

Greek Letters

λ	air equivalence ratio
ξ	percentage of effective surface area
$\Re$	universal gas constant
Ω_D^{AB}	Lennard-Jones intermolecular potential
σ	molecular diameter
ε	potential well depth
	void fraction

Chapter 1

Introduction

Environmental pollution is one of the biggest problems faced by human beings in the past decades and in generations to come. Approximately 1/3 of the pollution in the air is from the automobile fleet [1]. So it is of substantial significance to control automotive pollutions to achieve the goal of cleaner air.

Automotive emissions control is not something new; a lot of efforts have been rendered to reduce automotive emissions since the first *Clean Air Act* was put forward in early 1970's. The emissions regulations are becoming increasingly stringent with time, due to the fact that more and more vehicles are joining the fleet and the mileage each vehicle travels is increasing. Hence, the means for emissions control are becoming progressively demanding and complicated.

This thesis bears on one of the most effective ways of emissions control for spark-ignition (SI) engines - the three-way catalytic converters. Specifically, the focus is on the effects of aging and fuel sulfur on the catalyst oxygen storage capacity and performance. A comprehensive practical model of the three-way catalyst is introduced to interpret the phenomena observed in the experiments and to explain some of the mechanisms of catalytic action.

1.1 Automotive Emissions

Pollution from cars comes from incomplete combustion products conveyed by the exhaust gas, and from evaporative emissions of the fuel itself [2].

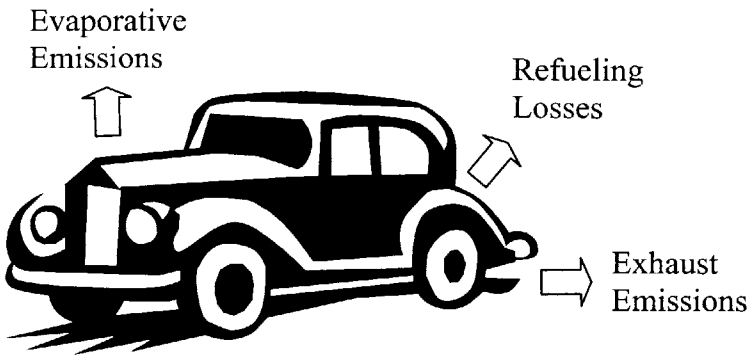

Fig. 1-1 Sources of emissions from a motor vehicle

1.1.1 Sources of automotive pollutants emissions

1. Evaporative Emissions

Hydrocarbon pollutants escape into the air through fuel evaporation. With today's efficient exhaust emission controls, evaporative losses could be a substantial part of the total hydrocarbon pollution on hot days when ozone levels are highest. However, evaporative emissions will not be addressed in this work.

2. The Combustion Process

Gasoline and diesel fuels are mixtures of hydrocarbons, compounds that contain hydrogen and carbon atoms. In a "perfect" engine, oxygen in the air would convert all the hydrogen in the fuel to water and all the carbon in the fuel to carbon dioxide. Nitrogen in the air would remain unaffected. In reality, the combustion process cannot be "perfect," and automotive engines emit several types of pollutants. In this thesis, emissions and emission control are focused on gasoline powered engines, so if not mentioned otherwise,

all of the conditions, characteristics and processes discussed are concerning gasoline engines.

1.1.2 Typical Engine Combustion

Ideally, when the ratio of the amount of fuel versus air is stoichiometric, the combustion of fuel in air will proceed to full completion. The products of such an ideal combustion process consist only carbon dioxide (CO2), water (H2O) and nitrogen (N2).

$$CHy + (1+y/2)(O2 + 3.76N2) \rightarrow CO2 + y/2\ H2O + 3.76(1+y/2)N2 \qquad (1.1)$$

In reality, however, this happens. Instead, in the products there are unburned fuel, nitrogen oxides and carbon monoxide along with carbon dioxide and water [6].

FUEL + AIR → CARBON DIOXIDE + WATER +UNBURNED HYDROCARBONS + NITROGEN OXIDES + CARBON MONOXIDE (1.2)

1.1.3 Exhaust Pollutants

1. HYDROCARBONS (HC):

Hydrocarbon emissions result when fuel molecules in the engine do not burn or burn only partially. Hydrocarbons react in the presence of nitrogen oxides and sunlight to form ground-level ozone, a major component of smog. Ozone irritates the eyes, damages the lungs, and aggravates respiratory problems. It is our most widespread and intractable

urban air pollution problem. A number of exhaust hydrocarbons are also toxic, with the potential to cause cancer.

2. NITROGEN OXIDES (NOx)

Under the high pressure and temperature conditions in an engine, nitrogen and oxygen atoms in the air react to form various nitrogen oxides, collectively known as NOx. Nitrogen oxides, like hydrocarbons, are precursors to the formation of ozone. They also contribute to the formation of acid rain.

3. CARBON MONOXIDE (CO)

Carbon monoxide (CO) is a product of incomplete combustion and occurs when carbon in the fuel is partially oxidized rather than fully oxidized to carbon dioxide (CO). Carbon monoxide is toxic; it reduces the flow of oxygen in the bloodstream and is particularly dangerous to persons with heart disease.

1.2 The history of reducing tail-pipe emissions [3,4]

1.2.1 1970-1975: The First Standards

In 1970, the US Congress passes the *Clean Air Act*, which called for the first tail-pipe emissions standards. The pollutants controlled are CO, volatile organic compounds (VOC), and NOx. The new standards went into effect in 1975 with a NOx, CO and hydrocarbon (HC) limits for cars and light-duty trucks at 3.1, 15.0 and 1.5 grams per mile (gpm) respectively.

1.2.2 1977-1988: Tightening Standards for the First Time

In 1977, Congress amends the Clean Air Act and tightens emission standards again in two steps. First, between 1977 and 1979, the NOx standard becomes 2.0 gpm for cars (CO and HC stayed unchanged). Then in 1981, the NOx standard for cars is reduced to 1.0 gpm (CO, HC to 3.4, 0.41 gpm respectively).

1.2.3 1990-1994: Tier 1

In 1990, Congress again amends the Clean Air Act, further tightening emission standards. The NOx standard is set at 0.6 gpm for cars (CO, HC at 4.2 and 0.31 gpm respectively), effective in 1994. The new standard — called "Tier 1"—is a 40 percent reduction for NOx from the 1981 standard. For trucks, the new standard ranges from 0.6 to 1.53 gpm, depending on the weight of the vehicle. The Clean Air Act Amendments of 1990 also require EPA to assess the air quality need, cost effectiveness, and feasibility of tighter emission standards for the 2004 model year and beyond.

1.2.4 1998: Voluntary Agreement For Cleaner Cars

In 1998, the Clinton Administration with the auto industry and the Northeast states strike an innovative, voluntary agreement to put cleaner cars on the road before they could be mandated under the Clean Air Act. The new cars are called National Low Emission Vehicles (NLEV). The first NLEV cars under the agreement reach consumers in New England in 1999 and will reach the rest of the country in 2001. NLEV cars operate with a NOx standard of 0.3 gpm (CO, HC at 4.2 and 0.09 gpm, respectively), a 50 percent reduction from Tier 1 standards for NOx and more than 70 percent for HC. In 1998, as required by the Clean Air Act Amendments of 1990, EPA issues the Tier 2

Report to Congress. The report contains strong evidence of the need, cost-effectiveness and feasibility for tighter tail-pipe emission standards in the future beginning in 2004. Three main factors support EPA's decision:

1) Currently vehicles make up 30 percent of smog-forming emissions nationally, and because the number of miles driven is increasing (up 127 percent since 1970) they will continue to be a significant contributor to pollution;

2) Larger vehicles like SUV's that currently do not meet the same standards as cars pollute 3-5 times as much and make up 50 percent of the vehicles sold today;

3) The technology to meet tighter standards is available and cost effective.

In 1998, EPA also determines that sulfur reductions in gasoline are needed to enable the full performance of low emission-control devices.

1.2.5 1999: Tier 2

In 1999, EPA proposes Tier 2 tail-pipe emissions standards beginning in 2004 - the first time both cars and light-duty trucks are subject to the same national pollution control system. The new standard is 0.07 gpm for NOx (CO, HC at 4.2 and 0.09 gpm, respectively). For NOx it is a 77-86 percent reduction for cars and a 92-95 percent reduction for trucks beyond the NLEV agreement. EPA also proposes a reduction in average sulfur levels to 30 parts per million (ppm) (maximum of 80 ppm) to achieve the full performance of vehicle emission control technologies.

As part of these new standards, EPA has included several measures to ensure maximum flexibility and cost-effectiveness. These flexibilities include:

- Allowing averaging to meet both the car emission and gasoline sulfur standards;
- Allowing extra time for larger vehicles between 6000 and 8500 pounds and smaller refiners to meet their respective standards;
- Allowing for a market-based credit trading-and-banking system for both industries to reward those who lead the way in reducing pollution.

1.3 Objectives and motivations

1.3.1 Development of Technology to Control Automobile Emissions

The Clean Air Act of 1970 gave EPA broad authority to regulate motor vehicle pollution, and the Agency's emission control policies have become progressively more stringent since the early 1970's [2].

EPA standards dictate how much pollution vehicles may emit but automakers decide how to achieve the pollution limits. The emission reductions of the 1970's came about because of fundamental improvements in engine design, the addition of charcoal canisters to collect volatile organic compounds (VOC) vapors, and exhaust gas recirculation (EGR) to reduce nitrogen oxides.

The advent of "first generation" catalytic converters in 1975 significantly reduced hydrocarbon and carbon monoxide emissions. The use of converters provided a huge indirect benefit as well. Because lead inactivates the catalyst, 1975 saw the widespread

introduction of unleaded gasoline. This resulted in dramatic reductions in ambient lead levels and alleviated many serious environmental and human health concerns associated with lead pollution.

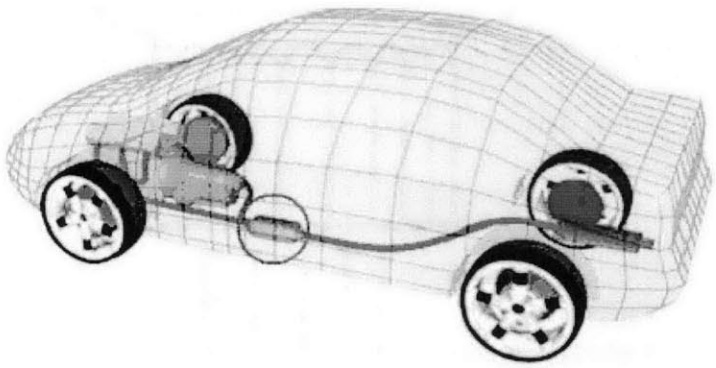

Fig. 1-2, Emission control system (catalytic converter in red circle)

The next major milestone in vehicle emission control technology came in 1980-81. In response to tighter standards, manufacturers equipped new cars with even more sophisticated emission control systems. These systems generally include a "three-way" catalyst (which converts carbon monoxide and hydrocarbons to carbon dioxide and water, and also reduces nitrogen oxides to elemental nitrogen and oxygen), plus an on-board computer and oxygen sensor. This equipment helps optimize the efficiency of the catalytic converter (Fig. 1-2, 1-3) [5,6,7].

Vehicle emissions are being further reduced by provisions of the 1990 Clean Air Act. Mobile source provisions include even tighter tailpipe standards, increased durability of emission control equipment, improved control of evaporative emissions, and computerized diagnostic systems that identify malfunctioning emission controls.

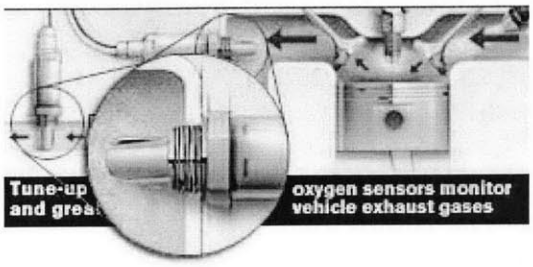

Fig. 1-3 Closed-loop control system

1.3.2 Motivations

Fig. 1-4 and 1-5 show how the NOx and HC emissions standards evolved over time. Notice the graphs are on a semi-logarithm scale. Over that past three decades, the emission levels of NOx and HC both decreased by more than 2 orders of magnitude.

Efforts by government and industry since 1970 have greatly reduced typical vehicle emissions. In those same years, however, the number of miles we drive has more than doubled. The increase in travel has offset much of the emission control progress.

The net result is a modest reduction in each automotive pollutant except lead, for which the aggregate emission has dropped by more than 95 percent.

With ozone continuing to present a persistent urban air pollution problem, future vehicle emission control programs will emphasize hydrocarbon and nitrogen oxide reductions. Carbon monoxide control will remain critical in many cities, and limits on vehicle-generated carbon dioxide may become important in the future.

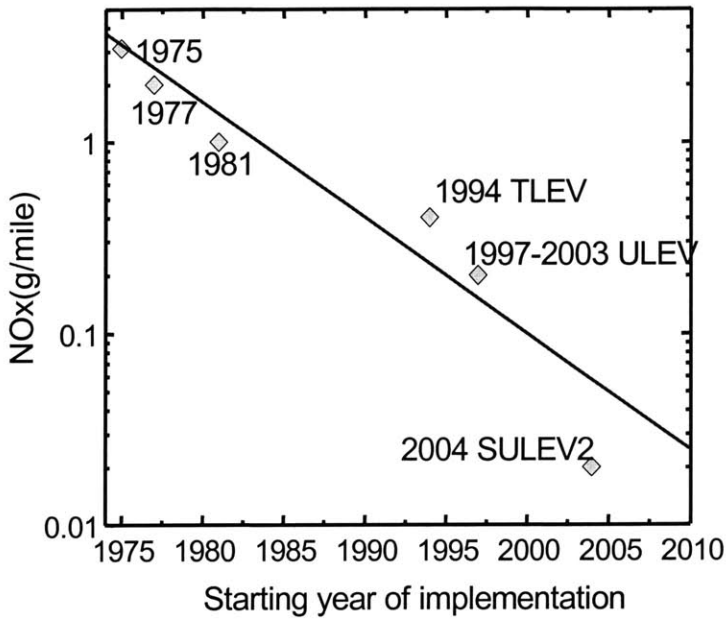

Fig. 1-4, NOx emission standards over the period of 1975 – 2005

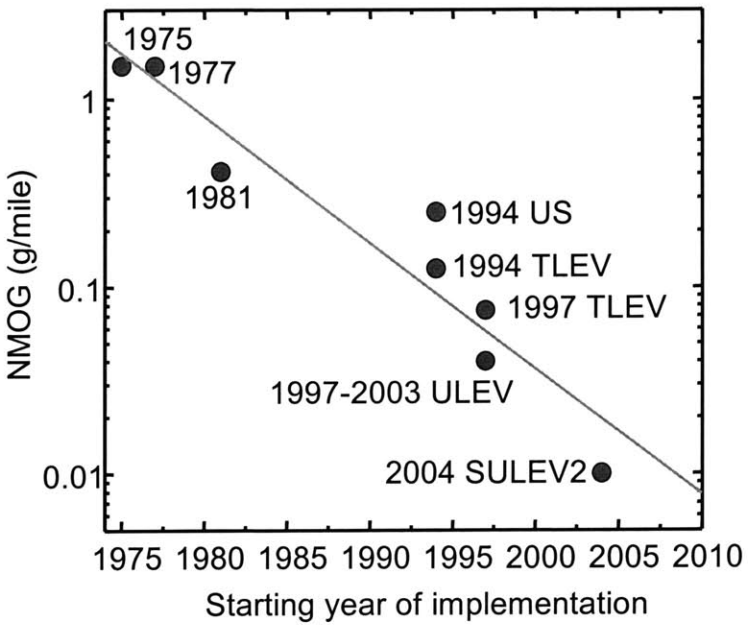

Fig. 1-5, NMOG emission standards over the period of 1975 – 2005

1.3.3 Objectives

Even though the three-way catalyst has been very effective in controlling exhaust emissions from SI engines, it is by no means perfect. Some of the characteristics of the three-way catalyst, the oxygen storage capacity for example, are still not well understood. The oxygen storage capacity is an important characteristic because it relaxes the precision requirement of the engine air/fuel ratio control and maintains catalyst performance during transients or air/fuel ratio excursions. This feature enables the catalyst to have very high conversion efficiencies during transient operations. The oxygen storage capacity, how it affects catalyst conversion effectiveness and how it can be taken full advantage will be studied in details in this project.

Also as important is the quantification of aging and fuel effects on the catalyst. As one can imagine, the effectiveness of a catalyst will be compromised when it becomes aged and/or when certain impurities are present in the fuels. A significant fuel factor is the sulfur level. The thesis investigates the effects of aging and of fuel sulfur have on oxygen storage capacity, and overall performance of the catalyst.

Lastly, a numerical model is built to help us understand how the catalyst works. The model designed to interpret some of the phenomena observed in the experiments, also to shed lights on the mechanisms of catalytic actions.

1.4 Thesis outline

The thesis is divided into 9 chapters. The 1st chapter is the introduction and overview of the objectives and motivations of this Ph.D. thesis. Chapter 2 describes the experimental setup and apparatus. Chapter 3 describes the basics of the three-way catalysts and the experiments showing the characteristics of the catalysts at different levels of aging and at various levels of sulfur fuel. Chapter 4 examines the oxygen storage capacity. Both experimental results and a model are discussed. Chapter 5 investigates the catalyst behaviors during throttle transients. Chapter 6 investigates the effects of air/fuel ratio modulation, with variation in both the amplitude and frequency of the modulation. Chapter 7 describes the study of catalyst behavior using a flow reactor. This setup provides better-controlled conditions to investigate the detailed mechanisms of the catalytic actions. The flow reactor results not only serve to interpret the phenomena observed in the engine experiments, but also provide a database for the catalyst model development in Chapter 8. Chapter 8 describes a comprehensive practical model of the three-way catalyst. The model results are compared to data retained from both the engine experiments and flow reactor experiments. The specific conclusions are presented in Chapter 9.

Chapter 2

Experimental Setup

The measurements of engine-catalyst system behavior, including oxygen storage capacity (OSC), overall conversion efficiencies, throttle transients, and air/fuel modulation, were performed on a engine-catalyst setup. As will be discussed in a later chapter, another flow reactor setup was built to investigate the catalytic actions of the catalysts.

2.1 Engine and Dynamometer

A production Daimler-Chrylser 2.4 L engine (Model year 1998) is used in the experiments. The engine was a modern 4-cylinder, 4-valves per cylinder, port-fuel injection engine with a return-less fuel line. Engine specifications are listed in table 2.1. The engine was coupled to a Froude eddy current absorbing dynamometer. The engine throttle was controlled by a stepper motor (Pacific Scientific Powermax II). The dynamometer worked at a constant speed mode; and the stepper motor controlled the load to the targeted level, in both steady state and in transient experiments [8,9].

Type	Dual Over Head Camshaft
Displacement volume	2.4 L
Bore	4
Stroke	87.5 mm
Compression Ratio	101 mm
Firing Order	9.4:1
Intake valve close	1,3,4,2
Intake valve open	51° ABDC

Exhaust valve close	1 ° BDC
Exhaust valve open	8 ° ATDC
Exhaust valve close	52 ° BBDC

Table 2-1, Engine specifications

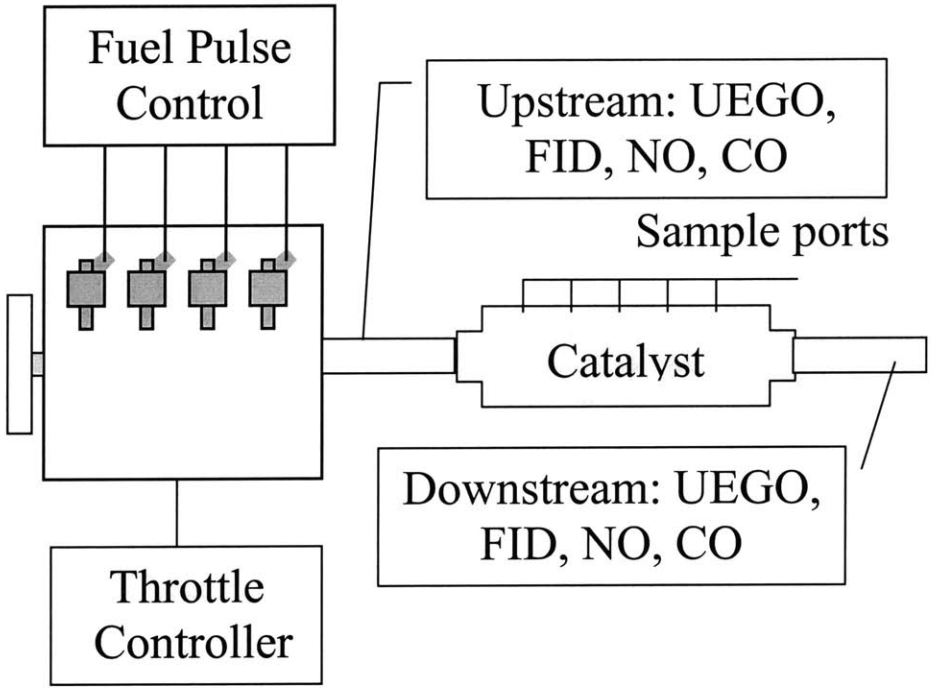

Fig. 2-1 Engine, catalyst, and instrumentation setup

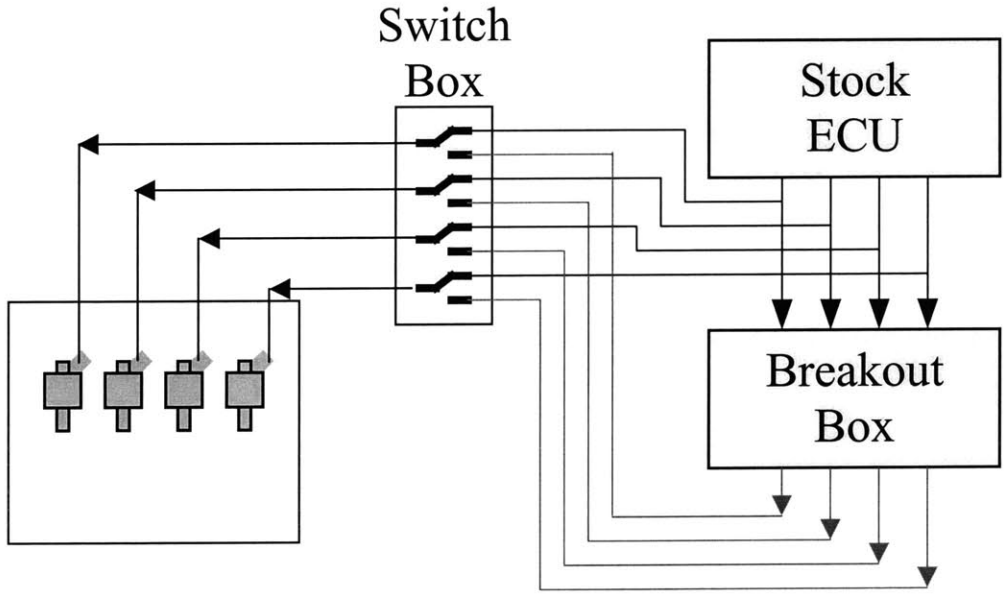

Fig. 2-2 Fuel injection control

2.2 Engine Control

The engine is essentially controlled by an original equipment manufacturer (OEM) engine control unit (ECU). The ECU modulates the air/fuel ratio around stoichiometric at a certain frequency and amplitude based on the feedback from an upstream heated exhaust gas oxygen (HEGO) sensor. Detailed mechanism of how different kinds of oxygen sensors work will be discussed in later sections. Air/fuel ratio modulation is elaborated in Chapter 5.

The exhaust composition varies with air/fuel ratio. In order to vary air/fuel ratio under steady state operation, a breakout box for the fuel injection was used. The breakout box worked as an external injection pulse generator. It was triggered by the ECU injection pulses and then delivered an injection pulse based on an externally supplied control voltage. The key components of the breakout box were a charging circuit and a voltage comparing circuit. The circuit was triggered by the stock ECU fuel injection signals. And the injection pulse width is varied by the circuits mentioned above (See Fig. 2-3). There was the option of either using the original ECU or the derived injection pulse.

Fig. 2-4 shows the exhaust composition as a function of air/fuel ratio. The numbers shown in the figure are calculated with Equilibrium. Experimental results are in very good agreement with simulations [6].

Because the HC emission is not simply determined by the equivalence ratio. It is not shown in the figure.

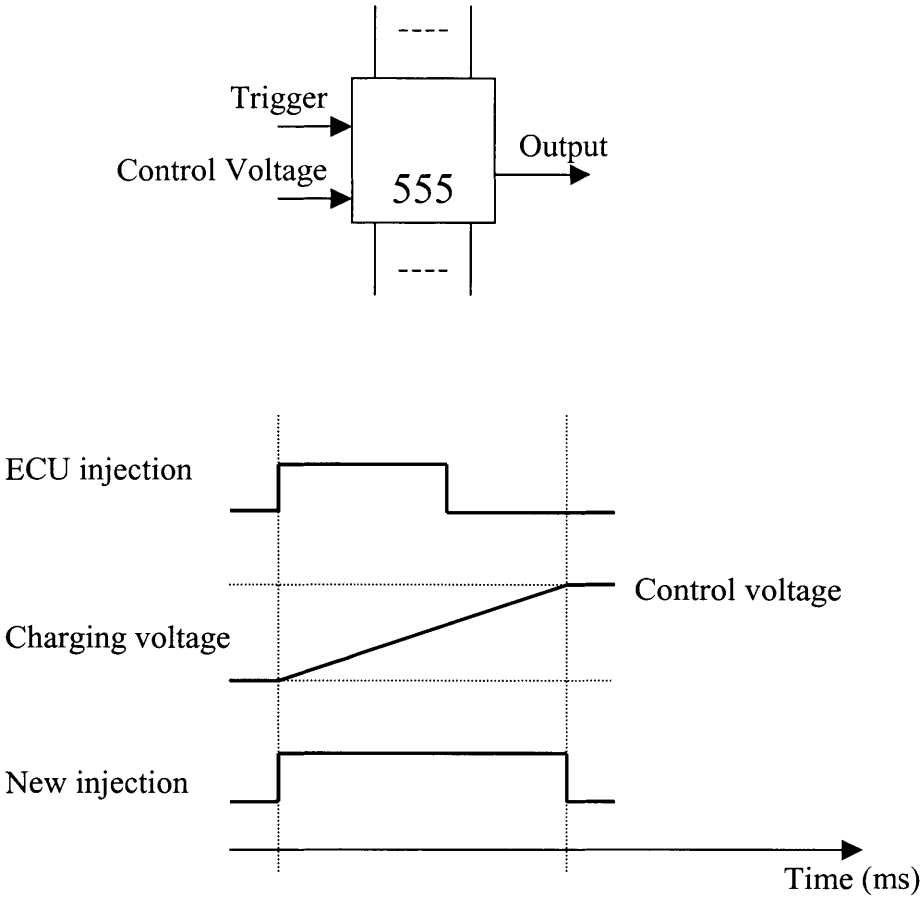

Fig. 2-3 Fuel injection pulse width control

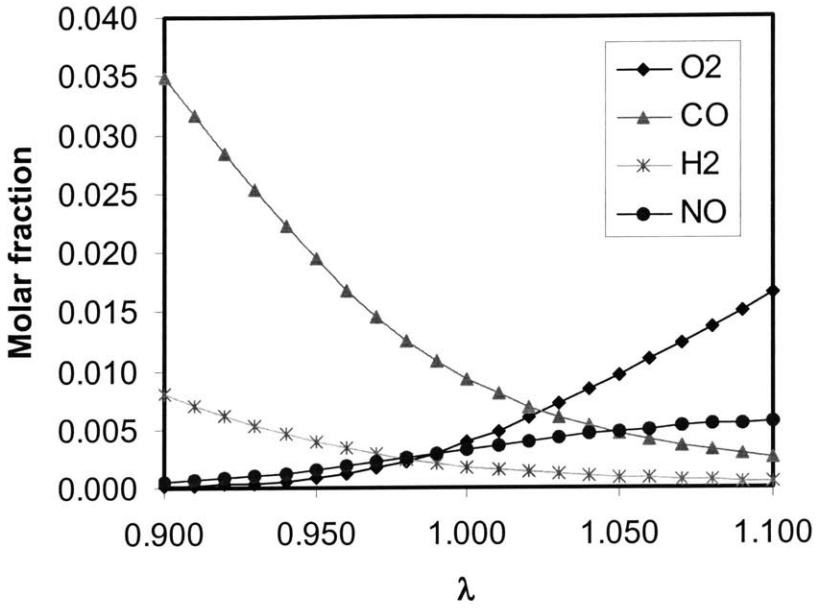

Fig. 2-4, Exhaust composition vs. air/fuel ratio. Condition: 1600rpm, 0.5 bar intake pressure

2.3 Catalysts

2.3.1 Catalyst Specifications

The catalysts used in the study are 2001 model year (MY) catalysts provided by Daimler-Chrysler Co. They are Ultra Low Emissions Vehicle (ULEV) certified. Corning made the substrates of the catalysts; and Johnson-Mathey applied the wash coat; finally Aarvin packaged the catalysts in the final cans.

The catalysts have a two-brick setup with a 1.23-liter volume per brick. The front bricks are loaded with palladium (Pd), and rear bricks with platinum (Pt) and rhodium (Rh). Each brick is 4-inch in diameter, and 6-inch in length. The front bricks have square cells at 400 cpi (cells per inch-squared); whereas, the rear bricks have triangular cells at 300 cpi (as shown in table 2-2).

	Front brick	Rear brick
Loading	Pd	Pt/Rh

Cell geometry	Square	Triangular
Cell density (CPI)	400	300

Table 2-2 Catalysts specifications

The catalysts have been dyno-aged to simulate 4k, 50k, and 150k vehicle miles.

Equivalent catalyst age (k-Miles)	Aging time (Hours)
4	14
50	178
150	534

Table 2-3 Catalysts aging

2.3.2 Sampling Points

The sampling locations for measuring the concentration profiles along the catalyst are shown in Fig. 2. Locations 1 and 7 were up- and down-stream of the catalyst respectively. Location 4 was in between the front and rear catalyst bricks. For each of the locations 2,3,5 and 6, a small hole was drilled through the ceramic substrate so that a sample probe could be inserted to the center of the catalyst cross-section. The sampling points inside the catalyst are evenly distributed, as shown in Fig. 2-5.

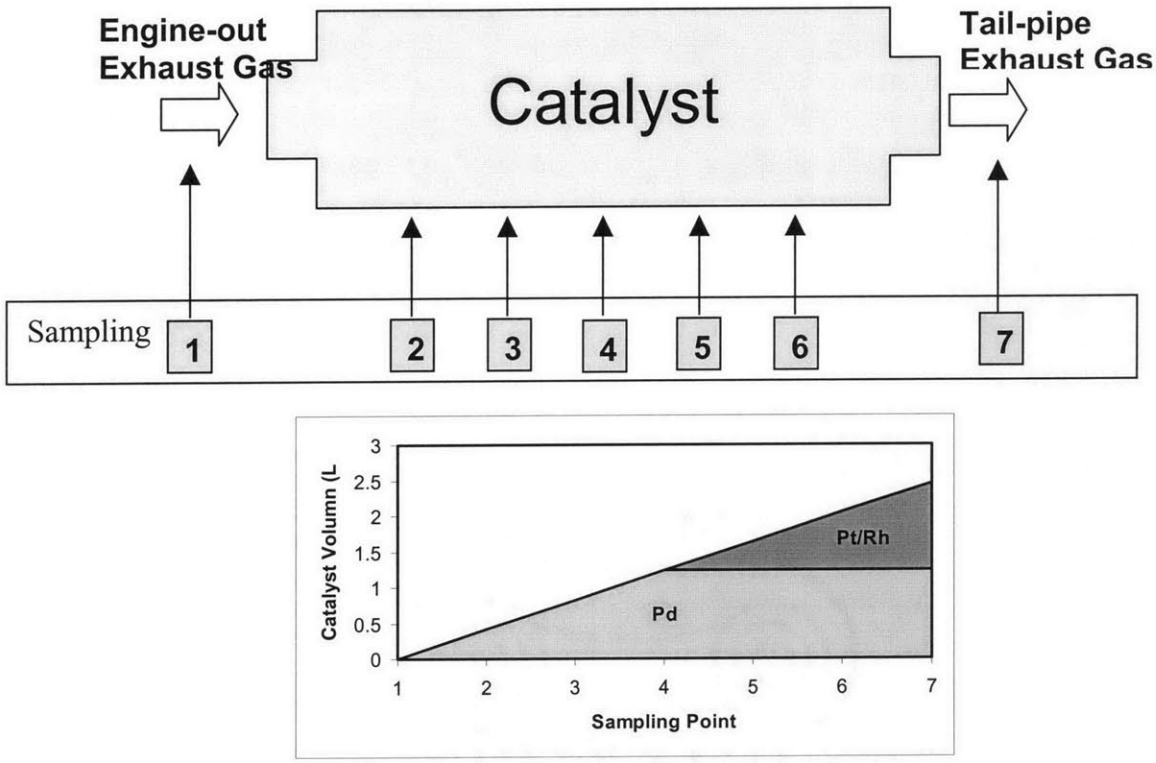

Fig. 2-5 Sampling ports along the catalyst

The sampling points are used for measuring temperature and species concentration along the catalysts. Sampling will be discussed in section 2.4, instrumentations.

2.4 Fuels

The fuels used in the experiments are PG-II blend, provided by Exxon-Mobil Co*. The equivalent research octane number (RON) is 92. The fuels are doped with sulfur containing compounds to simulate the fuel sulfur level at 7, 33, 266 and 500 part per million (ppm) respectively [10].

* Exxon-Mobil Co. was a member of the Engine and Fuels Consortium

2.5 Instrumentations

In the experiments, multiple instruments are used in measuring exhaust species concentrations. In brief, they are HC, NOx, CO and oxygen meters. This sector will discuss in detail how the meters work, and the precision of all the instrumentations.

2.5.1 HC measurement

A standard method in measuring HC emission is flame ionization detection (FID). The basic physical phenomenon that is exploited in a FID is that when a hydrocarbon is burnt, significant quantities of ions are formed. The number of ions produced is nearly proportional to the number of carbon atoms burnt in hydrocarbon (HC) form. The physical explanation for this effect is not yet fully understood. The process of ion generation is certainly to do with a non-equilibrium effect called chemi-ionization, as opposed to thermal equilibrium ionization, since the latter is responsible for negligible ionization at normal flame temperatures. In flames not involving HC, for example H2 and CO flames, ion generation is limited to equilibrium values and is very small indeed. However, if a HC sample is introduced into such a flame, significant ionization occurs.

In measuring, a stream of exhaust sample is drawn into a reaction chamber via a vacuum pump. The sample is burnt in a hydrogen flame held at a constant temperature. The reaction produces ionic hydrocarbons as shown in the following reaction scheme:

$$CH + O \rightarrow CHO^{+} + e^{-} \qquad (2.1)$$

$$CHO^{+} + H_2O \rightarrow H_3O^{+} + CO \qquad (2.2)$$

$$H_3O^{+} + e^{-} \rightarrow 2H + OH \qquad (2.3)$$

The last two equations listed above are formed because of the large amount of water present in the sample stream. All of the electron charges are then gathered to an electrode held at 150-200 volts negatively biased to the burner, and a current is produced which is proportional to the hydrocarbon concentration [11].

In the experiments both a fast-response FID (FFID) and a slow-response one are used. The FFID used is an HFR-400 FFID developed by Cambustion Ltd. The response time of the FFID is on the order of 5 ms. It is used in measuring HC during transients. A slow FID is also used in the experiments for steady-state HC measurements. The slow FID is a Rosemount Analytical Model 402 Hydrocarbon analyzer [12].

Number of channels	2
Ranges	0-2,000 to 0-1,000,000 ppm C1
Response time	< 4ms
Drift	<± 2% full-scale/hr
Linearity	<± 2% full-scale @ 150,000 ppm C1
Output	0-10 volts

Table 2-4 Cambustion HFR-400 FFID specifications

2.5.2 NOx measurement

The mechanism of NOx measuring is chemi-luminescence detection (CLD). CLD is the industry standard for the measurement of NO. In the method of measurement, a sample of the exhaust stream is drawn into the reaction chamber. A stream of ozone is then introduced into the chamber, causing the following reaction:

$$NO + O_3 \rightarrow NO_2^* + O_2 \qquad (2.4)$$

NO2* represents the NO2 that is in an excited state. This molecule then reverts back to the ground state, emitting radiation in the wavelength range from 600 to 3000 nm.

This light is then collected by a photo-detector. The light emitted is proportional to the NO concentration [13].

A Cambustion fNOx-400 NOx detector is used in the experiments. The measurement takes place in the head of the instrument directly behind the sampling probe, resulting in a small response time. As with the fast FID, a constant pressure chamber is used to keep the sample independent of the exhaust stream flow rate.

Number of channels	2
Ranges	0-10,000 ppm NO
Response time	< 4ms
Zero Drift	<± 1% full-scale/hr
Span Drift	<± 1% full-scale/hr
Linearity	<± 1% full-scale to 5,000 ppm, <± 2% full-scale to 10,000 ppm
Output	0-10 volts

Table 2-5 Cambustion fNOx-400 Fast CLD specifications

It should be noted that the FCLD measures only NO concentrations, but since NO/NO2 ratio in an SI engine exhaust is typically > 100. So no distinction is made between NO and NOx emissions (although there could be NO2 emissions in the exhaust under lean conditions) [14].

2.5.3 CO measurement

The industry standard method for the measurement of CO is non-dispersive infrared (NDIR) absorbance sensor. Most molecules can absorb infrared light. The amount of IR light absorbed is proportional to the concentration. The energy of the photons is not enough to cause ionization, and thus the detection principle is very different from that of a photo-ionization detector. The energy absorbed causes the gas to heat up.

Each molecule absorbs infrared light at wavelengths representative of the types of bonds present. For example, CO has a strong absorbance at 4.65μm, and CO2 at 4.26 μm (See Fig. 2-6).

The absorbance of the gas is directly proportional to its concentration, in accordance with the Lambert-Beer law [15]:

$$\frac{I}{I_0} \infty e^{-x_{CO} \cdot L \cdot k} \qquad (2.5)$$

Where,

I is light intensity after the cell,

I_0 the incoming light intensity,

Xco is concentration of CO,

L is the length of the cell,

K is a constant.

So, it's obvious that longer cells have higher sensitivity.

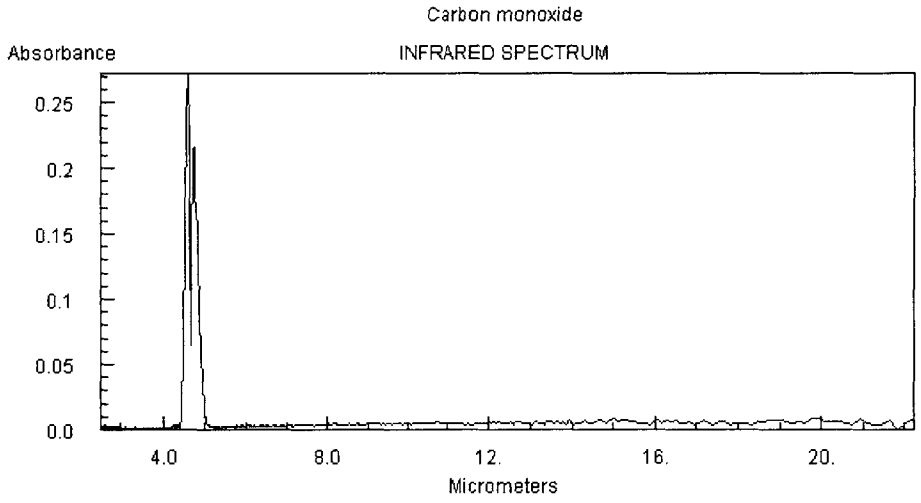

Fig. 2-6 CO infrared absorbance spectrum

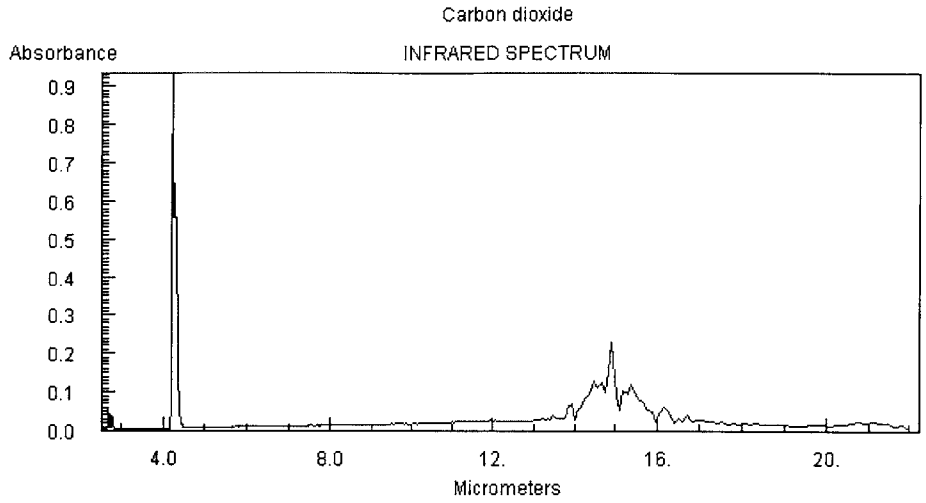

Fig. 2-7 CO2 infrared absorbance spectrum

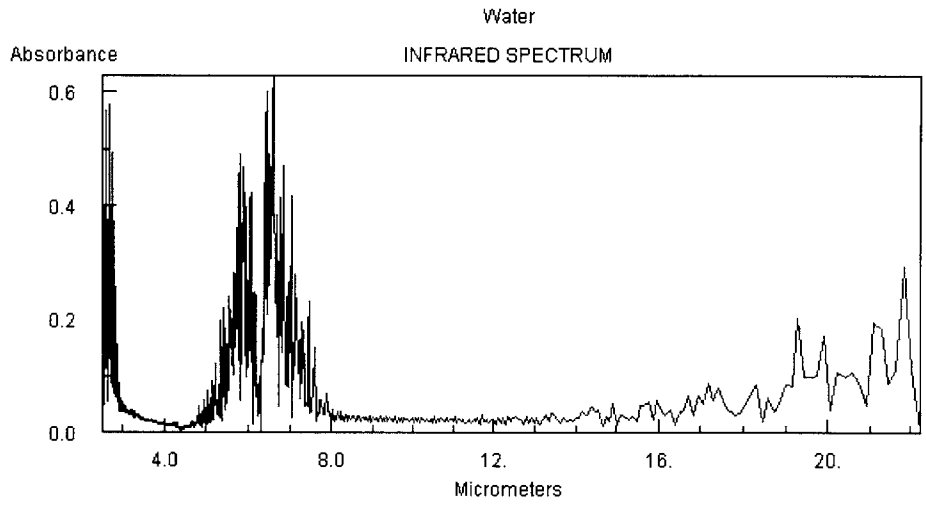

Fig. 2-8 Water infrared absorbance spectrum

In practice, the CO detectors output (V_0-V), in which V is proportional to I/I_0. So, the calibration curve of CO detector should look like Fig 2-9.

Notice in Fig. 2-8 there is some overlap in the absorbance spectrum of water and CO/CO2, so in practice. NDIR measures only CO/CO2 "dry" values. When water is

present in the sample, the water will distort the concentration readings. This will be discussed more in the following sector about sampling system.

The NDIR instrument used in the research is a Rosemount Analytical Model 880A CO detector. The CO meter is a slow response one, with response time on the order of 5 seconds [16].

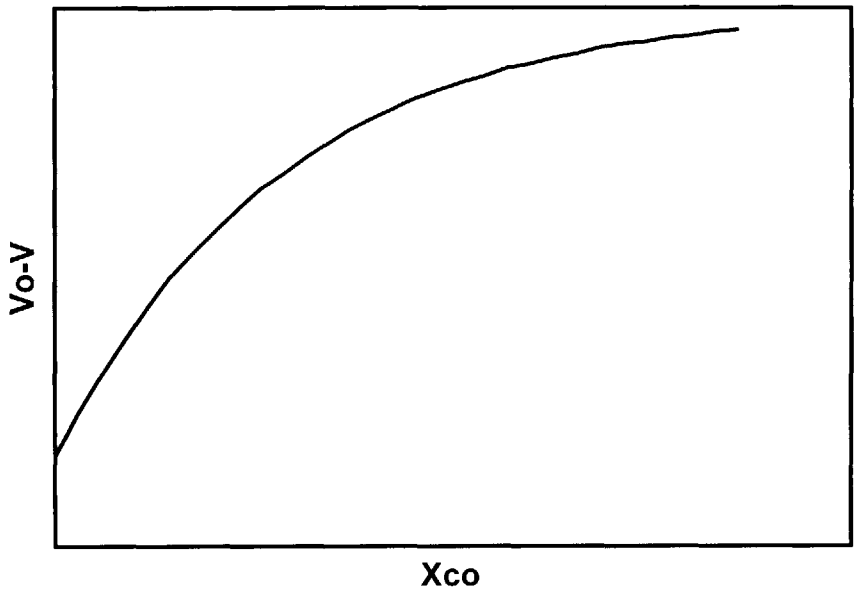

Fig. 2-9 CO detector voltage vs. CO concentration calibration curve

Number of channels	1
Measurement ranges	0-5% CO
Operating temperature	0-45 oC
Response time	~5 s
Noise	1% full-scale
Zero drift	<± 1% Full-scale/24 hrs
Span drift	<± 1% Full-scale/24 hrs
Sample pressure	Max 10 psi
Sensitivity	10 ppm CO

Table 2-6 Rosemount Analytical Model 880A specifications

2.5.4 Oxygen and air/fuel ratio measurement

There are two kinds of oxygen sensors: switch-type and broadband, or heated exhaust gas oxygen (HEGO) sensors and universal exhaust gas oxygen (UEGO) sensors. In SI engine closed-loop control system, the ECU gets air/fuel ratio feedback signal from an oxygen sensor mounted upstream of the three-way catalyst. Normally the oxygen sensor is a HEGO, it gives a switch-type signal to the ECU; the ECU then knows if the air/fuel ratio is lean or rich.

2.5.4.1 HEGO sensor

The sensor is a solid-sate electrolyte made of ZrO_2 ceramic material. At high temperatures, this electrolyte becomes a galvanic oxygen concentration cell with solid electrolyte. The oxide mix is a practically pure oxygen-ion conductor and separates the exhaust gas from the surrounding air.

When working, one side of the sensor is exposed to the exhaust stream having partial pressure $P_{O2}^{'}$, and the other side of the sensor is exposed to the atmosphere having oxygen partial pressure $P_{O2}^{''}$ (as shown in fig. 2-10).

An electrical voltage is generated across the platinum-coated electrodes in accordance with Nernst principle.

$$U_s = R \cdot \frac{T}{4F} \cdot \ln\left(\frac{P_{O2}^{''}}{P_{O2}^{'}}\right) \qquad (2.6)$$

Where, R is universal gas constant,

F is Faraday constant,

T is absolute temperature,

$P_{O2}^{''}$ is the oxygen partial pressure of the reference load,

P_{O2}' is the oxygen partial pressure in exhaust gas.

This type of sensor is referred to as the switching type sensor because the partial pressure of oxygen switches from the order of 10^{-10} Pascal when rich to 10^{3} Pascal when lean [6, 17, 22, 23]. Fig. 2-11 shows the characteristic voltage curve of this kind of sensor.

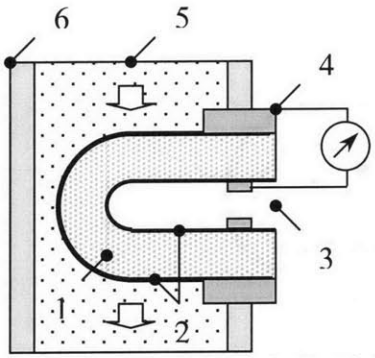

O2 sensor in exhaust pipe

1. Ceramic sensor
2. Electrodes
3. Air

Fig 2-10 Schematic of HEGO

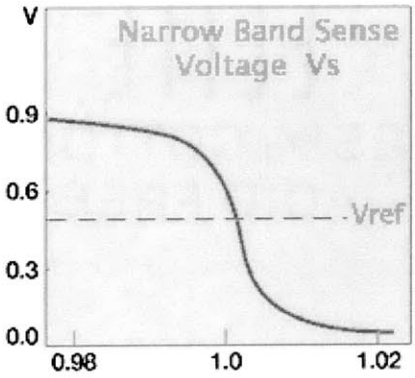

Fig. 2-11 HEGO voltage curve

2.5.4.2 UEGO sensor

The UEGO is a combination of the ZrO2 cells, with one pump cell, one Nernst cell and one reference cell (as shown in Fig. 2-12). The pump cell and the Nernst cell are made of ZrO2, and each is coated with 2 porous platinum electrodes. The cells are so arranged that there is a measuring gap of 10-50 μm between them. This measuring gap is connected to the surround exhaust gas through an opening in the solid electrolyte, and at the same time represents the diffusion barrier, which determines the limit current. An electronic circuit controls the voltage applied to the pump cell so that the composition of the exhaust gas in the measuring gap remains constant at $\lambda=1$. This corresponds to a voltage at the concentration cell of Un = 450 mV. With lean exhaust gas, the pump cell pumps the oxygen from the measuring gap to the outside.

On the other hand, when the exhaust gas is rich, the oxygen is pumped into the measuring gap from the surrounding exhaust gas and the direction of current flow is reversed. The pump current is proportional to the oxygen concentration or oxygen requirement. Fig. 2-13 shows the characteristic current curve of the broadband sensors.

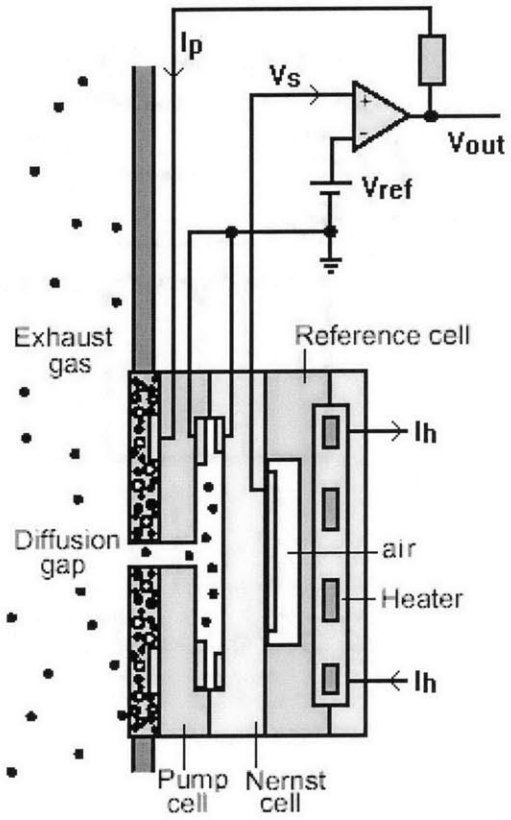

Fig. 2-12 Schematic of UEGO

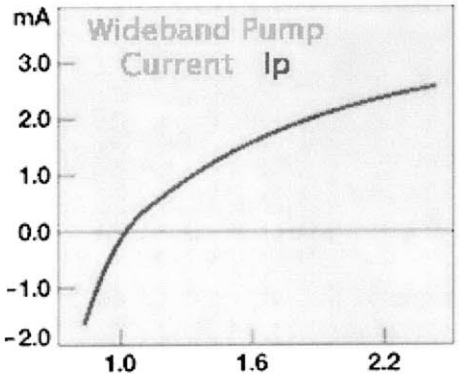

Fig. 2-13 UEGO current curve

2.5.5 Temperature measurement

Temperatures are measured with standard type K thermocouples. Type K thermocouples are good in measuring temperatures ranging from –200 C to 1250 C. In order to achieve fast-response, 1/8'' open-tip thermal couples are used. As shown in fig. 2-5, the sampling ports are all 1/8'' couplings. When temperatures are measured, the thermocouples can be directly plugged into those ports.

2.5.6 Sampling system

The experiments in this project can be categorized into two main types, transients and steady state. Accordingly, the sampling system is designed so that the different requirements in time response can be met.

2.5.6.1 Transient sampling

In order to achieve fast response in transient experiments, the sampling lines are omitted, in stead the fast response NOx and FFID probes are directly connected the sample points on the catalysts.

2.5.6.2 Steady-state sampling

In steady-state experiments, time response is not critical; a more complicated sampling system is built. With this system, multiple measurements can be carried out at the same time. It is also more convenient to switch among different sampling points along the catalyst.

As shown in fig. 2-14, UEGO sensors are located up- and down- stream of the catalyst. The 5 sampling points, together with the up- and down- stream ones, are lead through a heat exchanger and distiller first. The reason for cooling the sample is to condense most of the water out. As mentioned in previous section about CO measuring,

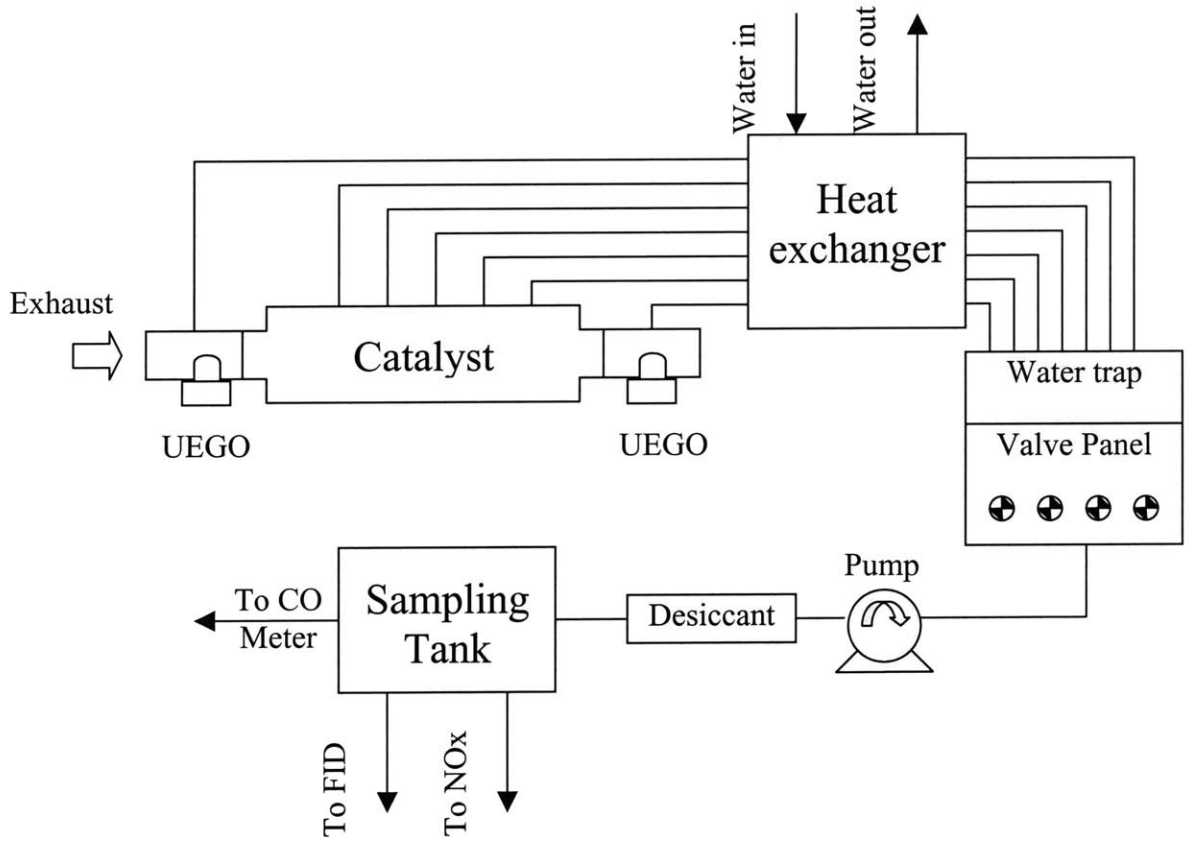

Fig. 2-14 Sampling system schematic

water needs to be removed before NDIR meter can properly work. Then, the sample is selected on a valve panel; only one channel can be selected at a time. The sample is pulled through its path by a diaphragm pump. After the pump, the sample is further dried. Then, it is filled into a sampling tank. The tank also acts as a stabilizer, so that most of the pulsations in the flow can be damped out. NO meter and FFID can directly measure

from this tank, because they both have their own sampling pumps. After the tank, the sample keeps on traveling into the CO meter.

The system is intentionally set up so that the sample is pushed into the CO meter instead of pulling through it. Because as described in the sector on CO meter mechanisms, the light intensity after the detector cell is a function of CO concentration, thus, a function of its density. In order to get more precise calibration of the CO meter, this setup is more desired.

2.5.6.3 Data acquisition system

Data is acquired using National Instruments Labview PCI-6025E internal multifunctional input/output board, a National Instruments BNC-2090 connector board, and Labview version 5.0.

Analog inputs	16 single ended or 8 differential
Resolution	12 bits
Maximum sampling rate	200 k-bit/s
Input range	+/- 10 V
Analog outputs	2
Analog output rate	10 k-bit/s
Analog output range	+/- 10 V
Digital I/O	32
Counter/Timers	2,24 bit

Table 2-7 National Instruments PCI-6025E specifications

2.5.7 Instrumentation Precision Analysis

Because the emissions levels at the catalyst output are very low, the instrument resolutions need to be addressed. The resolutions are shown in table 2-8. For comparison, the 2004 SULEV-2 standards (converted to mole fraction basis on a vehicle fuel economy of 20 mpg operating under stoichiometric condition) are also shown.

	Measurement resolution	SULEV-2 requirement	SULEV-2 equivalent*
NO	3 ppm	0.02 gpm	10 ppm
CO	4 ppm	1.00 gpm	50 ppm
HC	2 ppm	0.01 gpm	5 ppm

Table 2-8 Resolution of the emissions measurements

* Emission requirement values are converted to an equivalent average exhaust mole fraction by assuming a fuel economy of 20 mpg and stoichiometric operation.

The comparison shows that the instruments used in the experiments are able to discern the differences in tail-pipe emissions to the standards of SULEV-2 requirements.

Summary

- An experimental setup of engine-dyno system is designed to provide exhaust source for the three-way catalyst study.
- Instrumentations used in the experiments are described including specifications and measurement mechanisms.
- A customized fuel controller is designed to arbitrarily control fuel injection pulse width, thus to vary air/fuel ratio and exhaust composition.
- Analysis of the resolutions of the instruments compared to SULEV-2 standards.

Chapter 3

Overview of Three-Way Catalysts

3.1 Basics of Catalysts

3.1.1 Mechanisms of Catalysis

A catalyst in its simple term is a material that increases the rate of a chemical reaction while itself does not undergo any net permanent changes.

Reactants undergoing conversion must pass through various energy barriers,

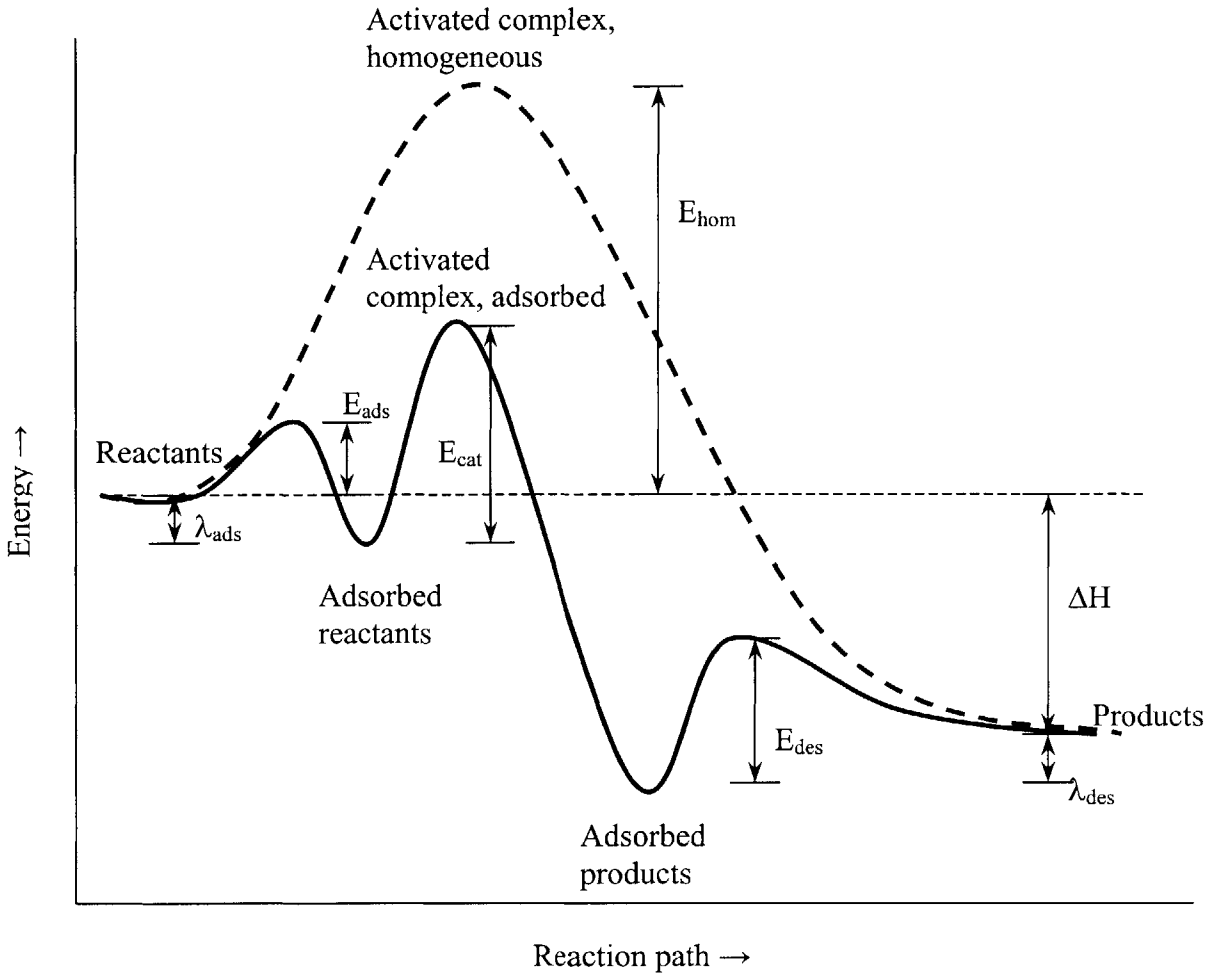

Fig. 3-1 Activation energies in different reaction schemes

called activation energies (E), before the final product is produced (shown in Fig. 3-1). The catalyst's role in a reaction is to lower these activation energies [7, 18].

The rate of reaction is inversely proportional to the exponential of the activation energy, as shown in equations (3.1) and (3.2). So it is obviously seen that by lowering the activation energies of the reactions, the catalyst can substantially increase the reaction rates at a fixed temperature, or lower the threshold temperature for reactions to commence.

$$r = k \cdot C_a^x \cdot C_b^y \tag{3.1}$$

$$k = k_0 \cdot \exp\left(-\frac{E}{RT}\right) \tag{3.2}$$

Where, r is the reaction rate,

k_0 is a constant,

C_a, C_b are concentrations of reactants,

E is the activation energy,

R is universal gas constant,

T is absolute temperature at which the reaction happens.

3.1.2 Monolithic Converter Structure [7, 19, 20]

Though the catalyst materials are proficient in expediting relevant chemistry reactions, it has to be deployed effectively to maximize the performance. The commonly accepted process of gaseous reactions being converted in a monolithic converter is as follows:

1), Reactants carried into the converter by bulk flow;

2), Reactants being transported from the bulk flow to the catalyst surface;

3), Reactants being adsorbed from the catalyst surface onto active sites;

4), Surface reaction on catalysts sites;

5), Products desorpted from sites back to the surface;

6), Products transported from surface back to bulk flow;

7), Products carried away by bulk flow.

It is then clear that the active materials in the catalyst is only involved in steps 3,4,5. Other limiting processes include diffusion rate, monolith dimensions and cell geometry, etc. Under different operating conditions, various processes can be the rate limiting one (diffusion rate in particular).

Fig. 3-2 shows a typical catalytic converter, ready to be integrated to the engine.

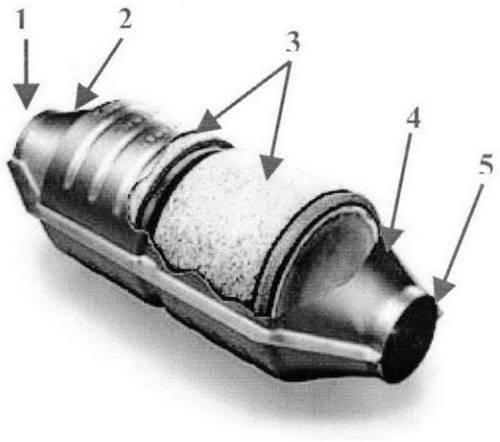

Fig. 3-2 Monolithic converter structure

The system consists of the following parts:

1) The entrance piping linking the catalytic converter to the engine
2) A diffuser to expand the flow uniformly across the face of the catalytic reactor
3) The catalytic reactor itself, the monolith
4) The exit nozzle

5) The exit pipe

Fig. 3-4 is a close-up look at one single cell of the monolithic converter. The cell has three major components:

1) Substrate, which provides the monolithic structure of the converter. Substrate can be made from different materials. Different materials have different properties that affect the application of the catalyst. A very commonly used material as the substrate is cordierite ($2MgO{\cdot}2Al_2O_3{\cdot}5SiO_2$). It is widely used due to the advantages of high thermal shock resistance, high melting point, etc.
2) Carrier (wash coat), which is the porous structure on top of the substrate. The main purpose of wash coat is to provide the high surface area on which the catalyst is impregnated. The most commonly used material for carrier is γ-Al_2O_3. Fig. 3-3 shows the scanning electron micrograph (SEM) of a specially prepared γ-Al_2O_3 crystal, which has a surface area on the order of $\sim 150 m^2/g$.
3) Catalysis material, this is the working part of the converter. The materials range from precious metal, such as the platinum group metal (PGM), to base metal oxides. On automotive applications, the materials used are almost unanimously the PGM. The term *Catalyst* is technically referring to the precious metal, but normally is loosely used to refer the whole converter.

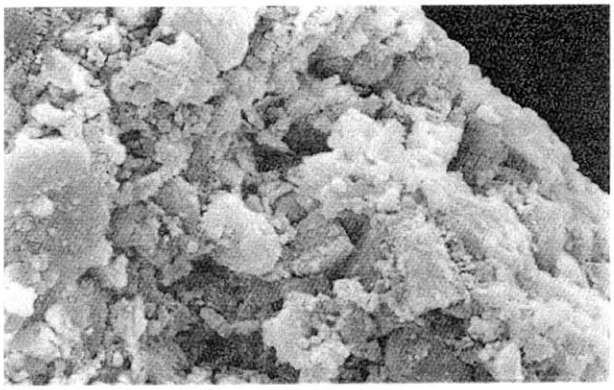

Fig. 3-3 Scanning Electron Microscope view of a washcoat layer

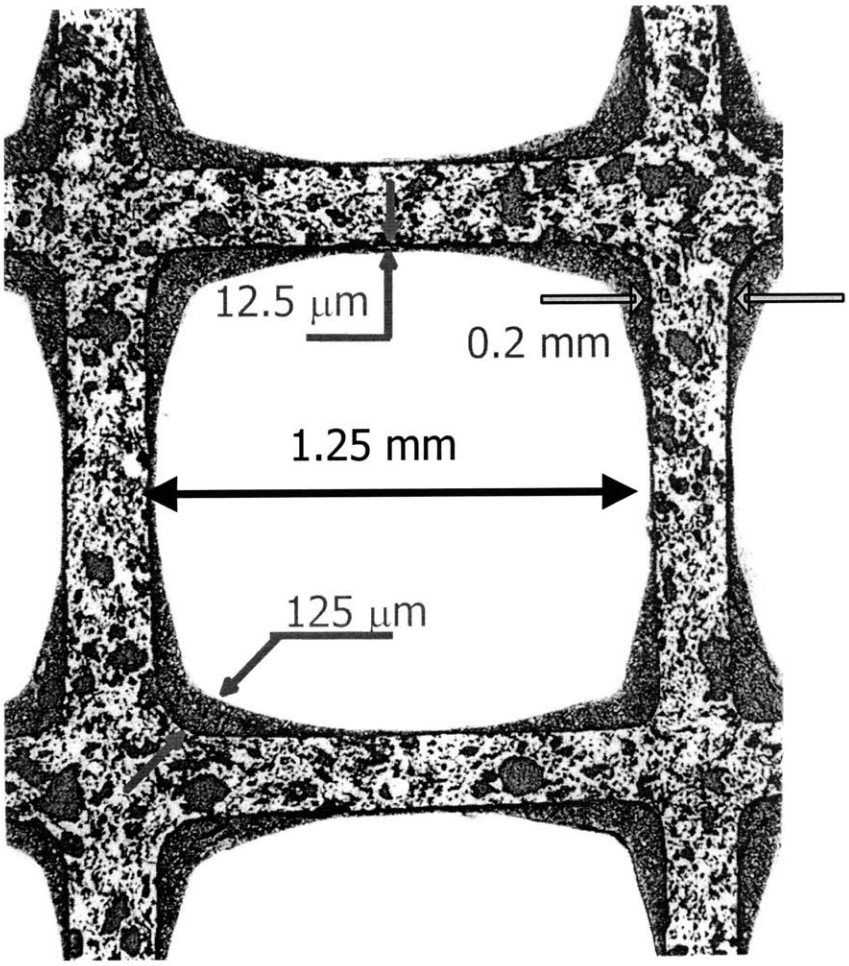

Fig. 3-4 Structure of monolithic cell

3.1.3 Catalyst Degradation

In automotive applications, there are two major sources of catalyst deterioration: thermal deactivation and poisonings [7].

3.1.3.1 Thermal Deactivation

This is especially a problem for automotive catalytic converters, where temperatures close to 1000 deg-C can occur.

The main mechanism of thermal deactivation is the sintering process. A general objective of the catalyst manufacturer is to maximize accessibility of the reactants to the active sites by depositing the catalytic components on a high-surface-area carrier. A perfectly dispersed (100% dispersion) catalyst is one in which every atom (or molecule) of active component is available to the reactants. Under high temperatures, the active materials tend to sinter and form physically more stable crystals. As a result, the crystals grow larger, thereby decreasing the surface to volume ratio and reducing the effectiveness of the active materials.

The reduction in surface area can also happen to the carrier. Take γ-Al_2O_3 for example: it can lose surface area by losing H2O under high temperatures. Another mechanism of loss of surface area is the conversion to a new crystal structure. For example, when γ-Al_2O_3 converts to α-Al_2O_3, there is a significant stepwise decrease in the internal surface area from about 150 to < 50 m^2/g.

3.1.3.2 Poisoning degradation

Poisoning effect is a common cause of catalyst degradation. Catalyst poisoning is caused by deposition of contaminants in the exhaust gas onto the catalyst surface. Poisoning can be categorized into two types. One is selective poisoning, which means the poisonous chemicals in the exhaust gas directly react with the precious metal or carrier. The catalyst essentially loses the sites that are attached by the poisonous chemicals. Depending on the nature of the reaction, the process may or may not be reversible. Another type of poisoning is called non-selective poisoning, or fouling. Fouling is caused by chemical depositing on the surface or blocking pores resulting in a loss of effectiveness.

One of the themes of this study is to quantify aging effects and fuel sulfur effects on three-way catalyst degradation, in particular, the oxygen storage capacity of the three-way catalysts. This topic will be discussed in more details in the following chapters.

3.2 Dependence of Conversion Efficiencies on Air/Fuel Ratio

The catalyst efficiencies for NO, HC and CO as a function of the air/fuel equivalence ratio (λ) are shown in Fig. 3-5. The data encompass catalysts dyno-aged to the equivalence of 4K, 50K and 150K miles, and the fuels with 7 and 33 ppm sulfur level. For each measurement, λ was held fixed (The engine ECU was not used; the fuel pulse width was externally controlled.). There was a substantial drop in efficiencies for all the three emissions when λ deviated slightly from 1. The drop was particularly drastic for NO; the efficiency decreased from the high 90 percents to the 10% level. For the CO and HC efficiencies, the sensitivity to λ (on the rich side) was more severe for the fuel with the higher S level.

This significant decrease in the three-way catalyst performance when λ deviates only slightly from stoichiometric implies that it is practically not possible to keep a precise enough value of λ for every engine cycle. Thus it is essential to have a strategy with λ modulation and catalyst oxygen storage. So that on the average, the λ value is stoichiometric in order to meet the low emissions requirement.

It is also important to notice that when λ is favorable, i.e., when λ is within a very narrow window of stoichiometry (λ=1), the difference in conversion efficiencies among the catalysts at different levels of aging is indeed negligible. This issue will be addressed in later chapters when the catalyst aging effects are discussed in more details [21].

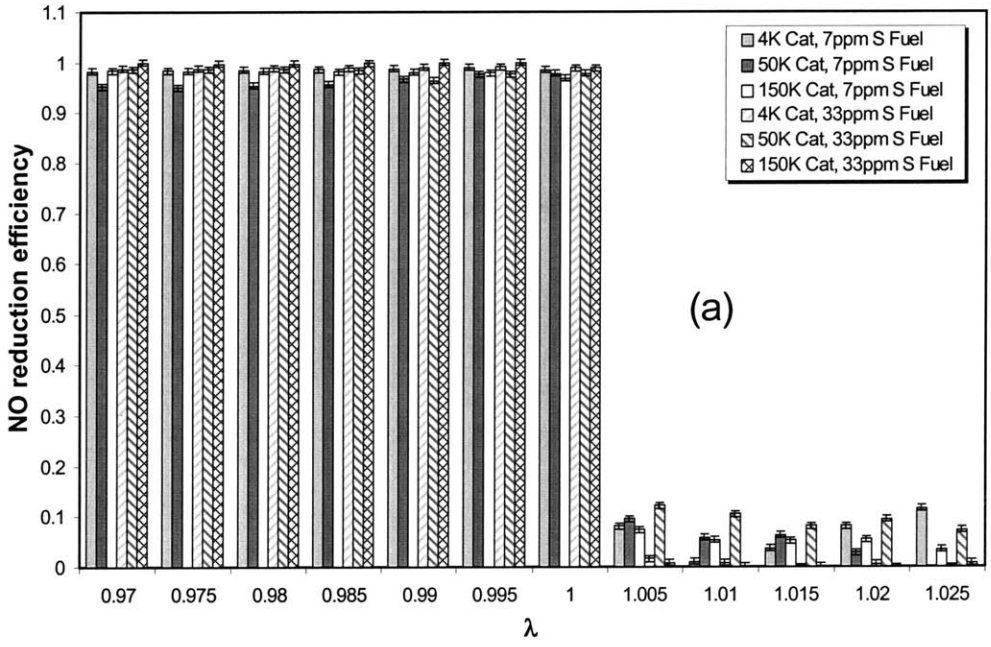

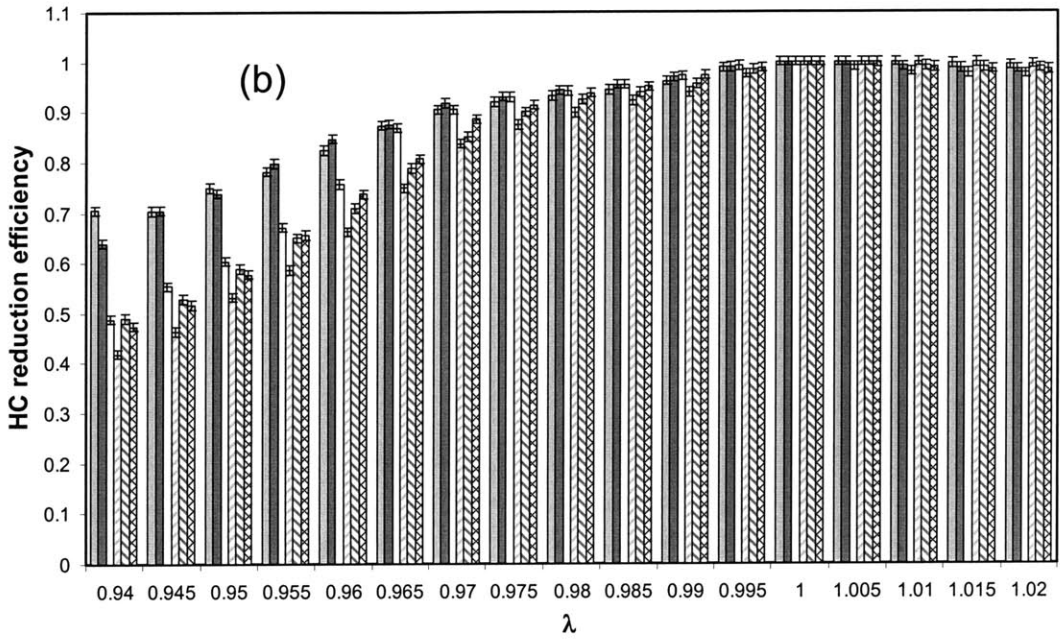

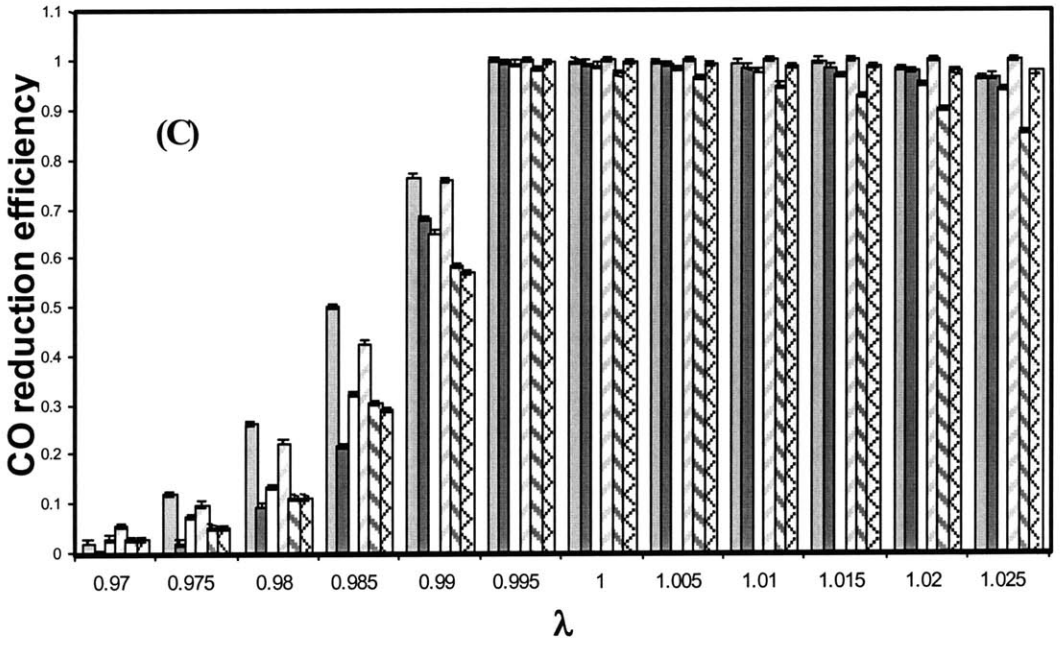

Fig. 3-5 Emission reduction efficiencies for 4K, 50K and 150K mile catalysts at 7 and 33 ppm S fuels as a function of λ. There was no modulation on λ. Engine at 1600 rpm, 0.5 bar intake pressure. (a)NO; (b) HC; (c) CO.

3.3 Air/Fuel Ratio Closed-Loop Control, Modulation, etc

3.3.1 Air/Fuel Ratio Closed-Loop Control

The three-way catalytic converters simultaneously reduce the three main types of harmful emissions -- CO, hydrocarbons (HC), and NOx. As mentioned in Chapter 2, the levels of engine-out emissions depend on the air-fuel ratio of the engine. Figure 3-5 shows that the performance of a TWC also depends on this air-fuel ratio. For instance, the CO conversion efficiency increases from 20% to 100% between λ=0.98 and λ=1. Moreover, the appropriate air/fuel ratio for high conversion depends on the relevant species. Thus, CO and HC are easily and almost completely converted under lean operations, where the exhaust contains abundant oxygen to oxidize them, whereas NOx is better reduced under rich operations when enough reducing species (CO, HC, H2, etc) are present in the exhaust. Hence, TWC can achieve high conversions of the three pollutants in a narrow window near stoichiometry.

So it is quite natural to make use of a closed-loop control system in combination with the TWC to achieve desired high conversion efficiencies for all three species simultaneously (as shown in Fig. 3-6). The closed-loop system uses a air/fuel ratio feedback signal to maintain a time-averaged λ close to 1. The sensor used is a simple Nernst cell as described in Chapter 2.

The oxygen sensor mounted upstream of the converter inlet which detects whether the system is running lean or rich. This information is then sent to the ECU that adjusts the air-fuel ratio so that, on the average, the A/F is stoichiometric.

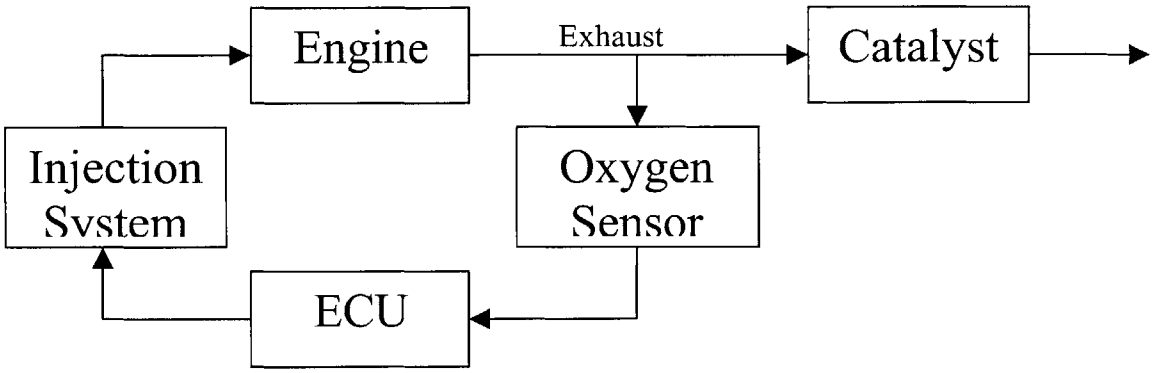

Fig. 3-6 Schematic of a closed-loop control system

3.3.2 Air/Fuel Modulation under ECU Control

In reality, however, it is practically difficult to keep λ precisely at 1 for every cycle (within the narrow window of simultaneous high conversion efficiency). The more stringent emissions standards require a more robust control algorithm to ensure high conversion efficiency of the TWC at all times. The practice is to add a special agent in the carrier that can store extra oxygen in the feed gas and release oxygen when needed. This oxygen storage medium allows the closed-loop control system to maintain λ at 1 on the average rather than for every cycle. The oxygen storage capacity is extremely important and effective especially during engine transients. More details on the oxygen storage capacity quantification, its degradation with aging and fuel quality, and modeling will be discussed in more details in the following chapter.

A commonly adopted air/fuel ratio control strategy, also a very effective one, is to keep the oxygen storage "half-filled" most of the times. Thus, when the engine experiences either instantaneous rich or lean operation, the oxygen storage medium will always have capacity to store or release oxygen.

Due to the non-linearity of the oxygen sensor output, the control algorithm is normally trying to modulate the air/fuel ratio at a certain frequency and with certain amplitudes. This will on the one hand effectively keep the oxygen storage at "half-filled". On the other hand, because the time-averaged air/fuel ratio is kept at stoichiometric, it essentially expands the high-efficiency window of the TWC.

A commonly adopted practice of air/fuel ratio modulation is λ between 0.975 and 1.025, at 1-2 Hz frequency. More quantified study of different ways of modulation will be discussed in the following chapter.

3.3.3 Conversion Efficiencies under ECU modulation

Experiments have been carried out for three catalysts at different levels of aging (4k, 50k and 150k miles), and 4 different sulfur fuels (7, 33, 266 and 500 ppm fuel sulfur level).

Fig. 3-7 shows the results of NO and HC breakthroughs (or inefficiencies) of these experiments. CO results are not shown here, due to the facts that the tail-pipe emission levels are too low to be detected by the NDIR instrument.

$$\text{Breakthrough} = 1 - \frac{\textit{Tailpipe Emission}}{\textit{Engineout Emission}} \qquad (3.1)$$

The experiments are run with the engine operating at 1600 rpm, 0.5 bar intake pressure (corresponding space velocity of 4.4×10^4/hr). The engine is under closed-loop ECU control, by which λ was modulated at 2 Hz with amplitude of $0.975<\lambda<1.025$.

The general trends were that both NO and HC breakthroughs increased with catalyst age and with fuel sulfur level. The sensitivity to fuel sulfur is more prominent for older catalysts. These results are consistent with those from fleet testing [24].

For the baseline fuel (7 ppm fuel sulfur) case, it is difficult to discern any correlation between conversion efficiency and aging. The data actually show some inconsistency in the trend (e.g., NO breakthrough for 150k is lower than 50k; HC for 150k is even lower than the 4k catalyst). This is due to the fact that under the operation condition (space velocity and temperature), conversion efficiencies for all three catalysts are so high, that the tailpipe emissions are too low for the instruments to resolve any consistent differences. The mechanism of conversion efficiency and more quantitative explanations will be discussed in later chapters.

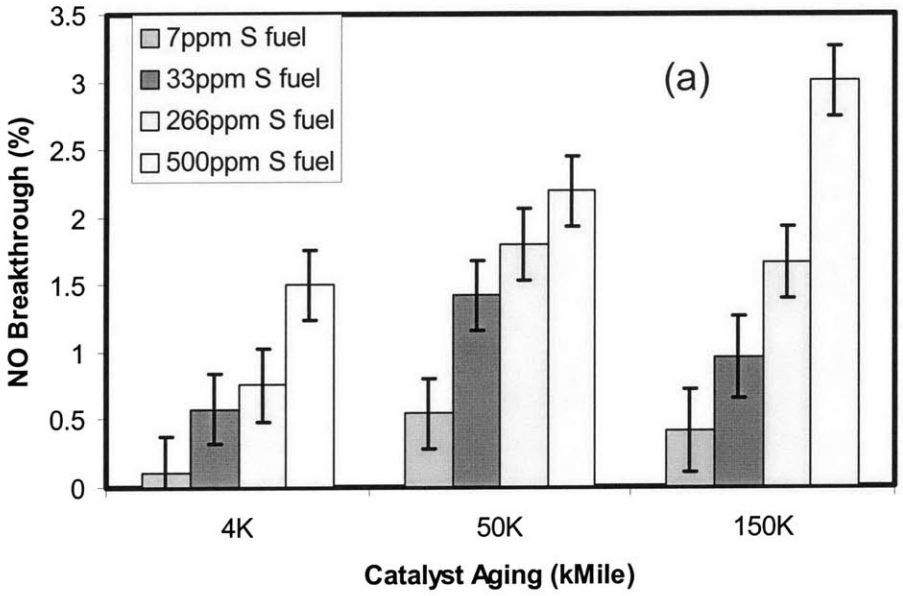

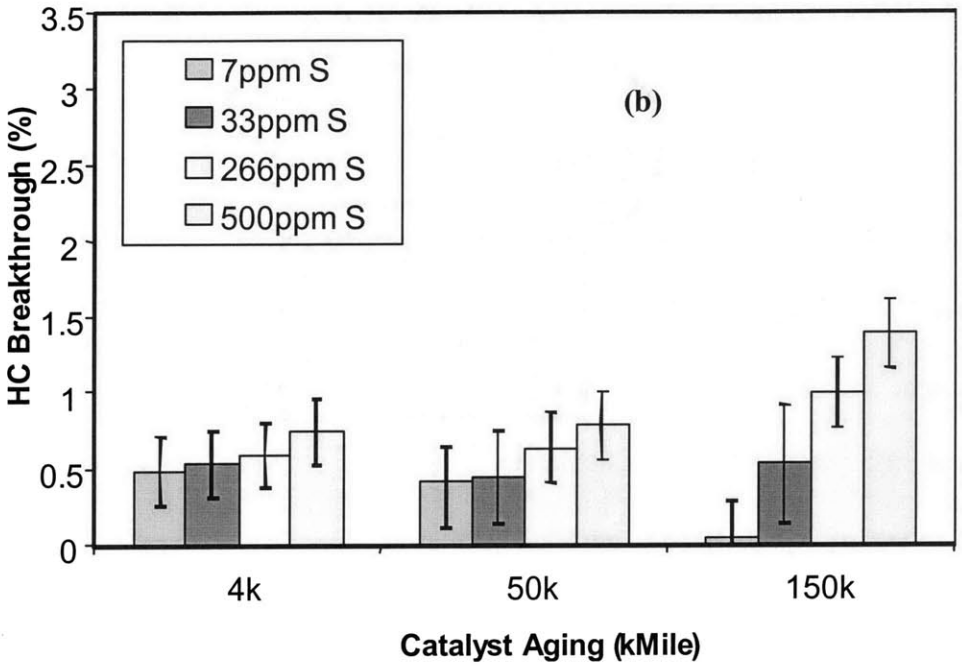

Fig. 3-7 Breakthroughs for catalysts of different ages using fuels at different fuel sulfur levels. Engine controlled by production ECU with λ modulated between 0.975 and 1.025 at 2 Hz; 1600 rpm, 0.5 bar intake pressure. (a) NO breakthrough; (b) HC breakthrough.

Summary

- Overview of three-way catalysts is discussed.
  - Mechanism of catalysis
  - Structure of monolithic converters
  - Degradations, etc
- An overview of the three-way catalyst conversion vs. air/fuel ratio, with different levels of aging and fuel sulfur.
- The ideas of an air/fuel ratio closed-loop control system, oxygen storage, air/fuel ratio modulation, etc, are introduced. The steady-state conversion efficiencies of catalysts at different levels of aging and fuels with different sulfur levels are presented.

Chapter 4

Oxygen Storage

For a warmed up vehicle, a major part of the tailpipe emissions comes from non-steady driving conditions, e.g. acceleration. This is particularly true for aged catalysts, which maintain a relatively good performance under steady-state operating conditions. Analysis of vehicle emissions during the warmed-up part of a certification cycle reveals that the most significant differences between differently aged catalysts lies in their performance in accelerations and decelerations. Therefore, study of the catalyst performance under transient conditions with air/fuel ratio excursions away from stoichiometric could provide valuable information concerning the impact of catalyst deactivation [25].

As described in previous chapters, the oxygen storage ability of the three-way catalyst is an important feature. It allows the catalyst to absorb oxygen when there is excess of oxygen in the exhaust gas; or release oxygen when the exhaust gas is short of oxygen. This ability helps the ECU to operate at air/fuel ratios within a reasonable band, while maintaining high 3-way conversion efficiency. It is especially important during transients and air/fuel ratio excursions. So in this part of the project the oxygen storage capacity is investigated. Special attention is focused on the methodology in quantifying oxygen storage capacity (OSC), and on quantifying the degradation of OSC with aging and fuel sulfur.

4.1 Oxygen Storage Measurements

The oxygen storage capacity of the three-way catalyst may be measured by introducing a perturbation in the feed gas. There are multiple ways of doing this type of testing. Previous research works have reported measurements of the OSC with synthetic exhaust gas [25]. In this research, the catalyst is tested "off-line" on a bench top setup. Synthetic exhaust gas was used instead of the exhaust from an engine. During the experiments, a perturbation in the concentration of CO and HC was introduced after steady-state lean operation was reached. Based on the measurement at downstream of the catalyst, the amount of oxygen stored was quantified.

Work has also been reported with "on-line" method through perturbation of the engine air/fuel ratio [26]. This method can be achieved by either increasing the engine λ modulation amplitude (and recording the amplitude at which the downstream UEGO just starts to show modulation), or it may use the difference in response in the upstream and downstream UEGO sensors when there is a step change in engine λ. The step-λ method was used in this project.

4.1.1 Methodology: λ Rich-to-Lean Step

The procedure is as follows. The engine is controlled by the OEM ECU (with λ modulation at ±0.025 from stoichiometric) until it was at steady state at 1600 rpm, 0.5 bar intake pressure, coolant temperature 85 °C. Then the fuel control was switched to custom control box that operates air/fuel ratio at a fixed rich lambda value until the UEGO signal and the emissions measurements downstream of the catalyst come to steady state. (It took up to 10 minutes; the limiting process was to wait till the HC emissions stabilized). At

this point, the oxygen storage in the catalyst is considered to be depleted. Then the injection duration was switched to result in a lean lambda value. Care was taken so that there was no switching in the midst of an injection process. Then the value of OSC is determined from the λ sensor response downstream of the catalyst.

4.1.1.1 Defining Oxygen Storage

There are two issues in the step-λ method. The first involves the interpretation of the signal so that an oxygen storage capacity can be obtained. The second is due to the fact that the oxygen storage so measured depends on the λ value of the lean mixture going through the catalyst [27]. Therefore a meaningful value for the oxygen storage needs to be defined.

The response of the UEGO sensors upstream and downstream of the catalyst in a rich-to-lean λ-step transient is shown in Fig. 4-1. Referring to the figure: in the period from t0 (start of the step) to t1, the engine-out stream contained excess of O2, but very small amount of CO and H2. That the downstream λ reading was rich was interpreted as a result of the release of CO and H2 that were stored in the catalyst during the rich operation before the step. These released gases consumed the feed-gas O2 supply until t1. Starting from t1 till t2, oxygen is being stored by the catalyst.

From t1 to t2, the difference in upstream and downstream λ value was due to the absorption of O2 by the catalyst storage mechanism. We assumed that in the period [t0, t1], since there was presence of reducing gases in the catalyst exit, the amount of the engine-out oxygen that was stored by the catalyst should be small compared to the amount that was consumed by the reducing gases. (In reality, there may still be a small

amount of oxygen storage in the presence of reducing gases; thus the following calculation method may underestimate the storage.)

Because the λ sensor measures oxygen concentration, conversion to mass flow needs to be done. The calculation is listed in equation 4.1.

$$m_{o2} = \frac{W_{O2}}{W_e} \int_{t_1}^{t_2} \dot{m}_e \left[x_{o2}(\lambda_u(t)) - x_{o2}(\lambda_d(t)) \right] dt \qquad (4.1)$$

Where t1 and t2 are defined in Fig. 4-1;

λ_u and λ_d are up- and down-stream air/fuel ratios;

xo2 is oxygen mole fraction in the exhaust;

$\dot{m}_e$ is mass flow rate of the exhaust;

Wo2 is molecular weight of oxygen;

We is average molecular weight of the exhaust.

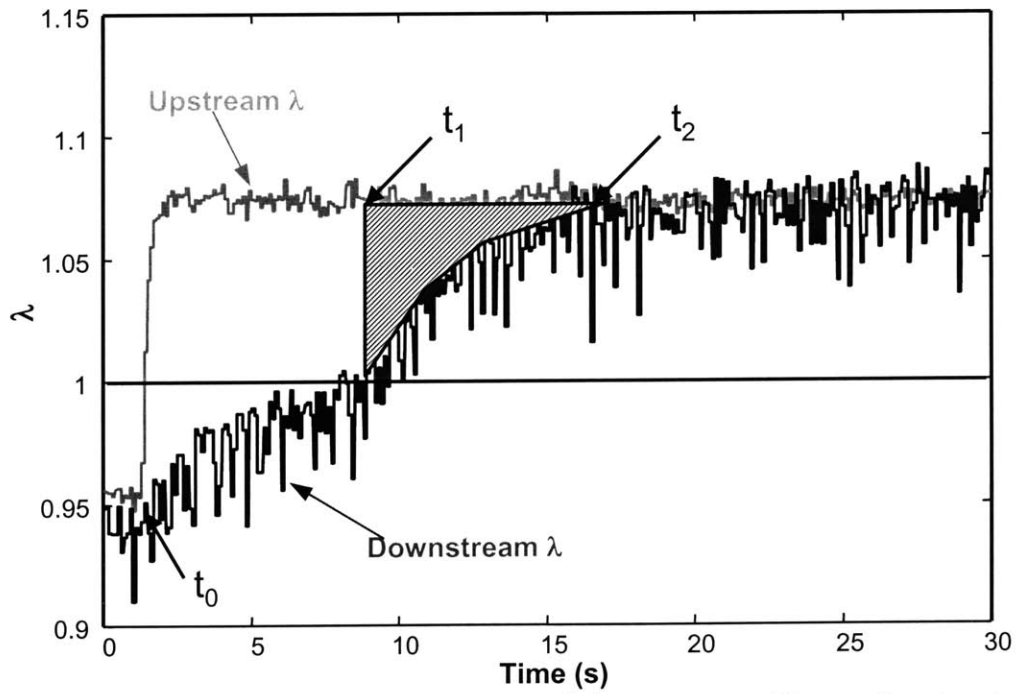

Fig. 4-1 Response of UEGO sensors upstream and downstream of the catalyst to a lean step transient

Since the λ values involved in Eqn. 4.1 are greater than 1, the oxygen mole fraction (xo2) as a function of λ only depends on the fuel H to C and O to C ratios. The relationship can be found in Appendix A.

4.1.1.2 Choice of λ Rich Value

As described above, and will be justified in the following sectors, the rich value of λ does not affect how much oxygen is stored by the catalyst with this method. So essentially any rich value will satisfy the experiments, as long as all oxygen stored in the catalysts is depleted. Since in our experimental setup we do not control the exhaust temperature, thus by varying the rich value, exhaust temperature will change. This will have an impact on the amount of oxygen stored in the process, since almost all reactions are affected by temperature changes.

So in the experiments, we try to make the rich value as close to stoichiometric as possible, thus to minimize the temperature effects. At the same time, it is made sure there is no oxygen left in the catalysts before the lean step.

On the other hand, the lean λ value (final value of the step change) is varied. This gives us a matrix of correlation of oxygen vs. λ final lean values. This will be discussed more in experimental results and modeling of the oxygen storage.

4.1.2 Method Justification

4.1.2.1 Interpretation of UEGO Sensor Response

In the absence of oxygen, the UEGO sensor oxygen pumping current i_p is proportional to the weighted sum of the reducing gas mole fractions x_j [28]:

$$i_p \propto \sum_j \xi_j \left(\frac{D_j}{D_{O_2}} \right) x_j \qquad (4.2)$$

Here the index j represents the different reducing gases (CO, H_2 and HC, which is taken as CH_m , where m is the same as the hydrogen to carbon ratio of the fuel). The symbol D denotes mass diffusivity, and λ_j is the number of O_2 molecules required to oxidize one molecule of the reducing gas j. (Refer to Chapter 3, where the mechanism of UEGO is discussed.) Thus when the λ meter registers a rich reading (i_p in equation 4.2 is non-zero), there must be the presence of a reducing gas in excess of oxygen.

Referring to Fig. 4-1, the λ value was stepped from 0.95 to 1.08. The upstream λ sensor indicates, within the 100ms or so response time of the sensor, that the engine out composition responds immediately. The steady-state engine out composition at λ = 1.08 was measured. The CO and HC mole fractions (on a wet basis) were 0.16% and 0.1% C1 respectively. The hydrogen to CO ratio is approximately 1/3, which is typical of engine out composition. (We were not able to calculate the hydrogen mole fraction by a materials balance from the fuel input and the exhaust measurements because the result was extremely sensitive to the accuracy of the CO2 measurement at such low CO and H2 concentrations.) With these values of concentration, air/fuel ratio can be calculated. The lower bound of calculated λ is approximately 0.99. This value is substantially higher than the actual UEGO output during the period t_0 to t_1 in Fig. 4-1. For example, at the mid point between t_0 and t_1, the λ value was 0.97. To register such a value, the corresponding CO mole fraction (assuming that the H_2 to CO ratio is 1/3 and HC concentrations were at 1000 ppmC1) would be 1.1%. This value was nearly an order of magnitude higher than the measured engine out CO value (0.16%). Thus materials balance across the catalyst

would indicate that there must be substantial reducing gases coming from the catalyst itself. Thus absorption of oxygen alone could not explain our observation quantitatively.

A piece of indirect evidence that there may be release of reducing gases from the catalyst in the rich-to-lean step transient (from a rich λ_1 to a lean λ_2) was that we had done the experiments at various combinations of λ_1 and λ_2 values. At fixed λ_2, when we calculated the oxygen storage by integrating over the whole recovery period from t_0 to t_2, the results were dependent on λ_1. This dependence disappeared when the storage was calculated by integrating from t_1 to t_2 instead. Our interpretation was that the total consumption of O_2 in the period $[t_0,t_1]$ was mainly due to oxidation of the reducing gases released from the catalyst. Since the amount stored was dependent on the value of λ_1, the storage so calculated would be dependent on λ_1. On the other hand, in the period $[t_1, t_2]$, the released reducing gases were oxidized already, and the storage so calculated would not be dependent on the initial λ value. Thus there is a consistency in the explanation.

4.1.2.2 Downstream Fast Response CO2 Results

The interpretation of the experimental data is in agreement with the observation of a post-catalyst CO2 peak during λ lean step changes, reported in [29].

As shown in Fig. 4-2, during λ rich-to-lean excursions, a post-catalyst CO2 peak can be observed (in period E, F); the peak then decays to the steady state level at start of period E.

The shaded area in Fig. 4-3 shows the amount of oxygen consumed during time period from t0 to t1. If we assume CO + ½ O2 → CO2, then an estimation can be made based on the peak in post-catalyst CO2 (refer to Fig. 4-4). The comparison of these two

numbers shows that it is justifiable during (t0-t1) the oxygen in the feed gas is mainly consumed by the release of CO from the catalyst.

The results reported in [29] were generated on a setup of a 4-cylinder 1.8L SI-engine. According to a general design guideline, the volume of the catalyst should be around the same as the displacement volume of the engine. This is not identical to the engine/catalyst setup as used in this project; however, the results qualitatively justify the way of interpreting the phenomena during a λ rich-to-lean excursion.

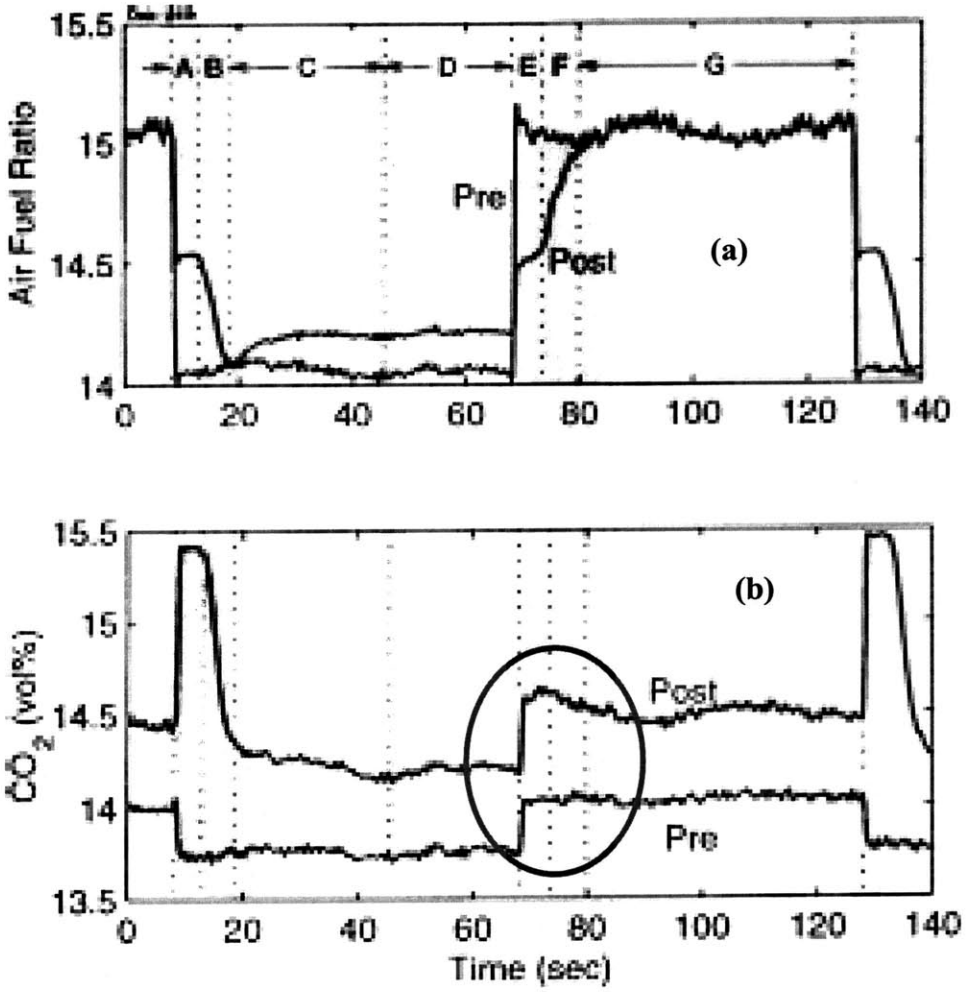

Fig. 4-2 Time-resolved CO2 during λ lean step, with fast-response CO2 meter

(a) pre- and post-catalyst air/fuel ratio, (b) pre- and post-catalyst CO2

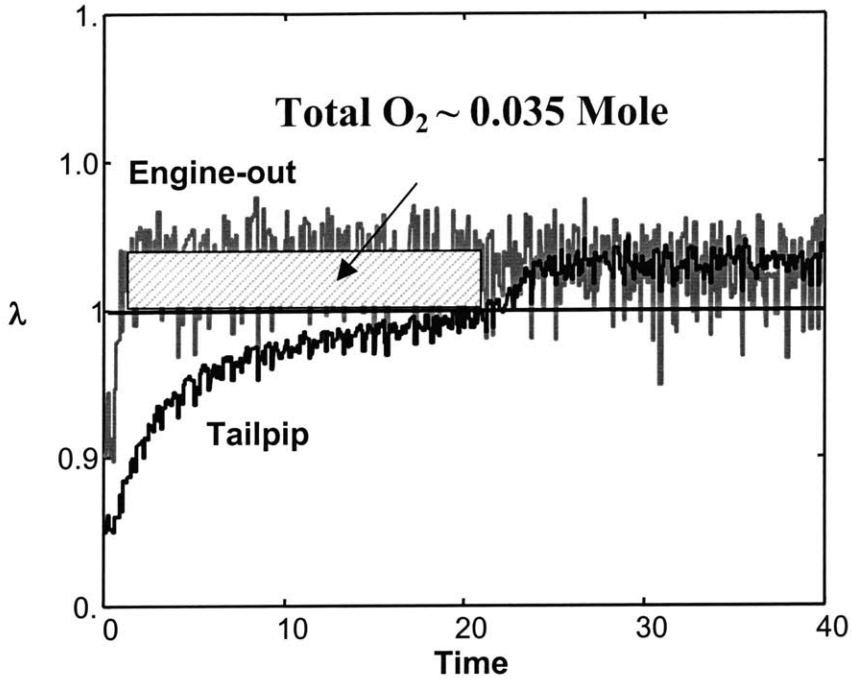

Fig. 4-3 Oxygen consumption during λ rich-to-lean excursion

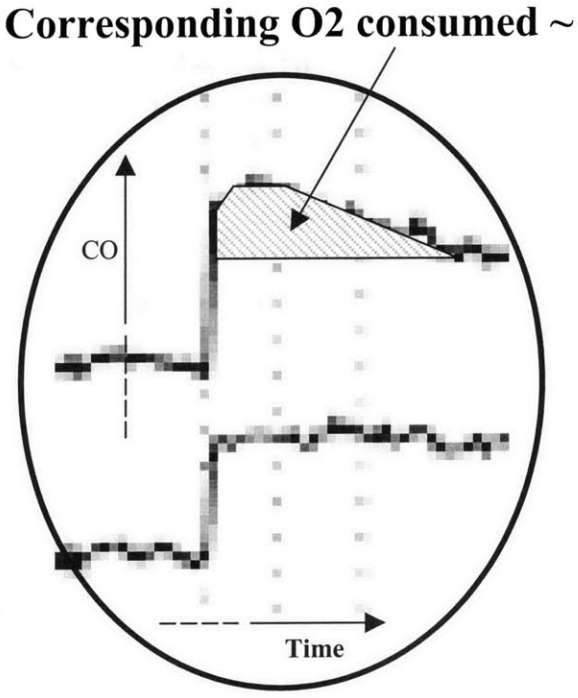

Fig. 4-4 Oxygen consumption calculated from post-catalyst CO2 peak during λ rich-to-lean excursion

4.1.3 Experimental Results

The OSC determined by Equation 4.1 is obtained for the whole test matrix. The tests include catalysts at 3 different levels of aging (4k, 50k, and 150k-mile), 4 different sulfur fuels (7ppm, 33ppm, 266ppm, and 500ppm), and different λ steady state values (shown in Fig. 4-5).

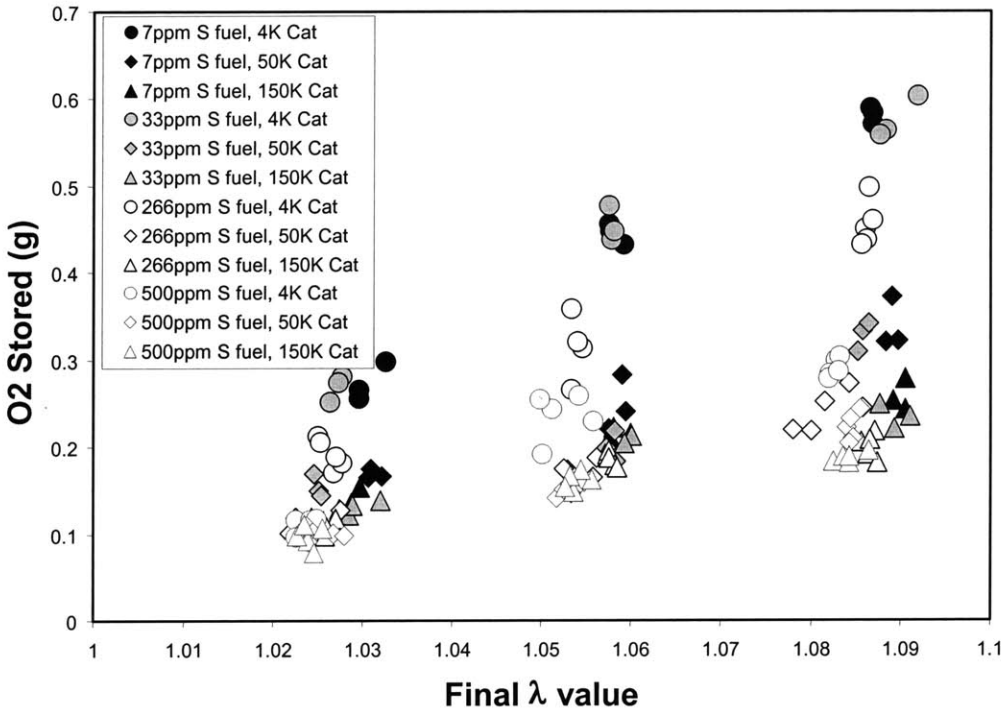

Fig. 4-5 Catalyst oxygen stored as a function of the final gas stream λ value in the λ - step transient. The results were independent of the starting λ (<1) value

The general trend shown in the figure can be easily seen: (1) with catalyst getting more aged, there is less oxygen stored; (2) with fuel sulfur level increasing, there is less

oxygen stored; (3) and with λ final value increasing, more oxygen is stored in the process.

Though the oxygen storage is a function of λ final lean values in the step transients, they are not dependent on the λ rich value before the step. These results are consistent with those of Ref. [27].

4.2 Oxygen Storage Modeling

To understand the fact that the OSC is dependent on the λ value of the feed stream, a simple thermal equilibrium model is formulated.

4.2.1 Thermal Equilibrium Model

The major oxygen storage medium in the three-way catalysts is cerium oxides (CeO_2, Ce_2O_3, etc). The governing reaction of oxygen storage is

$$Ce_2O_3 + 1/2O_2 \leftrightarrow (CeO_2)_2 \qquad (4.3)$$

Where, CeO_2 is the high value oxide (more valence bonded oxygen by cerium atom), and Ce_2O_3 is the low value oxide. When the exhaust gas is oxidizing (excessive oxygen) the low value oxide is oxidized to the high value oxide; whereas, when the exhaust gas is reducing, the high value oxide can release the oxygen stored back to the feed gas [21, 30].

In the following model, the oxygen storage capacity is assumed to be in equilibrium with the mole fraction of oxygen in the gas stream. Let the unoccupied oxygen storage sites be denoted by Z, and the occupied ones be denoted by ZO. (These names are symbolic; the actual molecular structures involving the tri-valent and quadra-

valent ceria are more complex. See Fig. 4-6 from [69].) Then the storage process may be described by

$$Z + 1/2O_2 \underset{k_b}{\overset{k_f}{\rightleftarrows}} ZO \tag{4.4}$$

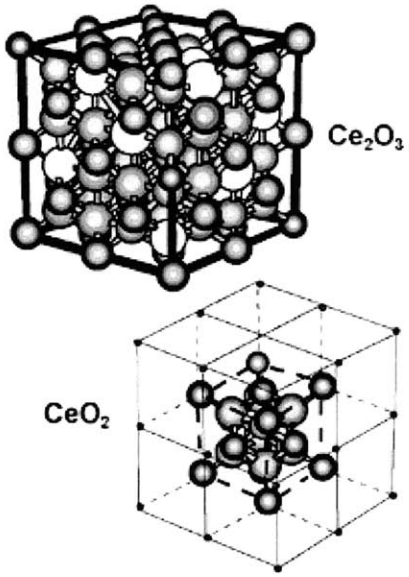

Fig. 4-6, Lattice unit cell for Ce2O3 and CeO2. Blue, read and white spheres indicate the cerium, oxygen atoms and vacancies, respectively. A cubic unit cell of Ce2O3 can be constructed out of eight CeO2 unit cells by increasing the volume by 3% and removing 25% of the oxygen atoms along four nonintersecting <111> diagonals.

If z and z' denotes the site density (in cm^{-2}) of Z and ZO, and n_{o2} denotes the gas stream oxygen concentration (in $mol \cdot cm^{-3}$), the forward and backward reactions in Eqn. 4.4 must be in equilibrium at the end of the transient. Thus

$$\frac{z'}{(n_{O2})^{1/2}\, z} = \frac{k_f}{k_b} \equiv k_e \tag{4.5}$$

Furthermore, the total site density z_{total} is

$z_{total} = z + z'$

Note that z_{total} should be a constant value for each case of catalyst aging and of fuel sulfur level, etc.

Combining Eqns 4.4 and 4.5, and making use of the ideal gas law (Eqn 4.6)

$$n_{O2} = \frac{P}{\Re T} x_{O2} \tag{4.6}$$

The occupied site density z' is related to the total site density z_{total} by Eqn 4.7.

$$z' = \frac{k(x_{O2})^{1/2}}{1 + k(x_{O2})^{1/2}} z_{total} \tag{4.7}$$

Where $k \equiv k_e P/(\Re T)$. Since the mass of the stored oxygen m_{O2} (which is the measured quantity) is proportional to z', it is therefore, according to Eqn 4.7, a function of the gas stream oxygen mole fraction (x_{O2}), which is a function of λ. Eqn 4.7 may be rewritten in terms of m_{O2}:

$$m_{O2} = \frac{k(x_{O2})^{1/2}}{1 + k(x_{O2})^{1/2}} m_{O2,max} \tag{4.8}$$

Where the maximum oxygen storage capacity, $m_{O2,max}$ (proportional to z_{total} with the same proportional constant as m_{o2} to z'), is independent of operating conditions.

The correlation between oxygen storage and oxygen concentration in the exhaust gas is plotted in Fig. 4-7. From the figure and Eqn 4.8, it is obvious that with oxygen concentration increasing in the exhaust, the amount of oxygen stored increases. The OSC saturates at a maximum value ($m_{O2,max}$) when oxygen concentration goes infinite.

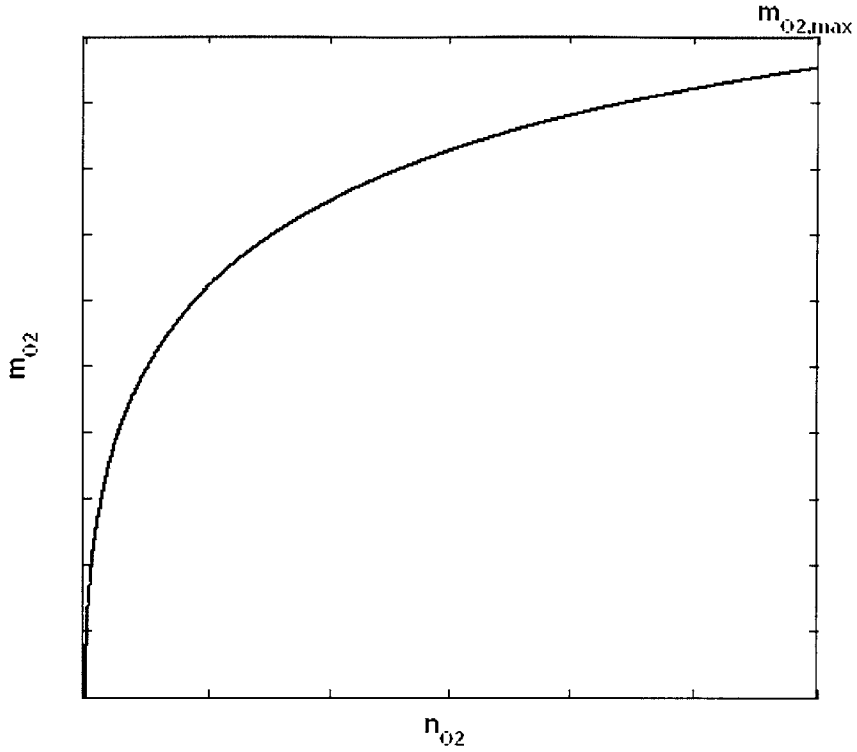

Fig. 4-7, Oxygen storage modeling – OSC as a function of oxygen concentration in exhaust gas

4.2.2 Maximum Oxygen Storage Capacity

In the experiments, m_{O2} was measured as a function of x_{O2}, which was varied by changing λ; refer to Fig. 4-5. If the value of k is known, the maximum oxygen storage capacity can be determined from Eqn 4.8. In general, k depends on the catalyst operating conditions; for example, the temperature. For the limited range of operating conditions we used, we make the simplifying assumption that k is not a function of x_{O2}. However, because an important mechanism for the storage process is the transfer of the absorbed oxygen from the PGM sites to the cerium oxide, the effective rates in Eqn 4.4 will depend on the available PGM sites, which deteriorate with age and fuel S. Therefore k will be both a function of the catalyst age and the fuel S level.

From the above discussion, analysis of the stored-O_2 data proceeded as follows: for each catalyst age and fuel S level, the k and $m_{O2,max}$ values were determined by a least square fit of the data for the different λ values according to Eqn. 4.8. (Note that k and $m_{O2,max}$ are physically independent quantities.) The fit to the model is shown in Fig. 4-8. In spite of the simplifying assumption, there is very good agreement between the model and the data.

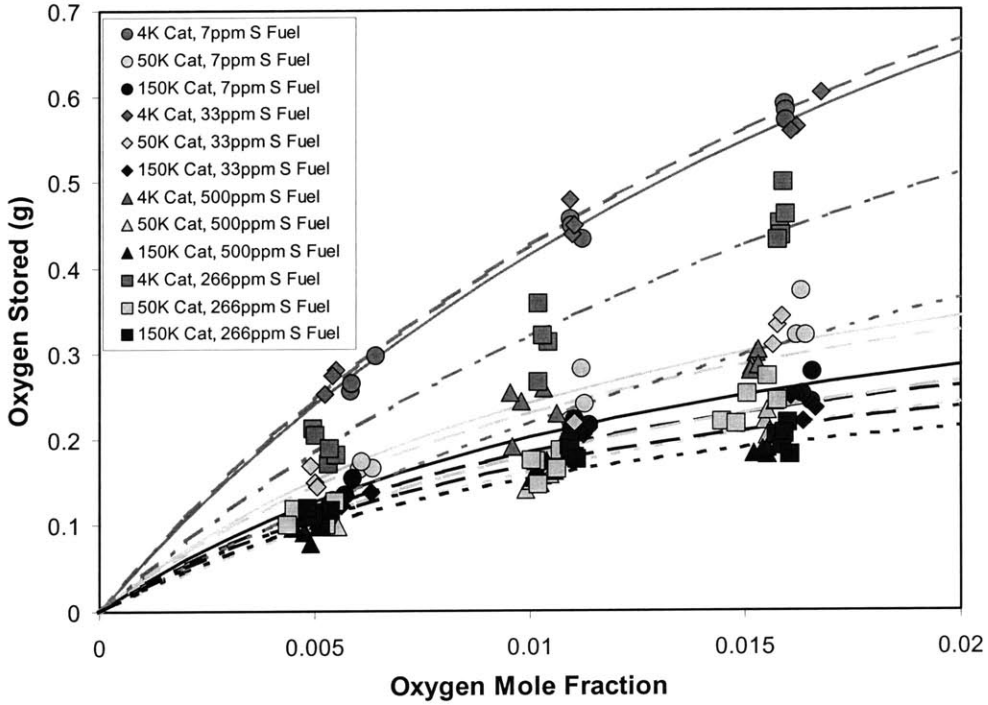

Fig. 4-8 Oxygen storage as a function of oxygen concentration in exhaust gas; the curves are least square fit of the model (Eqn. 4.8) to the experimental data.

When the model is calibrated with experimental data, the maximum oxygen storage capacities then can be estimated with the above-described model. There is one maximum oxygen storage capacity for each aged catalyst and with the fuels at different S levels are shown in Fig. 4-8. There was a substantial drop in the capacity (more than a

factor of 2) in the early part of aging (from 4K to 50K miles). The decrease, however, was more modest (~30%) from 50K to 150K miles.

When the data in Fig. 4-9 were normalized with respect to the storage capacity with 7 ppm-S fuel for each catalyst of the same age, the results were found to be relatively independent of the catalyst age; refer to Fig. 4-10. This result implies that the reduction in O2 storage capacity may be decoupled into two factors: degradation due to the catalyst age and one due to the fuel sulfur level. The effects of these two factors are multiplicative.

The averaged normalized O_2 storage capacities over the catalyst age are plotted versus the fuel S levels in a semi-log plot in Fig. 4-10. The slope of the plot implies that the storage capacity decreases by a factor of 1/e with every 1400 ppm increase in fuel S level (or equivalently, decreases by 10% with every 150 ppm increase in fuel S level.

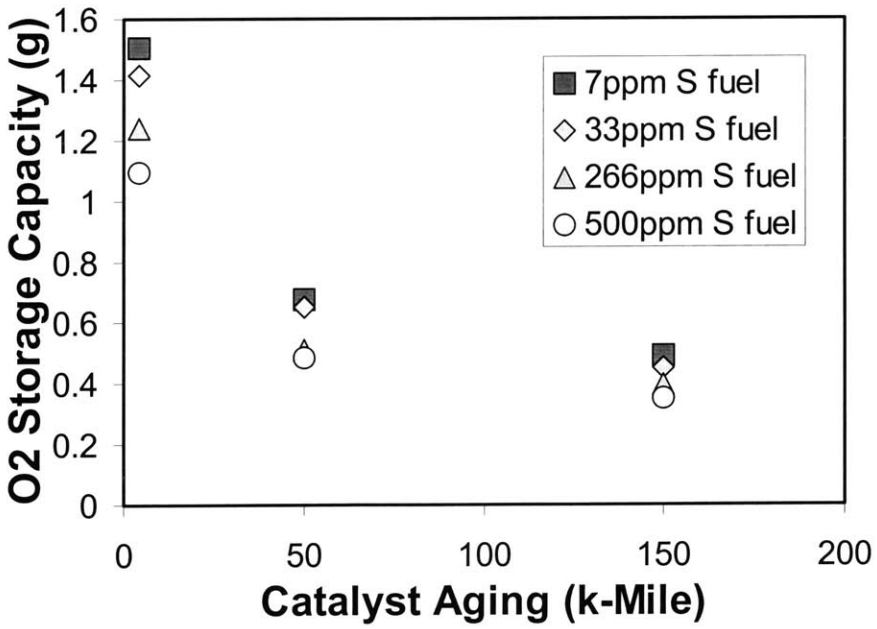

Fig. 4-9, Maximum oxygen storage capacity as a function of catalyst aging, with different levels of fuel sulfur.

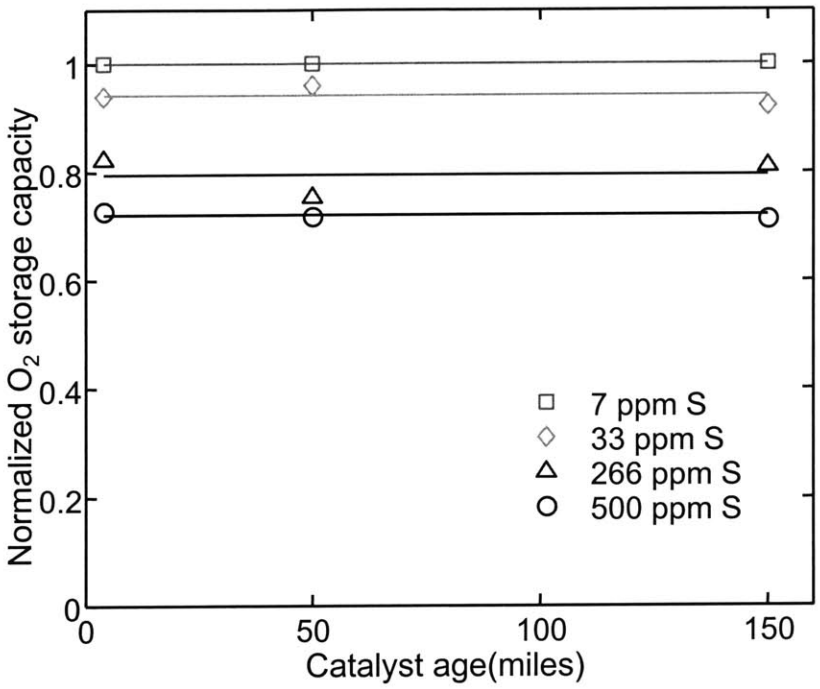

Fig. 4-10, Oxygen storage capacities normalized with respect to 7 ppm sulfur fuel for each catalyst aging. The horizontal lines are average values of OSC capacity of each sulfur fuel over all aged catalysts.

4.2.3 Sulfur Effects on Oxygen Storage Capacity

That the degradation of the catalyst oxygen storage capacity may be quantified multiplicatively by an age-factor and a sulfur-effect factor is an important result. And in theory it is reasonable. In the age degradation, there is permanent lost of the storage medium due to physical (fouling, and wash-coat abrasion) and chemical (poisoning) processes. On the other hand, the sulfur effect is, to a large extend, reversible [32-39]. Effectively there is a chemical equilibrium between the sulfur/ceria complex (which are the lost oxygen storage sites) and the gas stream sulfur content. Hence the loss of storage is a function of the sulfur level, and the sulfur effect is a multiplicative factor on top of the age effect.

Based on the normalized oxygen storage capacity shown in Fig. 4-10, the sulfur effects can also be investigated, see Fig. 4-11. If the data is looked at from a different

perspective, i.e., plotted vs. sulfur level in the fuels instead of aging. The new plot is shown in Fig. 4-11.

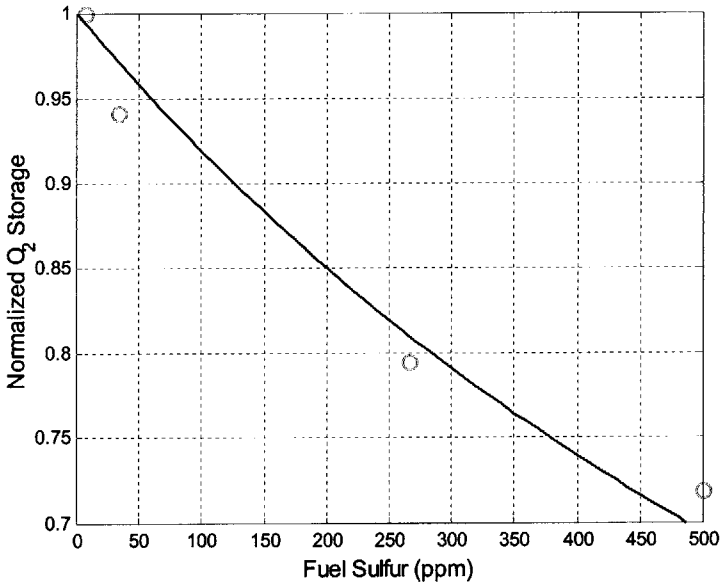

Fig. 4-11, Normalized oxygen storage capacity as a function of fuel sulfur level; the values in the plot are averaged values of all catalysts for each sulfur level.

It noticeable that fuel sulfur level has a negative impact on the oxygen storage capacity of the catalyst. This observation is consistent with other published work on sulfur effects on three-way catalyst, oxygen storage, etc.

According to other research work in this field, the sulfur oxides interact with CeO_2, which is the main medium for oxygen storage. The main reaction between sulfur oxides and the OSC medium include [40]:

$$CeO_2 + 2SO_3 \leftrightarrow Ce(SO_4)_2 \quad (4.9)$$

$$CeO_2 + SO_3 \leftrightarrow CeOSO_4 \quad (4.10)$$

$$3SO_2 + 6\,CeO_2 \leftrightarrow Ce_2(SO_4)_3 + 2Ce_2O_3 \quad (4.11)$$

Ce(SO4)2 formed by reaction 4.9 is stable at low temperatures but decomposes at temperatures > 195 degC. CeOSO4 (in Eqn. 4.10) is reported to be stable at temperatures

> 700 deg C [40]. SO2 is able to reduce CeO2 according to reaction 4.11 and is catalyzed by the presence of Pt [41,42]. Ce2(SO4)3 is thermally stable under approximately 625 degC in oxidizing or stoichiometric exhaust, but not under reducing conditions.

As described in the experiments sections, during the rich-to-lean step experiments the catalysts experienced extended period of reducing feed gas. And the temperature inside the catalyst under such operations (1600 rpm, 0.5 bar intake, etc.) is normally well above 650 degC. Thus, reaction 4.9 and 4.11 can be neglected for this analysis.

A similar thermal equilibrium model can be setup as the one described above (Eqn. 4.5 – 4.8). Define z_1 as density of Ce_2O_3 sites, z_2 for CeO_2 sites, z_3 for $CeOSO_4$; also define z_{total} as the total sites, so that

$$z_{total} = z_1 + z_2 + z_3 \tag{4.12}$$

Again, define $z'_{total} \equiv z_{total} - z_3$ (4.13)

So at equilibrium, we can get:

$$z_3 = \frac{k' x_{SO_3}}{1 + k' x_{SO_3}} z_{total} \tag{4.14}$$

$$z'_{total} = z_{total} - z_3 = \frac{z_{total}}{1 + k' x_{SO_3}} \tag{4.15}$$

$$z_2 = \frac{k x_{O2}^{1/2}}{1 + k x_{O2}^{1/2}} z'_{total} \tag{4.16}$$

plug 4.15 into 4.16

$$z_2 = \frac{k x_{O2}^{1/2}}{1 + k x_{O2}^{1/2}} \cdot \frac{z_{totla}}{1 + k' x_{SO3}} \tag{4.17}$$

Thus, Eqn. 4.17 shows that z_2 is proportional to $\frac{1}{1+k^{'}x_{SO3}}$. If plot z_2 as a function of fuel sulfur level (concentration of SO_3) in Fig. 4-11 (red curve). It proves that the model matches the normalized the maximum OSC for each fuel sulfur level quite well. This model of oxygen storage degradation by sulfur level is very important. It has reconfirmed the hypothesis that aging and sulfur effects act independently; and the sulfur effect on oxygen storage is reversible.

Summary

In this chapter, oxygen storage mechanisms of the three-way catalyst are investigated. Based on the engine-catalyst setup described in Chapter 2, λ rich-to-lean step change experiments are used to quantify the oxygen storage capacity of a three-way catalytic converter. It is found from the experimental data that the oxygen storage of the catalyst is a function of oxygen concentration of the exhaust gas (the storage ability deteriorates with catalyst aging and fuel sulfur level).

Based on the experimental observation, a hypothesis is put forward that the amount of oxygen stored by the catalyst is determined by thermal equilibrium, i.e., the availability of oxygen in the exhaust gas, and amount of oxygen storage sites. With the catalysts getting aged and/or the fuel sulfur levels increasing, available sites are diminished. With the thermal equilibrium hypothesis, a numerical model is setup. It turns out, the model matches the experimental data very well. This confirms the hypothesis is valid.

With the model, the maximum oxygen storage capacity can be estimated. The capacities of different catalysts and sulfur fuels are compared. An interesting

phenomenon is that the acts of aging and fuel sulfur in degrading the oxygen storage ability are independent.

Finally a similar thermal equilibrium model is setup in interpreting the sulfur effects on oxygen storage. The model matches the data very well, which reconfirmed the thermal equilibrium hypothesis and the fact that the sulfur effects are mainly reversible.

Chapter 5

Catalyst Behaviors during Throttle Transients

The monolithic catalytic converter is a very effective device in reducing exhaust pollutants from the exhaust gas. This is especially true when the catalyst is fully warmed up. Under steady states, the catalyst can achieve constant upper 90% conversion efficiencies for all species. Even for severely aged catalyst, the performance is still high enough to meet the equivalent emissions standards. This fact has been reported in numerous research works [21], also has been observed in this project (refer to Chapter 3). The biggest challenge in controlling the overall emissions from the exhaust lies in transients.

Past results show that during transient operations, the aging effects are very pronounced. The investigation into the emissions or pollutants breakthrough during transients are categorized into three main groups:

First, interaction among the species during such transients. This is discussed in this chapter.

Second, role of oxygen storage and its effects on pollutants breakthrough during transients. This will be covered in Chapter 6, air/fuel ratio modulation.

Third, loss of effective surface area, i.e., loss of effective mass transfer due to aging effects. This will be covered in Chapter 7, experiments on a flow-reactor setup.

In this chapter the behavior of the catalysts during throttle transients is investigated experimentally. The goal is to make some detailed observations of the species inside the catalysts during a transient. And the measurements and observations

will help shed light on what governs the pollutants breakthroughs during transients qualitatively. Also the aging effects can be investigated qualitatively with the help of in-catalyst measurements.

5.1 Observations of NO Breakthroughs during Throttle Transients

Previous work has shown that during a throttle transient (manifold air pressure (MAP) changes abruptly from a low opening to wide-open throttle (WOT)), there is a substantial post-catalyst NO emission breakthrough. The characteristic of the NO breakthrough is that there is a primary breakthrough right after the throttle transient is delivered, and a secondary breakthrough several seconds after the primary one. This phenomenon is very repeatable under controlled conditions. And another interesting observation is that for the more aged catalyst the breakthroughs are more noticeable than the fresher ones (refer to Fig. 5-1, 5-2, and 5-3). In Fig. 5-3 the primary breakthrough is significantly lower than those in 5-1 and 5-2. And the secondary breakthrough is hardly noticeable. [43]

These observations have shown that during throttle transients, the air/fuel ratio is very hard to be controlled at stoichiometric (see pre-catalyst λ in Fig. 5-1 to 5-3). Thus, the high conversion efficiencies observed at steady states are no longer achievable, especially for more aged catalysts.

So it is important to understand more of the behavior of the catalysts during transients. Later in this section, more experiments on throttle transients are carried out. With the help of in-catalyst sampling, more insights into what is going on inside the catalysts during transients are provided.

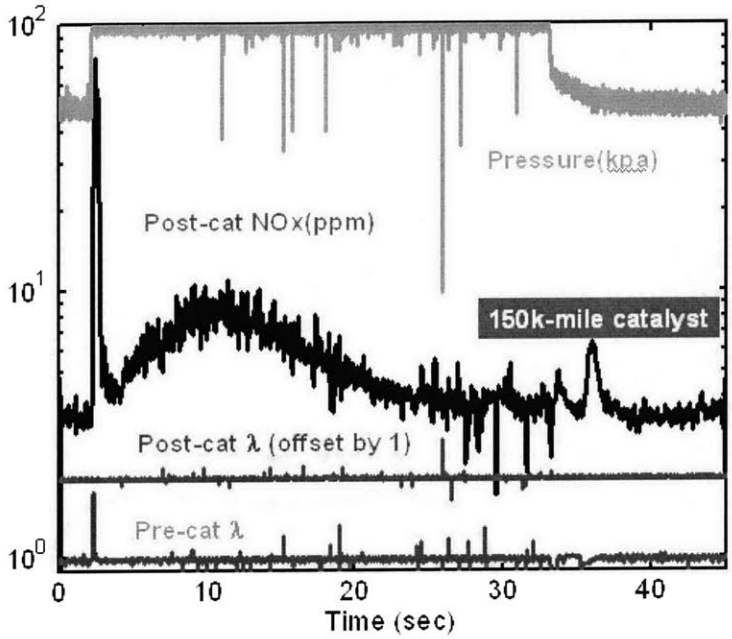

Fig. 5-1 NO breakthrough during throttle transients for the 150 k-mile aged catalyst

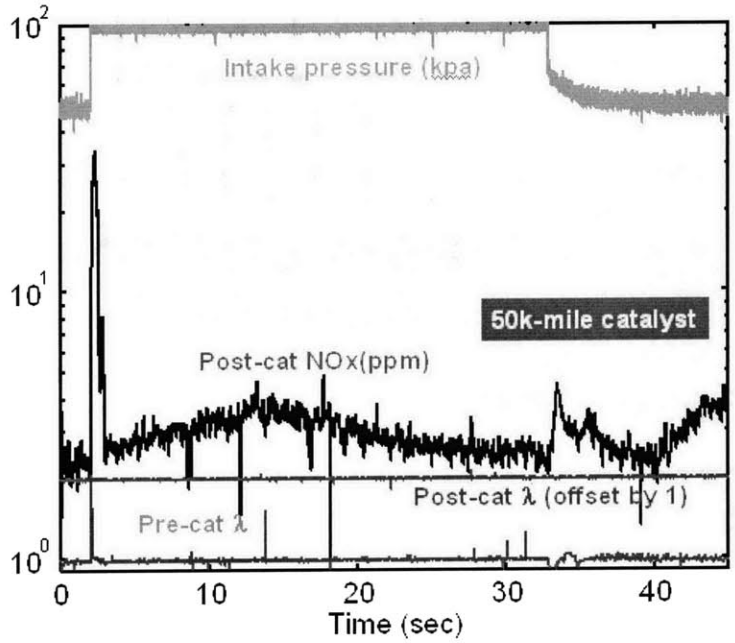

Fig. 5-2 NO breakthrough during throttle transients for the 50 k-mile aged catalyst

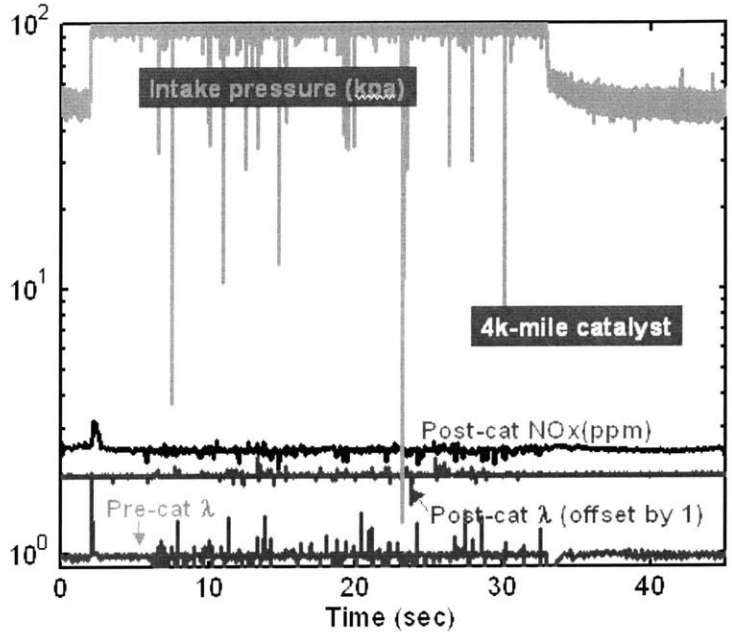

Fig. 5-3 NO breakthrough during throttle transients for the 4 k-mile aged catalyst

5.2 In-Catalyst NO Measurements during Different Modes of Throttle Transients

5.2.1 NO Measurements in Fast Throttle Transient Experiments

Since the NOx emission is very sensitive to transients, and NOx has a very strong correlation with the oxygen presence in the exhaust gas, NO profile along the catalyst during transients were used as the taleteller.

The throttle transients were carried out in a controlled manner. As introduced in the experimental setup chapter, the throttle is controlled by a stepper motor. In the experiments two sets of throttle transients were carried out. In both cases the engine speed were stabilized at 1600 rpm, coolant temperature at 85 degC, catalysts were fully warmed up. In the first case, the throttle was controlled so that the MAP changed from 0.5 bars to 1 bar (WOT) within 1 second. This is to simulate a very aggressive acceleration (shown in Fig. 5-4).

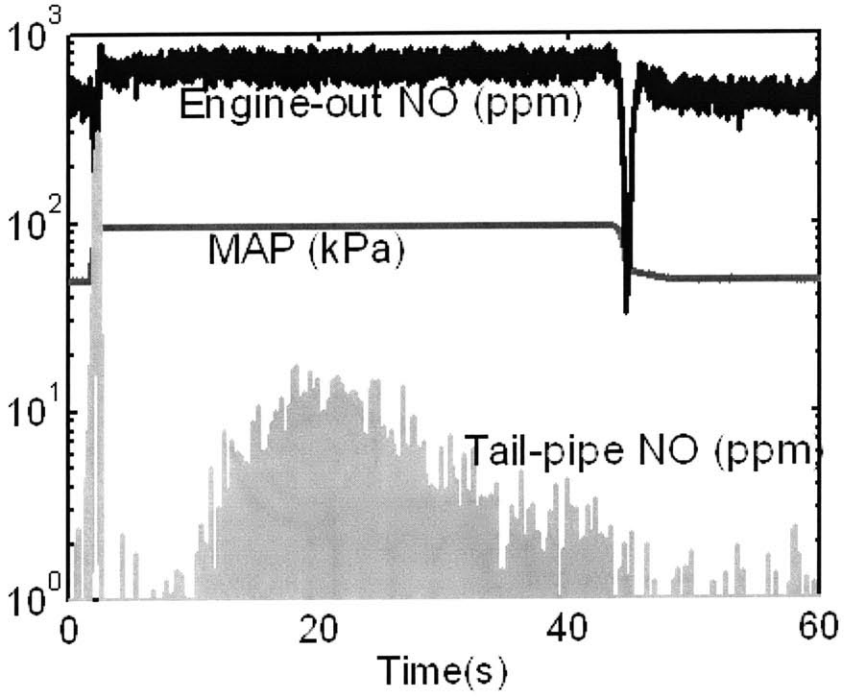

Fig. 5-4, Fast throttle transient experiments, MAP from 0.5 bars to 1 bar within 1 second.

Detailed NO concentration profile along the catalysts are shown in Fig. 5-5 to 5-7. On the left of the figures, up- and down-stream λ are shown, also the MAP value and engine-out NO mole fraction. On the right of the figures, there are 6 curves, each representing the sampling points along the catalysts, starting from the first point inside the catalysts (refer to Chapter 2, experimental setup).

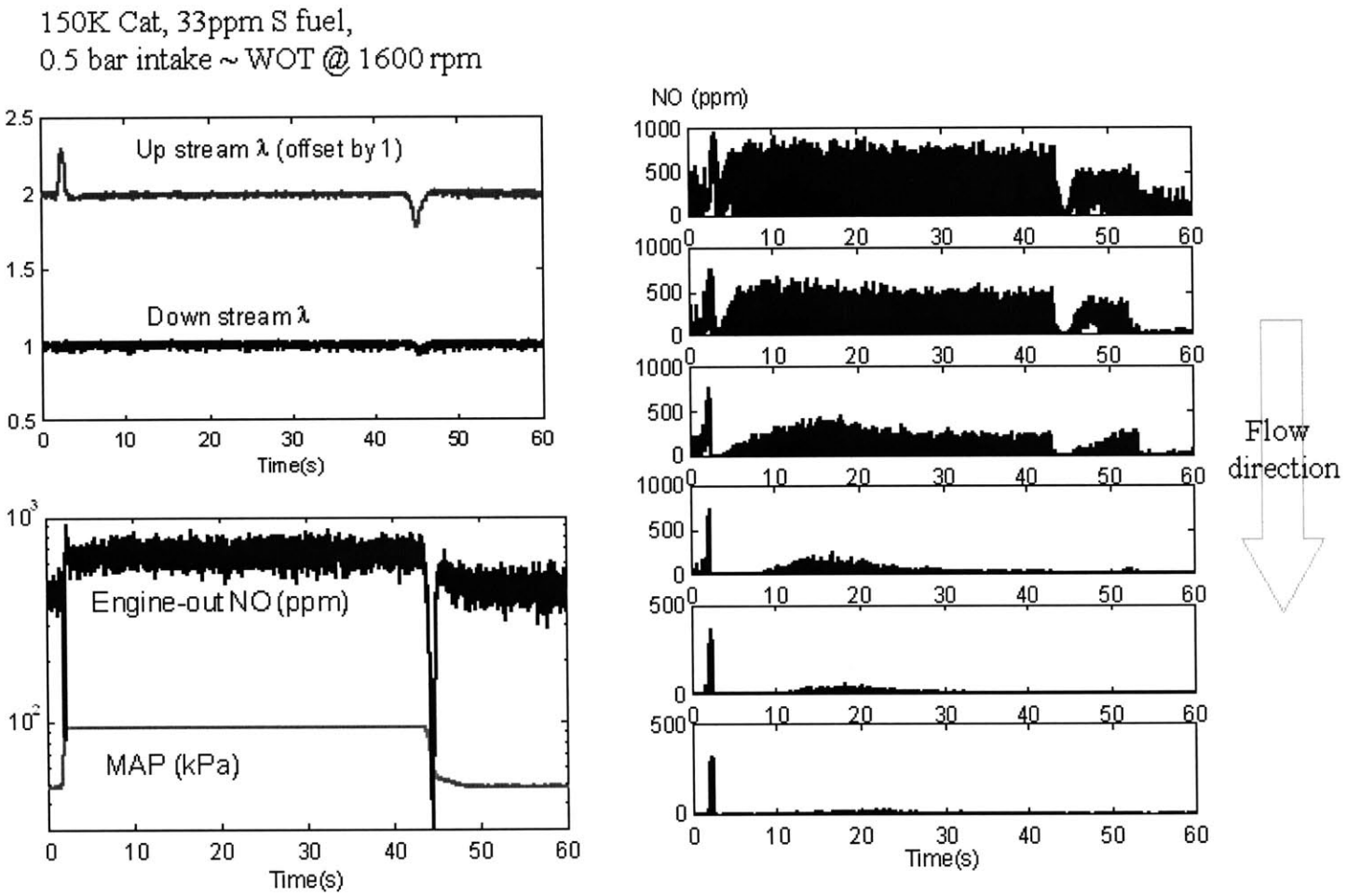

Fig. 5-5, NO concentration along the 150k catalyst during fast throttle transient,

MAP from 0.5 bars to WOT within 1 second

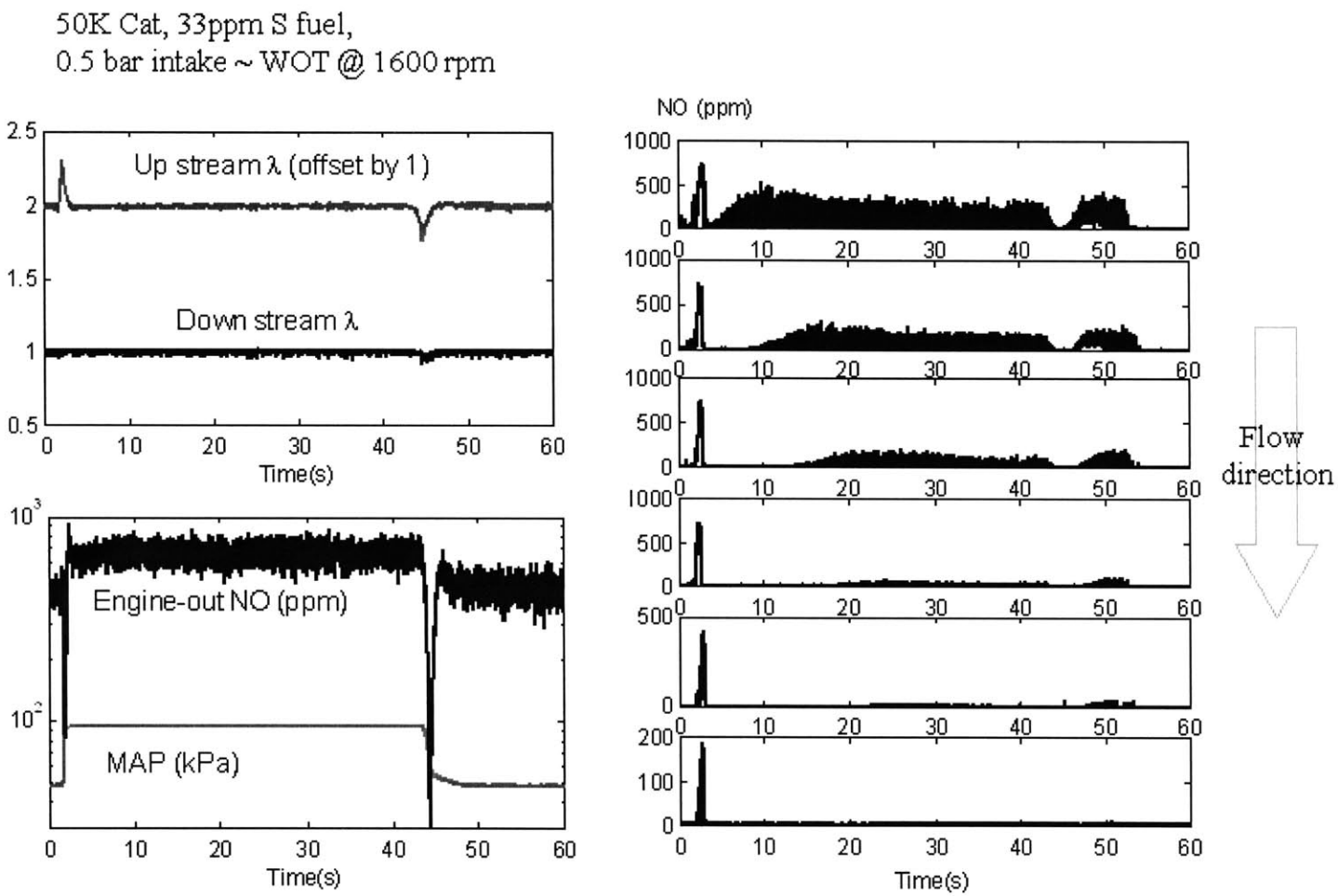

Fig. 5-6, NO concentration along the 50k catalyst during fast throttle transient,

MAP from 0.5 bars to WOT within 1 second

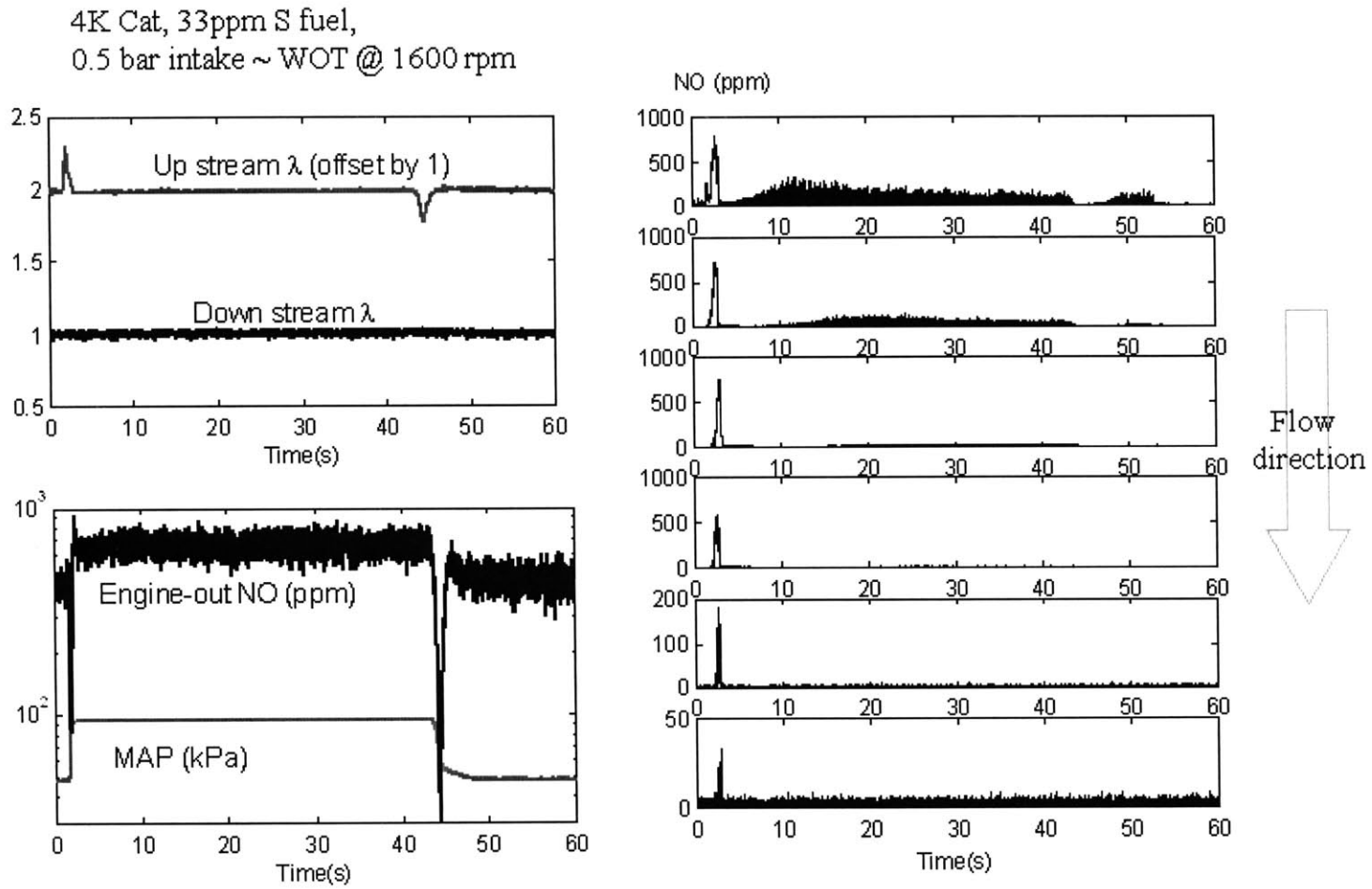

Fig. 5-7, NO concentration along the 4k catalyst during fast throttle transient,

MAP from 0.5 bars to WOT within 1 second

Note that in the figures the scales for NO mole fractions are different. Several observations can be made on these experiments.

1), During these throttle transients the fueling was not well compensated, so that the air/fuel ratio was thrown off unity during the transients. The engine-out λ has two substantial "spikes" when throttle was suddenly opened or closed (see Fig. 5-5 to 5-7). The magnitudes of the air/fuel ratio excursion reached 25~30% of stoichiometric values. These values are well beyond the region where the catalyst conversion efficiencies are high.

2), The NO primary and secondary breakthroughs are consistent with previous observations. They are decreasing in magnitude along the catalysts. The reduction is fast. By the time the exhaust gas reaches the tail pipe, substantial amount of the NO breakthrough is gone, only very small amount actually breakthrough the whole length of the catalysts.

3), For fresher catalysts, the breakthroughs are reduced faster (4k catalyst > 50k catalyst; 50k catalyst > 150k catalyst, etc.). So by the end, the fresher catalysts show better conversion efficiencies than the more aged ones. This observation is in agreement with the previous data that only showed engine-out and tail-pipe NO measurements.

4), The insight into these experiments is that even though under steady states the aged catalysts are still doing a good job in converting the pollutants, under transient conditions it is very obvious that the aging effects are playing a role. It shows that with the catalyst getting aged, the pollutants can breakthrough further along the catalysts. Therefore, the size of the catalysts is needed (this statement will be re-confirmed in later

chapters when the catalytic actions are studied in details), even though under steady state a smaller catalyst might be adequate.

5.2.2 NO Measurements in Milder Throttle Transient Experiments

Next a relatively milder transient experiment was run. The conditions were all kept at the same except for the MAP. In this set of experiments, the MAP was changed from 0.5 bars to 0.8 bars within 0.3 second. It is a less aggressive transient, as shown in Fig. 5-8.

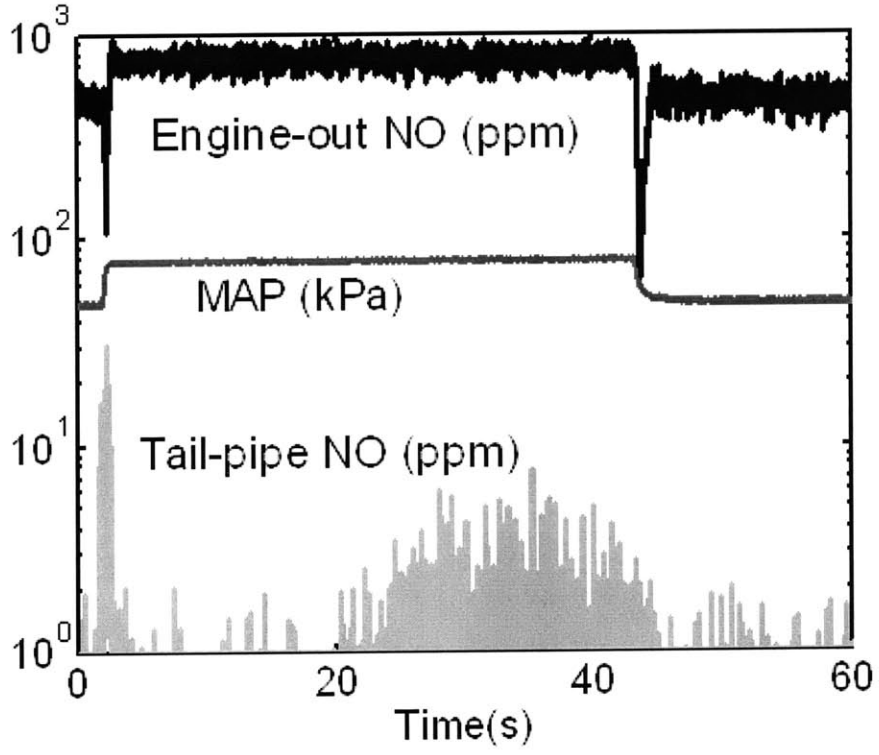

Fig. 5-8, Less fast throttle transient experiments, MAP from 0.5 bars to 0.8 bars within 0.3 second

Detailed NO concentration profile along the catalysts are shown in Fig. 5-9 to 5-11. Same as in Fig. 5-5 to 5-7, on the left of the figures, up- and down-stream λ are

shown, also the MAP value and engine-out NO mole fraction. On the right of the figures, there are 6 curves, each representing the sampling points along the catalysts, starting from the first point inside the catalysts (refer to Chapter 2, experimental setup).

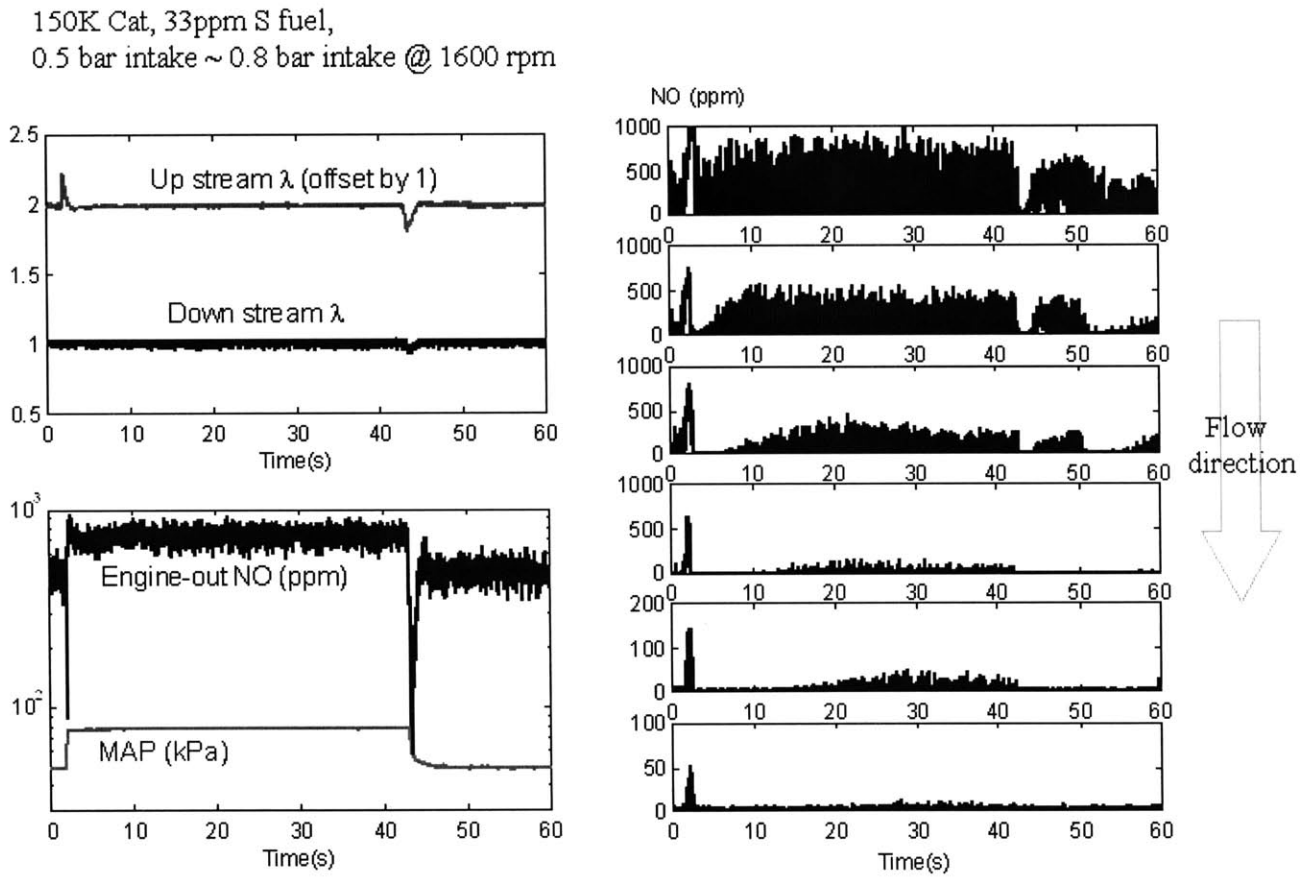

Fig. 5-9, NO concentration along the 150k catalyst during fast throttle transient,

MAP from 0.5 bars to 0.8 within 0.3 seconds

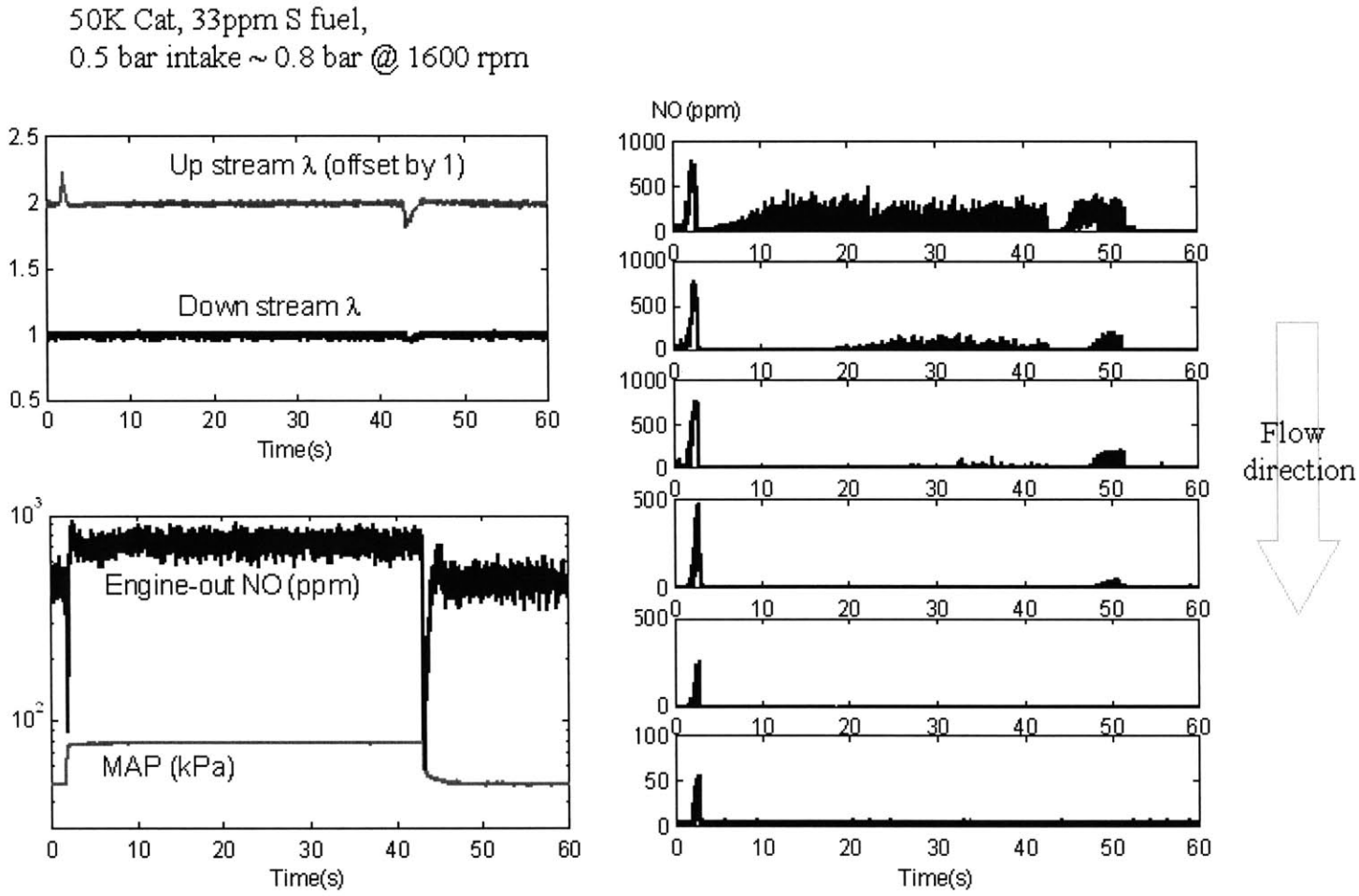

Fig. 5-10, NO concentration along the 50k catalyst during fast throttle transient,

MAP from 0.5 bars to 0.8 within 0.3 seconds

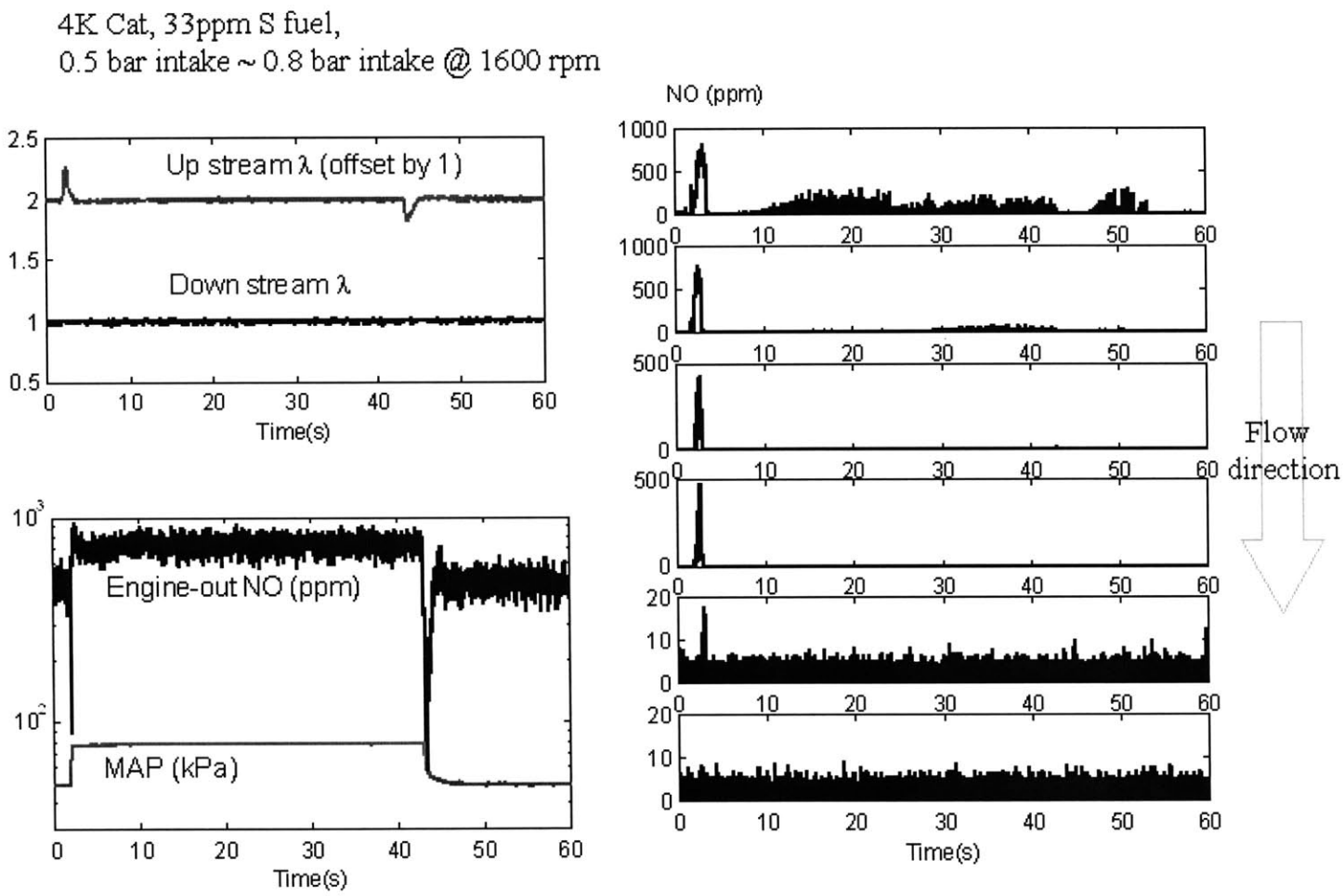

Fig. 5-11, NO concentration along the 4k catalyst during fast throttle transient,

MAP from 0.5 bars to 0.8 within 0.3 seconds

The less aggressive transient experiments yielded very similar results. Overall trends are identical to the previous experiment. The only difference is the overall breakthroughs are lower for all three catalysts. This is due to the fact that these transients are relatively less aggressive.

In order to get more information of what is happening inside the catalyst during a transient, more measurements were carried out on HC and CO emissions.

5.3 CO, HC, and NO Measurements in Fast Throttle Transient Experiments

In this section, not only was just NO concentration profile measured, the HC and CO concentrations were also sampled during the same fast throttle transients. The goal is to try looking at the interaction among these three species during such transients, as described in the beginning of this chapter.

5.3.1 Measurements of CO, HC, and NO during Throttle Transient Operations

The experimental conditions in this set of data are identical to the fast throttle transients described in 5.2.1. Again, the engine was stabilized at 1600 rpm, coolant temperature was at 85 degC. The air/fuel ratio was controlled by the ECU. During the transients, the throttle was opened in a way so that the MAP changes from 0.5 bars to 1 bar (WOT) within approximately 1 second (refer to Fig. 5-4).

In the mean time CO, HC and NO mole fractions were measured from the sampling ports along the catalysts (refer to Chapter 2, experimental setup). Several issues need to be clarified first:

1), When measuring time-resolved values, the probes of the fast-response meters were sequentially inserted into the sampling ports. So the measurements were not taken at the exact same time. Since the experiments were very well controlled, the results were very repeatable, although the phasing information from position to position was lost.

2), The measurement of CO was a little different from those of HC and NO, since as described in experimental setup, the CO instrument used in this project was a slow-response one. Also the exhaust needs to be dehydrated before fed into the NDIR CO meter. So there is a 5~10 seconds delay in the CO reading from the other two readings. Also because of the dehydration process, the long sampling tubing and the long NDIR cell the measurements were time averaged by the sampling system. The readings were on a dry basis.

3), Only the 4k and 150k catalysts were tested. Since they are representative of a fresh catalyst and an aged one. The 50k catalyst values should reasonably fit somewhere in between.

Fig. 5-12 shows the NO mole fraction along the catalysts. The left column is the 150k catalyst, from top to bottom there are 7 curves, each representing a sampling point along the catalyst, starting from the engine-out (top) and ending at the tail-pile (bottom). The right column is the 4k catalyst; the curves denotes the same points as the 150k catalyst.

Fig. 5-13 shows the CO mole fraction along the catalysts. It can be seen that the curves are smoother. This is due to the fact that the CO meter is a slow response one. The big spikes when throttle closes from WOT are caused by a large amount of CO coming

out of the engine during a λ rich excursion. The values simply exceeded the full range of the CO meter.

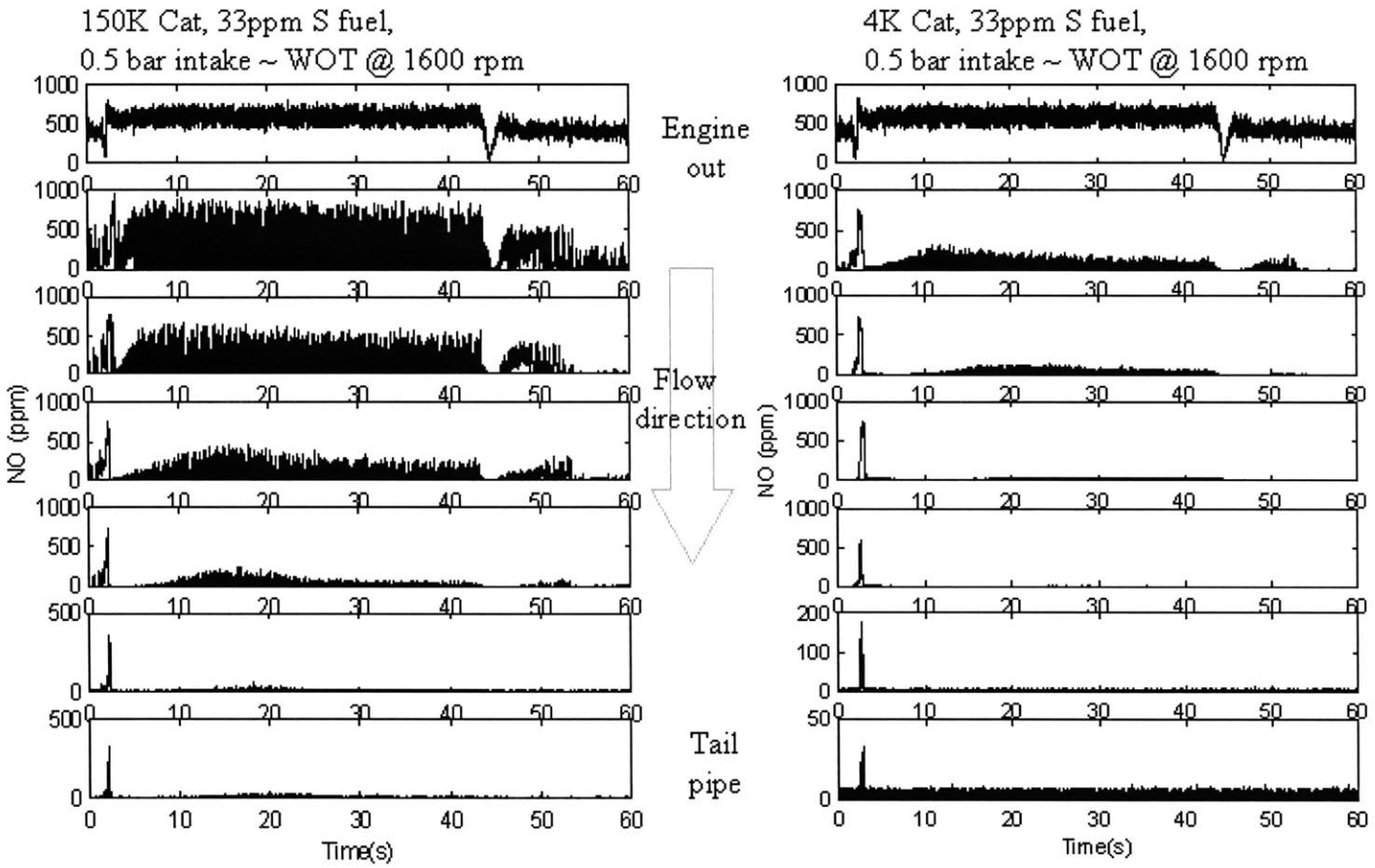

Fig. 5-12, NO mole fraction along the catalysts during a fast throttle transient,

On the left, 150k catalyst; on the right, 4k catalyst

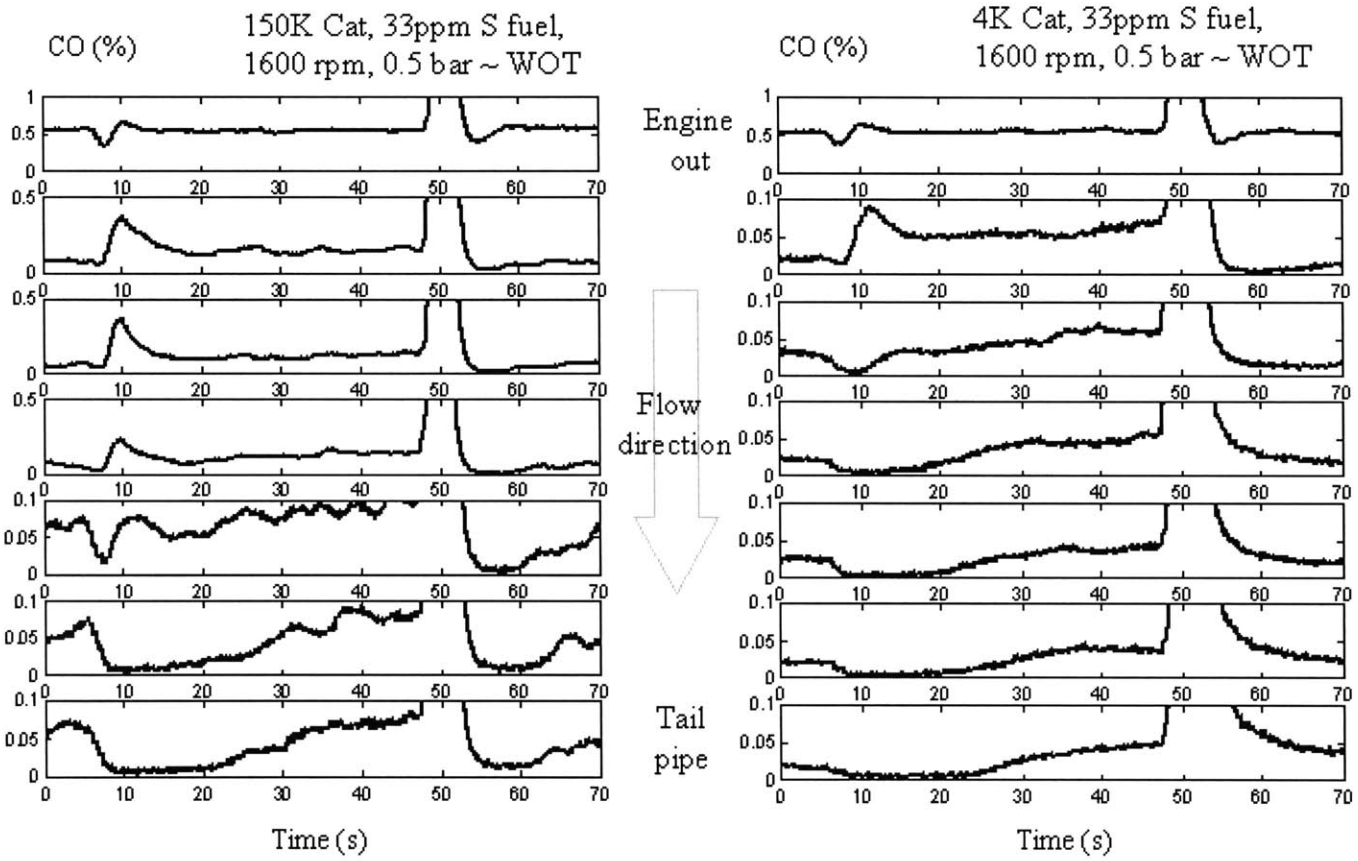

Fig. 5-13, CO mole fraction (slow-response) along the catalysts during a fast throttle transient.

On the left, 150k catalyst; on the right, 4k catalyst

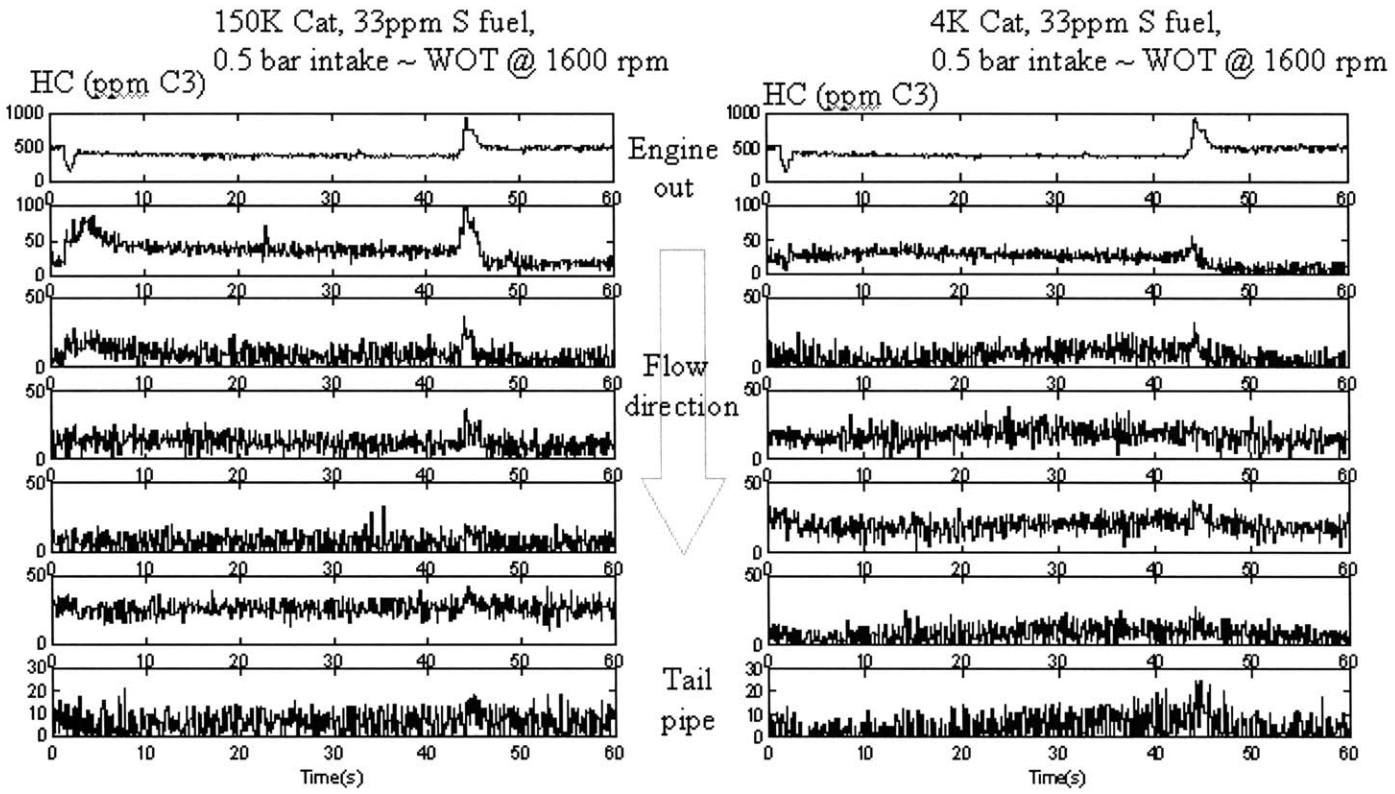

Fig. 5-14, HC mole fraction (C-3) along the catalysts during a fast throttle transient.

On the left, 150k catalyst; on the right, 4k catalyst

Fig. 5-14 shows the HC mole fraction along the catalysts in C-3.

5.3.2 Observations and Discussions

Based on the measurements of CO, HC and NO the following observations can be made:

1), Interestingly, there is no significant breakthrough of HC during the transients, even for the aged catalyst (150k). So NO and CO are the main species that are interesting.

2), Referring to Fig. 5-4, there is a lean excursion in λ when the throttle was opened; and a rich excursion when it is closed. The lean spike in λ caused the engine-out CO to drop substantially. And this is the direct reason there is a NO spike (primary breakthrough) soon after the throttle was fast opened.

3), Then the CO starts to recover and immediately following the lean spike, there is a brief period of small enrichment. The CO output from the engine during this period puts a depression in the NO time profile in the catalyst. Because of this depression the NO breakthrough was artificially separated into a "primary" and "secondary" breakthrough.

An interesting finding based on the measurements is that the composition of the exhaust gas is an important factor in deciding the pollutants breakthroughs. The availability of relevant reactants is crucial in breakthroughs. For example, referring to Fig. 12 & 13, the main reason for the NO primary breakthrough is due to the lack of CO (see the ditch in CO measurement right after the throttle was wide opened). From the charts, it can be seen, that the engine-out CO dropped to a substantially low value (less

than half the normal level). Furthermore, at the same time, there is more oxygen coming out of the engine, almost all of the CO available is consumed by O2 first (CO reacts preferably with O2). The amount of CO available is determined by mass transfer rate. This will be discussed in chapter 7 & 8.

Very similarly, when the throttle is fast closed, there is a rich excursion in λ. More CO is emitted from the engine, whereas O2 is in deficit, so is NO emission. Thus, there is not enough oxidizers to react with CO. As a result, huge amount of CO just break right through.

Other factors include the aging effects and oxygen storage (the oxygen storage capacity is trying to balance the exhaust composition by storing up or releasing oxygen in the exhaust stream). These effects will be covered in the following chapters.

Chapter 6

Air/Fuel Ratio Modulation

As has been discussed in chapter 2 & 3, the three-way catalyst can reduce all three harmful pollutants in the exhaust simultaneously. The high efficiency, however, can only be achieved when λ is precisely controlled within a narrow window in the vicinity of stoichiometry. In reality the engine is a very non-linear system, and because of the time lag from fuel injection to exhaust composition changes, it is essentially impossible to control the air/fuel ratio to be as precise as needed to guarantee high conversion efficiencies for all species. The solution is to modulate the air/fuel ratio within a certain range at a certain frequency so that on the average, the air/fuel ratio is stoichiometric. This is achievable only with the help of the presence of oxygen storage capacity.

This chapter will be discussing what different modes of air/fuel ratio modulation affect the three-way catalyst performance. What happens when the catalyst gets aged? Also when there is a steady state error in the λ sensor, what the catalyst behavior will be like and how it can be quantified.

6.1 ECU Air/Fuel Modulation

Data were taken with the engine running at 1600 rpm, 0.5 bars intake pressure (space velocity of 4.4×10^4 hr^{-1}). The engine is under ECU closed-loop control. The air/fuel ratio modulation under the ECU is at 2 Hz, with amplitude of $\pm 2.5\%$.

The time-averaged concentrations of the three pollutants are shown in Fig. 6-1. The values are normalized with respect to the catalyst inlet concentrations. It is noted that

there were no significant differences in these profiles for the 4K, 50K and 150K catalyst. Most of the emissions reduction took place in the front portion of the front brick – over 80% of the reduction occurred within the first 20% of the total catalyst volume. More than 90% of the emissions had been removed by the time the flow reaches the second brick. Less than 1% breakthroughs were obtained at the catalyst exit in all cases (different catalysts, and different species) [21].

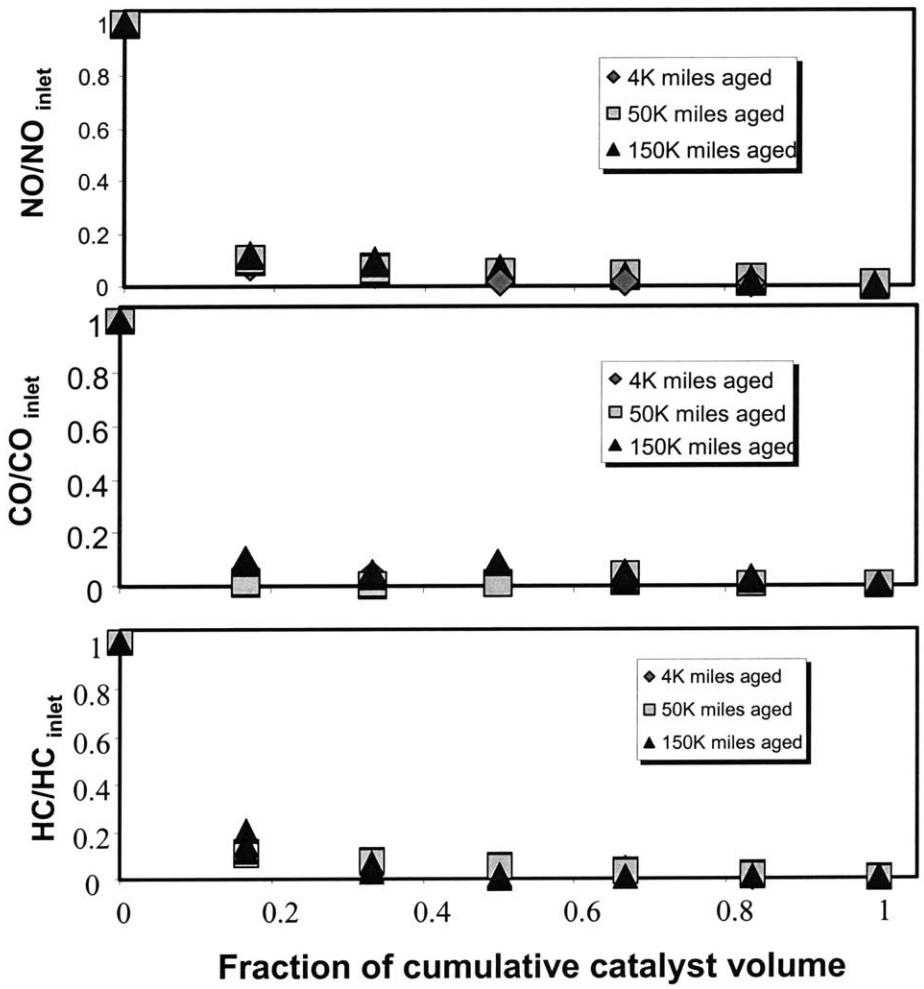

Fig. 6-1, Time averaged species profiles along the catalysts.

Conditions: space velocity= of 4.4×10^4 hr^{-1}, l modulation of ±2.5% at 2 Hz

The catalysts have very high conversion efficiencies under steady state. This is in agreement with the previous chapters. If looked closely enough, the charts (in Fig. 6-1) show that the values for the more aged catalyst (150k) are higher. The difference is not substantial, but very consistent. And the difference is not caused by inconsistency in measurements. In chapter 8 (modeling of the three-way catalyst) it will be fully addressed.

6.2 Arbitrary Air/Fuel Ratio Modulation

Next in this chapter, in order to understand better the role of air/fuel ratio or its characteristics, the air/fuel ratio is controlled with the breakout box introduced in experimental setup.

6.2.1 System Setup

The arbitrary fueling system was programmed so that the air/fuel ratio modulation can be customized for specific amplitudes and frequencies.

A custom program was developed in Labview system, which made use of the D/A (digital to analog) channel in the interface board of the system (refer to chapter 2 – experimental setup). Different modes of air/fuel ratio modulation were pre-programmed into text files. The program then translates the command air/fuel ratio values into corresponding voltages. Via the D/A channel, it then sends the voltages to the breakout box. The voltages were then used as the control voltages in the fuel pulse generation circuit. Thus the air/fuel ratio modulation can be customized. The refreshing rate of the program is on the order of 100 Hz, which is well above the modulation frequency.

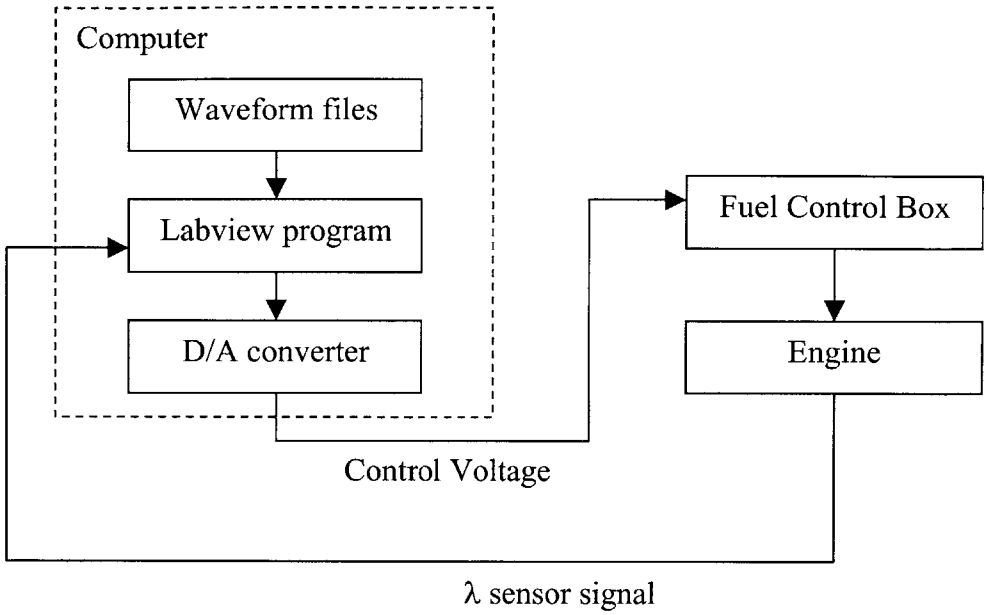

Fig. 6-2, Controlled air/fuel ratio modulation experimental setup schematic

6.2.2 Choice of Bounds for Modulation

Time resolved NO concentrations were measured at several sampling points along the catalyst. Nitric oxide was chosen as the telltale species because its catalytic reduction is most sensitive to the presence of oxygen. The baseline fuel (7 ppm sulfur) was used in the experiments, so that the fuel quality will not be a factor in the behavior. Only the 4K- and 150K- mile catalysts were tested. Because by comparing the fresh catalyst and the severely aged one can qualitatively show the aging effects. The 50k catalyst should reasonably lie somewhere in between these two.

To study the effect of λ modulation on the catalyst performance, triangular-shaped modulation amplitude about the stoichiometric point was varied from ± 0.015 to ± 0.12. These values were determined by the lambda sensor resolution, and engine workable zone. There are two reasons in determining the lower bound of amplitude. First,

any number below ± 0.015 will not influence the engine performance substantially; second, the lambda sensor is not able to give consistent readings for such low numbers. On the other hand, the upper bound was simply determined by the engine workable zone. With air/fuel ratio substantially away from stoichiometric, the engine calibration will not be appropriate and erratic engine behavior may result.

The frequency was also varied. At low frequencies, with lean excursion time comparable to or longer than the oxygen storage charge-up time (which corresponds to t_2-t_1 in Fig. 4-1; a value of ~ 5 s), there will be NO breakthrough because the O_2 storage capacity is used up in the lean period of the modulation. At 1600 rpm, the firing frequency of a 4-cylinder engine is ~50Hz. Therefore an upper limit for the modulation frequency is 25 Hz in order to have a good representation of the waveform (Nyquist criterion). In practice, because of port-fuel injection dynamics, the frequency should be substantially lower so that the λ modulation can be reproduced by the engine with sufficient fidelity. The frequencies used in the experiment were 0.3, 1, 5, 10 and 20 Hz.

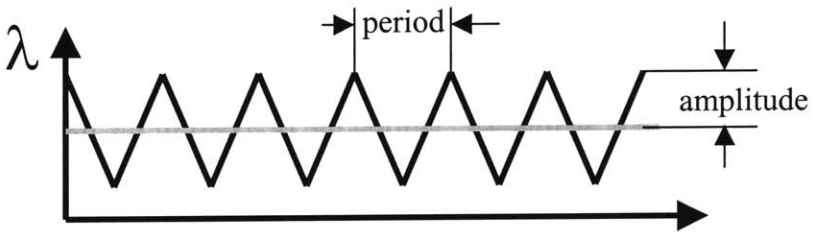

Fig. 6-3, Triangular waveform of air/fuel ratio modulation

The waveform of the modulations is chosen to be triangular. This is in agreement with commonly adopted waveform in commercial ECU's.

Another point that needs to be clarified is that the magnitude of the waveform is referred to as the command air/fuel ratio. Because of the dynamic characteristic of the

engine and the mixing effects in the exhaust system, there is some discrepancy between the command λ and actually measured λ.

6.2.3 Time-Resolved Profiles of NO

Fig. 6-4 to 6-6 show that the catalyst response to different modes of air/fuel ratio modulations in terms of NO mole fraction along the catalyst. In each figure, there are 7 curves; each represents a sampling point along the catalyst, starting from the engine-out values.

Only the data for 4k catalyst is shown here. The 150k catalyst has very similar profiles as the 4k one. The differences are not easily discernable. The time-averaged plots of the two catalysts will be compared, with which the differences in breakthroughs of the two catalysts can be seen more easily.

Some observations can be made on these charts (Fig. 6-4 to 6-6):

1), The NO profiles are clearly modulating with the λ modulation. This phenomenon is more obvious inside the catalyst (see the second curve from top in each chart, which is the first sampling point inside the catalyst at 17% of cumulative catalyst volume). The explanation is as follows. During the rich part of the modulation, the front part of the catalyst was able to substantially convert the exhaust NO because no excessive oxygen and plenty of reducing agents (CO, H2 and HC) were present. During the lean part of the modulation, the oxygen storage provided by the front part of the catalyst was not able to absorb all the engine-out oxygen. The NO conversion was poor because any reducing agents present will react preferentially with the O2 supplied by the engine (this is in consistence with previous results of conversion efficiency vs. λ, and in-catalyst

profiles during throttle transients). Hence there was a substantial NO breakthrough at this point. Further downstream, the amplitude of NO oscillation reduces substantially (frequency is always the same as the modulation). This is due to the fact that as the exhaust gas travels along the catalyst, the excess of oxygen is constantly being stored up by the catalyst via the oxygen storage medium. So more reducing species are available for the NO to react with. By the time, the exhaust gas reaches the exit of the catalyst, the amount of NO is barely traceable.

2), At lower frequencies, the NO oscillation is more consistent. Take the 5 Hz case for example, the oscillation in NO profile is less easy to observe than the 1Hz and 0.3 Hz cases. Also there are substantial changes in the amplitude in the oscillation. Whereas, the lower frequency cases have shown a much more consistent oscillation.

3), For each give modulation frequency, the bigger amplitude leaves more a longer traceable breakthrough along the catalyst. This is because with higher amplitude, there is more excessive oxygen in the exhaust gas during the lean part of the modulations. So that it takes more OSC medium to store up the oxygen, thus, the oxygen in the exhaust can breakthrough further down the catalyst. Hence, the trace of NO oscillation will last longer accordingly.

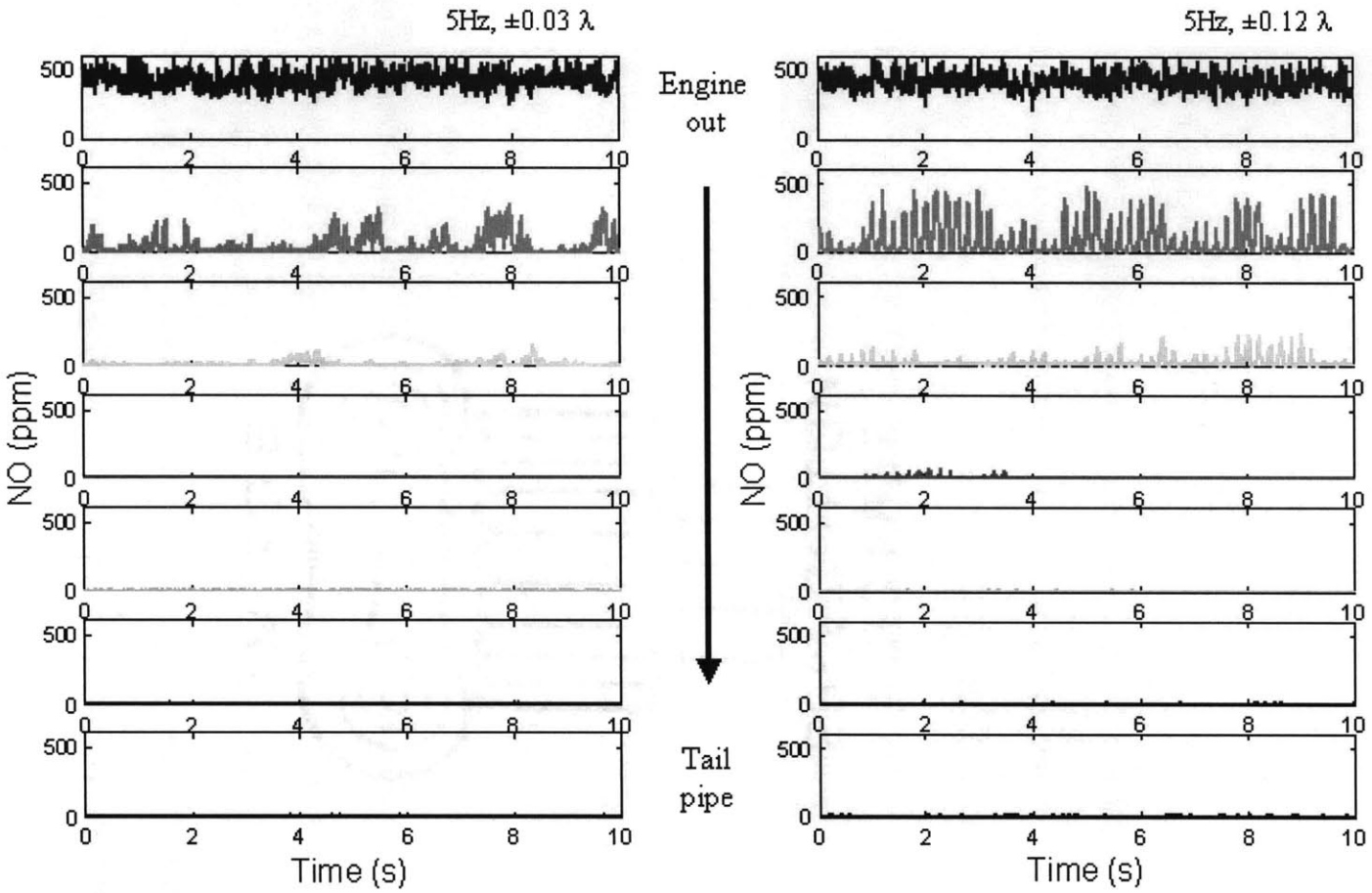

Fig. 6-4, 4k catalyst time-resolved NO concentration along the catalyst,

Space velocity 4.4×10^4/hr, modulation freq. 5hz, amplitude: ±0.03, ±0.12

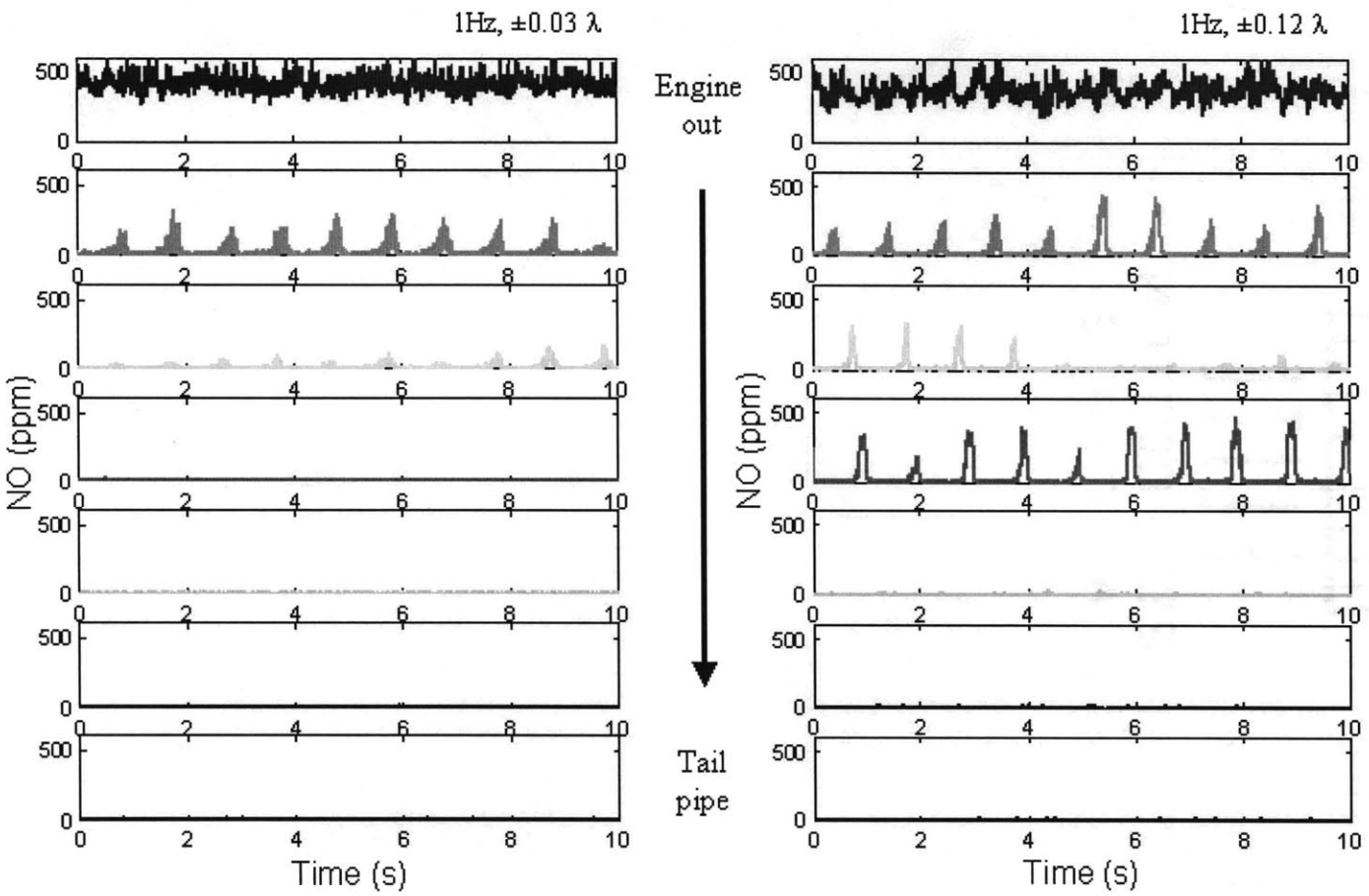

Fig. 6-5, 4k catalyst time-resolved NO concentration along the catalyst,

Space velocity 4.4×10^4/hr, modulation freq. 1hz, amplitude: ±0.03, ±0.12

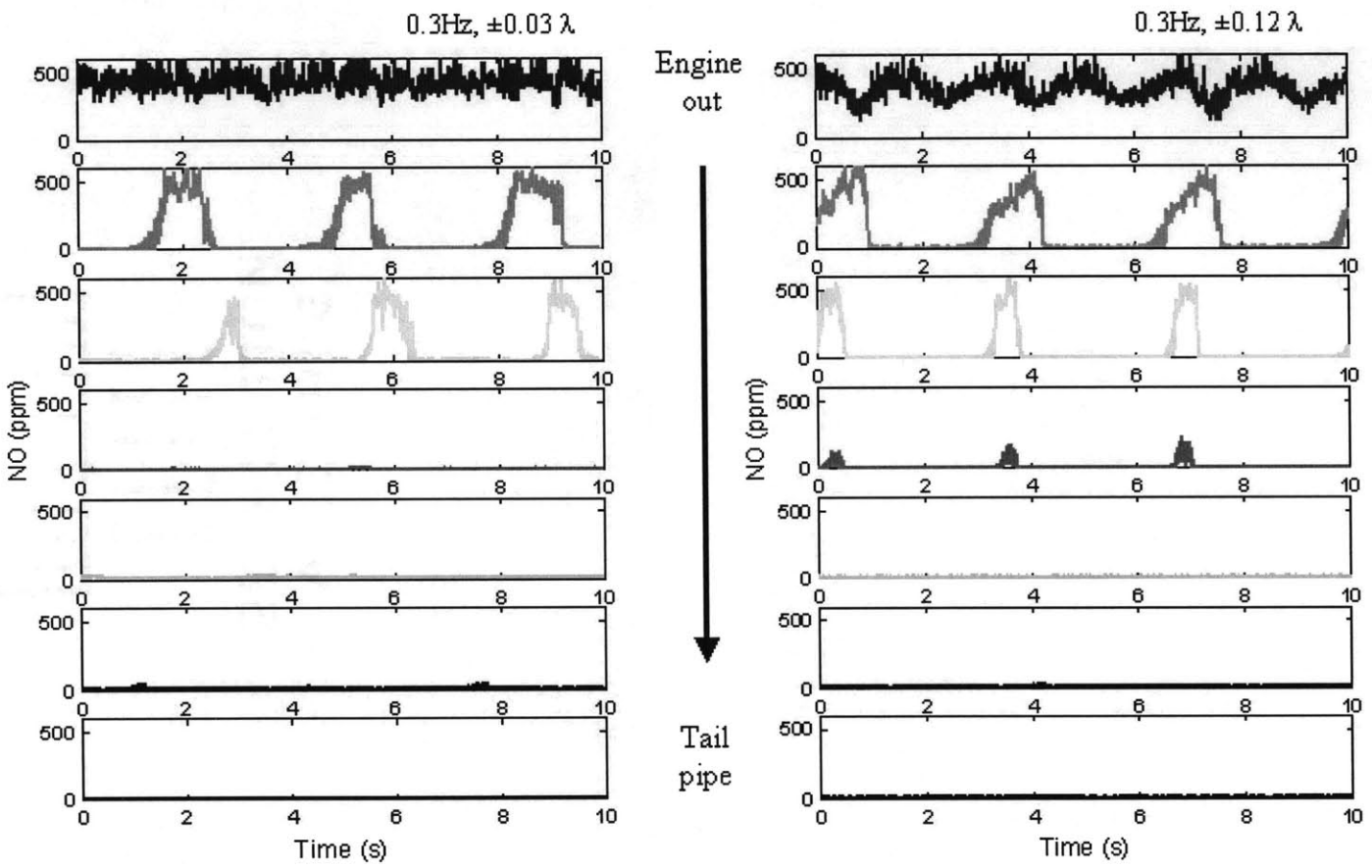

Fig. 6-6, 4k catalyst time-resolved NO concentration along the catalyst,

Space velocity 4.4×10^4/hr, modulation freq. 0.3 Hz, amplitude: ±0.03, ±0.12

6.2.4 Comparison and Discussion

Next, time-averaged NO profiles are compared between the 4k and 150k catalyst at different modes of air/fuel modulations. The reason time-averaged values are compared is that the time-resolved values are hard to compare not only between the two catalysts, but also among the different modes of modulations. For example, at 20Hz modulation, the firing frequency for all 4 cylinders at 1600 rpm is 53 Hz. The Nyquist criterion is just barely satisfied. The time resolved results would exhibit severe beating patterns. Whereas, the time-averaged values can provide the correct averaged values.

Shown in Fig. 6-7 to 6-16 are the time-averaged NO profiles along the catalysts for 4k and 150k catalysts at frequencies 20, 10, 5, 1, and 0.3 Hz, amplitudes range from ±0.012 to ±0.24. In some cases the exit concentrations were too low for the NO detector to measure any significant values (marked in the figures). Based on the figures, the following observation can be made:

1), There is no significant dependence of the NO distribution (normalized to the entrance values) along the catalyst as a function of the modulation frequency, except of the 0.3 Hz case. Then the cycle time is long enough for the oxygen storage to get saturated. As such, there is significant NO breakthrough during the lean part of the modulation, and the time-averaged value reflects that.

2), When different amplitudes are compared, there was no consistent trend, although the breakthrough at the larger modulation amplitude was higher at the rear part of the catalyst. For the 150k-mile catalyst, significant breakthrough at the catalyst exit was observed at large modulation amplitudes and low frequencies. This observation may

be related to the diminished oxygen storage capacity of the aged catalyst, so that an overall storage saturation was created under the high amplitude/low frequency condition.

3), When the two catalysts are compared, it is very clear to see that the 150k catalyst has a noticeable higher breakthrough than the fresh one. The reason that the aged catalyst has higher breakthroughs could be twofold. First, the aged catalyst has lost some of the effective reaction sites (or effective surface area covered in Chapter 7 & 8). Thus, the pollutants reduction rates are slower compared to the fresh catalyst. Second, as discussed in Chapter 4, the aged catalyst has less OSC, so as the exhaust travels along the catalyst, the excessive oxygen cannot be absorbed as effectively as in the fresh one. Both these effects tend to slow down the rate of NO reduction along the catalyst. That is what can be seen from the figures.

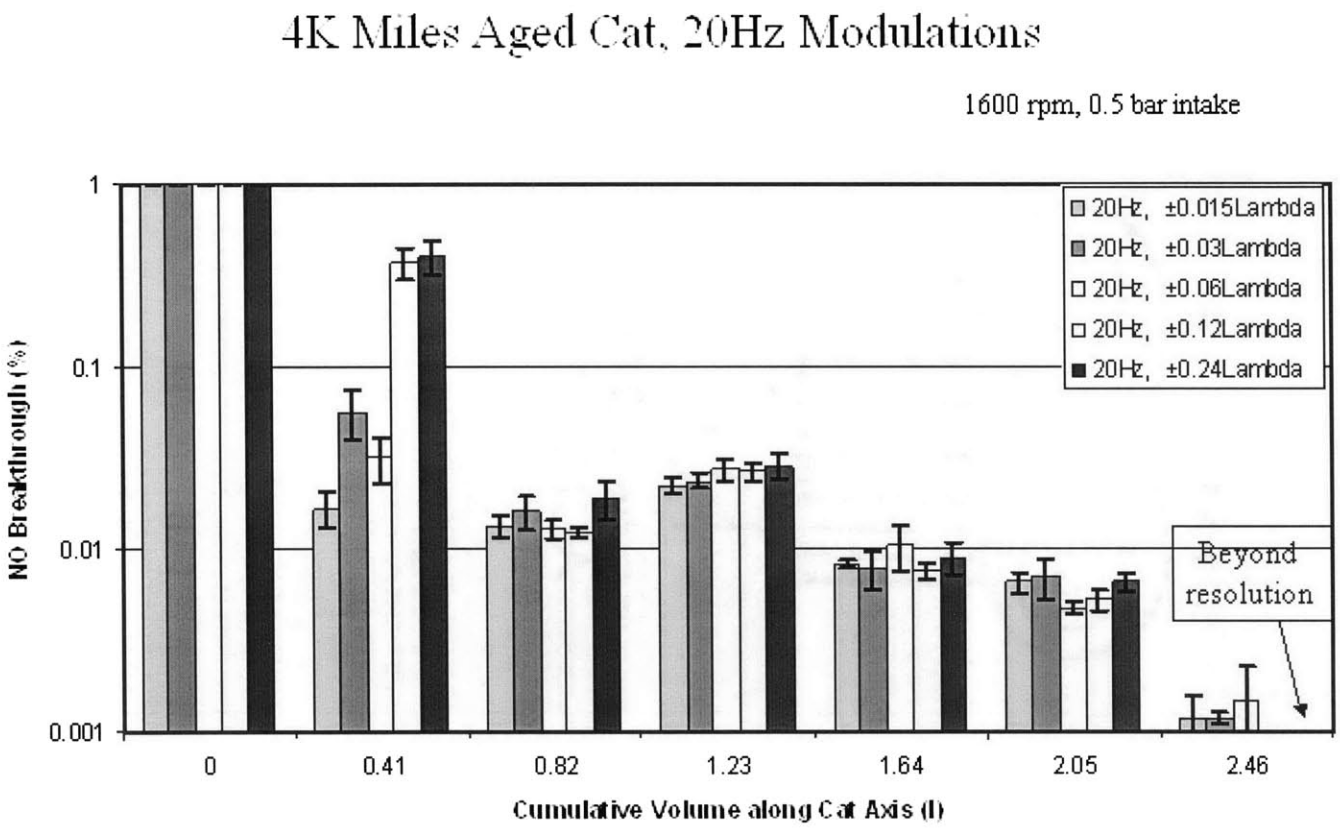

Fig. 6-7, Normalized time-averaged NO profile along the catalyst

4k catalyst, modulation at 20 Hz, amplitude range (±0.015, ±0.24)

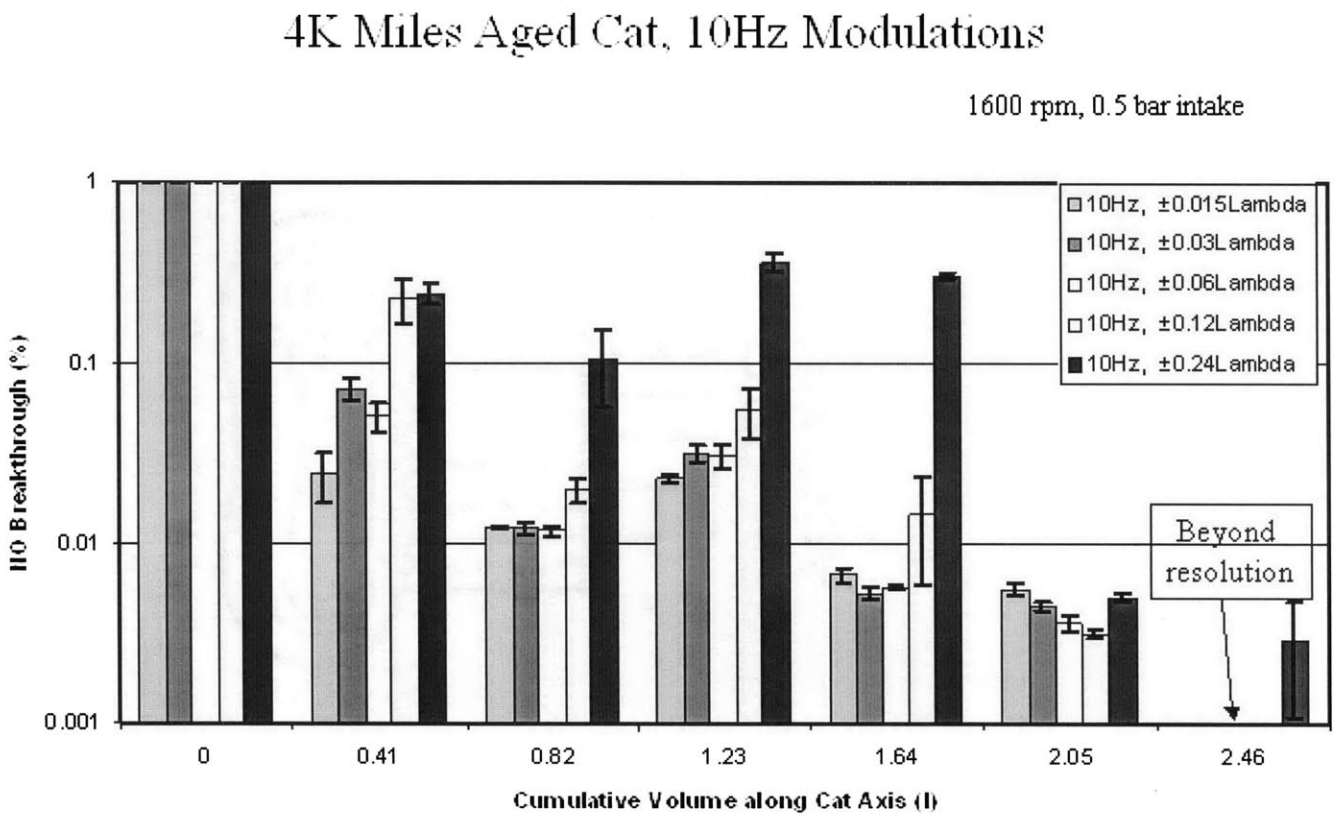

Fig 6-8, Normalized time-averaged NO profile along the catalyst

4k catalyst, modulation at 10 Hz, amplitude range (±0.015, ±0.24)

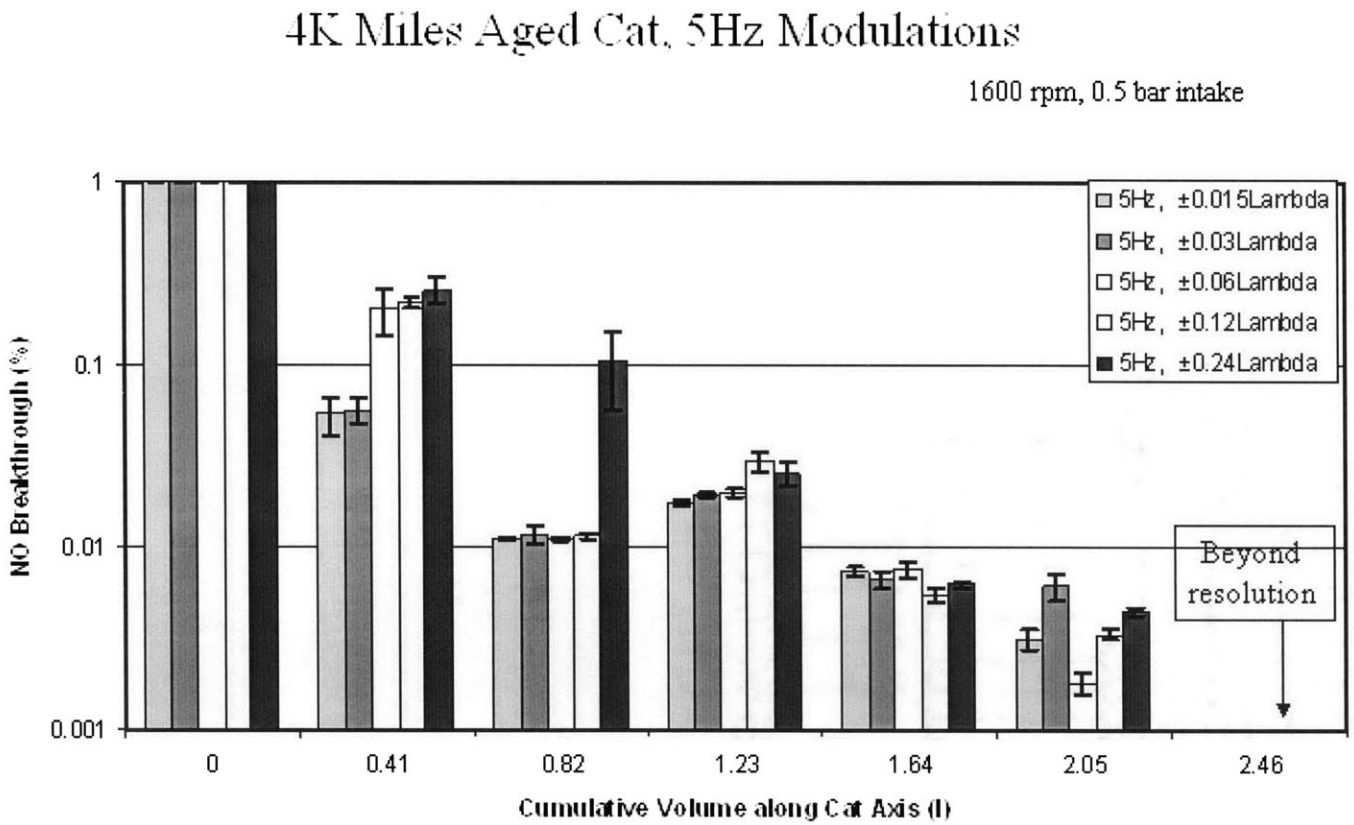

Fig. 6-9, Normalized time-averaged NO profile along the catalyst

4k catalyst, modulation at 5 Hz, amplitude range (±0.015, ±0.24)

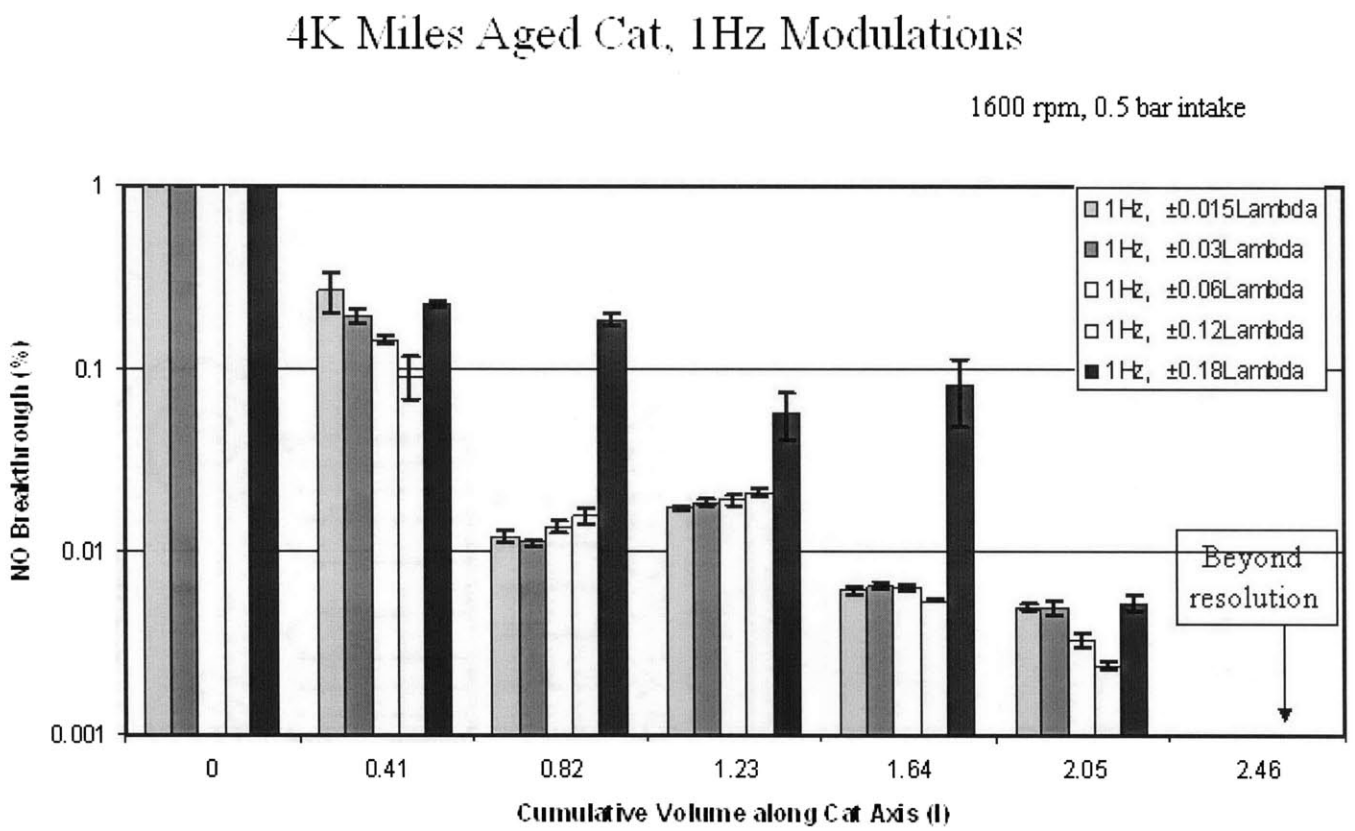

Fig. 6-10, Normalized time-averaged NO profile along the catalyst

4k catalyst, modulation at 1 Hz, amplitude range (±0.015, ±0.24)

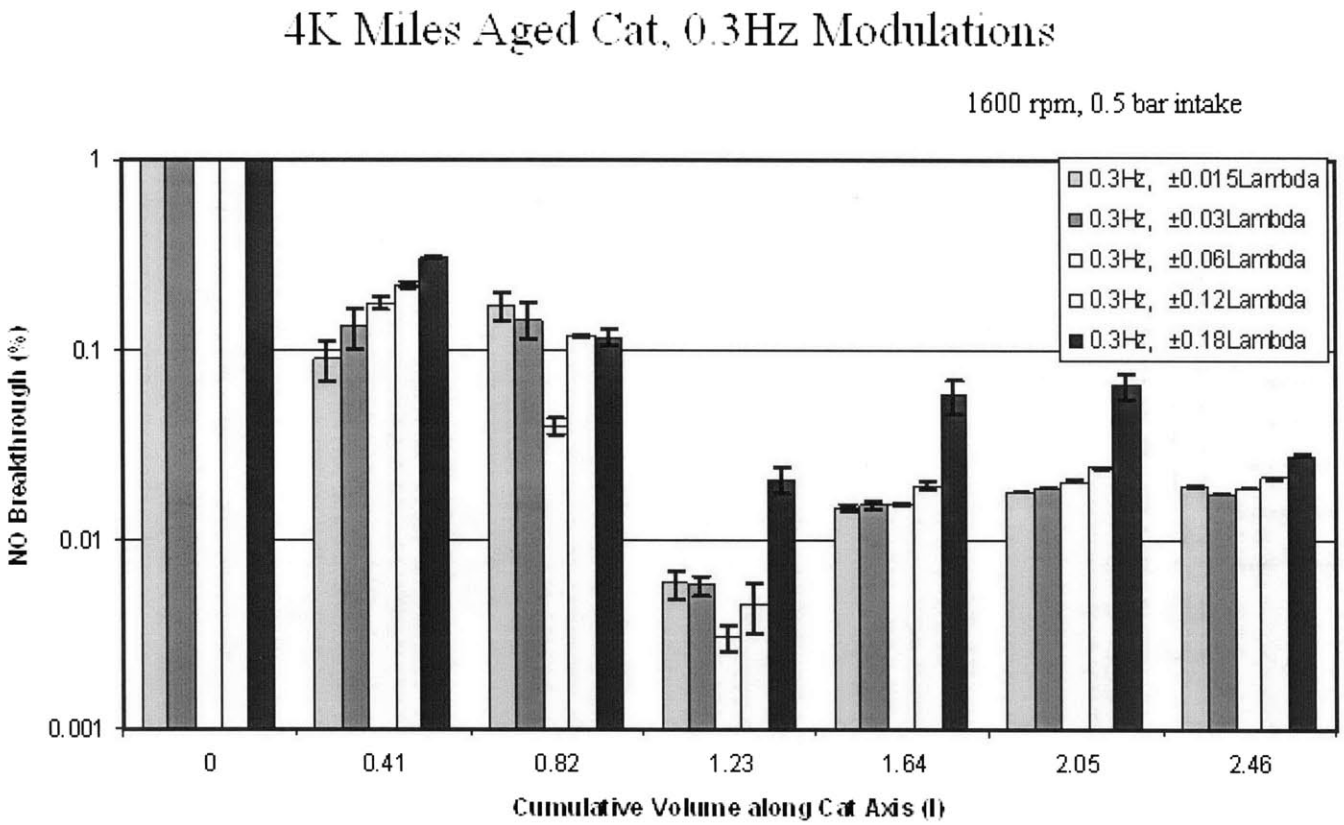

Fig. 6-11, Normalized time-averaged NO profile along the catalyst

4k catalyst, modulation at 0.3 Hz, amplitude range (±0.015, ±0.24)

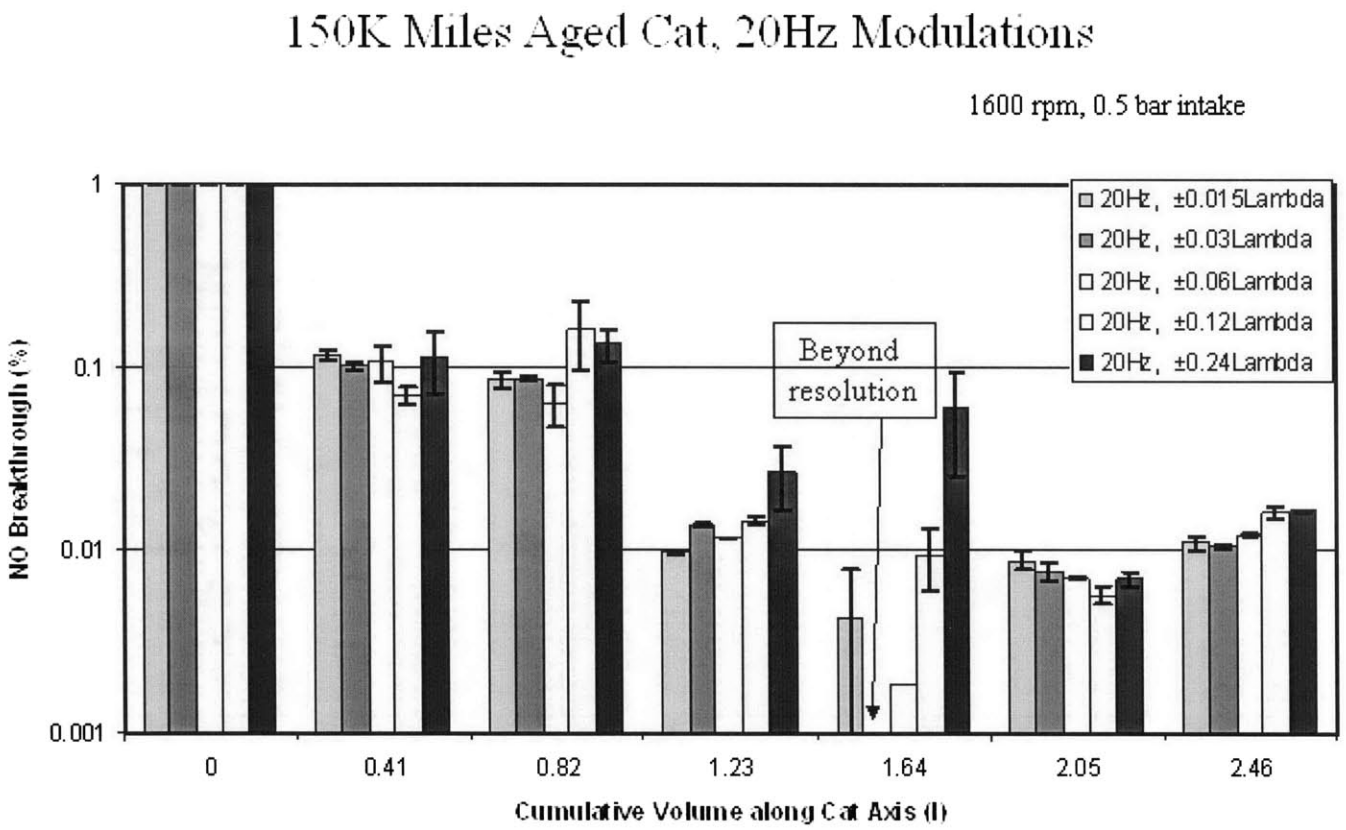

Fig. 6-12, Normalized time-averaged NO profile along the catalyst

150k catalyst, modulation at 20 Hz, amplitude range (±0.015, ±0.24)

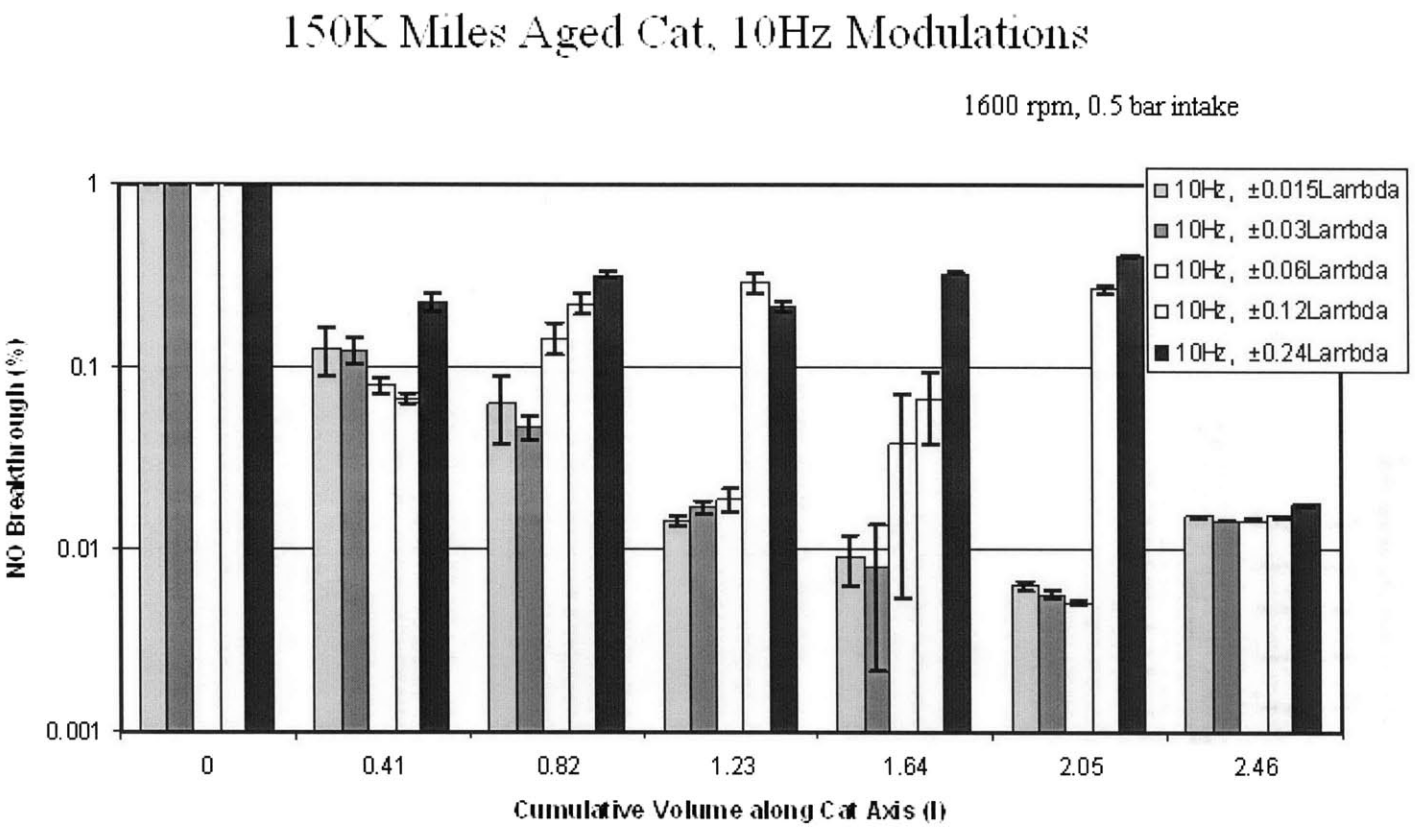

Fig. 6-13, Normalized time-averaged NO profile along the catalyst

150k catalyst, modulation at 10 Hz, amplitude range (±0.015, ±0.24)

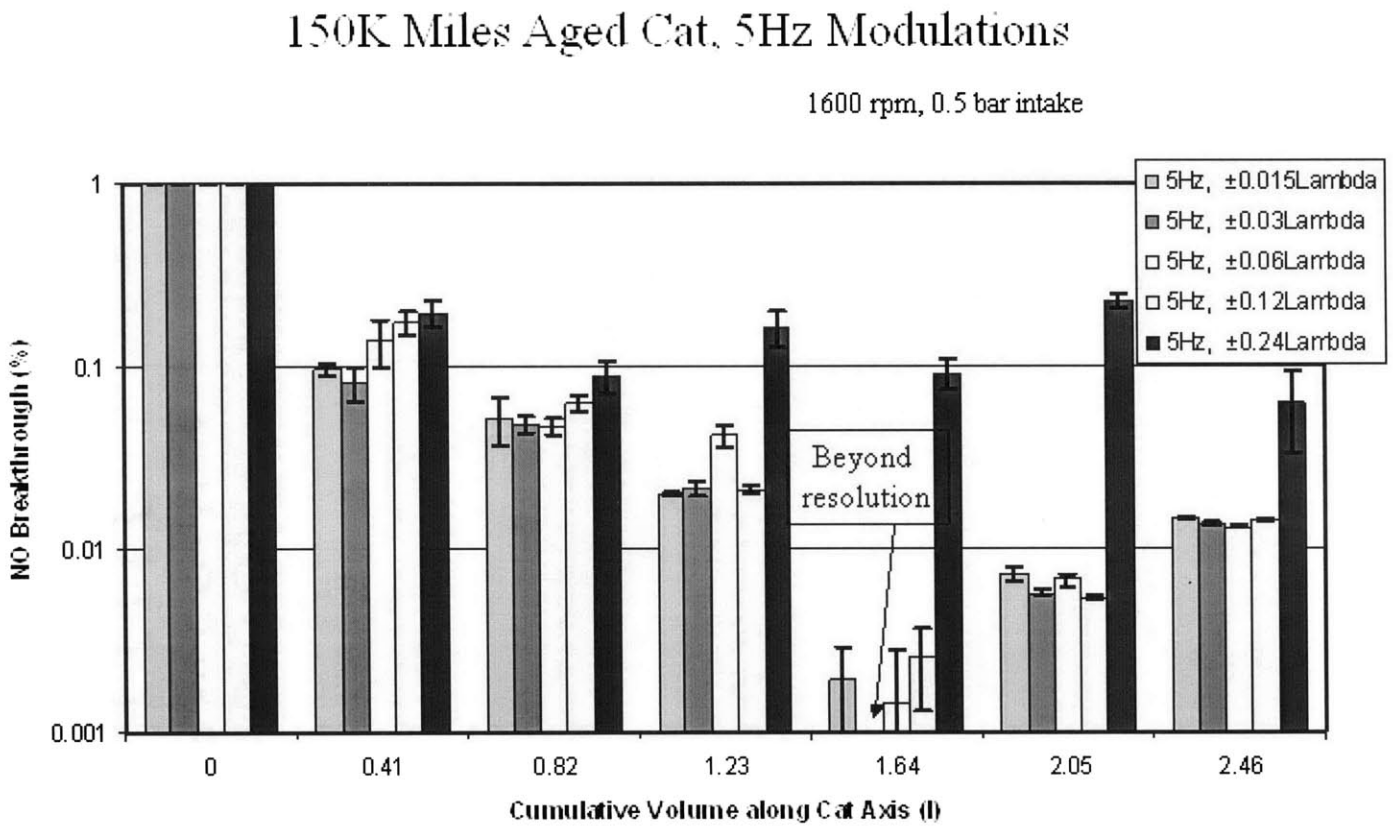

Fig. 6-14, Normalized time-averaged NO profile along the catalyst

150k catalyst, modulation at 5 Hz, amplitude range (±0.015, ±0.24)

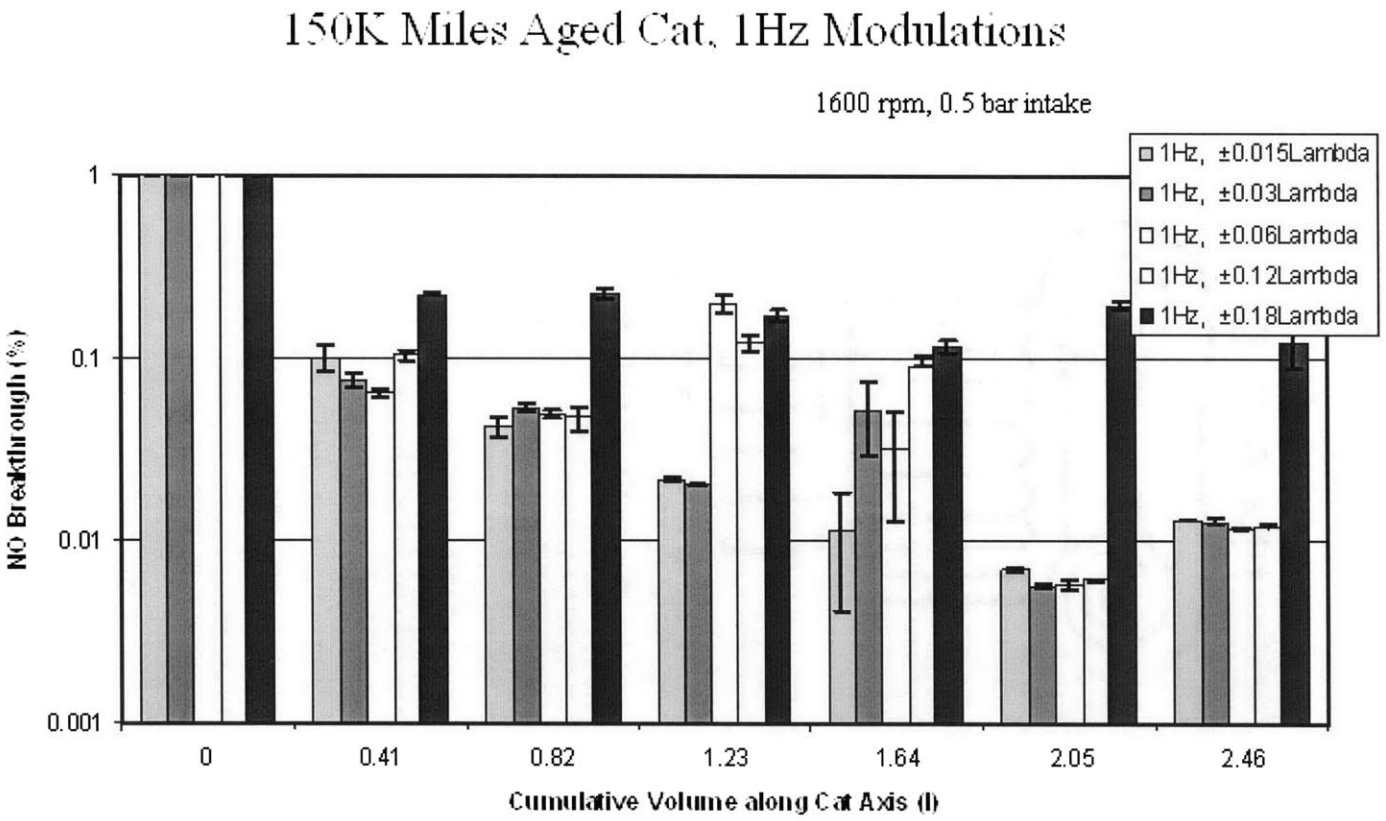

Fig. 6-15, Normalized time-averaged NO profile along the catalyst

150k catalyst, modulation at 1 Hz, amplitude range (±0.015, ±0.24)

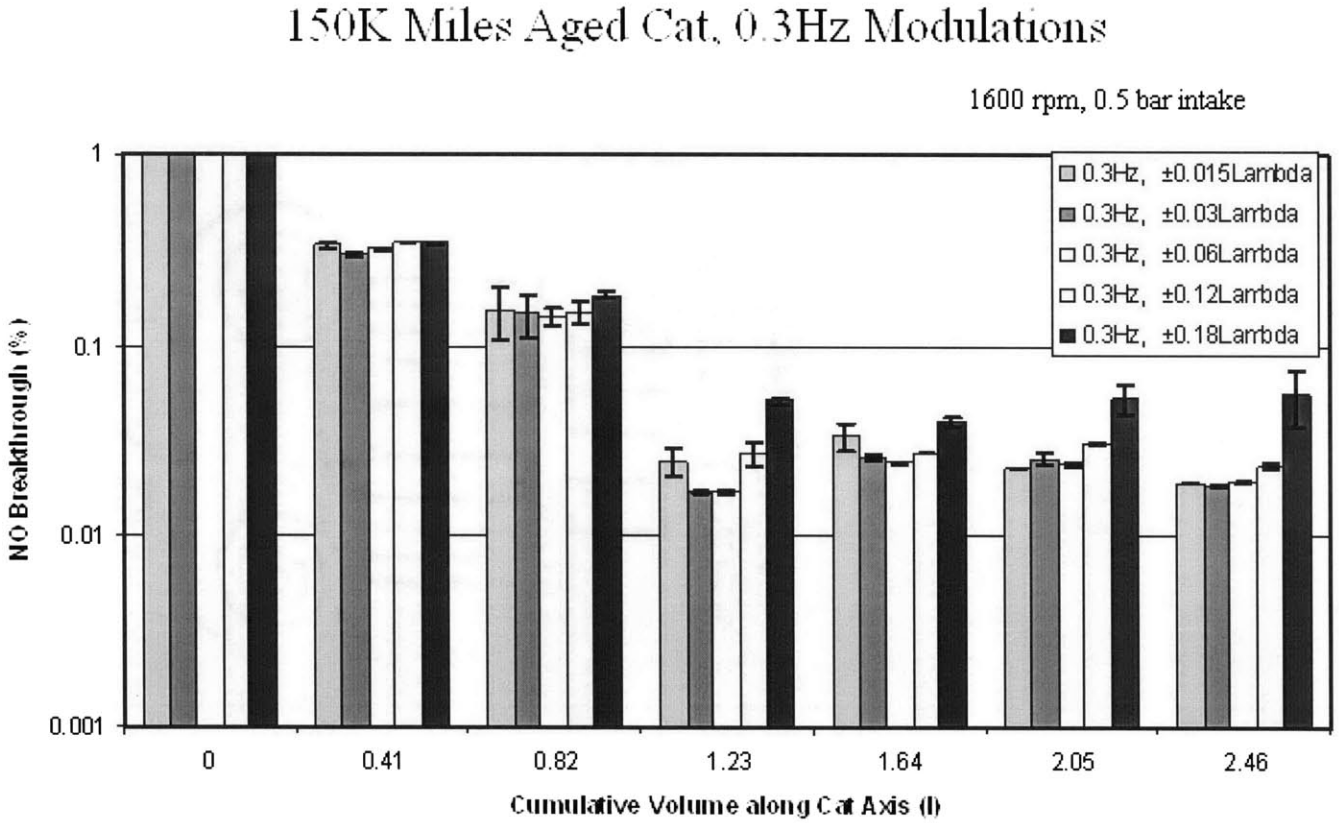

Fig. 6-16, Normalized time-averaged NO profile along the catalyst

150k catalyst, modulation at 0.3 Hz, amplitude range (±0.015, ±0.24)

The overall NO breakthrough for the aged and fresh catalyst under all different modes of modulations are compared in Fig. 6-17 & 6-18. For both catalysts, there are substantial overall NO breakthroughs at modulation frequency of 0.3 Hz, at which the time scale is comparable to the oxygen storage charge-up time for the catalysts. At frequencies from 1 to 20 Hz, the NO breakthroughs are not sensitive to either frequency or amplitude. This insensitivity reconfirms the explanation discussed above that the overall oxygen storage capacity is still enough to store up all of the excessive oxygen in the exhaust stream. In other words, if the catalysts were half the size they are, the results would have been more dependent on amplitudes.

When comparing NO breakthroughs in the 4k and 150k catalysts, it is mentioned that the higher NO breakthrough for the aged catalyst is due to two factors, one is oxygen storage capacity the other the aging effects on the catalysis sites. So the insensitivity of the aged catalyst to different modes of modulation (within reasonable range) is more likely a result of loss of PGM sites than of the inadequacy of OSC.

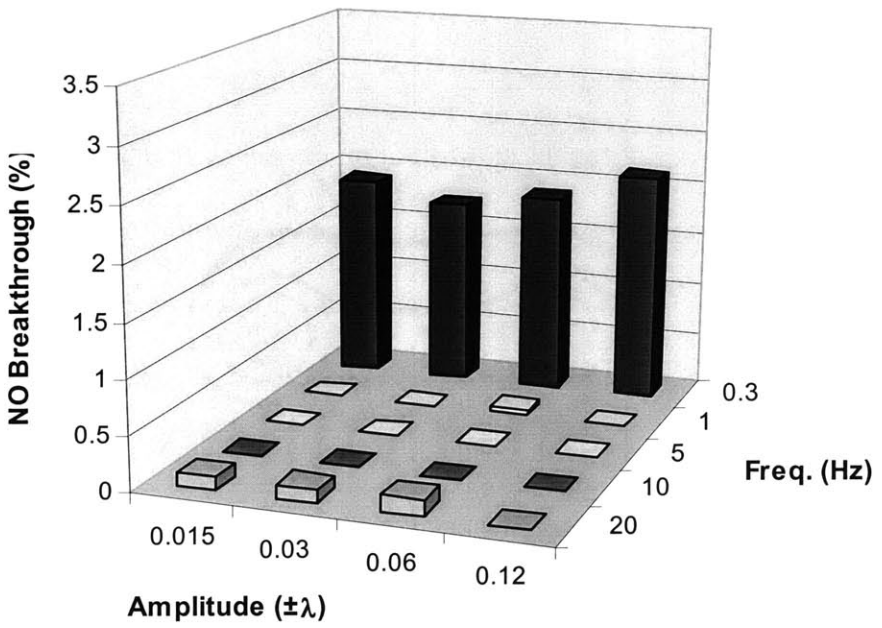

Fig. 6-17, NO breakthrough along the 4k catalyst as a function of modulation freq. and amplitude.

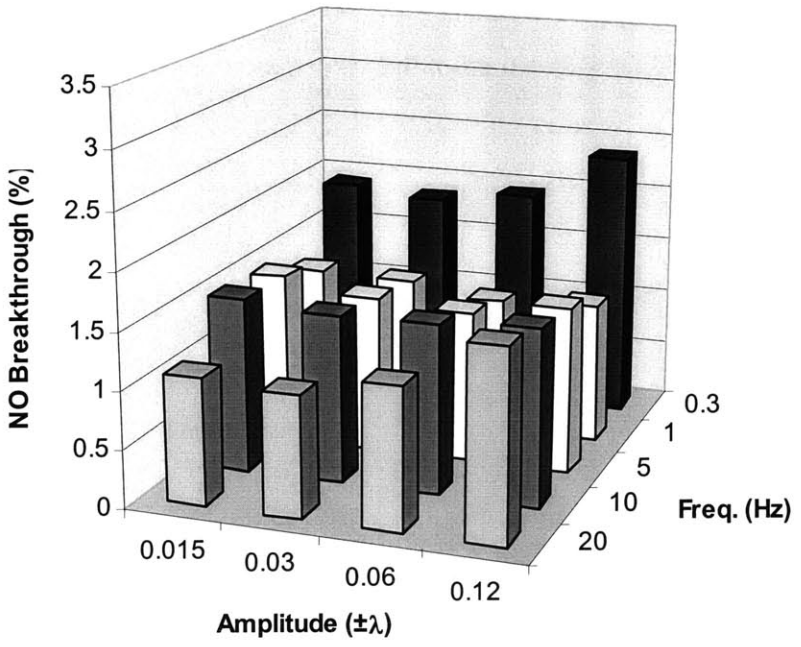

Fig. 6-18, NO breakthrough along the 150k catalyst as a function of modulation freq. and amplitude.

6.3 Biased Air/Fuel Ratio Modulation

Next, experiments to find out the relationship between oxygen storage capacity and NO breakthrough were carried out. These experiments were also intended to find out what will happen when there is a steady state error in the UEGO sensor. In other words, when there is a static error in the UEGO readings, then the air/fuel ratio modulation will be biased from stoichiometry. The experiments were designed so that arbitrary biased air/fuel ratio modulations can be delivered to investigate the above questions.

6.3.1 Description of Experiments

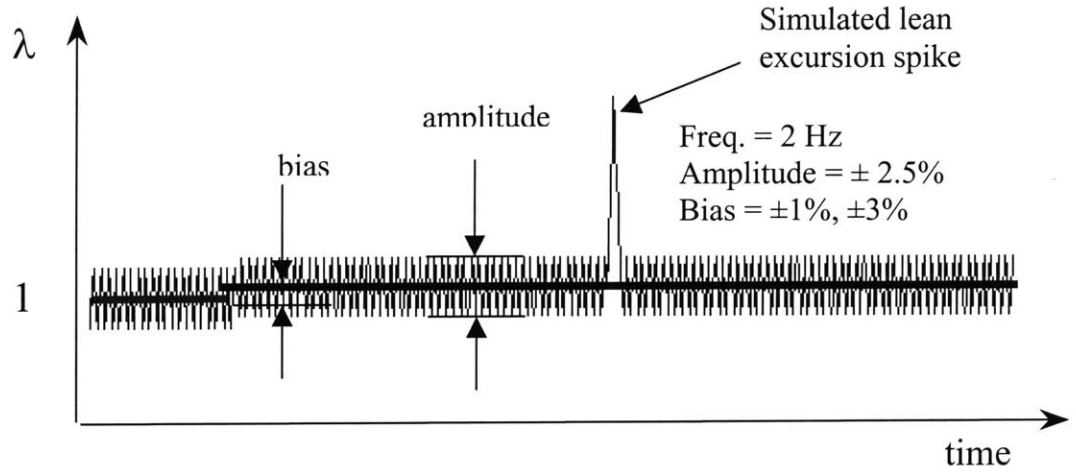

Fig. 6-19, Biased air/fuel ratio modulation

The experiments were carried out with the engine running at 1600 rpm, 0.5 bars intake pressure. The air/fuel ratio modulation experimental setup is shown in Fig. 6-2.

Fig. 6-19 shows a typical air/fuel ratio profile in these experiments. Before the experiments started, the engine and catalysts were stabilized at the prescribed operating condition. First, the air/fuel ratio was oscillated about the stoichiometric point with a

frequency of 2 Hz and amplitude of ±2.5%. 15 seconds after the experiments started, the air/fuel ratio modulation was superimposed by a static bias value (±1% or ±3%). This will last for 20 seconds. Then a lean or rich spike with the duration of 1 second and height of ±20% was delivered. After the spike, the air/fuel ratio was brought back to the biased modulation, until the end of the experiment. This will normally last another 20 seconds.

The test matrix consisted of 4 levels of bias (±1% or ±3%), two air/fuel ratio spikes (±20%) and at three different levels of aging; together there were 24 experiments. In these experiments, only the 33 ppm sulfur fuel was used.

6.3.2 Experimental Data

Shown in Fig. 6-20 to Fig. 6-31 are the data of the above experiments. Fig. 6-20 to 6-23 are for the 150k catalyst; Fig. 6-24 to 6-27 are for the 50k catalyst; and Fig. 6-28 to 6-31 are for the 4k catalyst. For each catalyst, the 4 figures show the 4 different combinations of lean/rich bias and lean/rich spikes.

Some observations on the experimental data can be made:

1), For the lean-biased cases, tail-pipe NO breakthrough will always happen (given that before the bias there was no substantial breakthrough). The sequence of tail-pipe NO breakthrough occurrence is 150k earlier than 50k, and 50k earlier than 4k catalyst. The rich air/fuel ratio spike is helpful in deterring the onset of NO breakthrough. The correlation between the NO breakthrough and oxygen storage capacity will be quantified in 6.3.3.

2), In the rich-biased cases, tail-pipe NO breakthrough never happened. Even in the cases where a lean spike is delivered, there down-stream NO did not have obvious increase.

3), Tail-pipe CO levels kept low in the lean-biased modulations. This is due to the fact that when the exhaust gas is overall lean, there is excess of oxygen in the feed stream. Engine-out CO level is lower than the richer case, so there is always enough oxidizer (O2 and NO) to react with the CO. Even an instantaneous rich spike will not cause CO to break through substantially, because oxygen is released from the catalyst to overcome the short period of high CO feeding.

4), Contrary to bullet 3, when the modulation is biased to the rich side, the exhaust gas is overall rich. There is not enough oxidizing species to counteract the relatively high CO level. This can be confirmed by looking at the lean-biased case, but with a lean spike. When the lean spike is delivered, down-stream CO can be seen to have an obvious ditch. This is due to the abundant oxygen in the exhaust stream.

5), Similar to the onset of NO breakthrough, CO breakthrough happens faster for the more aged catalyst; whereas, for the fresh catalyst, it occurs much later. Also, it can be seen from the figures that the down-stream CO is relatively lower for the fresh catalyst compared to the more aged one.

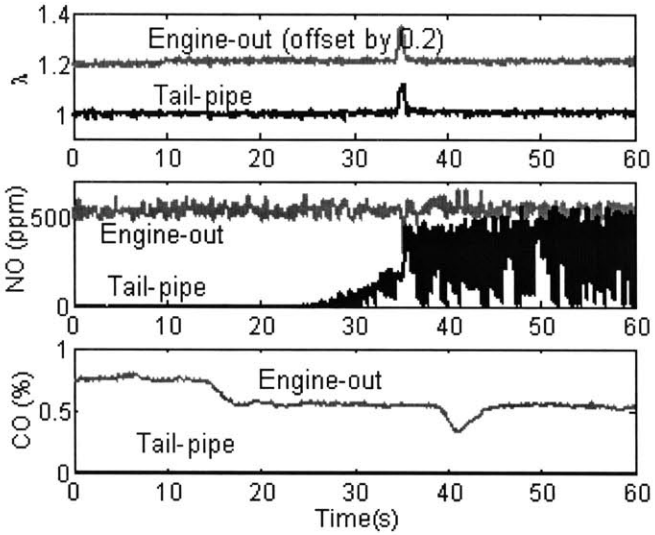

150K Cat, 33ppm S fuel,
0.5 bar intake, 1600 rpm
Lean spike, λ biased by 0.01

150K Cat, 33ppm S fuel,
0.5 bar intake, 1600 rpm
Lean spike, λ biased by 0.03

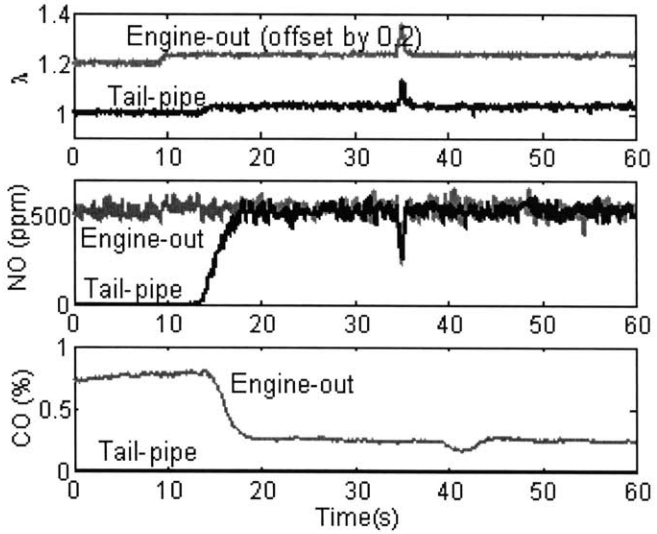

Fig. 6-20, 150k catalyst NO and CO pre- & post-catalyst time-resolved values.

Biased by 1% and 3% with lean spike (height of 20%).

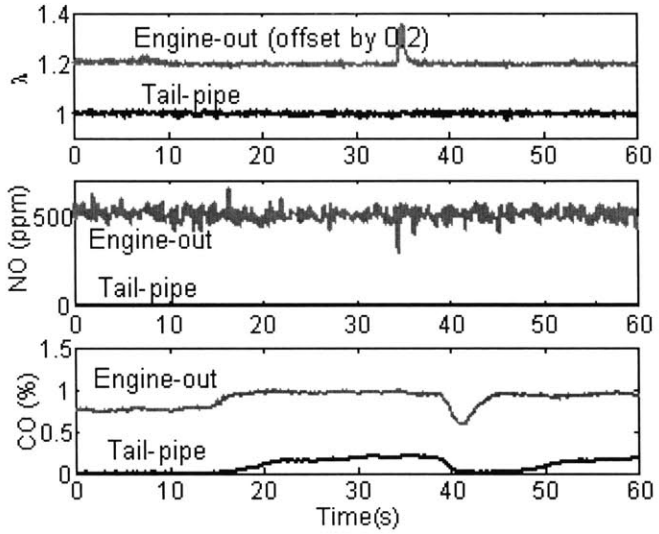

150K Cat, 33ppm S fuel,
0.5 bar intake, 1600 rpm
Lean spike, λ biased by –0.01

150K Cat, 33ppm S fuel,
0.5 bar intake, 1600 rpm
Lean spike, λ biased by -0.03

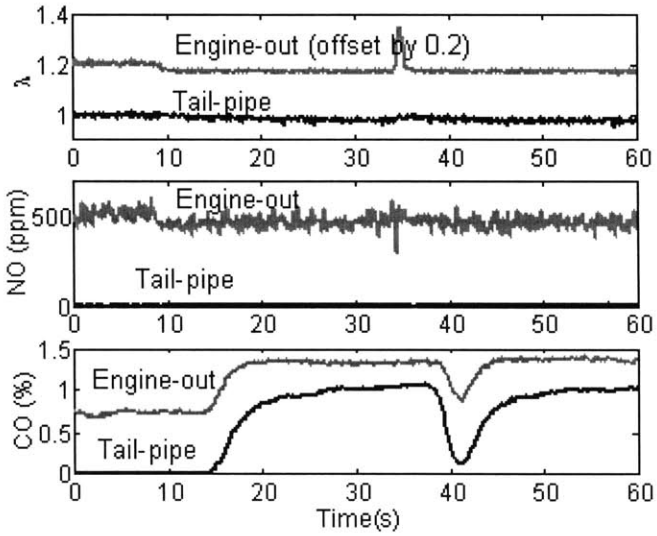

Fig. 6-21, 150k catalyst NO and CO pre- & post-catalyst time-resolved values.

Biased by -1% and -3% with lean spike (height of 20%).

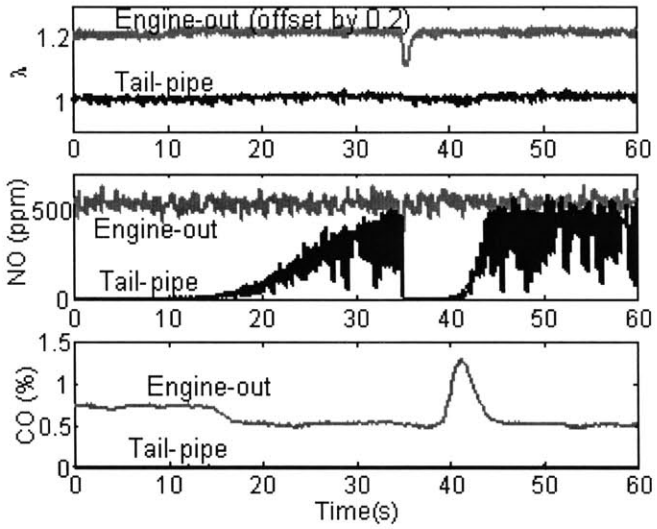

150K Cat, 33ppm S fuel,
0.5 bar intake, 1600 rpm
Rich spike, λ biased by 0.01

150K Cat, 33ppm S fuel,
0.5 bar intake, 1600 rpm
Rich spike, λ biased by 0.03

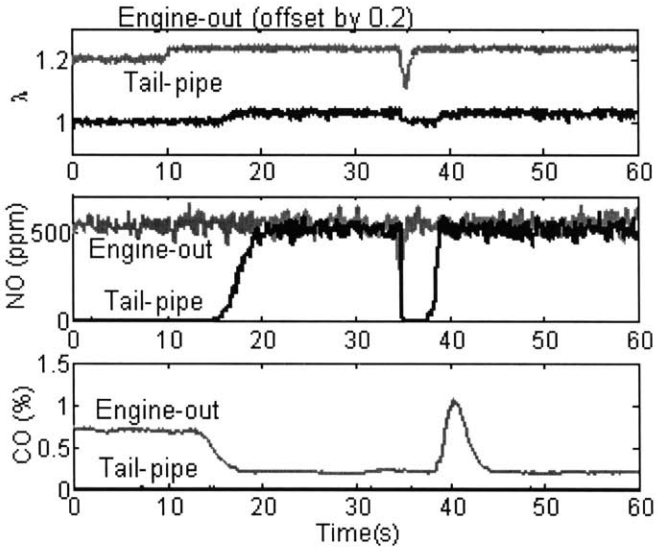

Fig. 6-22, 150k catalyst NO and CO pre- & post-catalyst time-resolved values.

Biased by 1% and 3% with rich spike (height of 20%).

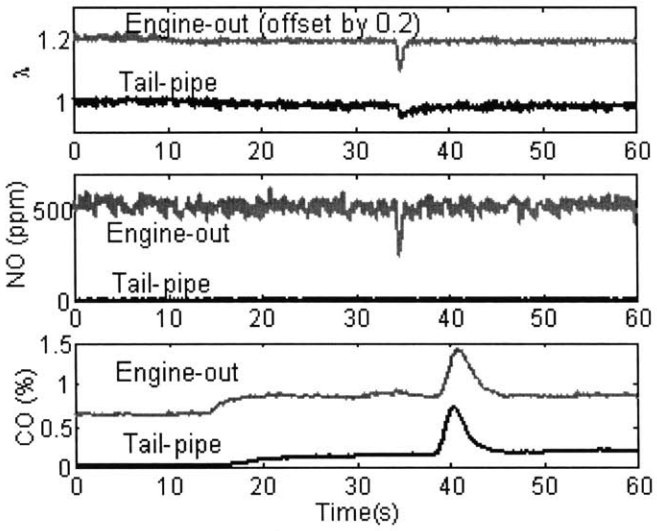

150K Cat, 33ppm S fuel,
0.5 bar intake, 1600 rpm
Rich spike, λ biased by -0.01

150K Cat, 33ppm S fuel,
0.5 bar intake, 1600 rpm
Rich spike, λ biased by -0.03

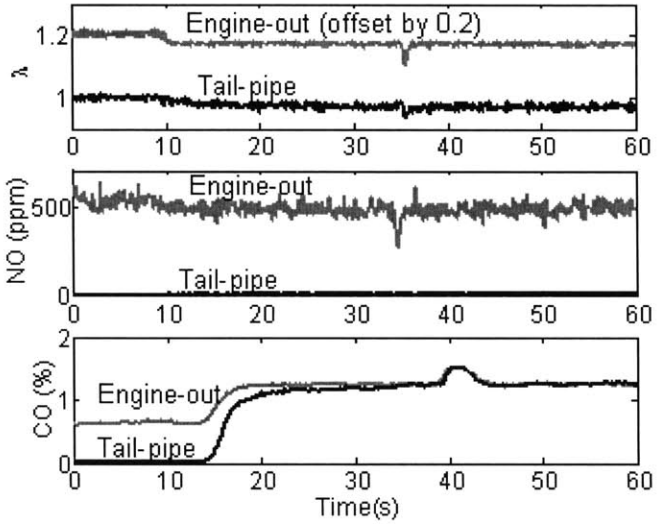

Fig. 6-23, 150k catalyst NO and CO pre- & post-catalyst time-resolved values.

Biased by -1% and -3% with rich spike (height of 20%).

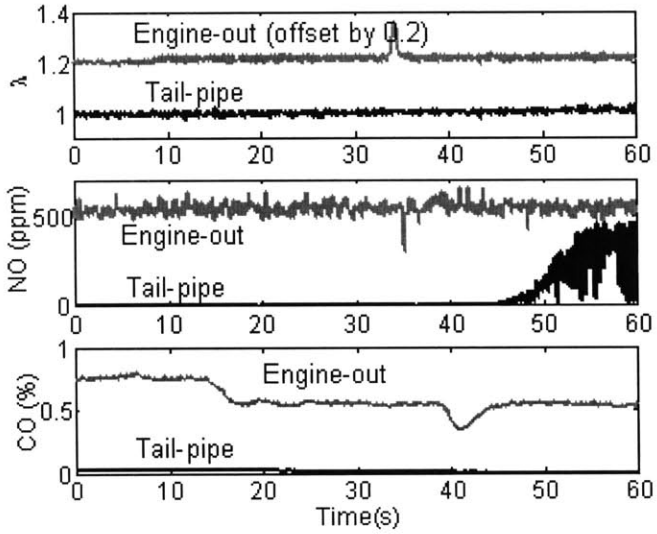

50K Cat, 33ppm S fuel,
0.5 bar intake, 1600 rpm
Lean spike, λ biased by 0.01

50K Cat, 33ppm S fuel,
0.5 bar intake, 1600 rpm
Lean spike, λ biased by 0.03

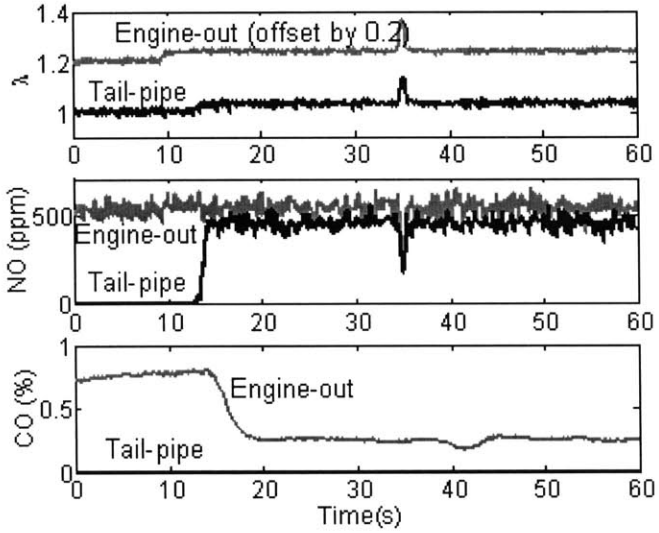

Fig. 6-24, 50k catalyst NO and CO pre- & post-catalyst time-resolved values.

Biased by 1% and 3% with lean spike (height of 20%).

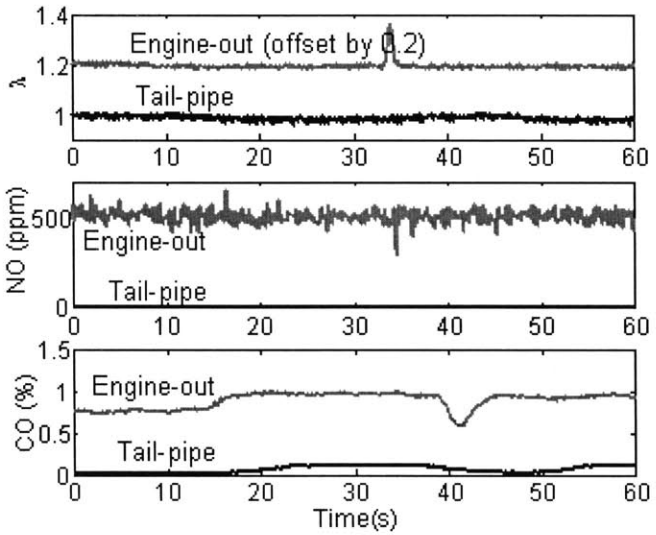

50K Cat, 33ppm S fuel,
0.5 bar intake, 1600 rpm
Lean spike, λ biased by -0.01

50K Cat, 33ppm S fuel,
0.5 bar intake, 1600 rpm
Lean spike, λ biased by -0.03

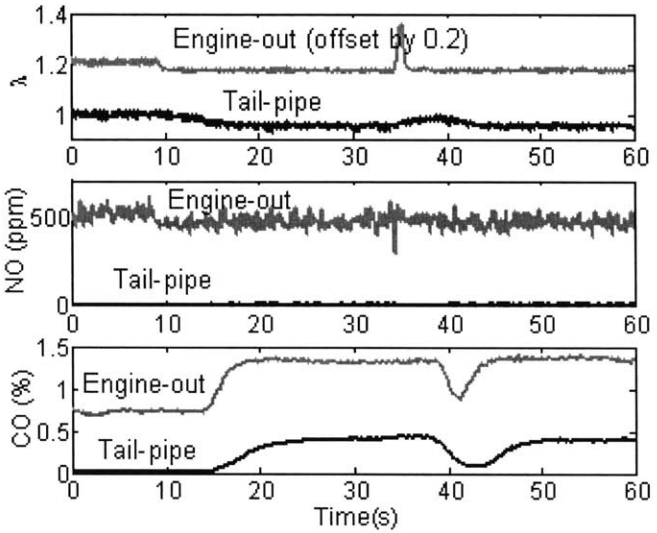

Fig. 6-25, 50k catalyst NO and CO pre- & post-catalyst time-resolved values.

Biased by -1% and -3% with lean spike (height of 20%).

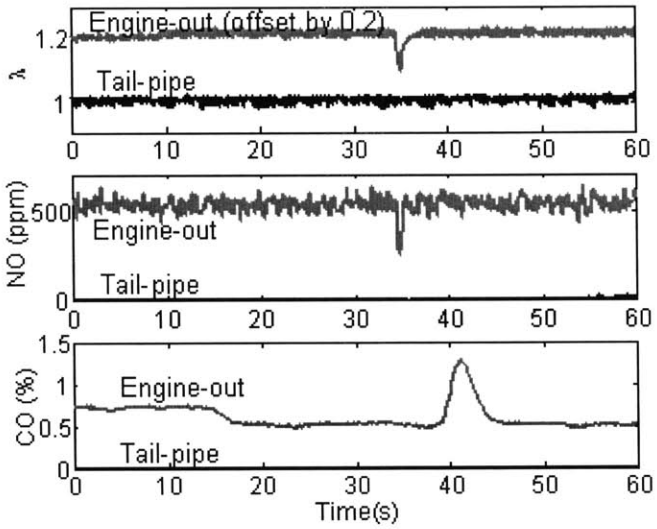

50K Cat, 33ppm S fuel,
0.5 bar intake, 1600 rpm
Rich spike, λ biased by 0.01

50K Cat, 33ppm S fuel,
0.5 bar intake, 1600 rpm
Rich spike, λ biased by 0.03

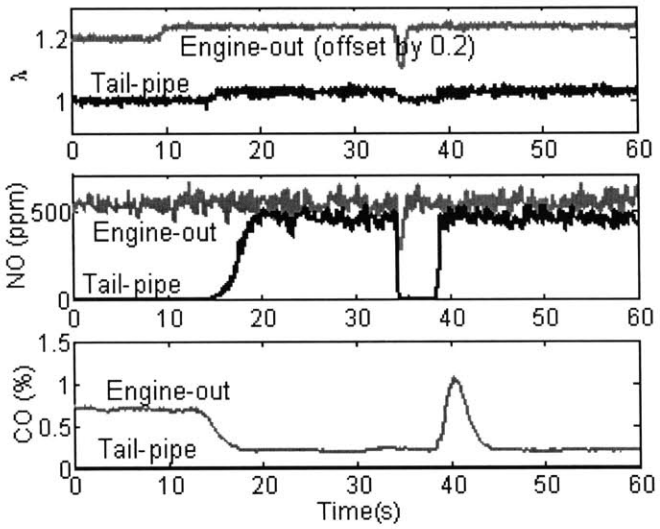

Fig. 6-26, 50k catalyst NO and CO pre- & post-catalyst time-resolved values.

Biased by 1% and 3% with rich spike (height of 20%).

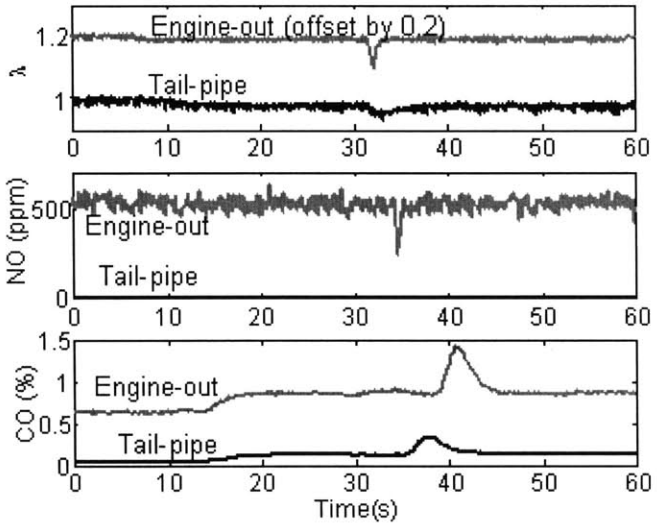

50K Cat, 33ppm S fuel,
0.5 bar intake, 1600 rpm
Rich spike, λ biased by -0.01

50K Cat, 33ppm S fuel,
0.5 bar intake, 1600 rpm
Rich spike, λ biased by -0.03

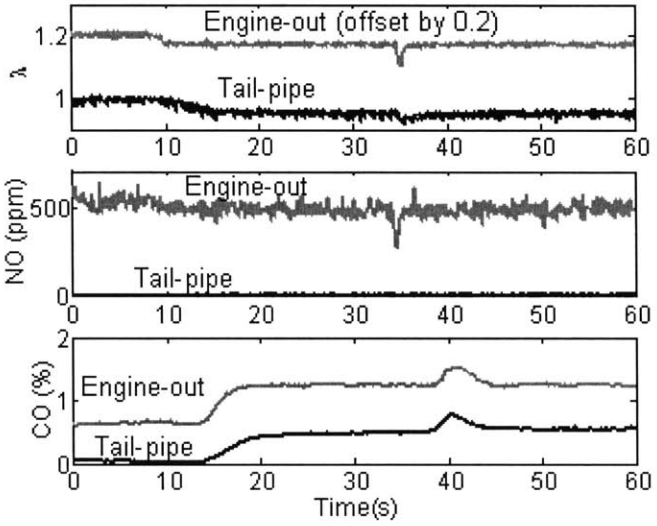

Fig. 6-27, 50k catalyst NO and CO pre- & post-catalyst time-resolved values.

Biased by -1% and -3% with rich spike (height of 20%).

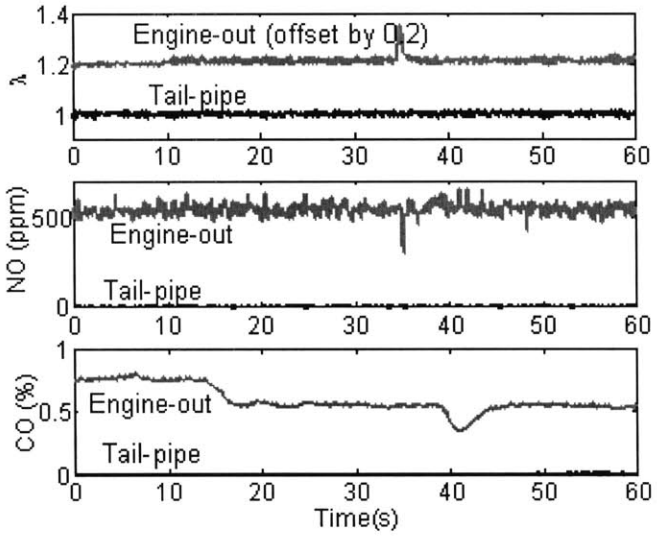

4K Cat, 33ppm S fuel,
0.5 bar intake, 1600 rpm
Lean spike, λ biased by 0.01

4K Cat, 33ppm S fuel,
0.5 bar intake, 1600 rpm
Lean spike, λ biased by 0.03

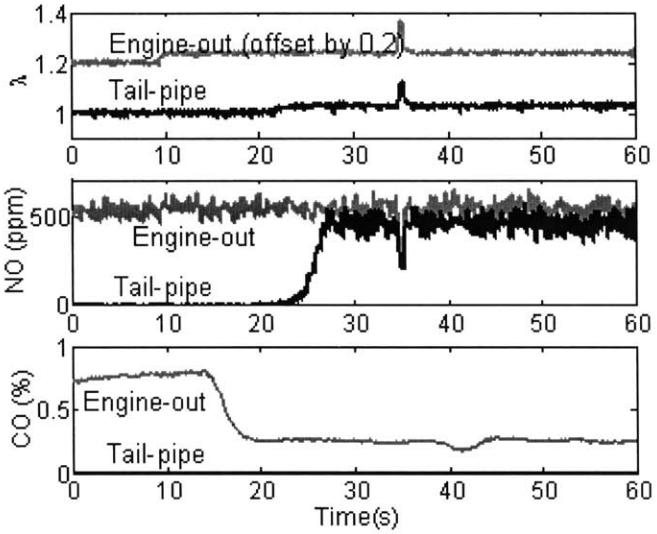

Fig. 6-28, 4k catalyst NO and CO pre- & post-catalyst time-resolved values.

Biased by 1% and 3% with lean spike (height of 20%).

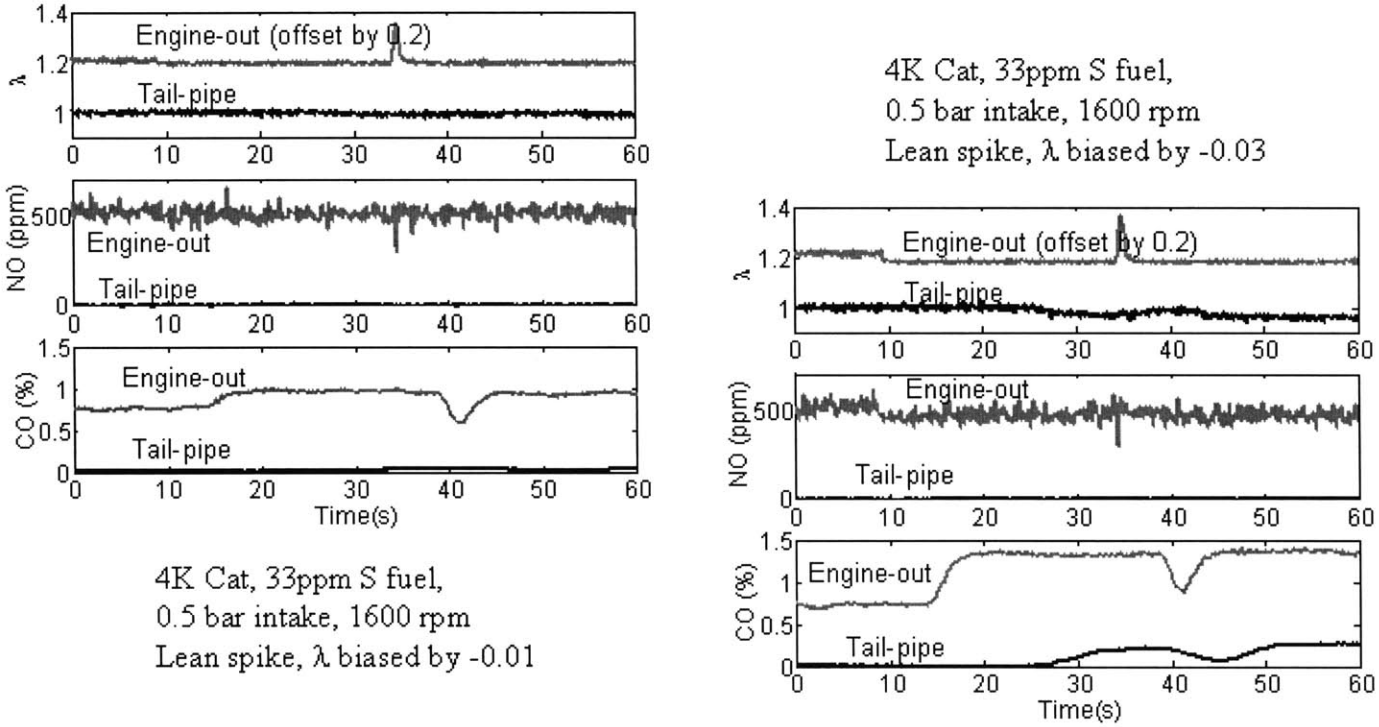

Fig. 6-29, 4k catalyst NO and CO pre- & post-catalyst time-resolved values.

Biased by -1% and -3% with lean spike (height of 20%).

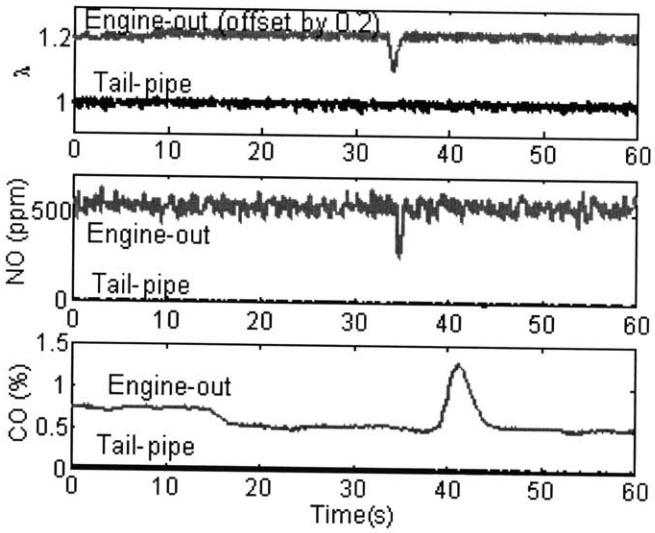

4K Cat, 33ppm S fuel,
0.5 bar intake, 1600 rpm
Rich spike, λ biased by 0.01

4K Cat, 33ppm S fuel,
0.5 bar intake, 1600 rpm
Rich spike, λ biased by 0.03

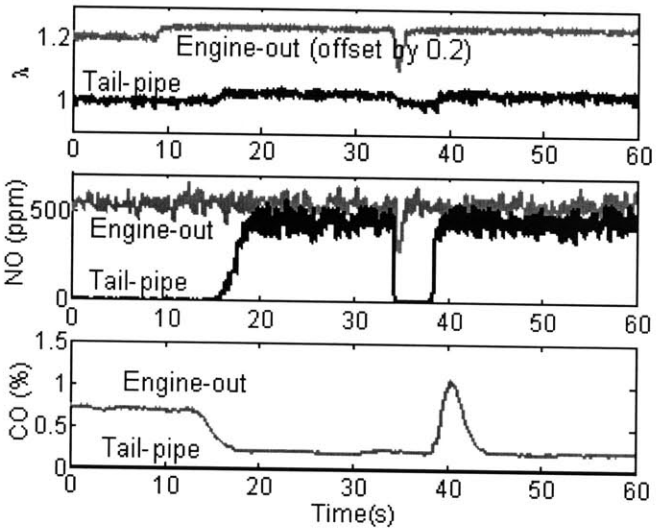

Fig. 6-30, 4k catalyst NO and CO pre- & post-catalyst time-resolved values.

Biased by 1% and 3% with rich spike (height of 20%).

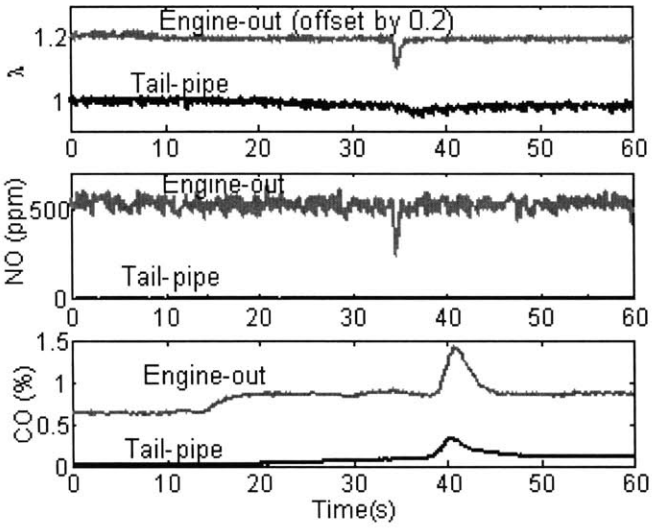

4K Cat, 33ppm S fuel,
0.5 bar intake, 1600 rpm
Rich spike, λ biased by -0.01

4K Cat, 33ppm S fuel,
0.5 bar intake, 1600 rpm
Rich spike, λ biased by -0.03

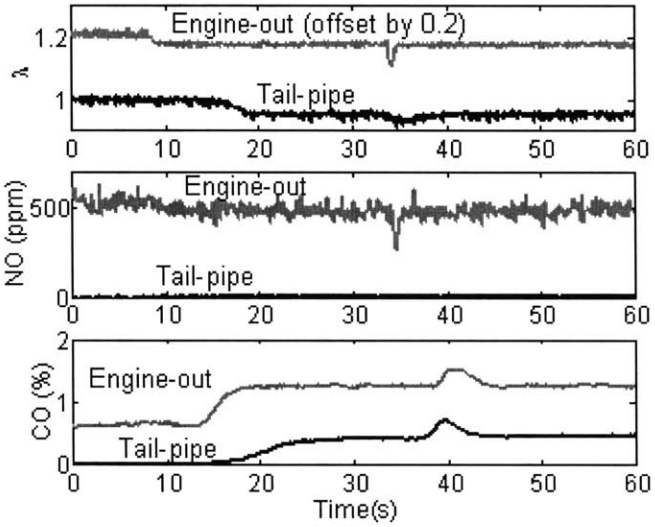

Fig. 6-31, 4k catalyst NO and CO pre- & post-catalyst time-resolved values.

Biased by -1% and -3% with rich spike (height of 20%).

6.3.3 Correlation of NO breakthrough and Oxygen Storage Capacity

From the observation and all previous experiments (throttle transients, air/fuel ratio modulation), it is obvious that there is a close correlation between NO breakthrough and oxygen storage capacity of the catalyst. In this section such relationship is quantified and compared to the oxygen storage results discussed in previous chapter (Chapter 4).

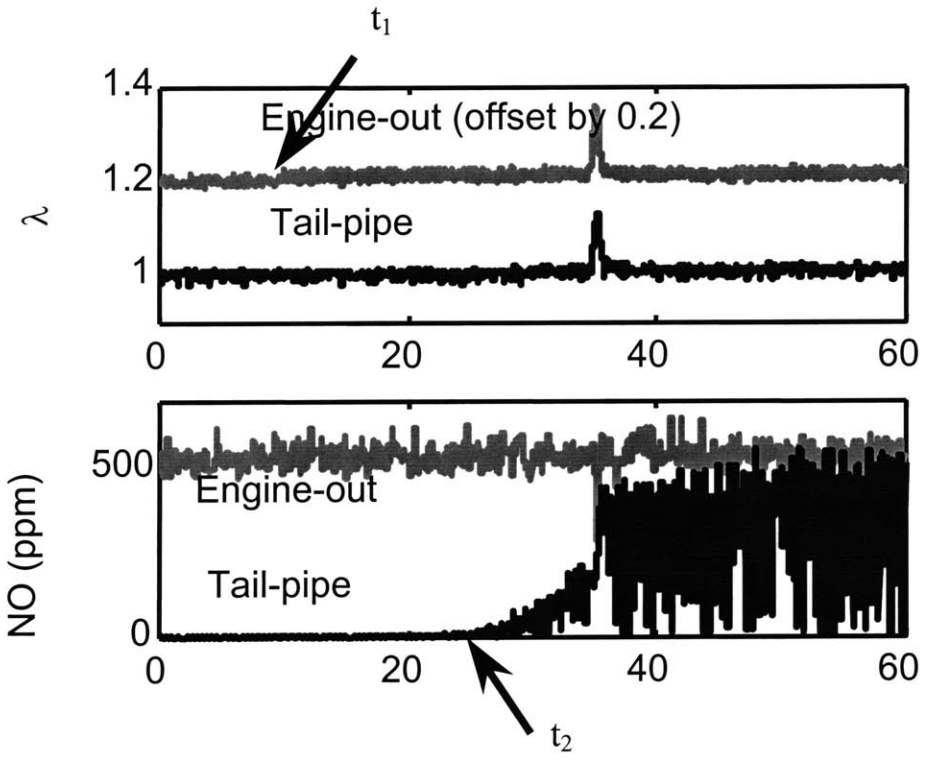

Fig. 6-32, NO breakthrough during lean-biased air/fuel modulation

Since we assume the NO breakthrough is related to the oxygen storage capacity, it is obvious that we should try to quantify the amount of oxygen stored during these processes. Fig. 6-32 shows the NO breakthrough during a lean-biased air/fuel modulation with a lean spike. The method in figuring out how much oxygen is stored is the following. We assume there is not oxygen stored in the catalyst before the start of biased

modulation. So the integration starts from t_1 in Fig. 6-32. We also assume that when the down-stream sees the first trace of substantial NO breakthrough, the oxygen storage is saturated. So the integration stops at t_2 in Fig. 6-32.

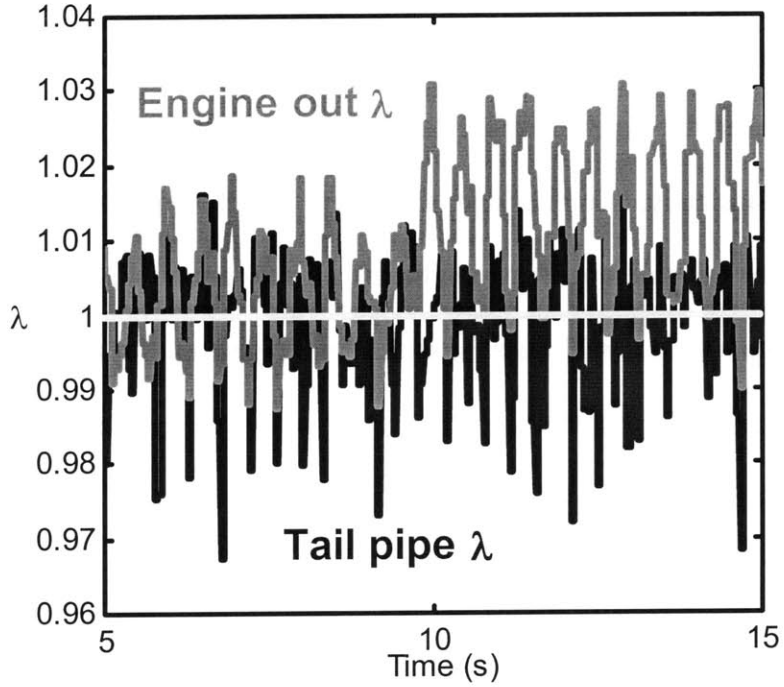

Fig. 6-33, A blown-out look at the air/fuel ratio before and during the biased modulation

Fig. 6-33 shows a close-up look at the up- and down-stream air/fuel ratio during this process. It can be seen that the air/fuel ratio crosses the stoichiometric value in the modulation. As discussed in Chapter 4, during the rich part of the modulation (when $\lambda <$ 1) reducing species (CO, H2, etc.) are being oxidized by the stored oxygen in the catalyst. To calculate the oxygen storage, the average λ is used, so that the net oxygen flow to the catalyst is taken into account.

The results of this analysis are shown in Fig. 6-34. In Fig. 6-34 (a), the top line denotes the maximum oxygen storage capacity for the catalyst at 33ppm fuel sulfur level. The oxygen storage capacity at the averaged biased λ values was determined from the

step-λ experiments described in Chapter 4; the relevant data are shown in Fig. 6-34. The values of these capacities are plotted as dotted lines for l values of 1.01 and 1.03 respectively in Fig. 6-34a. Finally the amount of oxygen stored between t1 and t2 in Fig. 6-32 is plotted in Fig. 6-34a as symbols (circles and crosses).

The analysis shows that the two sets of data on oxygen stored match very well. The result confirmed the hypothesis that the NO breakthrough may be related to the oxygen storage. Basically, it implies that when there is still oxygen storage capacity in the catalyst (under a certain operating condition), no substantial NO breakthrough will occur, since the catalyst can still store the excess of oxygen up. But as soon as the catalyst is saturated with oxygen, the excessive oxygen in the exhaust gas is competing with NO for reducing species, and NO breakthrough occurs.

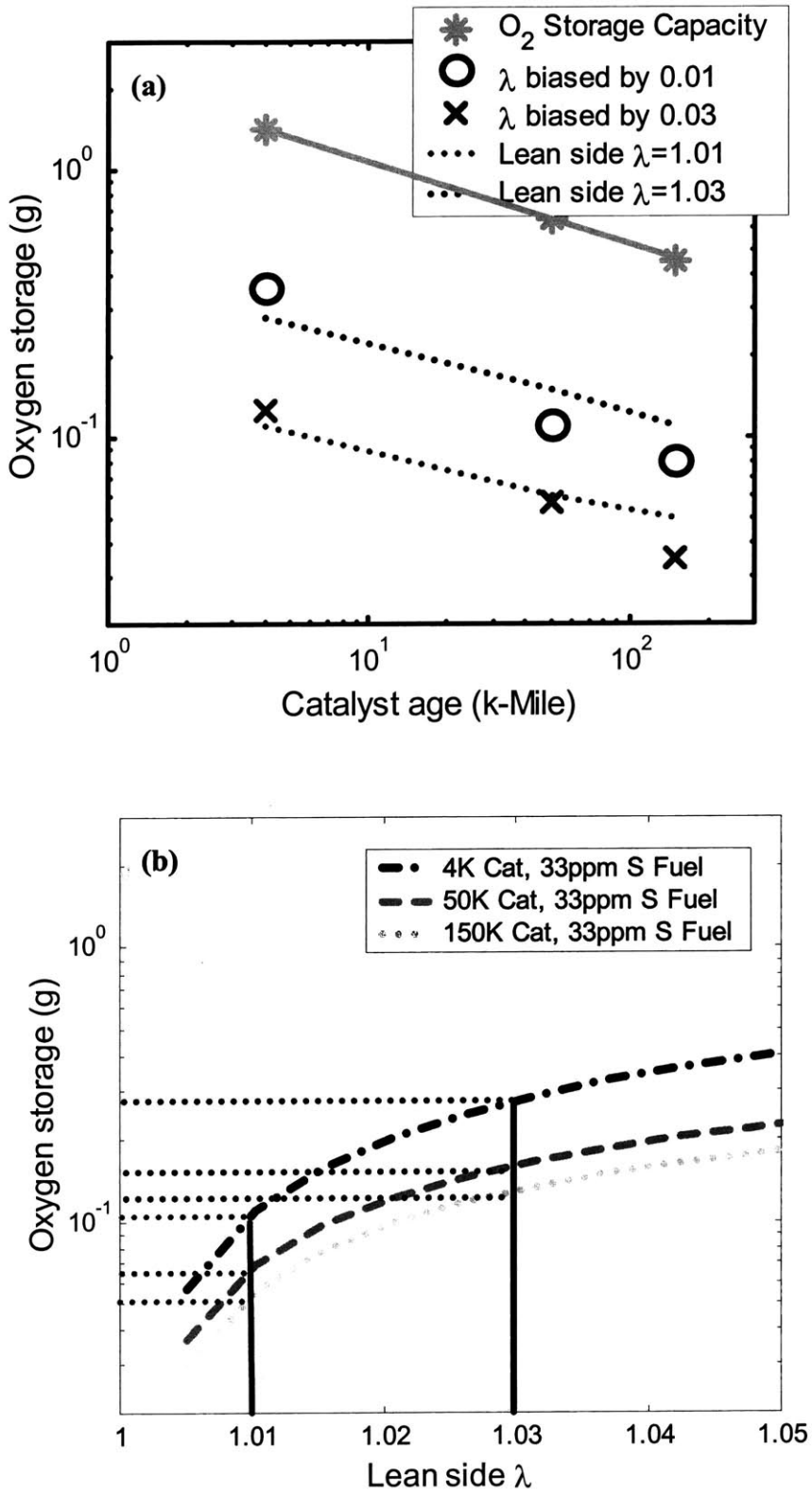

Fig. 6-34, Comparison of oxygen storage between lean-biased air/fuel ratio modulation experiments (a), and λ lean-step experiments (b).

Summary

This chapter mainly deals with different modes of air/fuel ratio modulation. We start off by looking at the baseline case, the stock ECU modulation. This particular engine has a mode of modulation at 2 Hz with amplitude of ±2.5%. The in-catalyst species profiles do not show substantial differences among the three catalysts at different levels of aging. And the general trend is more than 80% of the pollutants are removed in the very first fraction of the catalyst (17% volume).

Then air/fuel modulations at different amplitudes and frequencies were tested on the 150k and 4k catalysts. NO breakthroughs were observed in the front part of the catalyst during the lean part of the modulation. These breakthroughs, however, diminished substantially along the catalyst. The time-averaged NO profile revealed the differences between the catalyst ages. It also showed that when there is enough oxygen storage capacity in the catalysts, the conversion efficiency is insensitive to different modes of modulation within a certain range (relatively high frequencies and small amplitudes). This observation is in agreement with relating the NO breakthrough to oxygen storage capacity.

Next, biased air/fuel ratio modulation experiments were carried out to further investigate the relationship between NO breakthrough and oxygen storage. The results showed that there is a close relationship between NO breakthrough and oxygen storage capacity. As soon as the oxygen storage is saturated, NO will breakthrough the catalyst. The trend is in very good agreement with the λ rich-to-lean step experiments.

Chapter 7

Flow Reactor Catalytic Action Study

As described in the beginning of the thesis, the thesis has two main themes. The first one is to quantify oxygen storage mechanism, its limiting factors, and its effects on the three-way catalyst performance. The second theme is a practical comprehensive three-way catalyst model that takes into account oxygen storage and aging effects, and is able to simulate transient performance.

In chapters 4 - 6, oxygen related topics are covered. In chapters 7 and 8, the modeling of three-way catalyst will be addressed in detail. In order to get ready for the comprehensive model, the catalytic action mechanisms need to be understood first. This chapter is designated to investigate into some of the reactions and catalytic processes. In the experiments, limiting rates of catalytic process were measured under steady state. The experiments generated a dataset for the model to build on later.

7.1 Experimental Setup of Flow Reactor

In previous chapters, all of the experiments were carried out on an engine-catalyst setup. The advantages are the system is close to a real-world emissions control system. For example, the exhaust composition is controlled by adjusting air/fuel ratio; flow rate and inlet temperature are controlled by adjusting engine speed and load. But the disadvantages are a lot of the factors are coupled together. For example, when λ is changed, all species are changed simultaneously; individual component cannot be adjusted separately. Similarly is for flow rate and inlet temperature. When engine load is

increased, the flow rate of exhaust gas increases, but exhaust temperature is increased at the same time.

In order to investigate into each individual affecting factors of the catalyst, a new setup was built that can decouple the factors such as exhaust composition, inlet temperature, flow rate, etc.

7.1.1 System Configuration

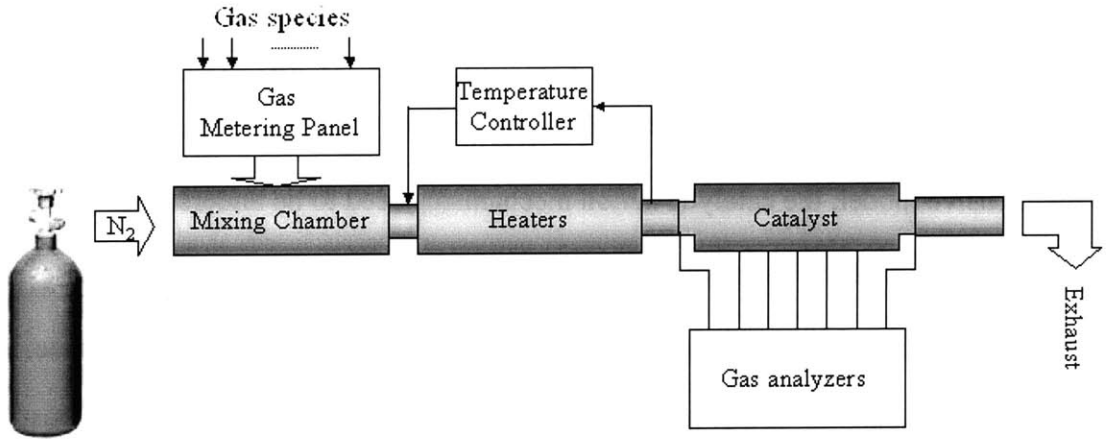

Fig. 7-1, Flow reactor setup schematic

As shown in Fig. 7-1, the system is composed of carrier gas source, mixing chamber, in-line heaters, catalysts, and gas analyzers.

1), Carrier gas – liquid nitrogen (LN2) is used as the carrier gas source. A standard AirGas® 240-liter 230-psi liquid nitrogen tank was used to provide abundant flow of N2 as the carrier gas. The tank has built-in heat exchanger that is enough to boil ~30 SCFM gaseous N2 under room temperature conditions. A high flow pressure

regulator was used to regulate gaseous N2 backpressure, thus controlling the flow rate. Coming out of the pressure regulator, the gas passes through a Sylvania® 038825 in-line heater, which is closed-loop controlled by an Omega® PID controller. The purpose of the heater is to bring the cold N2[1] up to room temperature. The gas is then led through a flow meter (rotameter) which precisely meters the flow that goes into the flow reactor. The pre-heater is crucial because, it keeps the gas that goes through the flow meter at a constant temperature[2].

2), Mixing chamber – the mixing chamber is essentially a manifold with a plenum, in which different gaseous species can be metered in and well mixed. The different gases are each individually metered via a rotameter. The precise synthetic exhaust composition measured by the gas analyzers.

3), Further down stream of the mixing chamber, the gas mixture is led through a series of high-power in-line heaters. The Sylvania® 038825 in-line heaters are 6kW each, the heaters are enough to heat the exhaust gas up to 700 degC.

4), Coming out of the heaters, the synthetic exhaust gas then goes into the catalyst. The catalysts are the same as used in previous experiments. In order to achieve high flow rates, they are downsized (see 7.1.2). Along the catalysts there are probes for the gas analyzers used in previous experiments (refer to Chapter 3).

---

[1] The LN2 tanks are not heated; the phase change from liquid to gas is only powered by natural heat transfer from the ambient. So the gas is at a much lower temperature when first coming out of the tank. Another reason the gas is cold is it experiences a sudden expansion across the pressure regulator.

[2] The rotameters are sensitive to gas temperatures, because the mechanism of measurement is that the flow rate Q is proportional to $(A\rho v^2)$. Where, A is the cross-section area of gas passageway; ρ is the gas density, which is a function of temperature; and v is flow speed.

7.1.2 Downsized Catalyst Bricks

Without substantial investment in the gas supply and heating capacity, the flow rate cannot be sufficiently high, even though current setup is good enough to simulate the space velocity as the engine running at 1600 rpm, 0.5 bars intake pressure.

Therefore the catalyst bricks were downsized. The same catalysts were used, only at a smaller size. Shown in Fig. 7-2 are two such bricks, the big one is the original brick from the converters. And the smaller one is cut from the big brick.

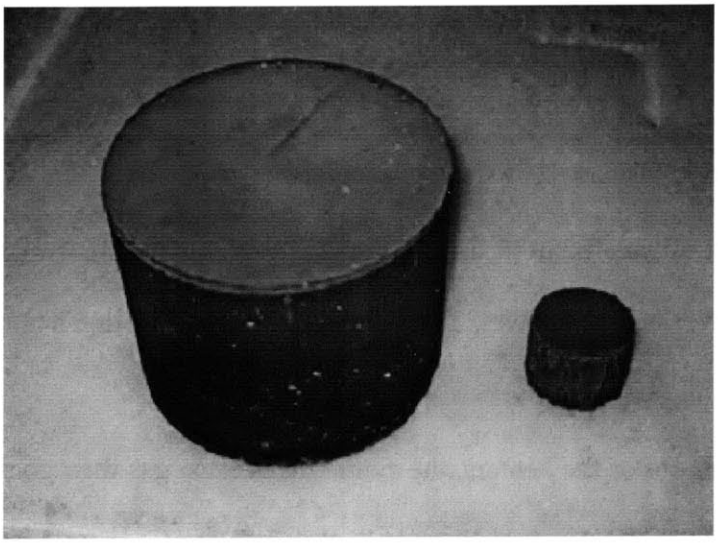

Fig. 7-2, Full-size and downsized bricks

The small bricks are at 1 ¼'' in diameter, and 1'' in length. Five of such bricks were stacked up and put into a piece of stainless steel pipe. See Fig. 7-3 and 7-4. There was the option to have all the stacked small bricks coming from a specific part of the original catalyst, or to have the individual brick in the stack coming from different parts of the catalyst. In between every two bricks there is a small gap (1/4'') for a probe (1/8''

in diameter) to fit in. High-temperature silicate cement was used to hold the bricks in place inside the steel pipe; it also serves as a sealant on the circumference of the bricks.

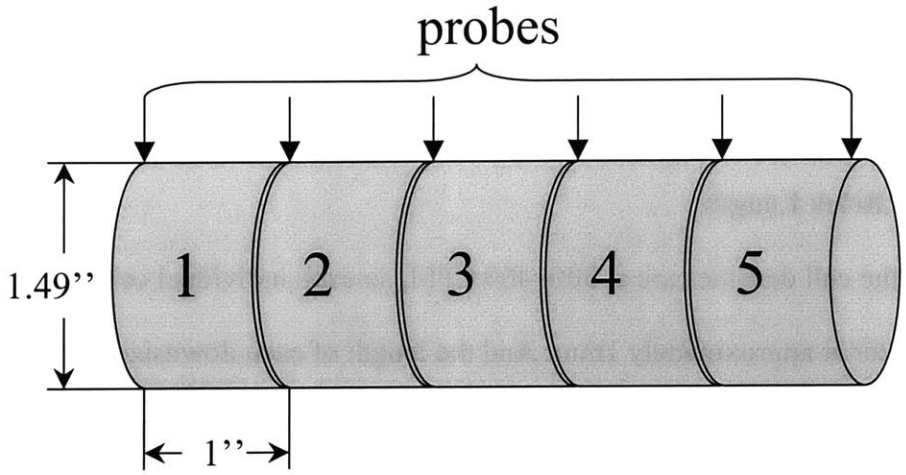

Fig. 7-3, Dimensions of the downsized bricks and stacked up bricks.

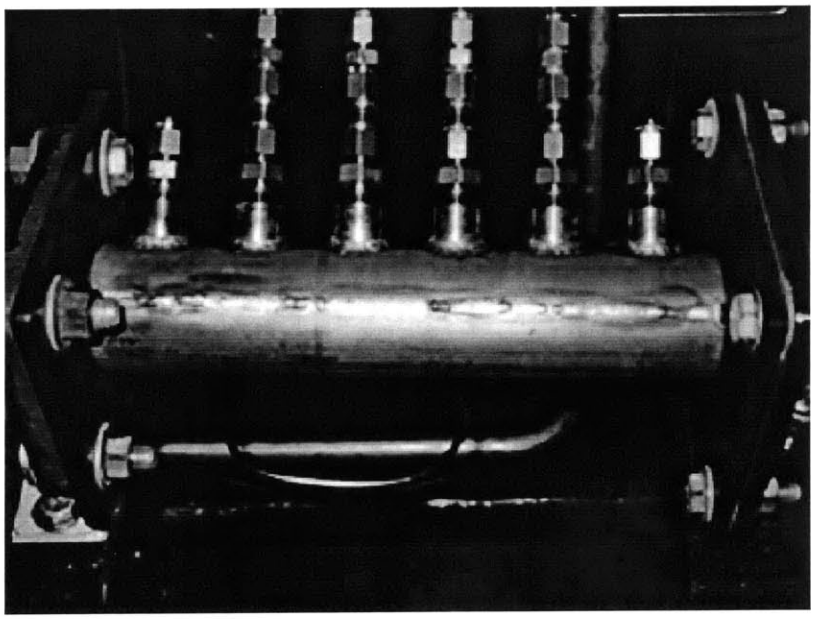

Fig. 7-4, Stainless steel pipe for brick canning and probes

The original catalysts have a two-brick structure. The front bricks have square-shaped cells at a density of 400 CPSI (cells per square inch). And the rear bricks have triangular-shaped cells at a density of 300 CPSI. The two different geometries were studied separately.

7.1.3 Effects of Brick Length

As said above, the cell densities are at 300~400 CPSI, so each individual cell has a hydraulic diameter at approximately 1mm. And the length of each downsized cell is 1''. So with $L/D > 25$, the entrance effects are negligible. In order to justify this assumption, some testing was done to compare the effects of different brick lengths.

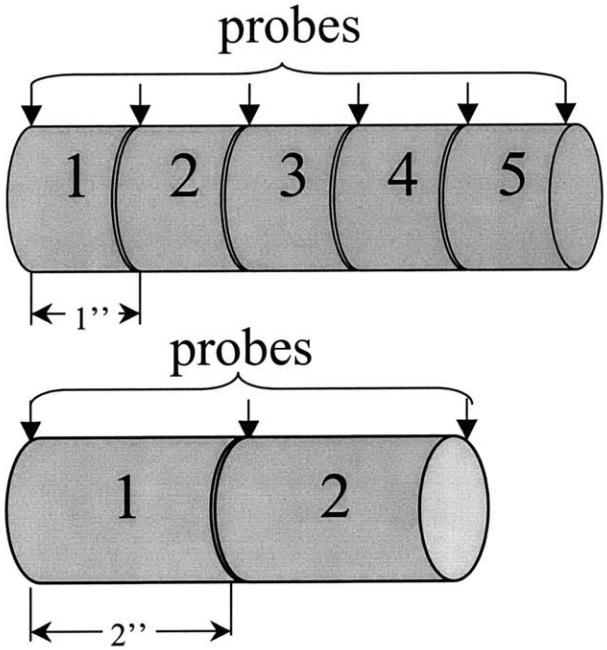

Fig. 7-5, Downsized bricks with different lengths

Another set of bricks with length of 2'' was made. The diameters were kept the same; and they are cut from the same original bricks. So the cell density, loading and

other properties are identical to the ones that are at 1'' in length. The 50k catalysts were used to compare the effects of different brick lengths.

A very simple reaction scheme of NO+H2 was tested on both downsized catalysts (at different length). As will be discussed in more detail in 7.2. The experiments were carried out at inlet temperatures above 400 degC, which is well above light-off temperature for the catalyst. Different flow rates were also tested. In the experiments, the overall environment was kept reducing, so no oxygen storage is involved, also NO always has enough reducing species to react with.

The results are shown in Fig. 7-6. The plots are for normalized NO ($NO/NO_{\_inlet}$) profile as a function of ($xT^{1.8}/v$). The reason why the horizontal axis is so chosen will be discussed in more detail in 7.2. Here the plot is just to show that effects of two different lengths. In the graph, the squares are for the long bricks (2'' in length), and the diamonds are for the regular bricks (1'' in length). And the lines are curve fits of the data (there are two lines on top of each other). So Fig. 7-6 shows that the two different bricks at different lengths are performing almost exactly the same. The assumption that the length effects are negligible is valid.

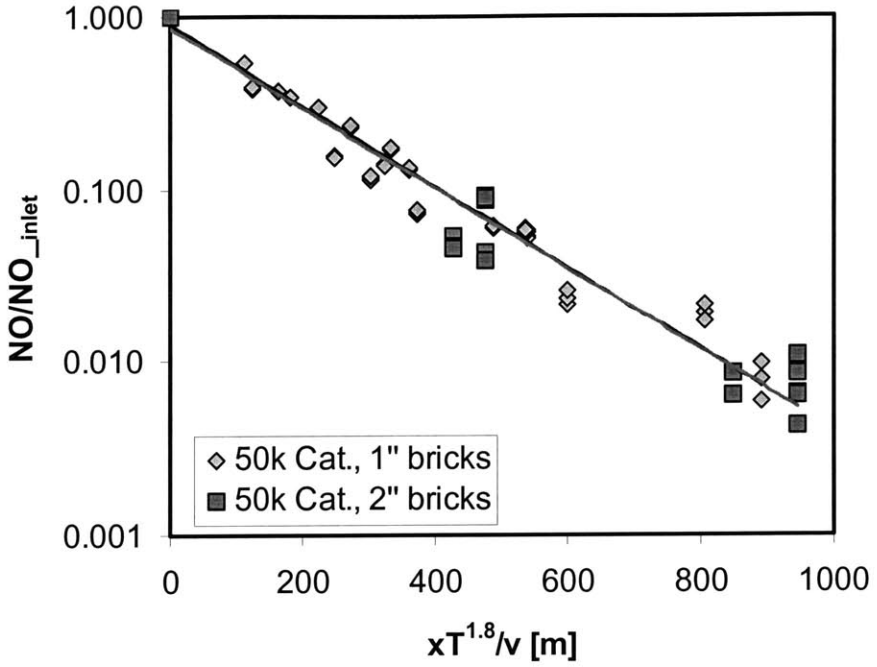

Fig. 7-6, Results of effects of individual brick length

7.2 Binary Reaction Experiments

The studies were started with the simplest reaction scheme, binary reactions. Still the interest was focused on NO related reactions. Experiments with NO reacting with a reducing species (H2, CO or C3H8) were run on the flow reactor. As introduced in the system setup, the system is capable of controlling flow rate, temperature and species concentration independently.

There are several things these experiments have in common. First, all of the experiments were run at inlet temperatures above 400 degC, which is well above the light-off temperature of the three-way catalyst. So the catalyst should be fully warmed-up. Second, a reducing overall environment was kept, i.e., there was always excess of reducing species. This will guarantee that the oxygen storage is not involved in the reactions.

The reactions between NO and the reducing species are as follows:

$$NO + CO \rightarrow \tfrac{1}{2}\, N2 + CO2 \qquad (7.1)^3$$

$$NO + H2 \rightarrow \tfrac{1}{2}\, N2 + H2O \qquad (7.2)$$

$$NO + 1/(2M_2)\, CH_\alpha \rightarrow 1/(2M_2)\, CO + a/(4M_2)\, H_2O + \tfrac{1}{2}\, N2 \qquad (7.3)$$

$$NO + 2.5/(2M_2)\, CH_\alpha + (3-\alpha)/(4M_2)\, H_2O \rightarrow NH3 + 2.5/(2M_2)CO \qquad (7.4)$$

Eqn. 7.1 and 7.2 are very well published reaction schemes. And Eqn. 7.3 and 7.4 are from [44]. Where α = hydrogen-to-carbon ratio of the HC, M2=[1/2 + α/4].

7.2.1 Experimental Results

Fig. 7-7 shows the NO reduction profile along the 50k catalyst. In this figure, different marks denote different experimental conditions (temperature, flow rate). The general trends can be observed from the figure, that at higher temperatures NO reduces faster (with steeper slope in the chart); and at higher flow rates NO reduces slower (with milder slope in the chart). In order to make the data more informative, a different way of plotting it is used. Instead of plotting the NO profile vs. cumulative catalyst volume, another parameter was used.

[3] Under low temperatures (before the catalyst is lit-off), NO can be reduced to N_2O instead of N_2. In these experiments, however, the temperatures are well above light-off temperature. So only the products only include N2 and CO2. See Appendix B for experiments at low temperatures that show NO is reduced to N_2O.

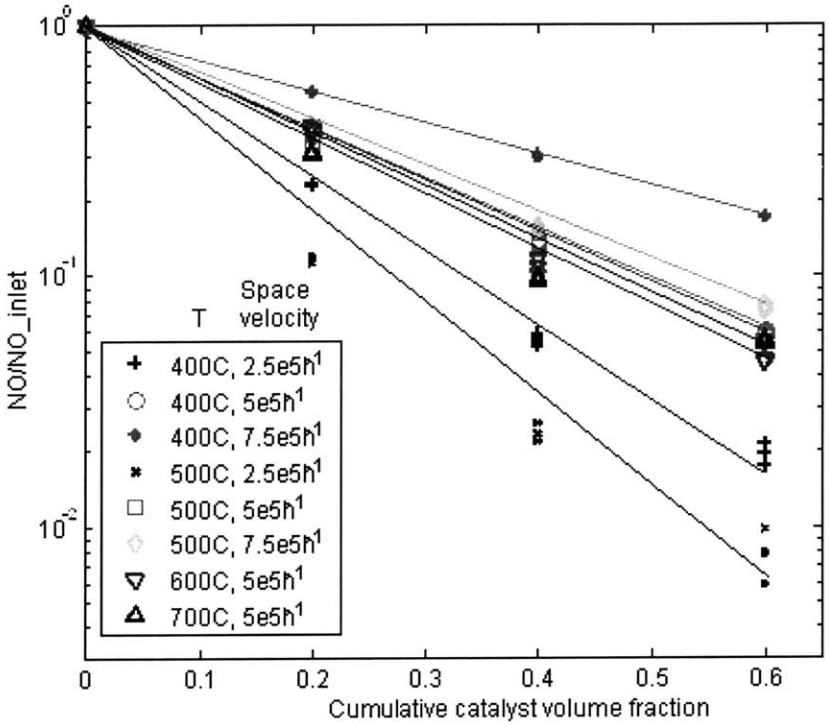

Fig. 7-7, 50k catalyst normalized profile of NO reduction with CO along the catalyst

As is well known, the activity of a catalytic converter is a function of temperature. Before the catalyst is lit-off (or warmed up), the reaction rates are low. So the reduction processes are limited by the kinetics other than transportation (refer to Chapter 3). However, when the catalyst has been fully warmed up, the reaction rates are so fast that the reduction process is limited by transport. Since in these experiments, the catalyst temperature was sufficiently high, it would be reasonable to assume the reduction process is limited by transport. A comparison of time scale between chemistry and transport is shown in Fig. 7-8.

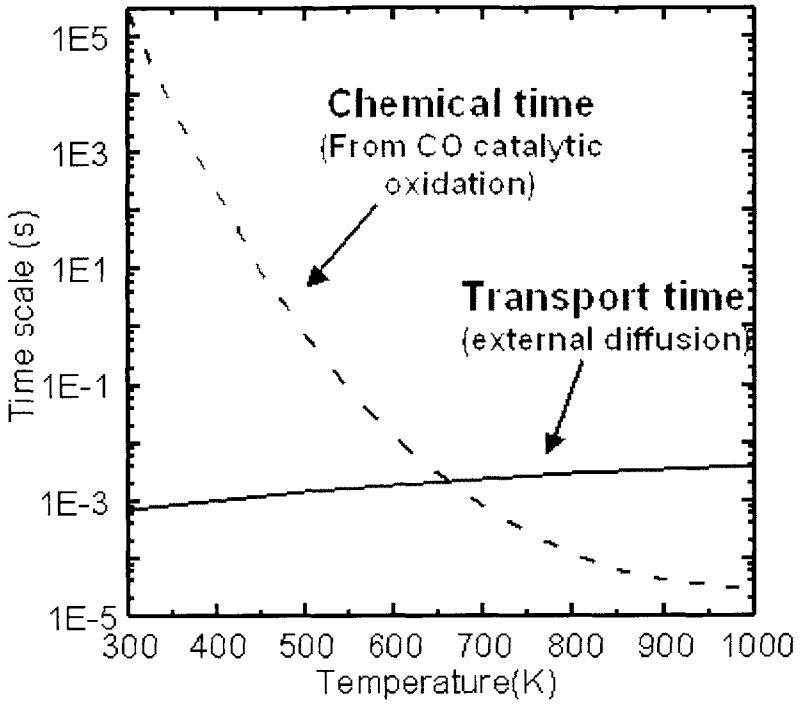

Fig. 7-8, Time scale comparison between chemistry and transport

In a diffusion-controlled process, the transport of species from bulk flow onto the boundary surface is controlled by the diffusivity of the species; the reactant concentration along the flow (in a duct of constant area) will decrease exponentially with a length scale of (vd^2/D), where v is the bulk flow velocity, d is the hydraulic diameter and D is the diffusivity. So instead of plotting the data in Fig. 7-7 as a function to x, they are plotted in Fig. 7-9 as a function of (xD/v), where x is distance the gas has traveled, since the hydraulic diameter, d, is a constant.

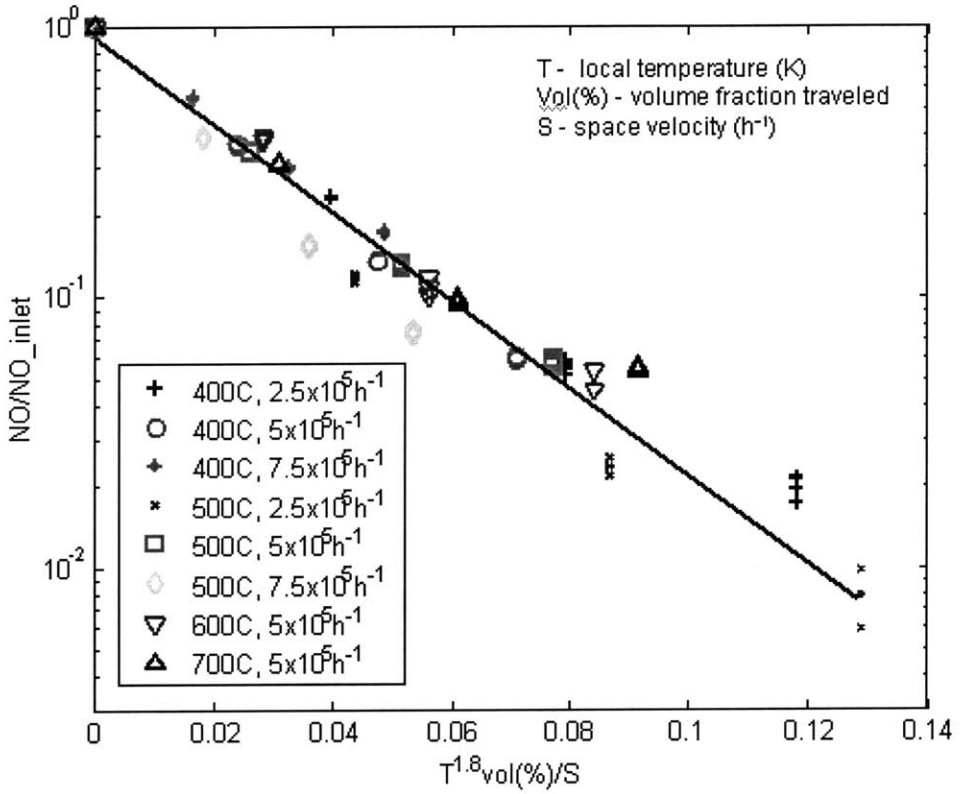

Fig. 7-9, 50k catalyst normalized profile of NO reduction with CO along the catalyst as a function of ($T^{1.8}vol/S$)

In Fig. 7-9, the data is the same data as in Fig. 7-7, only plotted differently. One thing needs to be pointed out is that instead of using diffusivity of NO, $T^{1.8}$ is used. This is because in the temperature range of interest, the diffusivity of NO in N2 is proportional to $T^{1.8}$. Also space velocity (S) is used in the plot instead of linear velocity, since they are proportional to each other. As can been seen in Fig. 7-9, the data points that are spread out in Fig. 7-7 are now all aligned onto one straight line on semi-logarithm scale. The result confirms the theory that the catalytic reduction process is diffusion controlled under such conditions.

7.2.2 Diffusion Limiting Species

Fig. 7-7 & 7-9 show the results of reaction NO+CO. NO reactions with other reducing species (H2 and propane) show the same trend. The NO reduction profiles as a function of (xD/v) are a straight line on a semi-logarithm scale. Notice one thing here is that the diffusivity (D) used to calculate the x-axis value is that of the slowest diffusing species of the reactants. The reduction process is limited by the rate of diffusion of the particular species with the lowest diffusivity.

Refer to Table 7-1, the diffusivity coefficients of NO and CO in N2 are essentially the same (7.3.2 discusses the calculation of diffusivity coefficient). So it will not change the plot in Fig. 7-9. Whereas, in the reaction of H2+NO, the limiting species is NO, therefore, the diffusivity used in calculation should be the one for NO. In other words, since the diffusivity of H2 in N2 is much higher than NO (refer to 7.3.2), there is always enough H2 diffused from the bulk flow onto the surface. Therefore, the speed of NO diffusion onto the surface decides the rate of the whole reaction process.

The case for NO+C3H8 is a little more complicated than NO+CO and NO+H2 (refer to Eqn. 7.3 and 7.4). The ratio of C3H8 diffusivity in N2 over NO diffusivity in N2 ($D_{C3H8\text{-}N2}/D_{NO\text{-}N2}$) $\approx$ 0.4. And the ratio of stoichiometry of C3H8 over NO is 0.47. So the there is always excessive NO on the surface. Thus, C3H8 is the limiting species between the two.

Fig. 7-10 shows the plot of NO reduction profile as a function of (xD_{limit}/v) in the reactions of NO+CO, NO+H2 and NO+C3H8. It is very clear the three plots all align on the same line, with the same slope. This is consistent with the hypothesis of limiting species determining the reduction rate.

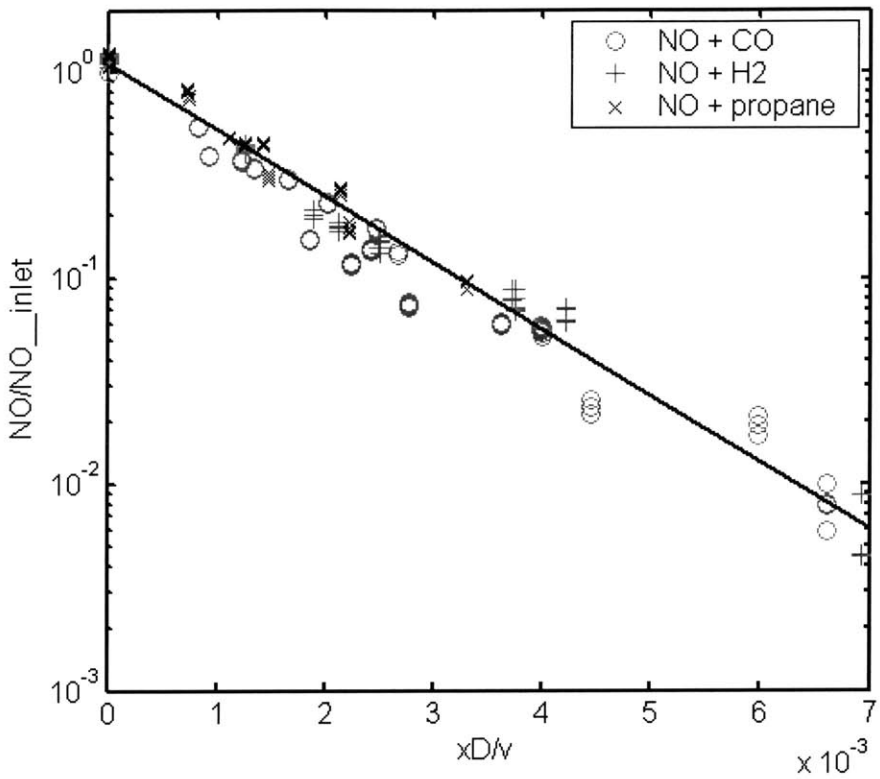

Fig. 7-10, NO reduction with different reducing species, the slope of the profile is determined by the limiting species. For NO+CO the limiting species is NO (or CO); for NO+H2 the limiting species is NO; for NO+C3H8 the limiting species is C3H8.

7.3 Model of Mass Transfer Limiting Processes

Since the data in 7.2 shows that the reduction of NO is diffusion-controlled after the catalyst is warmed up, the data can be used to calibrate an analytical model of the diffusion limiting process.

7.3.1 Analytical Model

Fig. 7-11 shows the schematic of a simple 1-D mass transfer model in a square-shaped cell (duct). The bulk flow has a velocity of u; the cell cross-section area is A; at any position (x), the concentration of species is $C(x)$. Other parameters include diffusivity

coefficient (D), Sherwood number (Sh), Hydraulic diameter (D_h) and effective surface area factor (ξ).

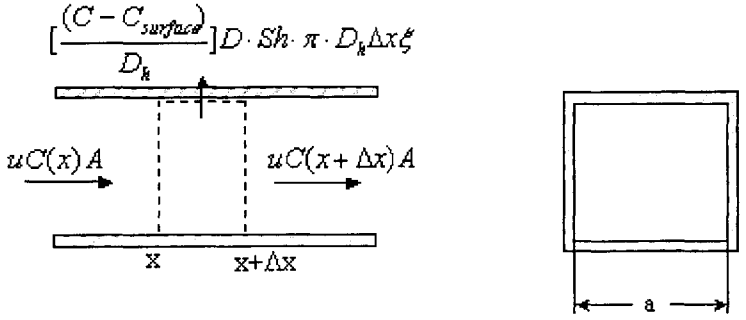

Fig. 7-11, 1-D mass transfer model in a square-shaped cell

The mathematical description of this model is the following differential equation:

$$u[C(x+\Delta x)-C(x)]A = -[\frac{(C-C_{surface})}{D_h}]D \cdot Sh \cdot P \cdot \Delta x \xi \qquad (7.5)$$

Rearranging Eqn. 7.5, we get the following expression for the concentration profile along the cell. Notice that the concentration profile is a function of *D, Sh, u, A, Dh, P, ξ and x*. This is what the data shows in Fig. 7-7.

$$\frac{dC}{C} = -\frac{D \cdot Sh \cdot \xi \cdot P}{u \cdot A \cdot D_h} dx \qquad (7.6)$$

Further rearranging Eqn. 7.6, we get Eqn. 7.7. In Eqn. 7.7 we can see that concentration profile over ($D \cdot x/u$), or $\frac{d \ln C}{\left(\frac{D \cdot dx}{u}\right)}$ is a function of $\left(\frac{P \cdot (Sh \cdot \xi)}{A \cdot D_h}\right)$. And in the experiments, perimeter, Sh, cross-section area and hydraulic diameter are all constants (for one specific catalyst). So this is why in Fig. 7-9 & 7-10 all of the data points align on one single straight line, no matter what the temperature and flow rate are.

$$\frac{d\ln C}{\left(\frac{D\cdot dx}{u}\right)} = -\frac{P\cdot(Sh\cdot\xi)}{A\cdot D_h} \tag{7.7}$$

7.3.2 Calculation of Diffusion Coefficient

The diffusion coefficient is the key transport property in a mass transfer problem. The Chapman-Enskog kinetic theory gives the following result for non-polar molecules:

$$D_{AB} = \frac{(1.8583\times10^{-7})T^{3/2}}{p\Omega_D^{AB}(T)}\sqrt{\frac{1}{M_A}+\frac{1}{M_B}} \tag{7.8}$$

Where the units of p, T and D_{AB} are atm, K, and m2/s, respectively. M_A and M_B are the molecular weight of the two species in question. The function $\Omega_D^{AB}(T)$ describes the collision between molecules of A and B. It depends, in general, on the specific type of molecules involved and the temperature.

The type of molecule matters because of the intermolecular forces of attraction and repulsion that arise when molecules collide. A good approximation to those forces is given by the Lennard-Jones intermolecular potential in Eqn. 7.9. This potential is dependent on two parameters, molecular diameter, σ, and the potential well depth, ε [45, 46].

$$\Omega_D^{AB}(T) = \sigma_{AB}^2\Omega_D(k_BT/\varepsilon_{AB}) \tag{7.9}$$

$$\sigma_{AB} = (\sigma_A+\sigma_B)/2 \tag{7.10}$$

$$\varepsilon_{AB} = \sqrt{\varepsilon_A\varepsilon_B} \tag{7.11}$$

Where σ_A, σ_B, ε_A, ε_B are all well tabulated.

Various analytical approximations are also available. The accurate relation of Neufield et al. is

$$\Omega_D = \frac{A}{(T^*)^B} + \frac{C}{e^{DT^*}} + \frac{E}{e^{FT^*}} + \frac{G}{e^{HT^*}} \tag{7.12}$$

where $T^* = kT/\varepsilon_{AB}$ A = 1.06036 B = 0.15610

C = 0.19300 D = 0.47635 E = 1.03587

F = 1.52996 G = 1.76474 H = 3.89411

This method does not involve looking up tables, but gives a very good approximation.

Since, the calculation of diffusivity is very complicated, considering for the application of three-way catalyst only involves a finite range of temperature, we further simplified the calculation. Within the working range of temperature, the diffusivity coefficients were curve fitted to a series of power functions (listed in Table 7-1). It turns out that the simplified calculation matches the experiments very well. The biggest advantage of doing so is in future modeling work; the calculation time is substantially saved.

Species	Diffusivity Coef. [cm^2/s]
C3H6	$8E\text{-}6T^{1.69}$
C3H8	$8E\text{-}6T^{1.69}$
CH4	$2E\text{-}5T^{1.68}$
CO	$2E\text{-}5T^{1.67}$
CO2	$1E\text{-}5T^{1.68}$
H2	$6E\text{-}5T^{1.66}$
H2O	$1E\text{-}5T^{1.75}$
NO	$2E\text{-}5T^{1.67}$
O2	$2E\text{-}5T^{1.67}$

Table 7-1, Approximation of diffusivity coefficient of species in N2 within the range of working temperature of the catalysts

The above calculation of diffusivity is for binary mixtures. When three or more species are present, the calculation needs to be modified. If a low concentration of species i diffuses into a homogeneous mixture of n species, then:

$$D_{im}^{-1} = \sum_{\substack{j=1 \\ j \neq i}}^{n} \frac{x_j}{D_{ij}} \tag{7.13}$$

Where D_{ij} is the binary diffusion coefficient for species i and j alone. This rule is sometimes called Blanc's Law [45].

If a mixture includes several trace gases and one dominant species, A, then the diffusion coefficients of the trace species are approximately the same as they would be if the other traces were not present. In other words, for each species i,

$$D_{im} \approx D_{iA} \tag{7.14}$$

This is exactly our case in the experiments, where the bulk part of the flow is simply N2, all other species are diluted (<1%). So in the calculations, only binary diffusivity in N2 was used for each species.

7.4 Multiple Reactants Experiments

In 7.3 it has been shown that when only two species are present in the synthetic exhaust gas, the reduction of species is controlled by transport (diffusion rate) after the catalyst is fully warmed up. So now we want to investigate what will happen when more than two species are present. Things that are interesting to see are if different reducing species have competition against each other in reacting with the oxidizer(s); what happens when water is added, which will create new reactants; and what effects does oxygen have in the reactions.

7.4.1 CO+NO+H2

The results for NO+CO and NO+H2 in Fig. 7-10 show that the reductions of NO by the two species respectively progress at the same rate downstream. And we know this is because the processes are limited by the diffusion of NO. However, will this still hold when there are more than one reducing species? Will there be competition between CO and H2? If yes, what effects will the competition have?

Shown in Fig. 7-12 and 7-13 are the NO profile and CO profile in reactions of NO+CO+H2. Notice in all experiments, there were excessive reducing species (except for the 0% CO case). Thus, in all cases, the NO profiles are identical. If we look at the CO profile for the cases without the presence of H2, the amount of CO consumption matches well with the NO consumption, as long as there is excessive CO. But in the case where there was 0.3% CO and 0.3% H2, the consumption of CO was approximately 70% of that at when there was 0.3% CO alone. The latter result shows that the reducing reactants of CO and H2 competed with each other within the diffusion-limiting regime. The detail modeling of this process will be discussed in Chapter 8.

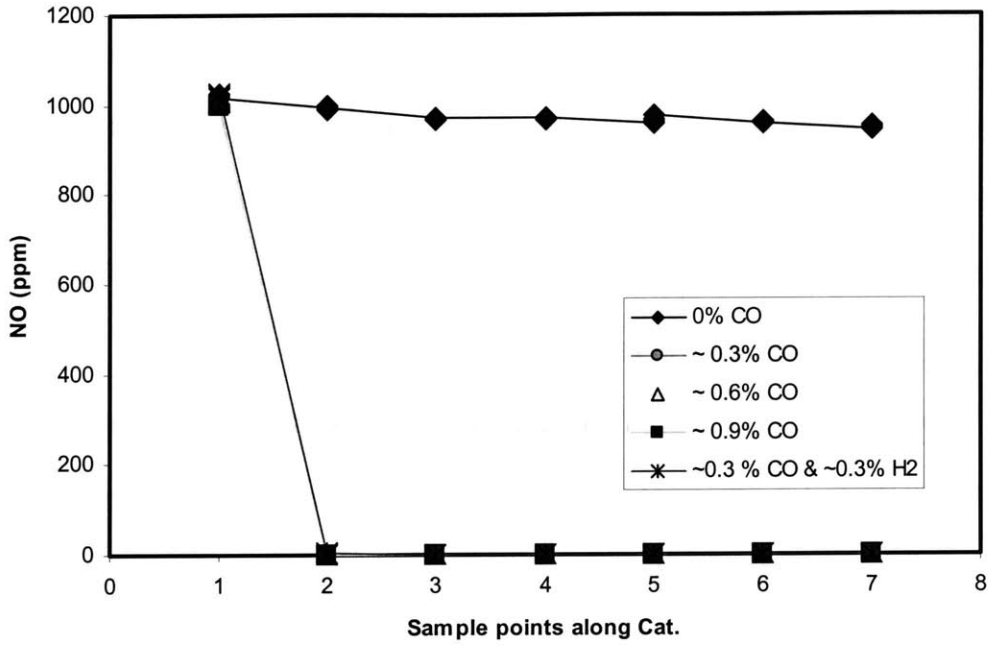

Fig. 7-12, NO reduction by CO and CO+H2 mixture.
Condition: full-sized catalyst

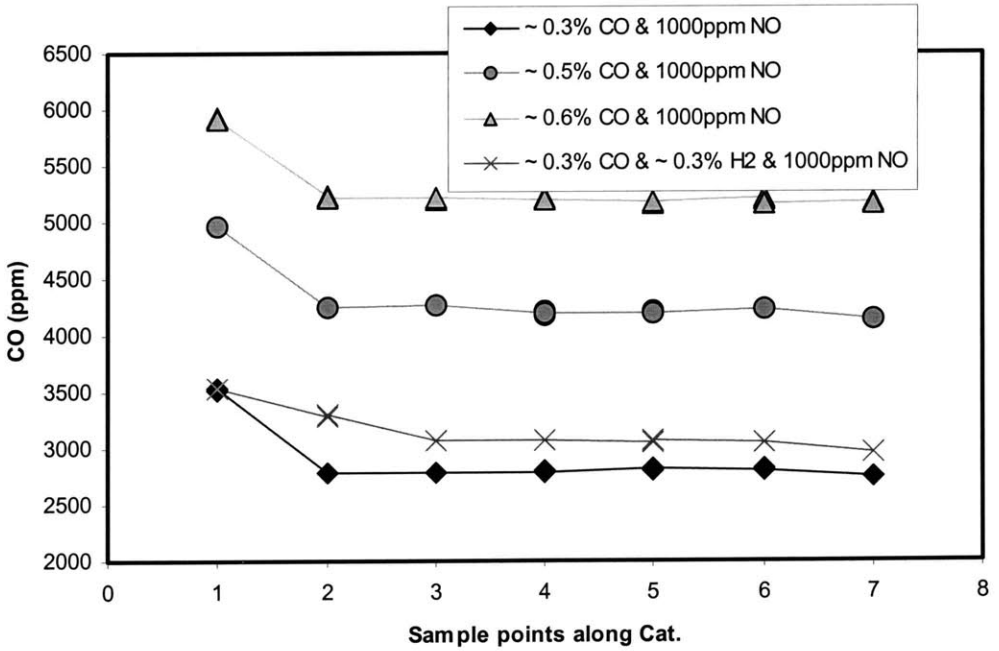

Fig. 7-13, CO profile in reaction with NO and NO+H2.
Condition: full-sized catalyst

7.4.2 CO+NO+H2O

This experiment is designed to look at the effects of H2O on NO reduction. The primary purpose was to investigate the effects of the water gas shift reaction on the catalytic action. In the test, the profile of NO in NO+CO experiment was first taken. Then approximately 10% mole fraction of water was injected into the feed stream, with other species molar flow rate kept unchanged (thus the H2O mole fraction in the reacting stream is 9%). NO profile was taken again. As shown in Fig. 7-14, in both cases, NO has identical reduction profile (diamonds for NO+CO, squares for NO+CO+H2O).

The interpretation of this phenomenon is that on the catalyst sites, H2O can react with each module of CO (the water gas shift reaction) to form one module of H2.

$$H2O + CO \leftrightarrow H2 + CO2 \qquad (7.15)$$

As shown in 7.4.1 H2 and CO have the same performance in reducing NO. Thus, the NO reduction profile kept unchanged.

Unfortunately, the experimental apparatus did not allow us to measure the exact amount of H2O and H2. But an indirect proof is available to justify the above interpretation. The proof of the water gas shift reaction's occurrence is that before and after the introduction of H2O in the system, the down-stream λ readings are different. After H2O is injected, the λ reading is noticeably lower than before ("richer"). The observation supports the fact that CO has been converted to H2. The lower λ sensor reading is because of the faster diffusion rate of H2 in the sensor; see Chapter 2 for a discussion of the λ sensor response.

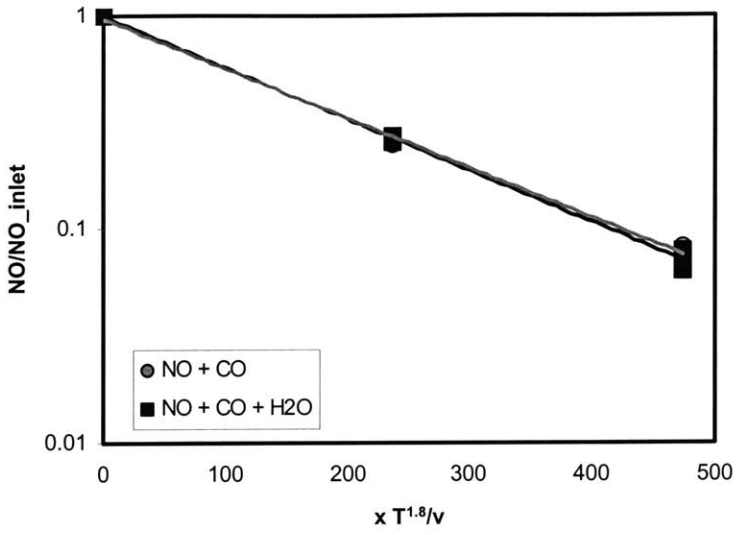

Fig. 7-14, NO reduction profile of NO+CO and NO+CO+H2O
Condition: ~1500ppm NO/~3000ppm CO/~10% H2O,
500 degC, SpaceVel. $5x10^5 hr^{-1}$

7.4.3 CO+NO+O2

Next the competition between NO and O2 for reducing species is investigated. This is closely related to the previous chapters on oxygen storage and NO breakthroughs. As has been discussed multiple times in previous experiments, NO breakthrough is directly related to oxygen storage capacity of the catalyst. We can investigate into more of the details of the competition between NO and O2 for reducing species with the help of the flow reactor. Note that with the current setup the O2 concentration could only be measured at up- and down-stream of the catalyst. No in-catalyst O2 reading is available. Another issue is the resolution of the λ meter in measuring O2 concentrations is only on the order of 100 ppm. So the readings of O2 is much courser than those of NO and CO.

The reaction between CO and O2 is the following:

$$CO + \tfrac{1}{2} O2 \rightarrow CO2 \qquad (7.16)$$

1), The Case When There Is Enough CO

The conditions of this experiment are 600 degC inlet temperature, $5x10^5hr^{-1}$ space velocity. Inlet CO mole fraction was fixed at 3200 ppm. The overall environment was kept reducing in all experiments, i.e., there is always enough CO to react both NO and O2. The amount of NO is fixed at 1000 ppm. The only variable is the amount of O2 in the mixture. The mole fraction of O2 is varied from 0 ppm to 1000 ppm, at 250 ppm increments. Since the overall environment is always kept rich, the oxygen storage of the catalyst does not play a role in the experiments.

Fig. 7-15 and 7-16 are the profiles of NO and CO along the catalyst in these experiments. It shows that as long as there is enough reducing species in the exhaust (CO in this case), NO reduction will not be substantially affected. Notice in Fig. 7-15, the NO reduction in cases of O2 at presence is the same as the one there is no O2 present.

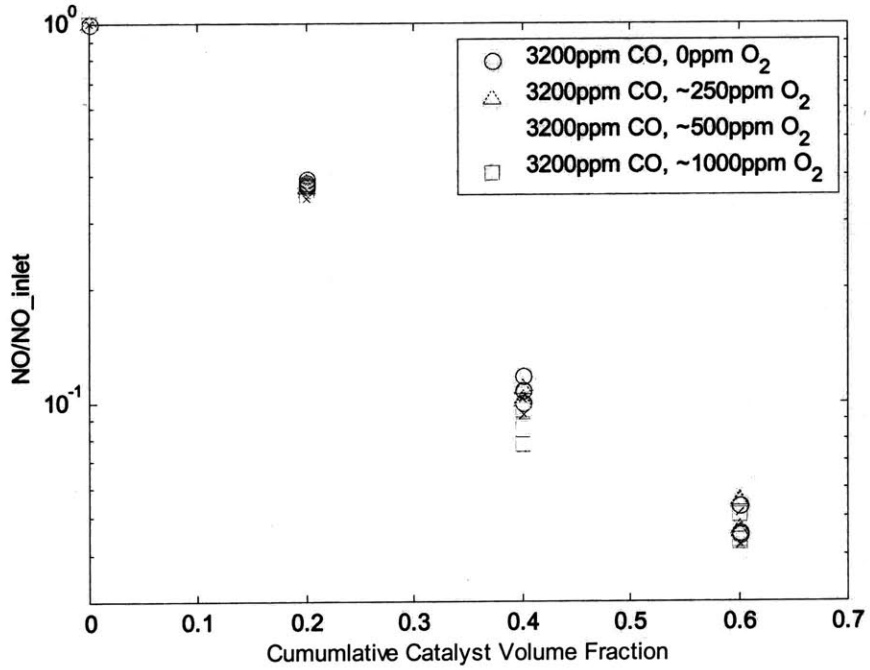

Fig. 7-15, NO reduction profile along the downsized catalyst
Conditions: inlet CO at 3200 ppm, inlet NO at 1000 ppm, inlet O2 varies from 0 to 1000 ppm; inlet temperature 600 degC, space velocity $5x10^5hr^{-1}$

The CO profile is shown n Fig. 7-16. With addition of O2, there is further reduction in CO. Since NO, CO and O2 have approximately the same diffusion rates, the role of the NO and O2 on CO reduction is the same. Model of the process is discussed in Chapter 8.

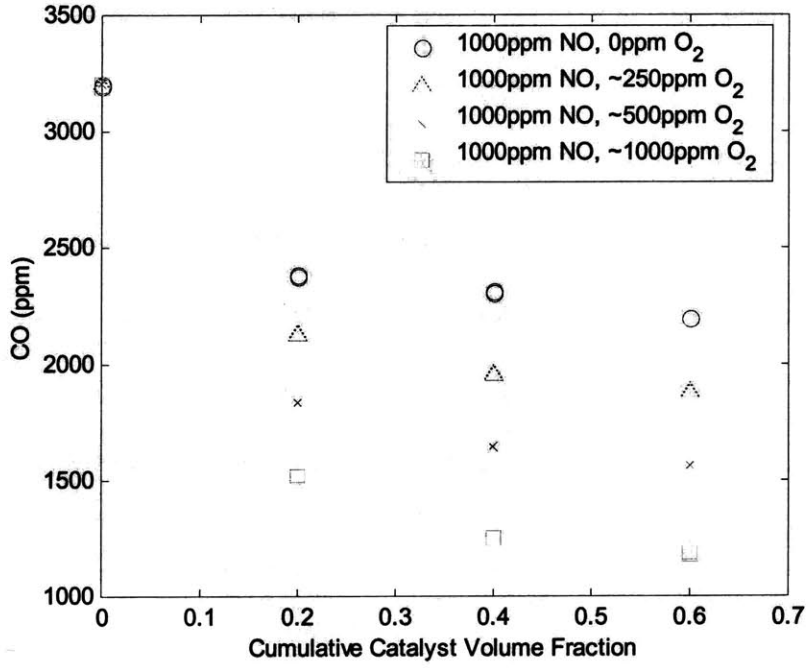

Fig. 7-16, CO profile along the downsized catalyst

Conditions: inlet CO at 3200 ppm, inlet NO at 1000 ppm, inlet O2 varies from 0 to 1000 ppm; inlet temperature 600 degC, space velocity $5x10^5 hr^{-1}$

2), The Case When There Is Not Enough CO

The experiments are kept at the same conditions as above, except for the amount of O2 is increased to 2000 ppm. Thus the overall environment is oxidizing. The data was sampled after steady state had been reached, so that the oxygen storage of the catalyst is saturated (no more oxygen can be stored by the catalyst). And from Fig. 7-17, it can be seen the phenomena in previous chapters (throttle transients and air/fuel ratio

modulation) are reproduced. There is substantial NO breakthrough, the blue circles in the plot. And CO profile shows an exponential decay along the catalyst. This reconfirms the previous hypothesis that when there is no more oxygen storage capacity or enough reducing species on the catalyst surface, NO will breakthrough.

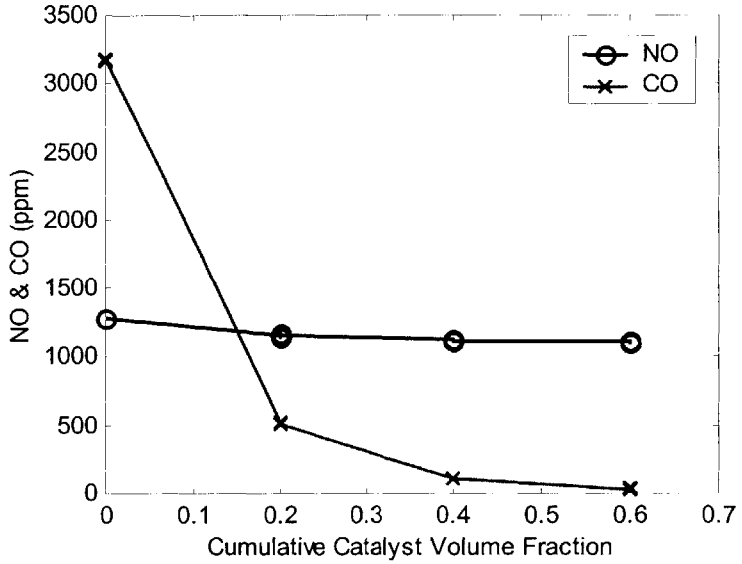

Fig. 7-17, Profiles of NO and CO when there is "too much" oxygen present
Conditions: inlet temperature 600 degC, space velocity $5x10^5 hr^{-1}$
inlet CO at 3200 ppm, inlet NO at 1000 ppm, inlet O2 2000 ppm

3), Quantification of the Competition Between NO and O2

Another implication of this phenomenon is that the reducing species (CO in this case) react preferably with O2 than NO. This can be proved by the following experiments.

The experimental conditions were still kept the same. The amount of inlet CO was kept at 3200 ppm; the amount of NO at 1000 ppm; and O2 was varied from 400 to 1600 ppm.

Fig. 7-18 is the measured NO profile along the catalyst, we can see that the reduction of NO is exponential (diffusion controlled) when O2 is below approximately 900 ppm. Or in other words, there is still enough CO. And if the amount of O2 kept on increasing, NO would breakthrough.

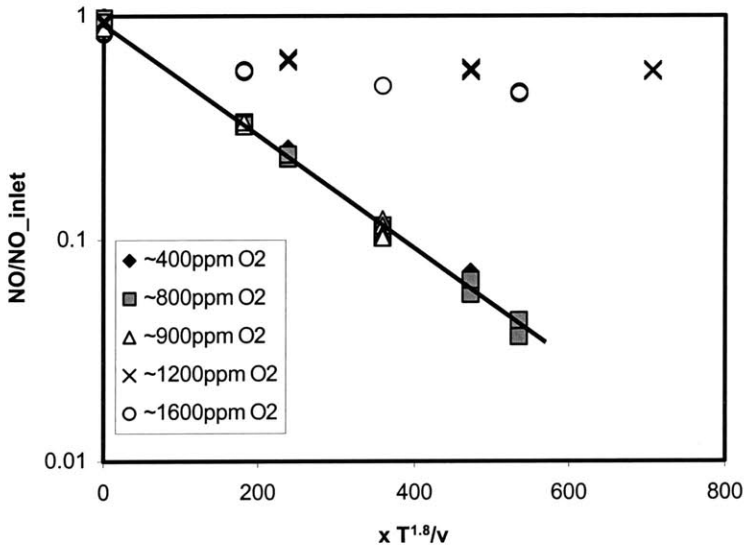

Fig. 7-18, Normalized NO reduction profile in reaction of NO+CO+O2
Conditions: inlet temperature 600 degC, space velocity $5x10^5 hr^{-1}$
inlet CO at 3200 ppm, inlet NO at 1000 ppm, inlet O2 varies from 400 to 1600 ppm

Fig. 7-19 shows the CO profile in these same experiments. When O2 is below approximately 900 ppm, the slope of the CO curve is milder than the exponential one; whereas, after that the CO curve becomes exponential. This means that when too much O2 is present, CO will be completely consumed, and the limiting factor is diffusivity of CO onto the surface.

Based on Eqn. 7.1 and 7.16, and the measurements of NO and CO, the in-catalyst O2 concentration can be calculated, shown in Fig. 7-20. It is quite clear that before the

amount of O2 reached the value when not enough CO is available, the reduction of O2 follows the exponential trend. Again, O2 reduction is limited by diffusivity.

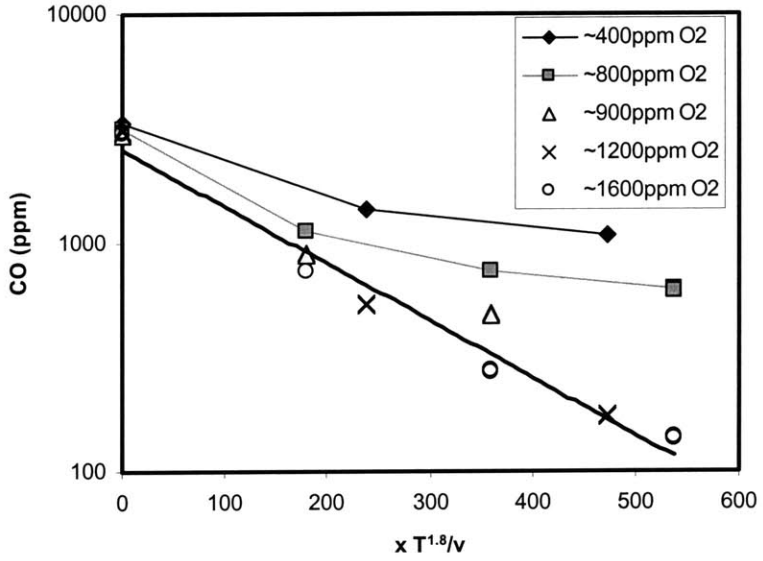

Fig. 7-19, CO profile in reaction of NO+CO+O2
Conditions: inlet temperature 600 degC, space velocity $5x10^5hr^{-1}$
inlet CO at 3200 ppm, inlet NO at 1000 ppm, inlet O2 varies from 400 to 1600 ppm

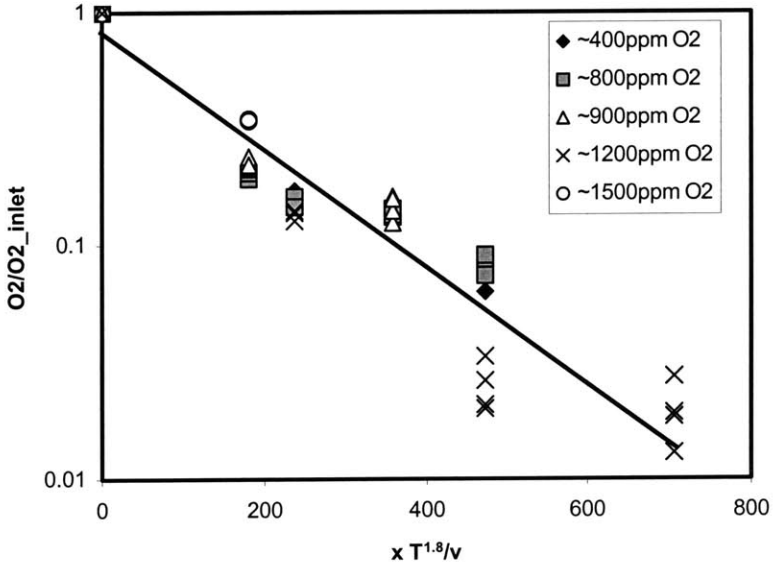

Fig. 7-20, O2 profile in reaction of NO+CO+O2 (calculated based NO and CO)
Conditions: inlet temperature 600 degC, space velocity $5x10^5hr^{-1}$
inlet CO at 3200 ppm, inlet NO at 1000 ppm, inlet O2 varies from 400 to 1600 ppm

7.5 Aging Effects

In previous chapters, it has been shown that at steady states, the catalysts all demonstrated very high conversion efficiencies. Even after the catalyst that has been aged for 150 k-miles, its overall breakthrough is not noticeably worse than the fresh catalyst. Only under transient conditions and some modes of air/fuel ratio modulation conditions did the aged catalyst show a deteriorated performance. The change in surface structure in the aged catalyst can be found in scanning electronic microscopic (SEM) pictures, see Appendix C.

7.5.1 Experimental results

The flow reactor setup was used to quantify the aging effects on conversion efficiency for the aged catalysts (50k and 150k catalysts). With the decoupled flow and temperature control, it is now feasible to differentiate the difference in performance. As shown above, after the catalyst is fully warmed up, the reduction processes are diffusion controlled. This explains the fact that the even the aged catalysts can perform fairly well, the reason being the monolith is simply long enough, so that the overall catalysis reduction is large.

Same experiments with CO or H2 reacting with NO were carried out to assess the aging effects. With aged catalyst, the active catalyst sites have been reduced. This is either caused by physical abrasion, sintering or chemical bonds formed with some poisonous species (refer to Chapter 2). Thus the catalyst loses part of its effective surface area when it is getting aged. Notice in Eqn. 7.7, the slope of $\frac{d\ln C}{\left(\frac{D\cdot dx}{u}\right)}$ is a function of

$\frac{P \cdot (Sh \cdot \xi)}{A \cdot D_h}$, where ξ is a parameter introduced to signify the available percentage of effective surface area. Or, when Sherwood number and ξ are put together, (Sh ξ) is called the *Effective Sherwood Number*. As we know, Sherwood number is a dimensionless number that directly decides the mass transfer coefficient. So from the experimental data, we can calibrate the 1-D mass transfer model in order to calculate the *Effective Sherwood Number*. Thus, the effective surface area can be quantified.

For a fully developed laminar internal flow in a duct, the Sherwood numbers are well defined. For example, such a flow inside a square shaped duct has the theoretical Sh equal 2.98; for triangular a duct, Sh = 2.4 [47].

Fig. 7-21 and 7-22 show the NO reduction curves in excess of CO as a function of ($xT^{1.8}/v$) in all 3 catalysts (4k, 50k, and 150k). Shown in Fig. 7-20 are the data for the reactor with catalyst elements from the front of the original front bricks. These elements have square cells at 400 CPSI. Shown in Fig. 7-21 are data for the reactor with catalyst element from the front of the original rear bricks. These elements have triangular cells at 300 CPSI.

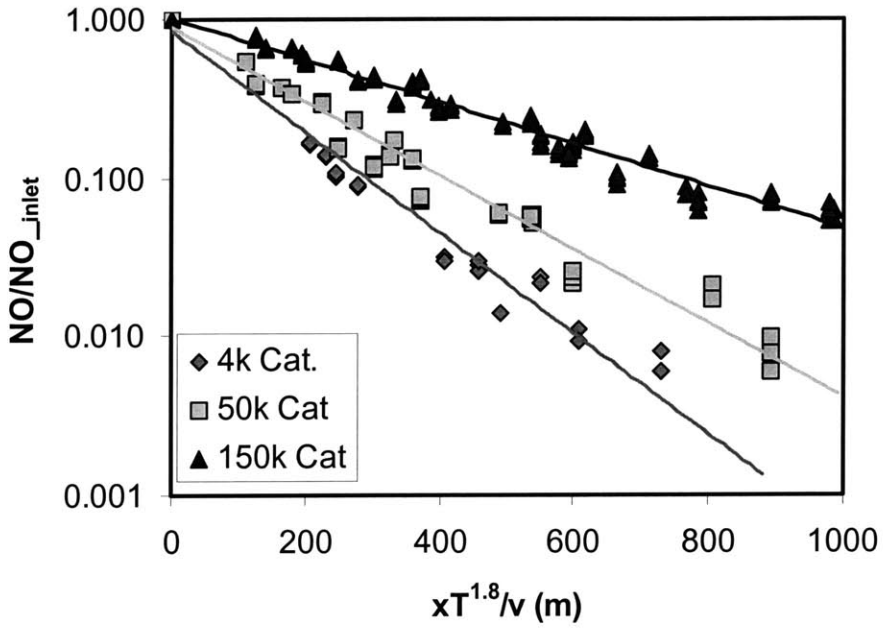

Fig 7-21, NO reduction as function of ($xT^{1.8}/v$) for all 3 catalysts at different levels of aging. Bricks with square cells, from the front of original front bricks.

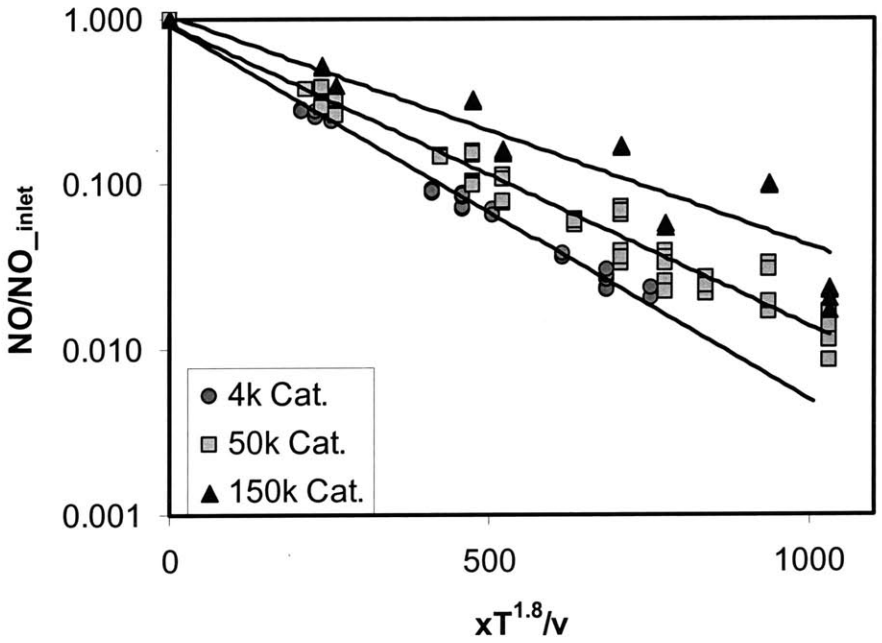

Fig 7-22, NO reduction as function of ($xT^{1.8}/v$) for all 3 catalysts at different levels of aging. Bricks with triangular cells, from the front of original rear bricks.

7.5.2 Observations and discussions

7.5.2.1. Loss of active surface area as a function of aging

Then from the experimental data we can calculate the effective Sherwood number ($Sh\ \xi$). And based upon the theoretical Sh, ξ can be calculated, and are plotted in Fig. 7-23 (The numbers are normalized against the 4k catalyst. For the 4k catalyst, the values of ($Sh\ \xi$) for the front and rear bricks are 3.01 and 2.41 respectively. Within experimental error, these values are equal to the theoretical limits of 2.98 for square ducts and 2.40 for triangular ducts.). Square marks are for bricks sampled from the very front of the front bricks; and the triangular marks are for the samples from the front of the rear bricks.

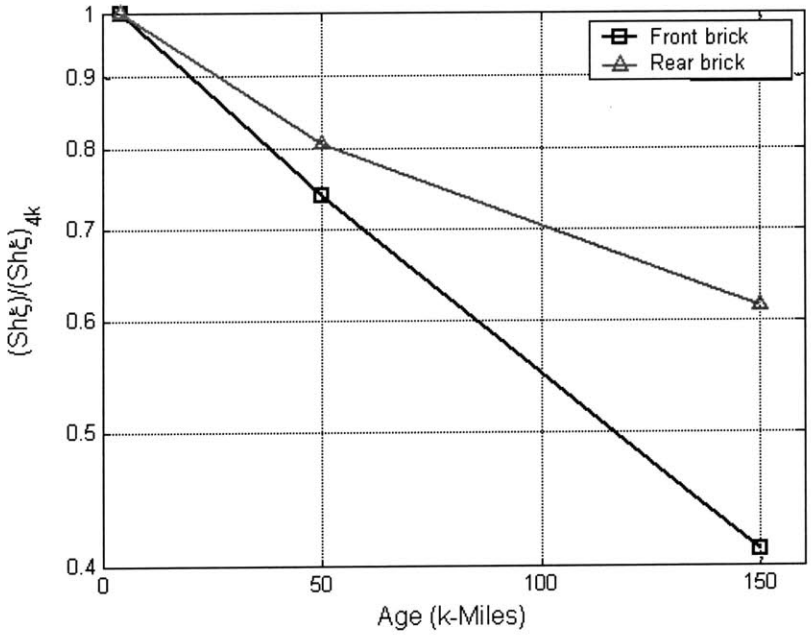

Fig. 7-23, Normalized Effective Sherwood Numbers for front and rear bricks (downsized bricks from the front of the original bricks); slope for front brick ~ 157 kMiles^{-1}

Notice that the plots are on a semi-logarithm scale. The values for the front brick are very close to an exponential trend. This exponential trend in loss of active surface area is in agreement with the results reported in [48] as shown in Fig. 7-24, although the

slope (= (157 kMiles)$^{-1}$) is almost three times less. The difference may be due to the fact that the catalysts used in this experiment were aged on a dynamometer rather than on a vehicle.

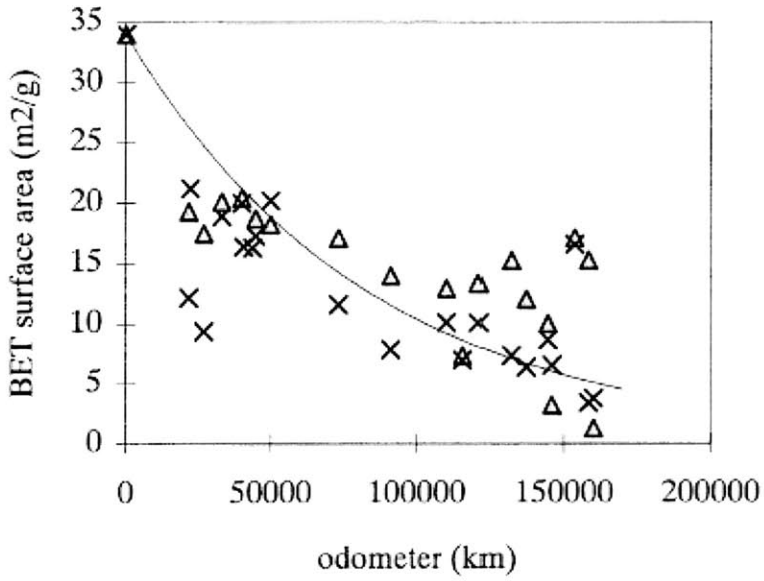

Fig. 7-24, Surface area loss as a function of mileage reported in SAE 2001-01-3691
×-front of brick, D- mid-brick, trend line – front of brick;
trend line was fit to exponential decay with characteristic age of 83000kM (51.5 kMiles)

7.5.2.2. Profiles of aging effects along the monolith

It is obvious that the two curves in Fig. 7-23 do not align with each other, which means the rear bricks are less aged than the front ones even though they are from the same catalyst. So further experiments were carried out with samples of monoliths from different locations of the bricks. Fig. 7-25 shows the more detailed measurements of the effective Sherwood numbers for bricks sampled from different locations of the catalyst bricks. Fig. 7-25 shows the measurements of 4K and 50K catalysts, with each curve representing one brick (monolith) from the original catalyst. It can be seen from the plot

that the 4K-mile catalyst does not show any aging effects no matter where the bricks were sampled.

At the same time, the curves for the bricks from the 50K-mile catalyst show some interesting trends in loss of active surface area. The general trends are the front brick shows more variation than the rear brick. And the front part of the front brick has lost the most effectiveness. The cause of this trend can be two-fold, thermal effect and poisonous effect.

1. Thermal effect

The front part of the catalyst is constantly working at higher temperatures than the real part. This results in the front part being more aged than the rear part.

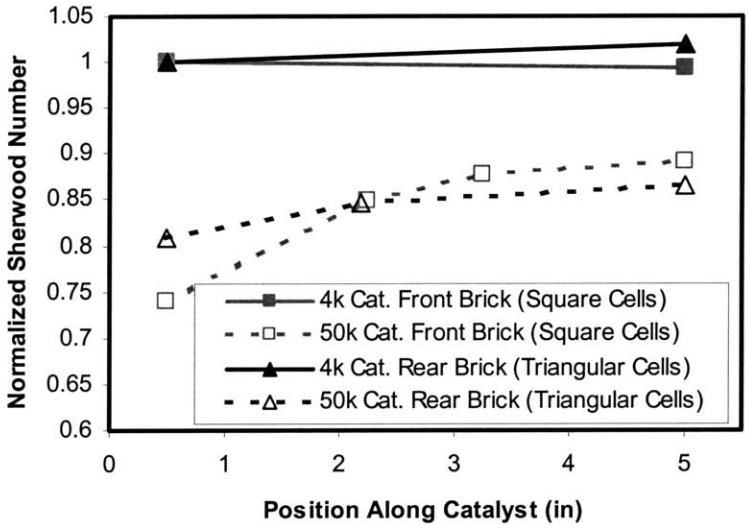

Fig. 7-25, Normalized effective Sherwood numbers for samples from different locations of the bricks

A justification of the hypothesis is the in-catalyst temperature sampling shown in Fig. 7-26. In Fig. 7-26, there are 6 data points: the 1st is the inlet temperature; 2nd and 3rd are the points inside the front brick; 4th is the gap between the front and the rear bricks (there is substantial heat loss from this gap); 5th and 6th are points inside the rear brick.

We can see that the front brick has undergone a more severe thermal aging than the rear brick. Hence this is qualitatively in agreement with Fig. 7-25 that the front bricks are more aged than the rear bricks.

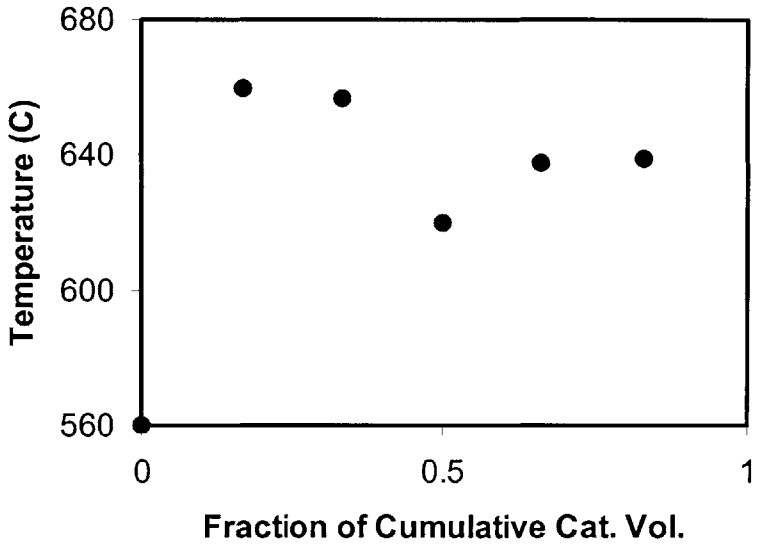

Fig. 7-26, In-catalyst temperature sample, 1st point is inlet temperature; 2nd and 3rd are in the front brick; 4th is a point in the gap between front and rear bricks; 5th and 6th are in rear brick.

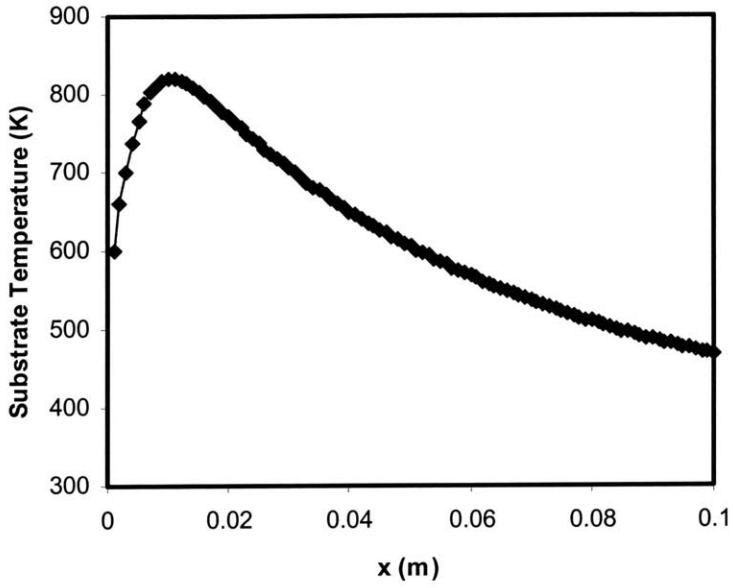

Fig. 7-27, Simulated temperature profile along a catalyst monolith

The simulation (will be discussed in Chapter 8) of temperature profiles along the monolith show fairly similar trend, which is the front part is working at a higher temperature than the rear part.

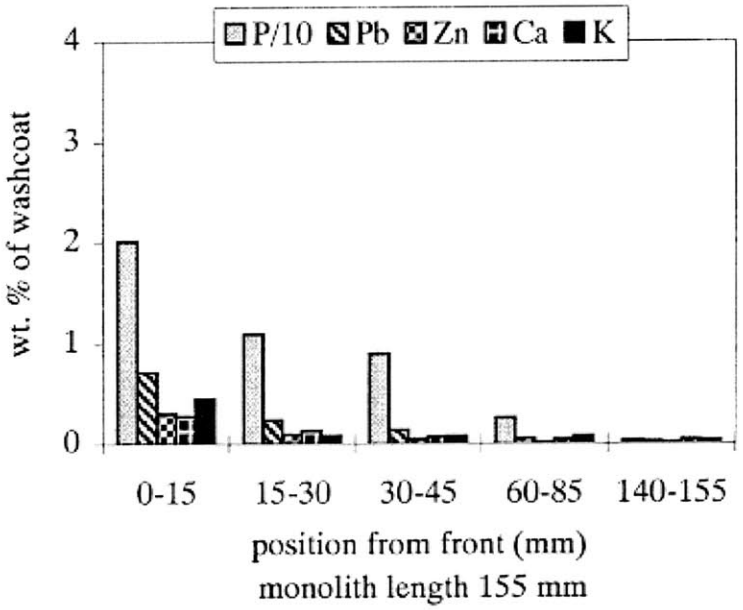

Fig. 7-28, Monolith contamination profile (aged for 40,000 kM), SAE 2001-01-3691

2. Poison effect

The work presented in [48] has shown the contamination profile along an aged (40,000 kM) monolith. Again, the trends are in agreement with what has been observed in our experiments. The front part of the brick is deposited with substantially more contaminations than the rear. The major contaminations include phosphorous, lead and zinc, etc.

7.5.2.3. Discussion

Measurements of aging effects on the front of catalysts show that the effectiveness at a fixed location within the catalyst decreases exponentially with the catalyst age. The measurements of aging effects at different locations along the catalyst monoliths show that the degradations in the front brick are more severe than those in the rear brick. Within each brick the front part is more aged than the rear part (the variation is large in the front bricks). The variation of effectiveness is not linear along the catalyst; the loss is substantially more in the very front of the bricks. The observation is consistent with contaminants analysis results reported in the literature.

The cause of such a phenomena is two-fold. Both the thermal effect and poison effect are contributing to the loss of active surface area, hence effectiveness of the catalyst. Qualitatively, the trend in loss of effectiveness is consistent with the temperature profiles and the contamination profiles.

Chapter 8

Three-Way Catalytic Converter Modeling

The experimental results in Chapter 7 have shown that, after the three-way catalyst is fully warmed up, the reduction rate of species is indeed limited by the diffusion rate of the "slowest" species (the species with lowest diffusion coefficient). This conclusion implies that with a relatively simple numerical model the catalyst behavior can be fairly well estimated, at temperatures above the light-off temperature.

A numerical model of the three-way catalyst is of essential importance, because only with a physical model can the emissions during transients (e.g. during air/fuel ration excursions).

8.1 Overview of catalyst modeling

Catalyst modeling is not something new. It actually has been in existence since the very first applications of monolithic converters on automobiles. Before discussing the model design in this project, we first take a look at what has been done in this area.

8.1.1 A brief review of previous work on catalyst modeling

The 1970's saw some of the earliest modeling works on monolithic converters. The most pioneering works include the two-dimensional model by Young and Finlayson published in 1976, one-dimensional model by Heck et al in 1976 and the work by Lee and Aris in 1977, etc. [49-51].

The characteristics in common of these early works are that they emphasized mathematically how a numerical model is feasible and how the differential equations can be solved. They showed that a monolithic converter could be modeled numerically. But they also have some limitations with them. For example, almost all of the early models assumed adiabatic boundary conditions and steady state operations. Also, the early monolithic converters were oxidation catalysts, so the reactions schemes are simple compared to today's modern technology three-way catalysts.

Some of the early modeling works based on oxidizing catalysts include the work by Otto and LeGray in 1980, and the work by Oh and Cavendish in 1982 [52, 53]. These works have some characteristics in common that include adiabatic boundary conditions, no accumulation of species on surface[1], only CO, HC and H2 oxidation by O2 is taken into account, etc. One thing needs to point out is the rates of internal diffusion are lumped together with kinetics. This approach proves to be a very practical simplification and is widely adopted in later research works. The kinetics data used are based on the research of Volts et al. in 1973 [54].

More recently, modeling works on three-way catalysts emerged. Some of the representative ones include the work by Siemund et al. in 1996, which is by and large based on previous works on oxidation catalysts by adding the reaction between CO and NO [55]. Then, Pattas et al. and Koltsakis et al. in 1994 and 1997 respectively, made the modeling on reaction schemes more complete by taking into account steam reforming reactions and oxygen storage capability [56, 57]. All these models are one-dimensional,

[1] Accumulation of species on surface is essentially the time-derivative terms of species on the surface. By neglecting these terms, it is assumed that at any given instant, the concentrations of species at the surface are at equilibrium, given chemistry being several orders of magnitude faster than mass transfer. This makes it much easier to solve the model. However, during fast transients, this is not a legitimate assumption to make. This issue will be addressed in more details in Section 8.2 Model design.

and lump internal diffusion with kinetics. And the kinetics data are almost all based on the research of Volts et al. in 1973 [54]. This is because that it takes tremendous amount of effort to get a complete set of kinetics data; and the kinetics data is dependant on specific precious metal in question also its loading etc. There is no easy ways to measure the kinetics of a specific catalyst. Thus over the years, the modeling of the monolithic converters has not changed substantially, rather it is being slowly improved with new schemes included.

Efforts to come up with a very detailed modeling of the processes going on inside a catalyst have been made, such as Gottberg et al. in 2000 and Pauwels et al. in 2003. But they faced the same challenge of lack of complete and reliable kinetics data [58, 20].

Even though the models are limited by the availability of kinetics data, over the years of application, it has been proved that with some of the well developed kinetics data and careful calibration, the numerical models can give developers an estimation of the tail-pipe emissions within reasonably good ranges.

8.1.2 Characteristics of modeling in this work

Previous works done by other researchers on catalyst modeling all have one thing in common that the structure of the model is always energy/mass balance of gas phase and energy/mass balance in solid phase. Only thing that can be slightly different is the accumulation of species on surface term. Some people drop the term for sake of easiness, some do not. One reason for dropping the term is based on the assumption of chemistry is so fast, at any given time, the reactions have already reached equilibrium.

In the past three decades, the modeling has not changed very much in terms of approach and structure. Newer models improve by adding new reaction schemes or calibrating kinetics data on specific precious metals and loadings (e.g. oxidizing cat became three-way cat, then gas shift reaction was added, then steam reforming was added, then oxygen storage etc.); there have not yet been any substantial changes.

On the other hand, as far as kinetics data is concerned, a lot of the papers have mentioned the lack of reliable kinetics data is the biggest barrier preventing the modeling work from being developed; or keep researchers from building more comprehensive models. The majority of authors adopted the format and kinetics data that were published 30 years ago, which were calibrated on very different technology catalysts, under very much different operating conditions. And the models are still in fairly good agreements with experiments. Some researchers have made small adjustments to the kinetics, when maintaining the format or kinetics. To make life simple, almost all of the work kept their reaction rate in the form of *Lagmuir-Hinshelwood* formats. So that with simple experiments the parameters in the reaction rates can be calibrated.

With one-dimensional models, it is very hard to model internal diffusion. So lumping internal diffusions with kinetics seems to be a fairly straightforward approach, and is justified by multiple works.

8.2 Model design

In this project, modeling of the three-way catalyst is not the main goal. The purpose of the modeling work is more to help explain the phenomena observed in the experiments, and to support some of the hypothesis when interpreting the experimental

data. So instead of trying to come up with very detailed and original modeling, the efforts are rather trying to make use of whatever that is available. For example, in order to get the exhaust gas compositions, the model uses commercialized packages (such as Equil®, Wave®, etc.) and experimental data when available. And in terms of kinetics data, some of the widely accepted data are used. Oxygen storage model is calibrated with experimental data (refer to Chapter 4). Aging effects are based on experimental data in chapter 7.

The partial differential equations (PDE) are solved by programming in the integrated development environment (IDE) of Jacobian®. Jacobian® is a commercialized PDE solving package with fairly friendly user interface. It has its own unique programming language to setup the PDE's and to interface with the input/output.

So it can be seen that the model is not developed from scratch, rather it sort of puts things that are available together.

8.2.1 Model structure

The structure of the model is shown in Fig. 8-1. The model is divided into two main parts: engine and catalyst. The engine model serves to provide the "exhaust gas" to the catalyst model. As stated above, the engine model is adopted from commercialized software's and experimental data. Essentially, the engine model provides the flow pattern (flow rate, temperature, etc.) and exhaust compositions (air/fuel ratio, concentrations of species, etc.). And the catalyst model is basically a PDE system. And the major component of the catalyst model is the PDE solver. In between the engine and catalyst

models is an interface that interprets the exhaust information into boundary conditions (B.C.) and initial conditions (I.C.) to the PDE system.

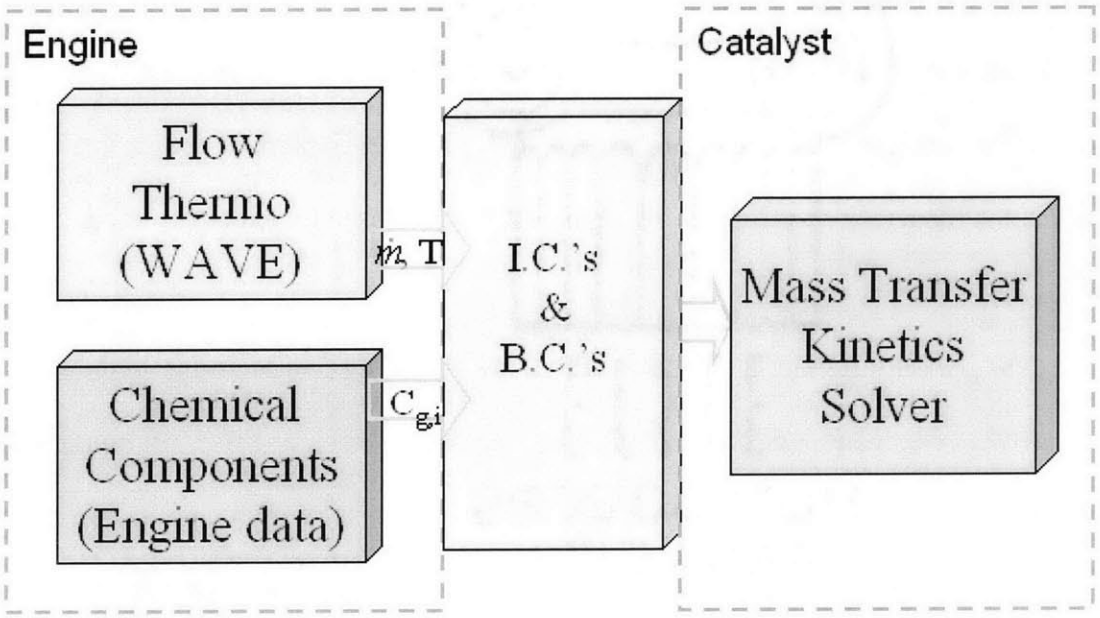

Fig. 8-1, Structure of catalyst model

Since the catalyst model is one-dimensional, one cell can be representative of the whole catalyst. In the model, each cell is divided into two zones, bulk flow and solid surface. Fig. 8-2, 8-3 show the schematics of mass and energy balance in these two zones.

As shown in Fig. 8-2, in the bulk flow, there are species convection along side the cell, and diffusion from the flow onto the surface. Also, on the surface there is species consumptions, whose rates are controlled by the kinetics. Diffusions in the longitude direction are neglected in both the bulk flow and on the surface, since convection is dominant (with linear velocity v >> D/L).

From the schematic, equations can be written as:

$$\varepsilon \cdot \frac{dc_{g,i}}{dt} = -u \cdot \frac{dc_{g,i}}{dx} - h_{m,i} \cdot \frac{P}{A} \cdot \left(c_{g,i} - c_{s,i}\right) \tag{8.1}$$

$$\varepsilon_s \cdot (1-\varepsilon) \cdot \frac{dc_{s,i}}{dt} = h_{m,i} \cdot \frac{P}{A} \cdot \left(c_{g,i} - c_{s,i}\right) - \varepsilon_s \cdot (1-\varepsilon) \cdot \sum_{j=1}^{M} R_j\left(c_{s,1..N}, T_s\right) \tag{8.2}$$

Where, ε and ε_s are the void fraction of the cells and the surface; $c_{g,i}$ and $c_{s,i}$ are the concentration of species i in the bulk and on the surface; u is the linear velocity; $h_{m,i}$ is the mass transfer coefficient of species i; P and A are the perimeter and cross-section area of the cell respectively; and R_j is the reaction rate of reaction j.

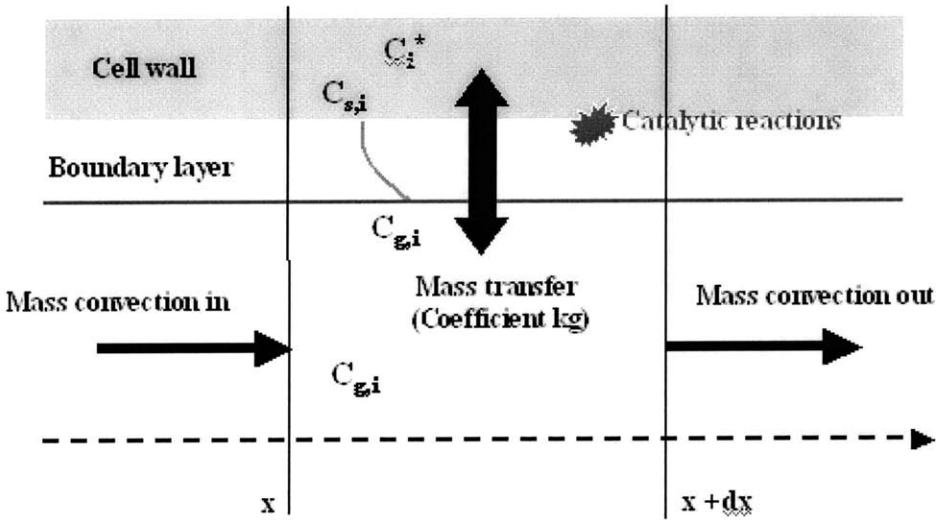

Fig. 8-2, Schematic of mass conservation within each cell

Similarly to the mass conservation, energy conservation in the cell is shown in Fig. 8-3. In the bulk flow, there is heat flux along the cell, and forced convection between the bulk and the solid wall. On the solid surface, heat is being conducted along the wall;

also heat is being generated with the reactions; lastly heat loss to the ambient is also taken into account.

PDE's of energy balance can be written as:

$$\varepsilon \cdot \rho_g \cdot C_{pg} \cdot \frac{dT_g}{dt} = -\rho_g \cdot u \cdot C_{pg} \cdot \frac{dT_g}{dx} - h_{gs} \cdot \frac{P}{A} \cdot (T_g - T_s) \tag{8.3}$$

$$(1-\varepsilon) \cdot \rho_s \cdot C_{ps} \cdot \frac{dT_s}{dt} = k_s \cdot (1-\varepsilon) \cdot \frac{d^2 T_s}{dx^2} + h_{gs} \cdot \frac{P}{A} \cdot (T_g - T_s) - h_{amb} \cdot \frac{P_{amb}}{A} \cdot (T_s - T_{amb}) + \dot{q}_{reaction} \tag{8.4}$$

Where, r_g and r_s are the density of gas in the bulk flow and on the surface; T_g and T_s are the temperatures of gas and surface; C_{pg} and C_{ps} are the heat capacity of gas in the bulk flow and on the surface; $q_{reaction}$ is the heat generation on the surface; and all other variables being the same as above.

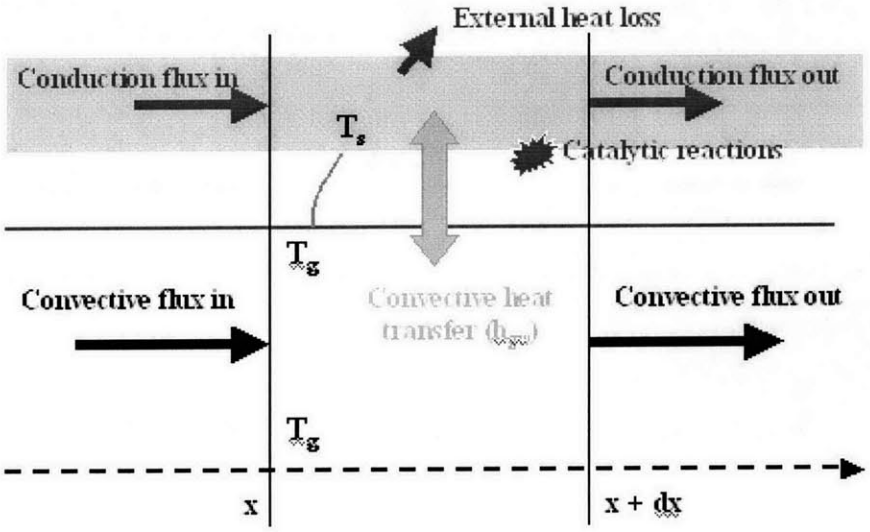

Fig. 8-3, Schematic of energy conservation within each cell

8.2.2 Reaction schemes

In the model, the basic reaction schemes are included. These reactions are considered the major reactions going on in a three-way catalyst. The most important reactions include the oxidation of CO,HC and H2, reduction of NO and O2, and some other reactions such as water-gas-shift reaction and oxygen storage and release, etc.

The reactions can also be categorized as follows.

Oxidation by O2:

$$H_2 + \tfrac{1}{2} O_2 \rightarrow H_2O \quad (8.5)$$

$$CO + \tfrac{1}{2} O_2 \rightarrow CO_2 \quad (8.6)$$

$$C_3H_6 + 4\tfrac{1}{2} O_2 \rightarrow 3CO_2 + 3H_2O \quad (8.7)$$

$$CH_4 + 2O_2 \rightarrow CO_2 + 2H_2O \quad (8.8)$$

Oxidation by NO:

$$H_2 + NO \rightarrow H_2O + \tfrac{1}{2} N_2 \quad (8.9)$$

$$CO + NO \rightarrow CO_2 + \tfrac{1}{2} N_2 \quad (8.10)$$

$$C_3H_6 + 9NO \rightarrow 3CO_2 + 3H_2O + 4\tfrac{1}{2} N_2 \quad (8.11)$$

$$CH_4 + 4NO \rightarrow CO_2 + 2H_2O + 2N_2 \quad (8.12)$$

Water-gas-shift reaction:

$$CO + H_2O \rightarrow CO_2 + H_2 \quad (8.13)$$

Oxygen storage related:

$$(Ce_2O_3)_2 + O_2 \leftrightarrow (CeO_2)_4 \quad (8.14)$$

$$(CeO_2)_2 + H_2 \rightarrow Ce_2O_3 + H_2O \quad (8.15)$$

$$(CeO_2)_2 + CO \rightarrow Ce_2O_3 + CO_2 \quad (8.16)$$

Reducing species attaching to PGM sites:

$$H2 + 2S \leftrightarrow 2H^* \tag{8.17}$$

$$CO + S \leftrightarrow CO^* \tag{8.18}$$

The reaction rates of the equations are expressed in *Lagmuir-Hinshelwood* formats. And for the easiness of calculation and calibration, almost all previous works assumed first order reaction. Thus, the reaction rate is simply:

$$R_{a,b} = k_{a,b}\,[a]\,[b]\,G^{-1} \tag{8.19}$$

Where, $k_{a,b}$ is the rate constant for reaction between reactants a and b;

$[a]$, $[b]$ are the concentrations of a and b in k-mol/m^3;

G is the inhibition factor, which quantifies the competitions among reactants when adsorbing onto the catalyst surface.

$k_{a,b}$ is a function of temperature and activation energy of a particular reaction on a particular precious metal surface (refer to Chapter 3). Expression of $k_{a,b}$ is as follows:

$$k = k_0 \cdot \exp\left(-\frac{E}{RT}\right) \tag{8.20}$$

Where, k_0 is a constant,

E is the activation energy,

T is absolute temperature at which the reaction happens, in the model, T is the basically the surface temperature.

The kinetics data used in the model, as described above, are mainly from literature. They are widely used in previous modeling works. The only exception is the oxygen storage model. The kinetics data is derived from previous experimental results. The data is tabulated in Appendix D.

Note that the PGM loading and dispersion in the wash coat is not explicitly accounted for in the model. Thus these physical parameters are integrated into the kinetic rates.

8.2.3 Simulation results of different reaction schemes

The functions of the basic reaction schemes were tested with simplified simulation cases.

1. Simple scheme

Reactions of NO+CO, and NO+CO+H2 were tested on the model. The catalyst is simulated at constant temperature (800k) and flow rate (10m/s). In this particular case, the cells are square shaped with dimensions of 1mm. The overall environment was kept reducing with excess of CO.

Fig. 8-4 shows that the trends of NO and CO match with experiments very well. The slope of NO reduction works out to be limited by diffusion rate with the theoretical Sherwood number of 2.98. This proves that the model is working reasonably well under simple reaction schemes. And the trend of NO reduction matches with what has been observed in experiments as expected.

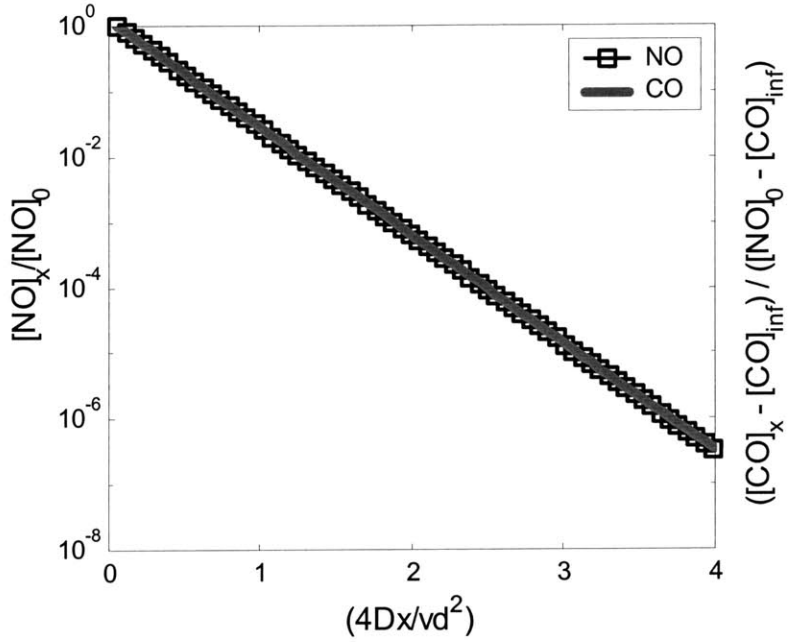

Fig. 8-4, Reaction between NO and CO at 800K and 10m/s flow rate

Fig. 8-5 shows the reaction with NO+CO+H2 at the same operations as in 8-4. The inlet CO and H2 concentrations are kept the same with overall environment kept reducing. Then the NO profile is the same as the case with the presence of CO alone. With the H2 addition, the CO, because of the competition with H2, is oxidized less. The relative levels of CO and H2 oxidation depends on the relative reaction rates. The results in Fig. 8-5 are consistent with the data shown in Fig. 7-13.

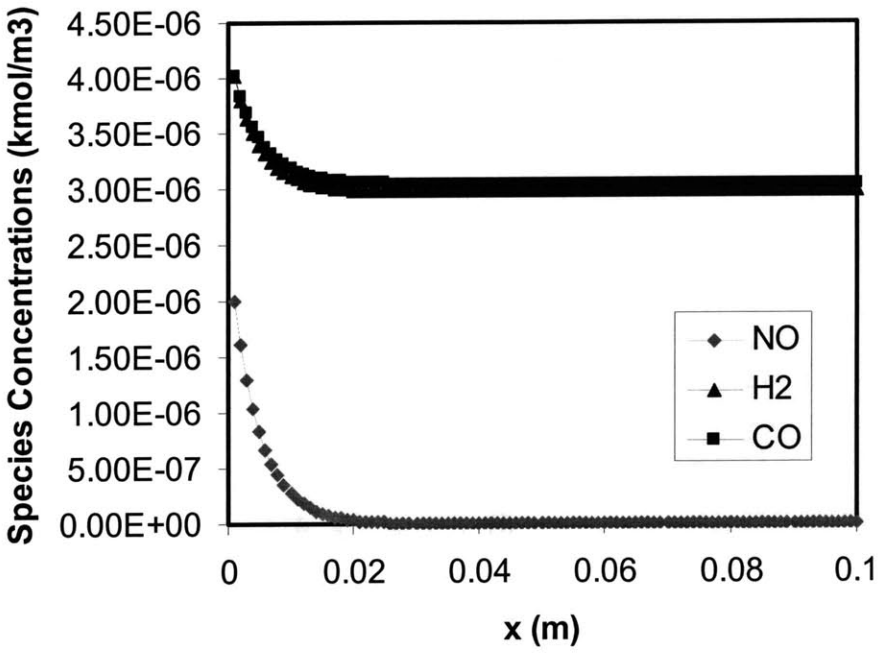

Fig. 8-5, Reaction with NO+CO+H2 at 800K and 10m/s flow rate

2. Complex schemes

Results of simple reaction schemes agree with experimental results on the flow reactor very well. The model is then tested with complex reaction schemes, which take into account all reactions other than water-gas-shift reaction and oxygen storage reactions.

The operation conditions are kept the same as in previous cases. Temperature is kept constant at 800k, flow speed at 10m/s.

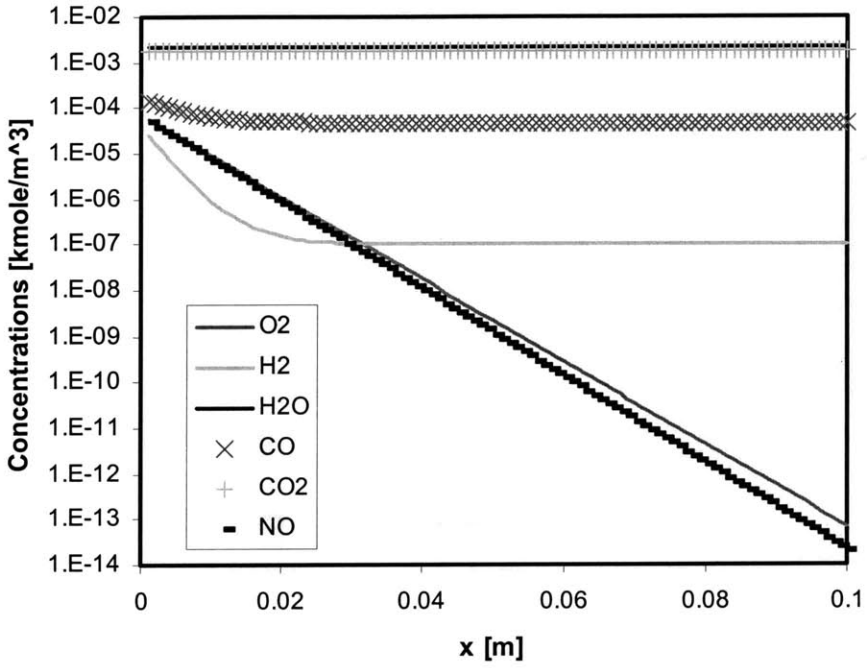
1.E-02
1.E-03
1.E-04
1.E-05
1.E-06
1.E-07
1.E-08
1.E-09
1.E-10
1.E-11
1.E-12
1.E-13
1.E-14
Concentrations [kmole/m^3]
O2
H2
H2O
CO
CO2
NO
0
0.02
0.04
0.06
0.08
0.1
x [m]

(a)

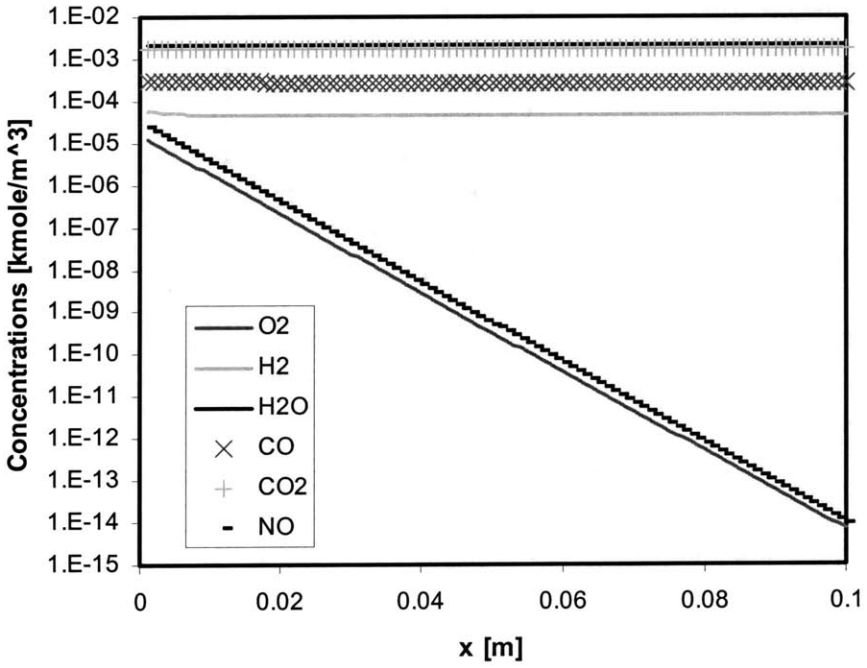
1.E-02
1.E-03
1.E-04
1.E-05
1.E-06
1.E-07
1.E-08
1.E-09
1.E-10
1.E-11
1.E-12
1.E-13
1.E-14
1.E-15
Concentrations [kmole/m^3]
O2
H2
H2O
CO
CO2
NO
0
0.02
0.04
0.06
0.08
0.1
x [m]

(b)

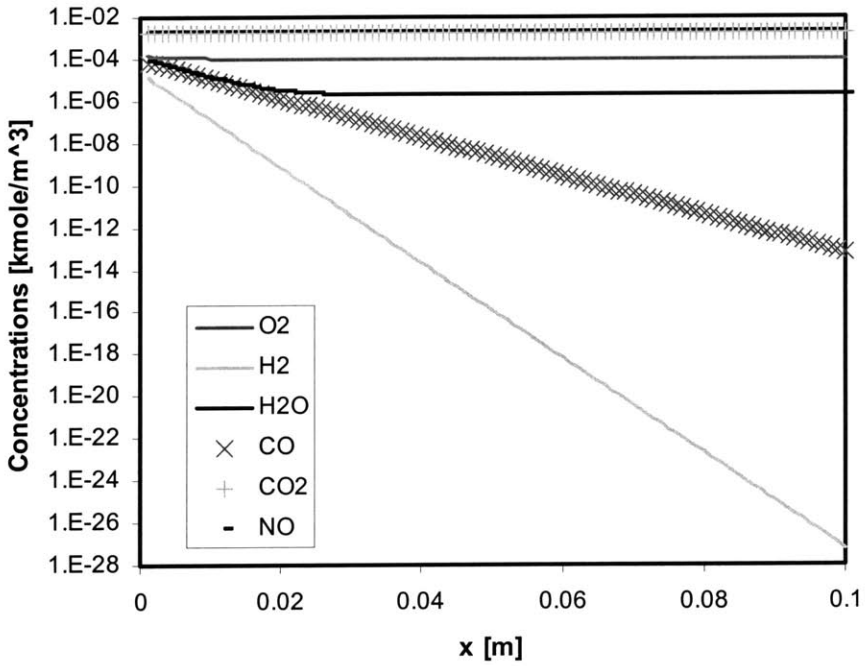

(c)

Fig. 8-6, Concentration of species with complex reaction scheme. Operation condition: 800K, 10m/s.
(a).λ=1; (b) λ=0.95; (c) λ=1.05;

Fig. 8-6 (a)-(c) show the cases when air/fuel ratio is stoichiometric, fuel rich and fuel lean respectively. As expected, when air/fuel ratio is stoichiometric, all pollutants are removed to very low levels when the exhaust gas reaches the exit of catalyst. And when it is fuel rich, there is more reducing species than needed, so at the catalyst exit, NO is reduced to very a low level (so is O2); whereas, there is substantial breakthrough of CO, HC and H2. When the air/fuel ratio fuel lean, there is excess of O2 in the exhaust gas, so CO, HC, H2 are at very low levels at the exit; NO and O2 will have substantial breakthrough.

It needs to be pointed out that in case (a), where λ=1, CO level at exit is not very realistic. This is because in reality, water-gas-shift reaction is also playing an important

role in reducing CO. In this example water-gas-shift reaction has been turned off. It is compared with the case when this reaction is turned on in (3).

3. Water-gas-shift reaction

As stated in (2) the CO level at exit is not very realistic, the reason being the water-gas-shift reaction is turned off. Fig. 8-7 shows the case when λ=1 and water-gas-shift reaction is taken into account. It can be seen that no only are NO, O2 levels very low at exit, CO level is much lower and more realistic. In this process, H2O is consumed by CO to form H2 and CO2 (can be seen from the figure).

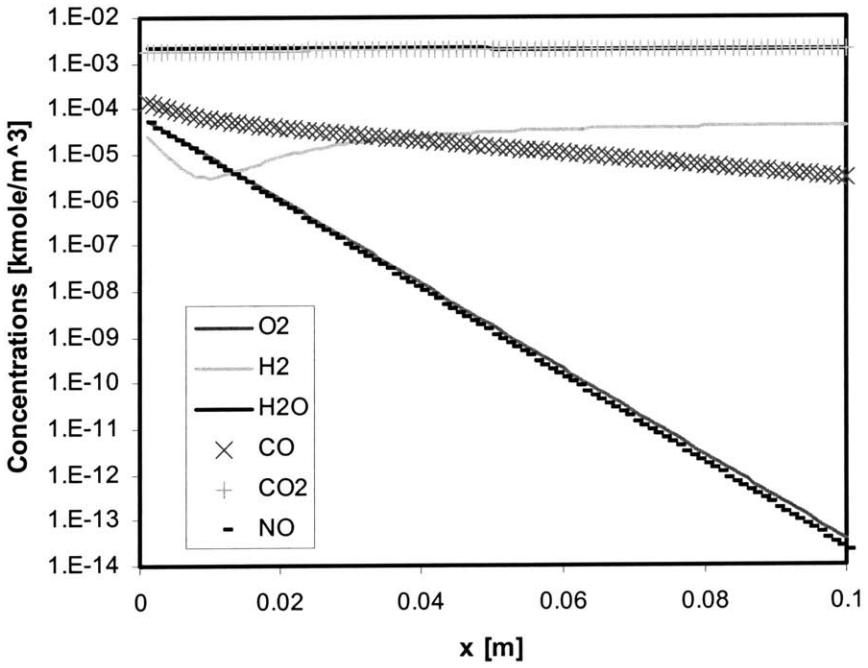

Fig. 8-7, Concentration of species with complex reaction scheme (water-gas-shift reaction included). Operation condition: 800K, 10m/s, λ=1.

4. Oxygen storage [57, 59]

The model has incorporated oxygen storage capacity. Reaction related to oxygen storage are listed in equations 8.14 – 8.16. When the exhaust gas is oxidizing (with excessive O2) the Ce2O3 can store O2 by reaction with it to form CeO2. Reaction 8.14 is reversible; it goes backwards at a different rate. When the exhaust gas is reducing (deficit of O2), the backwards reaction becomes dominant giving off O2 into the exhaust stream. This helps balance the air/fuel ratio to keep removal of pollutants at high efficiencies. Besides reaction 8.14, CeO2 can also directly oxidize H2 and CO (8.15, 8.16). These reactions become crucial when air/fuel ratio changes from lean to rich. Together with reaction 8.14, they help keep O2 concentration at the right level. To simulate the release of reducing species during rich-to-lean steps (t0-t1 in Fig. 4-1), reactions 8.17, 8.18 are also taken into account (detailed explanation is given in Section 4.1.1). These two reactions simulate the reducing species (H2 and CO) attaching onto PGM sites when the air/fuel ratio is rich; and can be released from the sites when the air/fuel ratio is lean.

Fig. 8-8 shows a simulation of the up- and down-stream λ during an air/fuel ratio step change from rich to lean (0.97 to 1.03). It shows that the down-stream λ changes in a pattern similar to what we have observed in experimental data. The down-stream λ will stay rich for a period of time, due to the effects of H2 and CO attachment to the active sites. Then the λ reaches 1; afterwards it gradually follows up with the up-stream λ value. Concentration of Ce2O3 is chosen based on oxygen storage experiments. From the OSC for fresh catalyst in Fig. 4-9, the amount of Ce2O3 in a catalyst can be estimated. The number is then divided by the volume of catalyst substrate, which yields the volumetric concentration of Ce2O3. 0.25 k-mole/m^3 is chosen for fresh catalyst in the simulations.

Fig. 8-8 shows a qualitative simulation, the parameters are fine tuned in later sections, which compares the simulation results with the experimental ones.

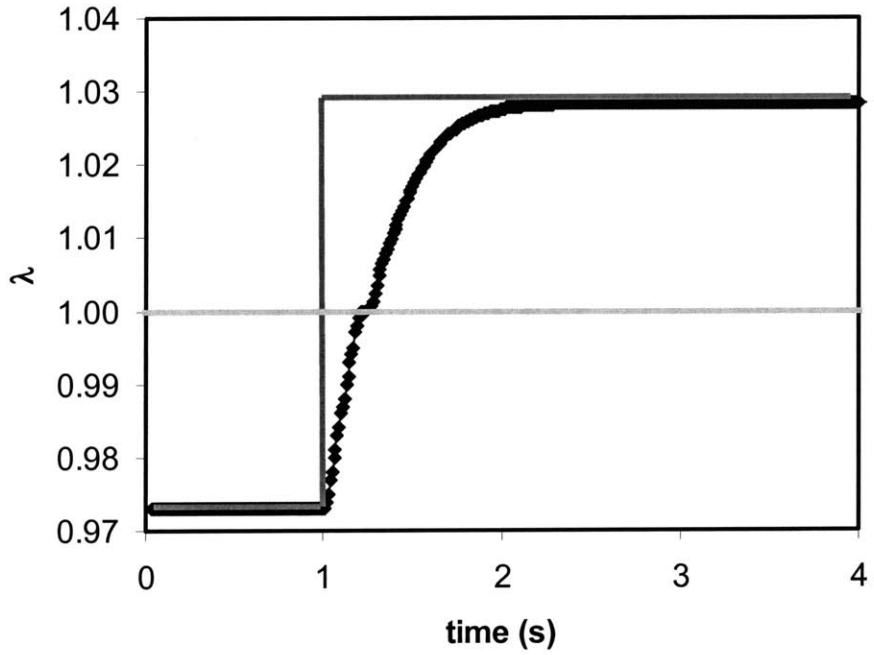

Fig. 8-8, Simulation of down-stream air/fuel ratio during a λ lean step.

5. Catalyst warm-up simulation

The model has the ability to simulate catalyst warming-up processes, even though this is not the main focus of this particular project. We assume everything is working at temperatures above the light-off temperature. But with the available kinetic rates catalyst behavior can be simulated during engine/catalyst warm-up.

During start-up process, i.e. when the engine is started, hot exhaust gas start coming into the catalyst to warm it up. When the catalyst is cold, the rate of chemical reactions is very low. But with the catalyst being heated up by the hot gas, reaction rates start to pick up speed; and this in return will help the warming-up process due to the heat

generation as a result of the reactions (most of the reactions involved are exothermal). So the catalyst light-off process is not simply a process of the monolith being passively heated up. Rather the process is sort of "auto-catalyzed".

Fig. 8-9 shows the case when the catalyst is simply heated with hot gas. The incoming hot gas is at a constant temperature of 600K (to simulate the exhaust temperature at engine start-up) and flow rate of 10m/s. The catalyst starts from room temperature (300K). The simulation can be easily done with all the reactions turned off.

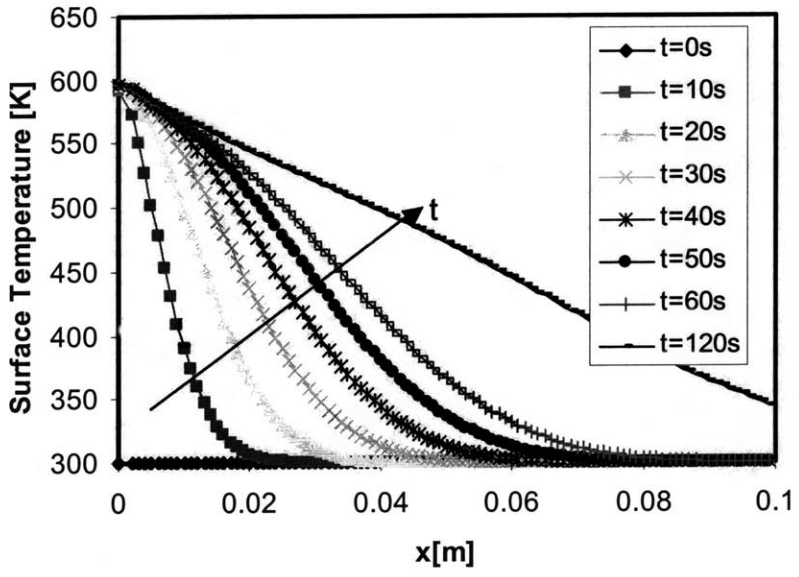

Fig. 8-9, Warming-up process by forced convection.

To compare with the above case, Fig. 8-10 shows the warming-up of catalyst when there is chemical reaction happening (all other conditions kept the same). It can be seen that the catalyst is warming up faster because of the heat release from oxidation of the feed gas.

Another way to look at the light-off process is to look at the conversion efficiency of CO. Conventionally, it is so defined that the temperature at which CO conversion efficiency reaches 50% is called the light-off temperature. So the change in CO conversion with time also shows the warming-up process. Fig. 8-11 shows the CO conversion with time. It should be noticed that the simulations are only showing the functions of the model. Specific initial and boundary conditions and calibrated kinetics data are needed to get more realistic results.

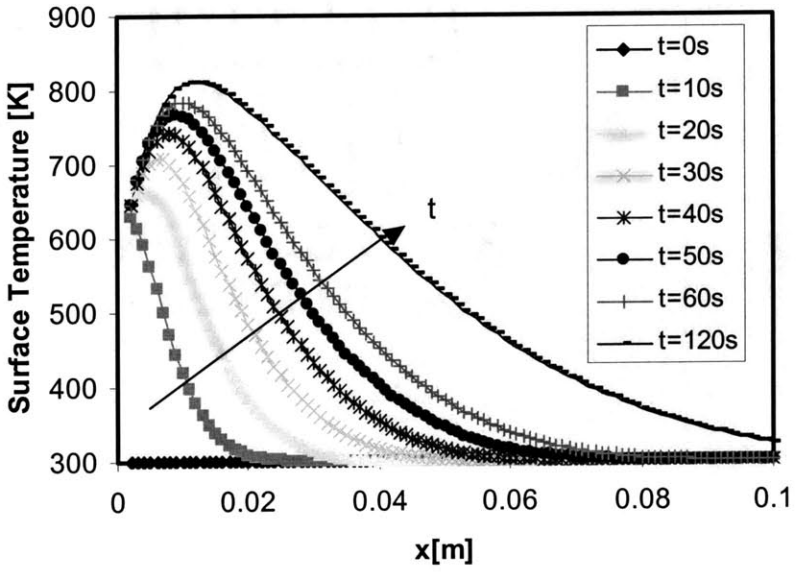

Fig. 8-10, Simulation of catalyst warming-up process

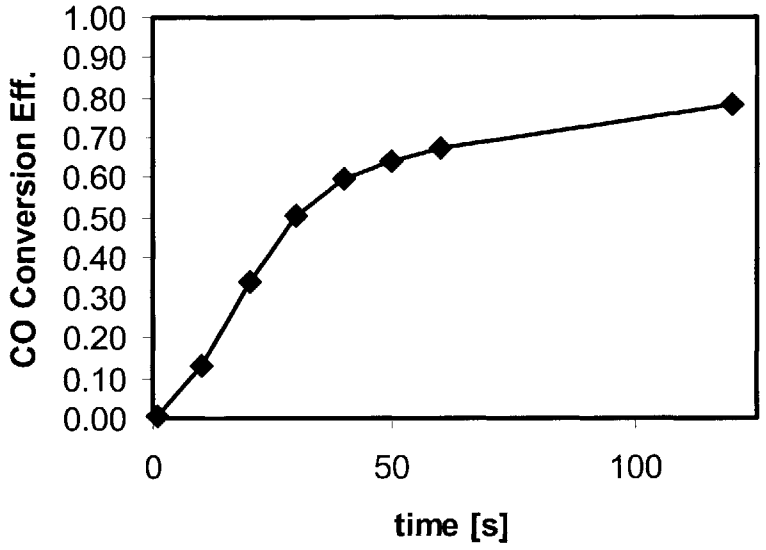

Fig. 8-11, CO conversion efficiency during catalyst light-off process

8.3 Air/fuel ratio modulation simulation

To further utilize the model, the NO breakthrough during different modes of air/fuel ratio modulation is calculated. In order to make the experiments and simulation comparable, measured flow rates, temperatures and air/fuel ratios are all fed into the model as boundary and input conditions. The experiments are described in Chapter 6. In the experiments, air/fuel ratio is oscillated in different modes (frequencies and amplitudes), with everything else kept constant. In the mean time, NO breakthrough along the catalyst is measured (refer to Fig's 6-4 to 6-16). Notice that in the experiments NOx data along the catalyst was not taken simultaneously. Rather they were taken at different times. Due to the limitation of hardware setup, only one location can be measured at a time.

8.3.1 Time-resolved results

In Fig. 8-12, 13 inlet air/fuel ratios are shown. In Fig. 8-12, the air/fuel ratio modulation is at 1Hz; with oscillation amplitude equals 2.5% of stoichiometric value[2]. Fig. 8-13 shows similar modulation; only the oscillation amplitudes are doubled to 5%[3].

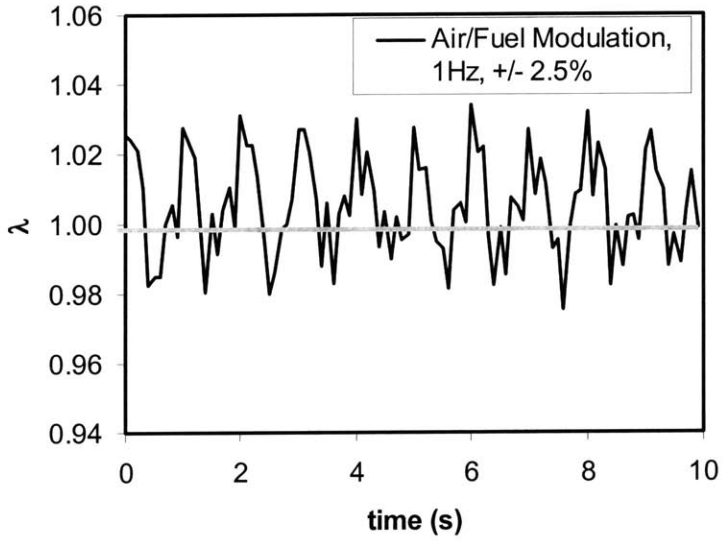

Fig. 8-12, Inlet λ measurement in customized air/fuel ratio modulation experiments. Frequency: 1Hz, Amplitude: +/- 2.5%

[2] The amplitude mentioned here is specified by the control signals, i.e., the fuel injection pulse width that corresponds to the specific modulation amplitudes (2.5%, 5.0%, etc.). Notice that the amplitudes are not slightly lower than the fuel-injection-specified values. This is because of the mixing effects in the engine and the measurement errors built-in the λ sensor. The 2.5% λ values (in Fig. 8-12) are slightly biased towards lean side of stoichiometric. This is due to measurement errors. But for comparison between the experiments and simulation, it should serve its purpose.

[3] Same as 2.

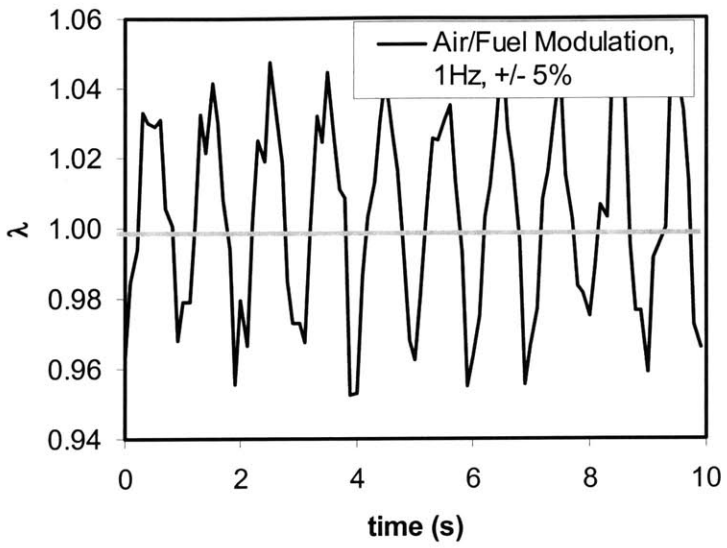

Fig. 8-13, Inlet λ measurement in customized air/fuel ratio modulation experiments. Frequency: 1Hz, Amplitude: +/-5.0%

Fig. 8-14 and 8-15 show the NO concentrations along the catalyst. The time-resolved simulation results have the same features as experimental ones. The NO concentration modulates with the same frequency as the air/fuel ratio oscillates. And with the gas going along the catalyst, the NO concentration diminishes. The explanation of the phenomena is described in Chapter 6. Fig. 8-16 shows the case when there is no oxygen storage capacity in the catalyst. It can be seen that NO will not be reduced during the lean parts of the modulation. This is in agreement with previous interpretation as well. The fact that the simulations results agree with the experiments is a good support of the hypothesis proposed in previous chapters. So qualitatively, the model is doing a good job in estimating NO breakthroughs during air/fuel ratio modulations.

Notice in Fig. 8-14 and 8-15 only the qualitative trends are shown. More detailed and quantitative comparisons will be made in the next section.

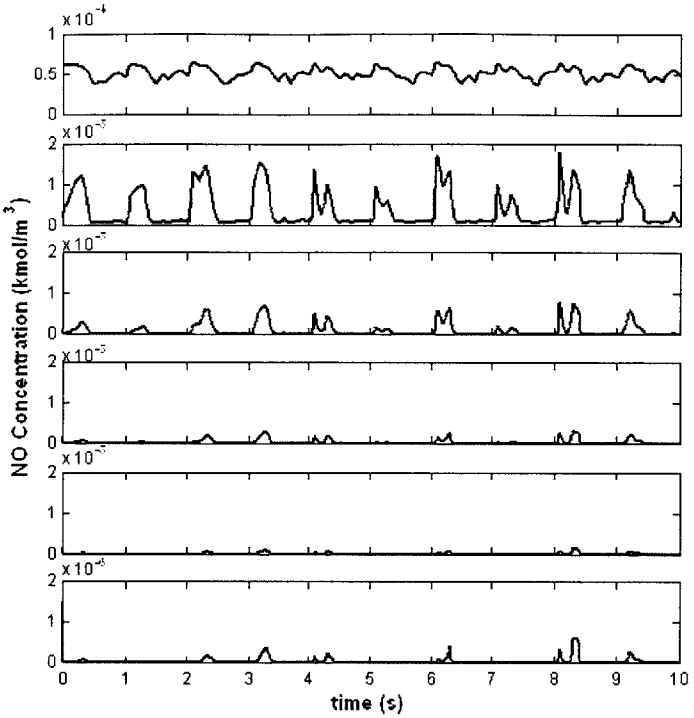

Fig. 8-14, NO breakthrough along the catalyst, during 1hz, 2.5% modulation

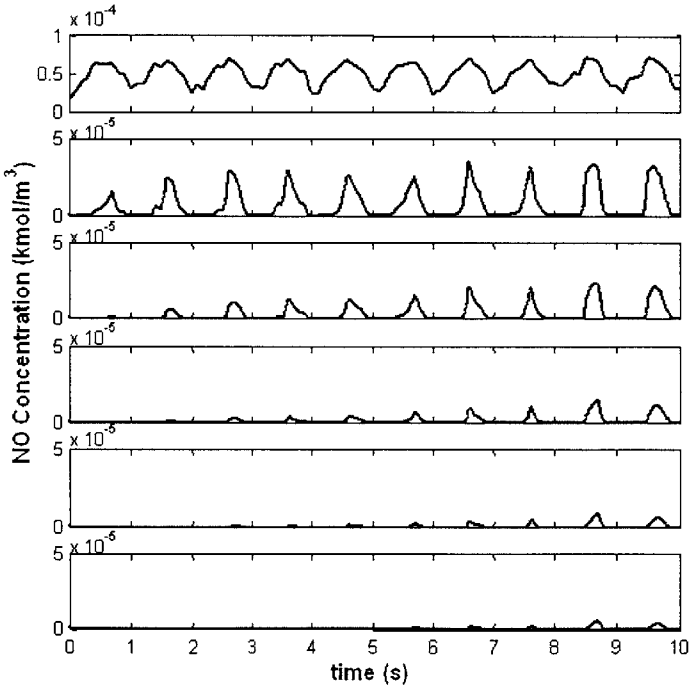

Fig. 8-15, NO breakthrough along the catalyst, during 1hz, 5.0% modulation

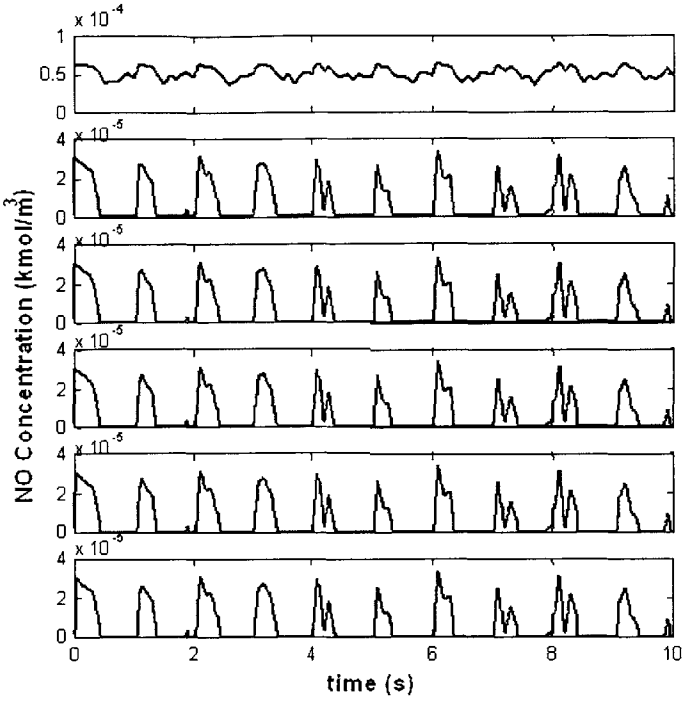

Fig. 8-16, NO breakthrough along the catalyst, during 1hz, 2.5% modulation (without oxygen storage capacity)

8.3.2 Time-averaged results

In order to better quantify the estimations made by the model, time-averaged results are compared. As shown in Fig.'s 6-7 through 6-16, the experimental data for each sampling location are averaged over time. Similar graphs are generated with time-averaged simulation results, as shown in Fig.'s 8-17 to 8-20.

Fig. 8-17 through 8-19 are the comparison on the fresh catalyst. Since it is a fresh catalyst, there is no aging effect in the simulation. And the oxygen storage capacity is derived from previous experimental data and the OSC model in Chapter 4. For fresh catalyst, Ce atom concentration of 0.50 k-mole/m^3 is used, with 90% of the sites being vacant at starting point of simulation. In Fig. 8-17 to 8-19 the experiment and simulation

on the 4k catalyst are compared. One particular mode of modulation is compared in each case. They are 5Hz, 1Hz and 0.3Hz respectively; and amplitude of modulation is kept at ±3% in all cases.

Fig. 8-20 is the comparison of experiment and simulation on the 150k catalyst. This particular case is for air/fuel ratio modulations at 1hz, ±3% amplitude. To simulate the aging effects, both the oxygen storage capacity and loss of effective surface area are taken into account. In simulating the oxygen storage capacity of the 150k-mile catalyst, 0.16 k-mole/m^3 of Ce atom concentration is used (approximately 1/3 that of the fresh catalyst), with 90% of the sites being vacant when simulations started, according to Fig. 4-9. And the loss of effective surface area is simulated by changing the effective surface area factor (ξ) in Equations 7.5 and 7.6. The effective surface area factor for 150k catalyst is set at 0.41 based on Fig. 7-23[4].

It can be concluded that the model does reasonably well in estimating NO breakthroughs along the catalyst at different modes of air/fuel ratio modulations. Especially it has shown the dynamic effects during transient operations, and supported the previous interpretation of data.

There are a couple of points that need to be clarified in interpreting the comparison between the model and experiments:

1). The model can be better tuned to match the data even better. But as mentioned above, the data used is not an absolute standard. There is some inconsistency in the data

[4] Note that according the discussion on aging effects in Section 7.5.2, the loss of effectiveness along the catalyst is not uniform or linear. So the loss of surface area for the front end of the brick tends to over estimate the aging effects. Thus this partially explains why the simulation tends to over estimate NO breakthrough during air/fuel ratio modulation in Fig. 8-20.

itself. This is why we did not spend too much time fine-tuning the model parameters to make them match "perfectly".

2). Parameters such as temperatures and aging effects etc. along the catalyst are put as constants in the model for the sake of simplicity. The number for the front end of the aged catalyst was used, this explains why the model tends to over estimate NO breakthrough on the aged catalyst. Whereas in reality, the temperatures and aging effects all have distribution profiles along the catalyst. If these effects are taken into account, the model should have done a better job.

3). The goal of the model is to help us understand the mechanisms inside a catalyst, and provide us a way to interpret the experimental data especially during transient operations, rather than to come up with a model that can precisely estimate tail-pipe emissions.

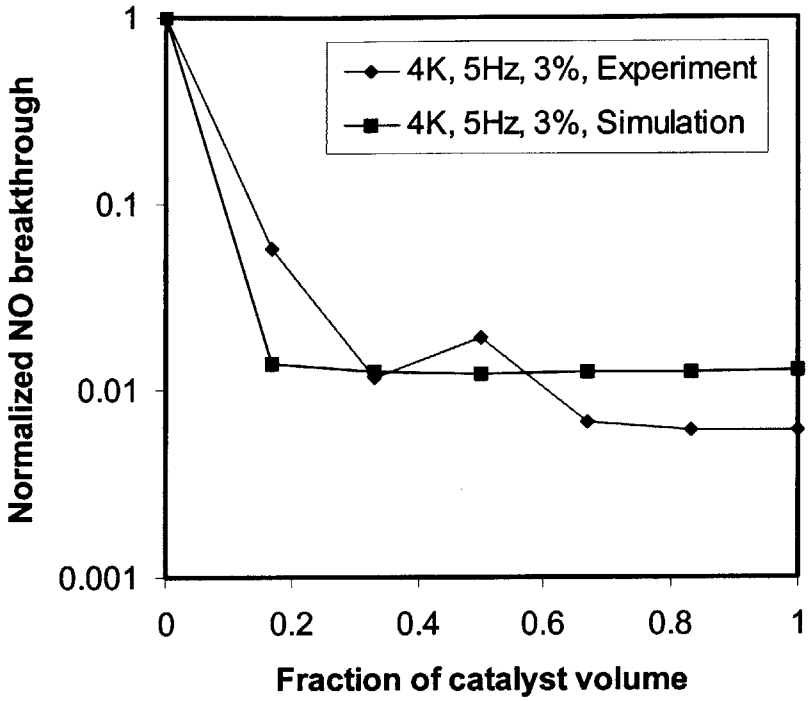

Fig. 8-17, Normalized time-average NO breakthrough along the catalyst. Operation conditions: 4k catalyst, 1600 rpm, and 0.5 bar intake, modulations at 5hz, ±3%

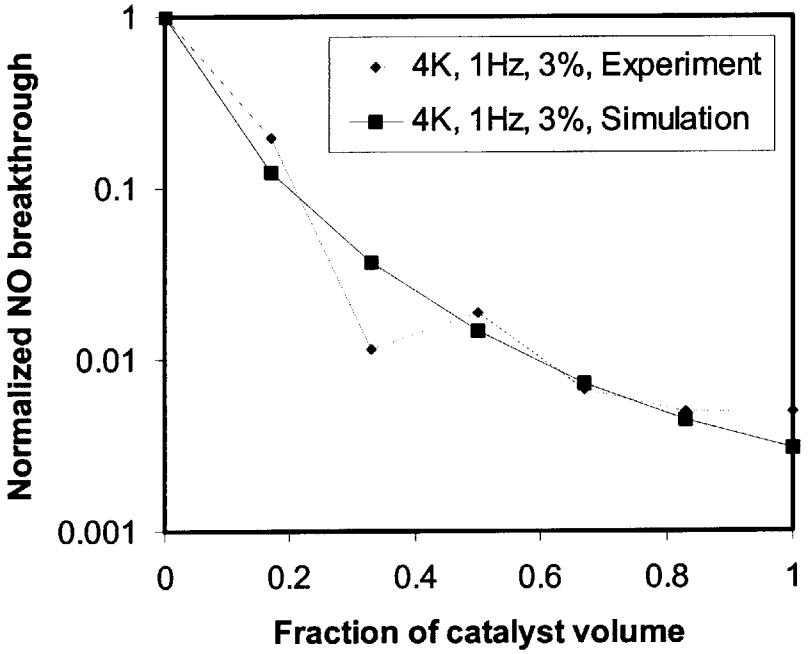

Fig. 8-18, Normalized time-average NO breakthrough along the catalyst. Operation conditions: 4k catalyst, 1600 rpm, and 0.5 bar intake, modulations at 1hz, ±3%

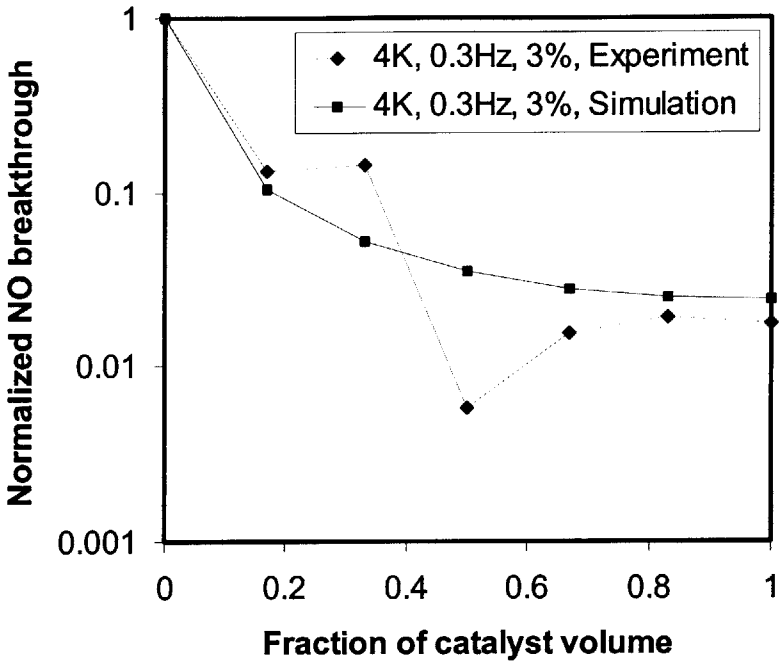

Fig. 8-19, Normalized time-average NO breakthrough along the catalyst. Operation conditions: 4k catalyst, 1600 rpm, and 0.5 bar intake, modulations at 0.3hz, ±3%

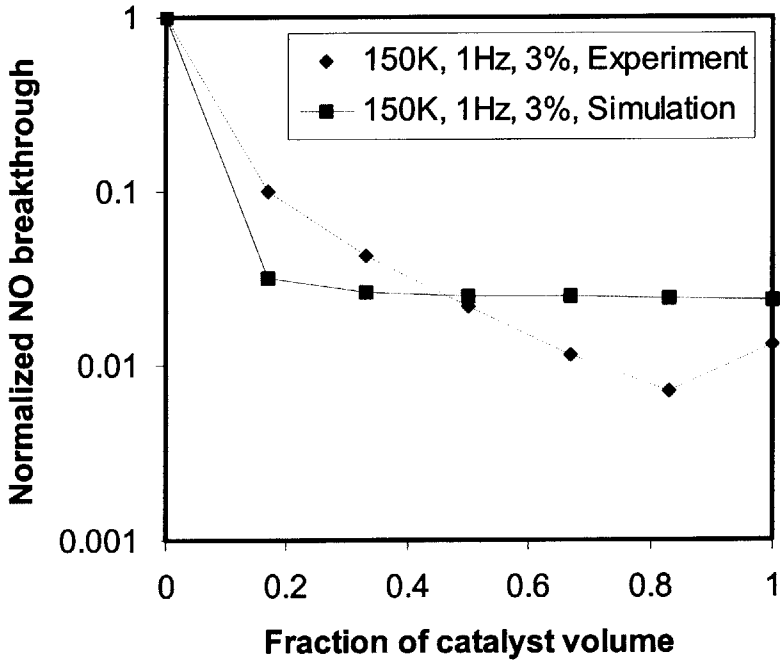

Fig. 8-20, Normalized time-average NO breakthrough along the catalyst. Operation conditions: 150k catalyst, 1600 rpm, and 0.5 bar intake, modulations at 1hz, ±3%

Chapter 9

Conclusions

The performance of three-way catalyst with oxygen storage capacity was assessed through engine experiments, bench scale tests and modeling. The following conclusions may be drawn.

9.1 Oxygen storage capacity quantification

For catalysts at different levels of aging (4,000 miles, 50,000 miles and 150,000 miles) and with fuels at different levels of sulfur content (7ppm, 33ppm, 266ppm, and 500ppm), the aging effects and fuel sulfur effects were found to act independently on the oxygen storage capacity. The aging effects on the oxygen storage capacity scales with $(age^{-0.84})$. The oxygen storage capacity is proportional to $\frac{1}{1+k' x_{SO3}}$ (k' = constant, x_{SO3} is mole fraction of SO_3 in the exhaust gas). The empirical value of (k') is 8.8×10^{-4}.

9.2 Air/fuel ratio modulation

Within a certain range of modulation, the NOx breakthrough is not sensitive to the mode of oscillation. However, when the frequency becomes too low, or the amplitudes become too large so that the cumulative amount of oxygen fed into the catalyst during the learn part of the modulation is close to the limit of storage capacity, NO breakthrough will substantially increase.

When the l modulation has a bias error, NO breakthrough occurs when the cumulative net O2 fed to the catalyst exceeds the OSC. Thus these results are quantitatively consistent with the OSC storage measurement results.

9.3 Loss of effectiveness as a result of aging effects

The catalytic reactions on a catalyst beyond the light-off temperature were found to be diffusion controlled. For the relatively new catalyst (4k miles) the NO reduction along the catalyst agrees with the theoretical laminar values with Sherwood number of 2.98 and 2.41 for square and triangular cross-section channels. As the catalyst ages, the reduction is still diffusion controlled, but the effective Sherwood number decreases exponentially with age. The degradation is more rapid in the front brick than in the rear one. For the dyno-aged catalysts, the characteristic decay "time" is 150k miles for the front brick and 270k miles for the road-aged ones.

9.4 Three-way catalyst modeling

A comprehensive practical model was developed. It is a one-dimension model, with a reduced set of reaction scheme. Oxygen storage and aging effects are taken into account empirically.

The model results reproduce quantitatively the phenomena observed in experiments and supports that the NO reduction is limited by the OSC.

Bibliography

[1] EPA 230-R-99-001, *Indicators of the Environmental Impacts of Transportation*, October 1999

[2] EPA 400-F-92-007, *Fact Sheet OMS-5*, August 1994

[3] EPA420-F-99-017, *Emission Facts*, May 1999

[4] EPA400-F-92-014, *Fact Sheet OMS-12: Milestones in Auto Emissions Control*, August 1994

[5] EPA, *Control of Air Pollution From New Motor Vehicles: Tier 2 Motor Vehicle Emissions and Gasoline Sulfur Control Requirements; Final Rule*, February 2000

[6] J.B. Heywood, *Internal Combustion Engine Fundamentals*, McGraw-Hill, 1988

[7] R.M. Heck, R.J. Farrauto, *Catalytic Air Pollution Control Commercial Technology Second Edition*, Wiley-Interscience, 2002

[8] Daimler-Chrysler Corporation, Se*rvice Manual-1998 Town & Country, Caravan, and Voyager*, 1997.

[9] Digalog Corp, *Series 1000A Dynamometer Controller-Revision A*, 1984

[10] Y. Kwon, et. al., *The effect of fuel sulfur content on the exhaust emissions from a lean-burn gasoline direct-injection vehicle marketed in Europe*, SAE 1999-01-3585, 1999

[11] Cambustion Ltd., *HFR 400 Fast Fid User Manual and Specifications TH 91.6*, 2001

[12] Cheng, W.K., Summers, T., Collings, N., *The Fast-Response Flame Ionization Detector*, Prog. Energy Combustion Science, Vol. 24, pp. 89-124, 1998

[13] Cambustion Ltd., *fNOx400 Fast Response Nitric Oxide Measurement System User Manual version 1.10*, 2001

[14] Y. Zhang and W.K. Cheng, *Fuel sulfur and aging effects on the oxygen storage capacity in three way catalytic converters*, JSAE Technical Paper No. 20030224, 2003

[15] National Institute of Standards and Technology, *NIST Standard Reference Database Number 69*, June 2005

[16] Rosemount Analytical, Inc., *Rosemount Analytical Model 880A Non-Dispersive Infrared Analyzer Instruction Manual*, 1998

[17] SAE, *Bosch Automotive Handbook 5th Edition*, 2000

[18] C.N. Satterfield, *Heterogeneous Catalysis in Practice*, McGraw-Hill Book Company, 1980

[19] Ertl, G., Knozinger, H., and Weitkamp, J., *Environmental Catalysis*, 1999

[20] I. Pauwels, *Microkinetics Modeling of Automotive Three-way Catalysts*, MIT master's degree thesis, 2003

[21] Y. Zhang, W. Cheng, *Fuel Sulfur and Aging Effects on the Oxygen Storage Capacity in Three-Way Catalytic Converters*, SAE 2003-01-1874 (a.k.a. JSAE 20030224), 2003

[22] Horriba Ltd., *MB-200 Air Fuel Ratio Sensor*

[23] Etas, *Lambda Meter LA4 User's Guide*, 2001

[24] Coordinating Research Council, *CRC Sulfur/LEV Program, CRC Project No. E-42*, December 1997

[25] S. Eriksson, et. al., *Deterioration of three-way automotive catalysts part II~Oxygen storage capacity at exhaust conditions*, SAE 930944, 1993

[26] K. Miyamoto, J. Takebayashi, T. Ishihara, H. Kido, K. Hatamura, *Measurement of Oxygen Storage Capacity of Three-way Catalyst and Optimization of A/F Perturbation Control to its Characteristics*, SAE Paper 2002-01-1094, 2002

[27] G. Smedler, S. Eriksson, M. Lindblad, H. Bernier, S. Lundgren, E. Jobson, *Deterioration of Three-Way Automotive Catalysts, Part II – Oxygen Storage Capacity at Exhaust Conditions*, SAE 930944, 1993

[28] T. Yamada, N. Hayakawa, Y. Kami, and T. Kawai, *Univeral Air-Fuel Ratio Heated Exhaust Gas Oxygen Sensor and Further Applications*, SAE 920234, 1992

[29] R.A. Jackson, et. al., *Chemical aspects of the dynamic performance of a three-way catalyst*, SAE 1999-01-0312, 1999

[30] R.A. Jackson, J.C. Peyton Jones, J. Pan, J.B. Roberts, P.R.N. Childs, *Chemical Aspects of the Dynamic Performance of a Three-Way Catalyst*, SAE 1999-01-0312, 1999

[31] Yamada, T., Hayakawa, N., Kami, Y., and Kawai, T., *Universal Air-Fuel Ratio Heated Exhaust Gas Oxygen Sensor and Further Applications*, SAE 920234, 1992

[32] T.J. Truex, *Interaction of Sulfur with Automotive Catalysts and the Impact on Vehicle Emissions – A Review*, SAE 1999-01-1543, 1999

[33] G. Bartley, B. Bykowski, S. Welstand, and D. Lax, *Effects of Catalyst Formulation on Vehicle Emissions with Respect to Gasoline Fuel Sulfur Level*, SAE 1999-01-3675, 1999

[34] C.H. Schleyer, J. Eckstrom, K.D. Eng, J. Freel, R.A. Gorse, M. Natarajan, R.F. Gunst, A.M. Schlenker, *Reversibility of Sulfur Effects on Emissions of California Low Emission Vehicles*, SAE 1999-01-1544, 1999

[35] K. Koseki, T. Uchiyama, M. Kawamura and S. Sembokuya, *A Study on the Effects of Sulfur in Gasoline on Exhaust Emissions*, SAE 2000-01-1878, 2000

[36] J.M. Lyons, D. Lax, S. Welstand, *Investigation of Sulfur Sensitivity and Reversibility in Late-Model Vehicles*, SAE 1999-01-3676, 1999

[37] H.J. Stein, N.G. Elliott, J.P. Pochic, *European Program on Emissions, Fuels and Engine Technology (EPEFE) vehicle and engine testing procedures*, SAE 961068, 1996

[38] J. Baronick, B. Heller, G. Lach, B. Ramacher, *Impact of sulfur in gasoline on nitrous oxide and other exhaust gas components*, SAE 2000-01-0857, 2000

[39] J.C. Summers, J.F. Skowron, W.B. Williamson, K.I. Michell, *Fuel Sulfur Effects on Automotive Catalyst Performance*, SAE 920588, 1992

[40] Twu, J., et. al, *Raman Spectroscopy Studies on the Sulfation of Cerium Oxide*, App. Cat. B: Environ., 12 pp. 309-324, 1997

[41] Waquif, M., et. al., *Study of Ceria Sulfation*, App. Cat. B: Environ., 11 pp. 193-205, 1997

[42] Bazin, P., et. al., *Influence of Platinum on Ceria Sulfation*, App. Cat. B: Environ., 13 pp. 265-274, 1997

[43] C. Smutzer, *Behavior of Fresh and Aged Catalysts in Response to Engine Control Perturbations*, MIT master's degree thesis, 2002

[44] C.N. Montreuil, *Modeling current generation catalytic converters: laboratory experiments and kinetic parameter optimization~Steady state kinetics*, SAE 920096, 1992

[45] J. Lienhard, *A Heat Transfer Textbook Third Edition*, Phlogiston Press, 2001

[46] R. Reid, J. Prausnitz, B. Poling, *The Properties of Gases and Liquids Third Edition*, McGraw-Hill Press, 1987

[47] A.F. Mills, *Heat Transfer 2nd Edition*, Prentice Hall, 1999

[48] M.V. van der Schoot, et al., *Deterioration of automotive catalytic converters: Physical catalyst characterization*, SAE 2001-01-3691, 2001

[49] L.C. Young and B.A. Finlayson, *Mathematical Models of the Monolithic Catalytic Converter, Part 1. Development of Model and Application of Orthogonal Collocation*, AIChE J., 22(2)(1976) 331-343, 1976

[50] Heck, R.H., Wei, J. and Katzer, R.J., *Mathematical Modeling of Monolithic Catalysts*, AIChE J. 22 477-484, 1987

[51] Lee, S.T. and Aris, R., *On the Effects of Radiative Heat Transfer in Monoliths*, Chem. Engng. Sci. 32, 827-837, 1977

[52] N. Otto and W.J. LeGray, *Mathematical Models for Catalytic Converter Performance*, SAE 800841, 1980

[53] S.H. Oh and J.C. Cavendish, *Transients of Monolithic Catalytic Converters: Response to Step Changes in Feed Stream Temperature as Related to Controlling Automobile Emissions*, Ind. Eng. Chem. Prod. Res. Dev. 21, 29-37, 1982

[54] S.E. Voltz, C.R. Morgan, D. Liederman, and S.M. Jacob, *Kinetic Study of Carbon Monoxide and Propylene Oxidation on Platinum Catalysts*, Ind. Eng. Chem. Prod. Res. Dev. , 12(4), 1973

[55] S. Siemund and J.P. Leclerc, *Three-Way Monolithic Converter: Simulations Versus Experiments, Chemical Engineering Science*, Vol. 51(15), pp 3709-3720, 1996

[56] K.N. Pattas, A.M. Stamatelos, P.K. Pistikopoulos, G.C. Koltsakis, and P.A. Konstandinidis, *Transient Modeling of 3-Way Catalytic Converters*, SAE 940934, 1994

[57] G.C. Koltsakis, P.A. Konstantinidis, A.M. Stamatelos, *Development and Application of Mathematical Models for 3-Way Catalytic Converters*, Applied Catalysis B: Environmental 12, 161-191, 1997

[58] I. Gottberg, J.E. Rydquist, O. Backlund, S. Wallman, W. Maus, R. Brueck, H. Swars, *New Potential Exhaust Gas After-treatment for Clean Car Legislation*, SAE 910840, 1991

[59] R.K. Herz, *Dynamic Behavior of Automotive Catalysts. 1. Catalyst Oxidation and Reduction*, Ind. Eng. Chem. Prod. Res. Dev. 20, 451-457, 1981

[60] E. Jobson, M. Laurell, E. Högberg, H. Bernier, S. Lundgren, G. Wirmark, G. Smedler, *Deterioration of Three-Way Automotive Catalysts, Part I – Steady State and Transient Emission of Aged Catalyst*, SAE 930937, 1993

[61] T. Shamim, et. al., *Comparison of Chemical Kinetic Mechaniss in Simulating the Emission Characteristics of Catalytic Converters*, SAE 2000-01-1953, 2000

[62] G. Groppi, et. al., *A Comparison of Lumped and Distributed Models of Monolith Catalytic Combustors*, Chemical Engineering Science, Vol. 50(17) pp. 2705-2715, 1995

[63] A. Nakhjavan, et. al., *Numerical Analysis of the Transient Performance of High-Temperature Monolith Catalytic Combustors: Effect of Catalyst Porosity*, Chemical Engineering Science, Vol. 50(14), pp. 2255-2262, 1995

[64] D.K.S. Chen and K.E. Cole, *Numerical Simulation and Experimental Verification of Conversion and Thermal Responses for a Pt/Rh Metal Monolithic Converter*, SAE 890798, 1989

[65] G.C. Koltsakis, et. al., *Modeling Dynamic Phenomena in 3-Way Catalytic Converters*, Chemical Engineering Science Vol. 54 4567-4578, 1999

[66] W. Cai and N. Collings, *A Catalytic Oxidation Sensor for the on Board Detection of Misfire and Catalyst Efficiency*, SAE 922248, 1992

[67] S. Sriramulu, et. al., *Microkinetics Modeling of Catalytic Converters*, SAE 2001-01-0936, 2001

[68] C.N. Montreuil, et. al., *Modeling Current Generation Catalytic Converters: Laboratory Experiments and Kinetic Parameter Optimization – Steady State Kinetics*, SAE 920096, 1992

[69] Skorodumova, N.V., Simak, S.I., Lundqvist, B.I., Abrikosov, I.A., and Johansson, B., *Quantum Origin of the Oxygen Storage Capability of Ceria*, Physical Rev. Letters, 89, 16, 2002.

Appendix A

The calculation of mole fraction of oxygen in the lean exhaust gas is given as in equation (A.1). For fuel with H to C molar ratio of m, O to C ratio of n, and for $\lambda \geq 1$, assuming that the fuel burns completely to CO_2 and H_2O, the combustion may be represented by:

$$\begin{aligned} CH_mO_n + \lambda(1+m/4-n/2)(O_2+3.773N_2) \longrightarrow \\ CO_2 + \frac{m}{2}H_2O + 3.773\lambda(1+\frac{m}{4}-\frac{n}{2})N_2 \\ +(\lambda-1)(1+\frac{m}{4}-\frac{n}{2})O_2 \end{aligned} \qquad (A.1)$$

The mole fraction x_{O2} of O_2 is therefore, given by

$$x_{O2} = \frac{(\lambda-1)(1+\frac{m}{4}-\frac{n}{2})}{1+\frac{m}{2}+3.773\lambda(1+\frac{m}{4}-\frac{n}{2})} \qquad (A.2)$$

Appendix B

In the flow reactor experiments, NO and CO reaction is used to measure NO reduction rate and effective diffusion rate. From those results the aging effects of a catalyst brick can be quantified.

The reaction between NO and CO is the following:

$$aNO + CO \rightarrow CO_2 + (1- a/2)N_2 + (a-1)N_2O$$

So, the equation shows that when a=1, then the product of NO will be solely N2; whereas when a=2 then the product will be all N2O. The reaction is temperature dependent. At low temperatures, the reaction tends to produce more N2O, at high temperatures, it tends to produce more N2.

The plots in Fig. A-1 shows that at the temperatures the experiments were conducted, the amount of N2O is negligible.

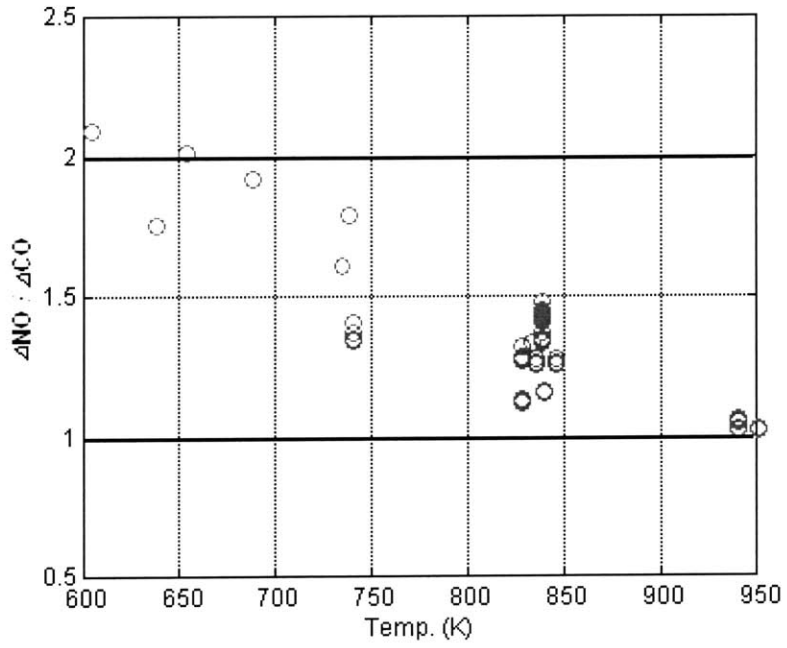

Fig. A-1, Ratio of NO consumption over CO consumption (dNO/dCO) as a function of temperature. The plots help interpret the amount of N2O produced.

Appendix C

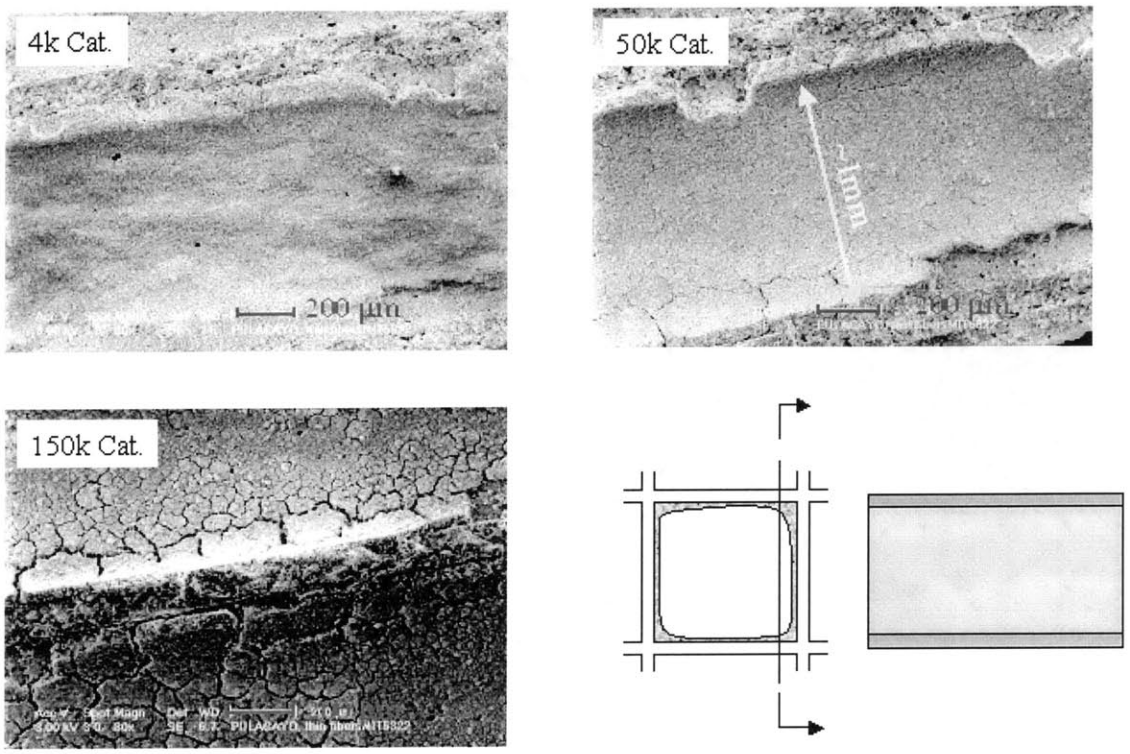

Fig. B-1, 80X SEM view of 4K, 50K, and 150K catalysts washcoat

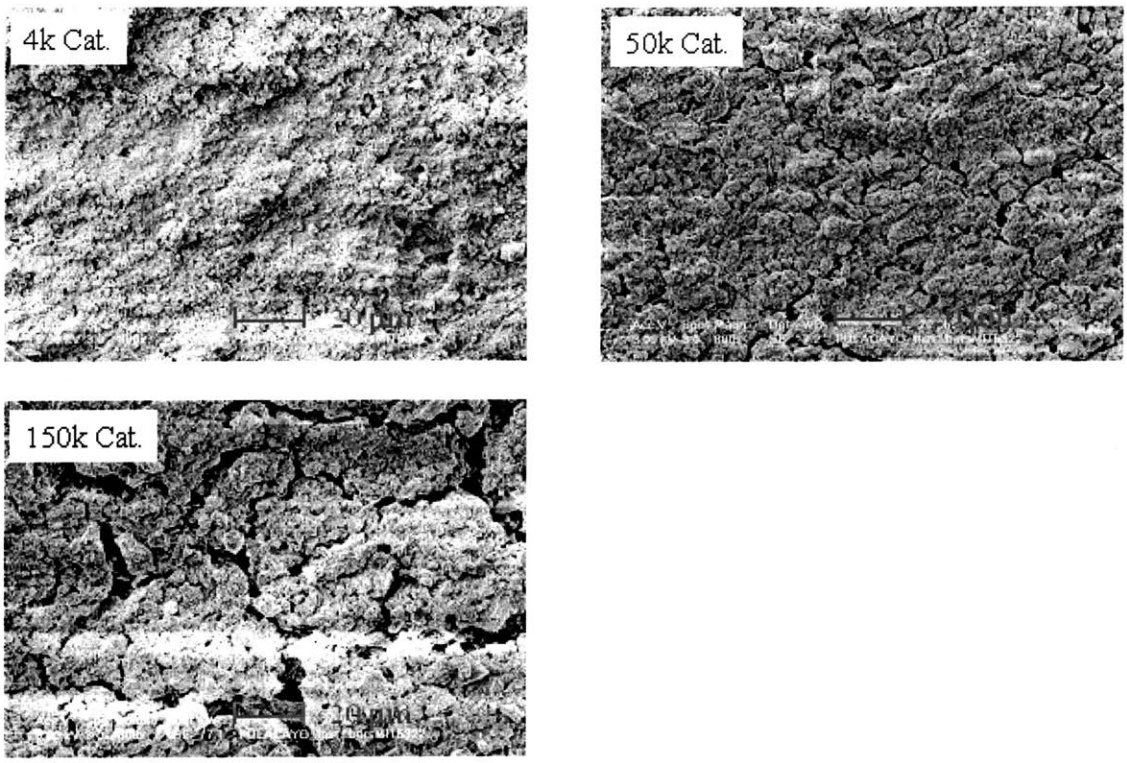

Fig. B-2, 800X SEM view of 4K, 50K, and 150K catalysts washcoat

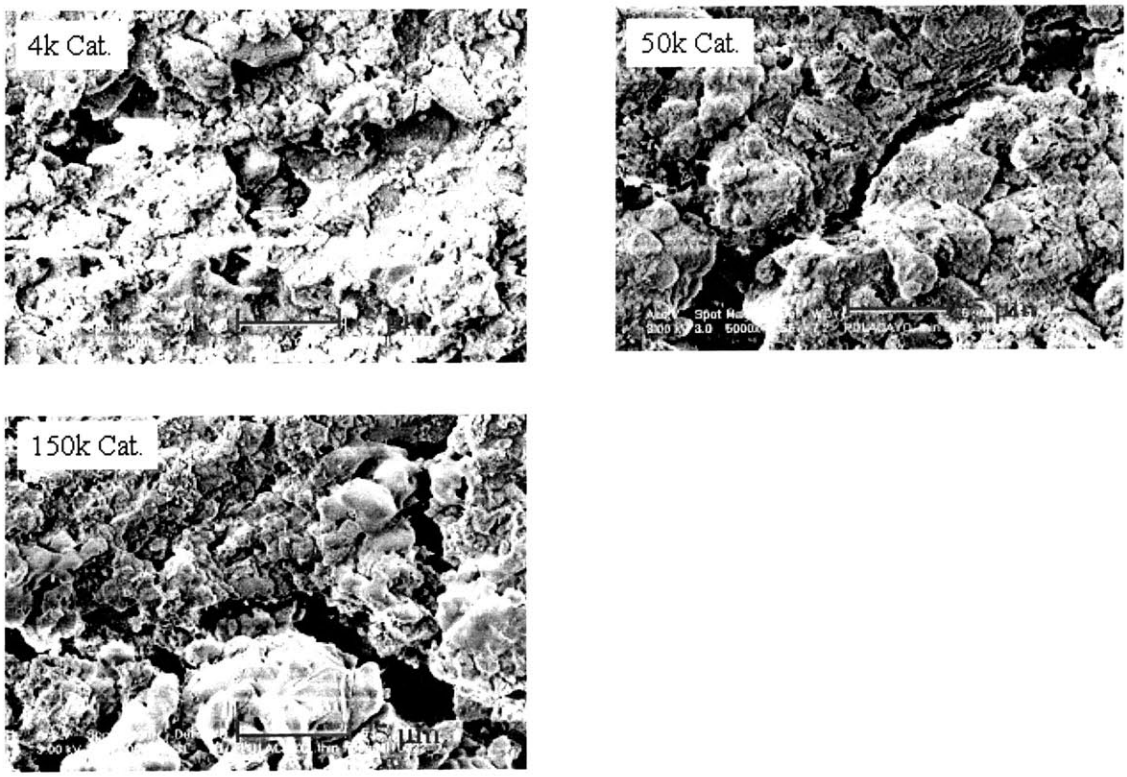

Fig. B-3, 5000X SEM view of 4K, 50K, and 150K catalysts washcoat

Appendix D

$$H_2 + \tfrac{1}{2} O_2 \rightarrow H_2O \quad (1)$$

$$CO + \tfrac{1}{2} O_2 \rightarrow CO_2 \quad (2)$$

$$C_3H_6 + 4\tfrac{1}{2} O_2 \rightarrow 3CO_2 + 3H_2O \quad (3)$$

$$CH_4 + 2O_2 \rightarrow CO_2 + 2H_2O \quad (4)$$

$$H_2 + NO \rightarrow H_2O + \tfrac{1}{2} N_2 \quad (5)$$

$$CO + NO \rightarrow CO_2 + \tfrac{1}{2} N_2 \quad (6)$$

$$C_3H_6 + 9NO \rightarrow 3CO_2 + 3H_2O + 4\tfrac{1}{2} N_2 \quad (7)$$

$$CH_4 + 4NO \rightarrow CO_2 + 2H_2O + 2N_2 \quad (8)$$

$$CO + H_2O \rightarrow CO_2 + H_2 \quad (9)$$

$$(Ce_2O_3)_2 + O_2 \leftrightarrow (CeO_2)_4 \quad (10)$$

$$(CeO_2)_2 + H_2 \rightarrow (Ce_2O_3)_2 + H_2O \quad (11)$$

$$(CeO_2)_2 + CO \rightarrow (Ce_2O_3)_2 + CO_2 \quad (12)$$

$$2H^* \rightarrow H_2 + 2S \quad (13)$$

$$CO^* \rightarrow CO + S \quad (14)$$

Reaction	Pre-exponential factor (mol K/m^3 s)	Activation energy (J/mol)
1	6E10	-12508
2	6E10	-12508
3	3e11	-12629
4	4e11	-15034
5	3.061e9	-8771
6	3.061e9	-8771
7	--	--
8	--	--
9	6e5	-12629
10	f: 3e8; b: 3e6	-10825
11	1.5e8	-10825
12	1.5e8	-10825
13*	f: 3e8; b: 3e6	-10825
14*	f: 3e8; b: 3e6	-10825

Table D-1, Kinetics constants used in the model

* Reaction rates for 13, 14 were calibrated with rich-to-lean step experiments